A Study of Magnetic Materials Based Upon the Organic Acceptor 7,7,8,8-Tetracyanoquinodimethane

ADAM BERLIE

A Study of Magnetic Materials Based Upon the Organic Acceptor 7,7,8,8-Tetracyanoquinodimethane

Adam Berlie

A Thesis presented for the degree of
Doctor of Philosophy

X-ray Scattering and Magnetism Group
Photonics, Sensors and Materials Group
Physics Department
Durham University
South Road
Durham
United Kingdom

Febuary 2013

"It's 106 miles to Chicago, we've got a full tank of gas, half a pack of cigarettes, it's dark... and we're wearing sunglasses"

"Hit it"

A Study of TCNQ Based Magnetic Materials

Adam Berlie

Submitted for the degree of Doctor of Philosophy
Febuary 2013

Abstract

The study of organic based materials is a flourishing area of interest as the physical/chemical properties of the compound can be tuned through functionalisation or simple chemical changes to the organic component. This thesis will focus on the magnetic behaviour of metal-organic magnetic materials where a variety of techniques will be used to study the magnetism such as bulk magnetometry and muon spin relaxation. As well as the magnetic properties, some comments will be made on the chemical properties such as molecular structure. The thesis begins with an overview of the theory of magnetism and details regarding experimental techniques.

$Ni(TCNQ)_2$ is a recently discovered non-solvated metal organic magnet that was reported to show ferromagnetic behaviour below 20 K where there was evidence of a glassy magnetic component. This thesis reports the synthesis of both a protio and deutero form of the material where upon deuteration of the TCNQ molecule, a shift in critical temperature (T_c) was observed to a higher temperature by approximately 15%. Diffraction experiments were conducted to attempt to provide information on the atomic structure however this proved unsuccessful. Magnetometry experiments showed a ferromagnetic transition at approximately 20 K in the deuterated and 17 K in the protonated materials where at low temperatures the sample appeared to be a three-dimensional magnetically order material. Muon spin relaxation studies were conducted on the deuterated sample which showed two peaks within the dynamical relaxation in zero-field; one associated with the transition and a low temperature

(5 K) spin freezing effect where it is believed there are interactions between magnetic clusters that enter a quasi-static regime. It may be possible that the glassy component and the ferromagnetic behaviour of the material are not due to the same exchange mechanism or magnetic interactions.

KTCNQ is a compound that undergoes a spin-Peierls transition, T_{sp}, at approximately 400 K where below this temperature there is a dimerisation of the TCNQ radical spins that couple antiferromagnetically and the system goes from a conductive to insulating state. In an attempt to tune the TCNQ-TCNQ interactions different materials were synthesised where the protons on the TCNQ ring were substituted for fluorine and bromine atoms. On substitution of the protons with other elements a dramatic shift in T_{sp} was observed where for the fluorine based compounds T_{sp} = 150 K and the KTCNQ-Br_2 compound showed no evidence of a transition. Both KTCNQ-H_4 and KTCNQ-F_4 were studied further using muon spin relaxation where the transition is clearly modelled using a stretched exponential where an increase in electronic fluctuation rate is shown by a gradual move from an exponential to Gaussian relaxation. At low temperatures the relaxation again changes and within the KTCNQ-F_4 sample 2 F-μ^+-F states are observed.

Another controversial organic based magnet is Ni_2TCNQ which was first synthesised in 2007. Here a study of a similar material is reported where the TCNQ has been swapped for $TCNQF_4$ and the magnetic properties are shown to be a result of nickel nanoparticles trapped within a metal-organic or purely organic based matrix. The room temperature ferromagnetism is not strictly due to only the bulk Ni particles as this would result in a blocking temperature below 20 K and so the matrix is shown to play an important role. The size of the Ni nanoparticles was shown to be tuneable when using different solvents within the reaction, generally use of chlorinated solvents lead to rapid decomposition of the starting material, $Ni(COD)_2$ and lead to larger nanoparticles, however use of a nitrile based solvent led to Ni clusters that were approximately 1 nm in size and dispersed within the matrix. A novel scaling of the magnetisation curves as a function of field showed that once the ferromagnetic component had been subtracted the matrix or Ni based clusters show an

antiferromagnetic ground state at low temperature. The final chapter describes an investigation of the starting material, $Ni(COD)_2$ which was studied using a SQUID magnetometer where it was shown that there was a high level of magnetic impurities, which was attributed to small Ni clusters that showed a similar scaling relationship of the magnetisation as for the Ni_2TCNQF_4 based material. This demonstrates the inappropriate nature of $Ni(COD)_2$ as a starting material for metal-organic based magnetic compounds.

Declaration

The work in this thesis is based on research carried out within the X-ray Scattering & Magnetism and Photonics, Sensors & Materials Groups, Condensed Matter Physics Section, Physics Department, Durham University, UK. No part of this thesis has been submitted elsewhere for any other degree or qualification and it is all my own work unless referenced to the contrary in the text.

Acknowledgements

Firstly I would like to thank the dynamic duo of the physics department, Ian Terry and Marek Szablewski. Ian has taught me a lot over the past few years always taking the time to talk to me about many topics within physics, not just magnetism, and at times his enthusiasm for the subject has been a real inspiration. I have equally learnt a huge amount about TCNQ based chemistry/physics from Marek and throughout my PhD Marek has kept the chemist in me sane when surrounded by a sea of physicists. My thanks and gratitude can not be expressed enough for giving me the chance to study/work towards my PhD and it has been a fun ride.

I would also like to thank other members of the physics department: Duncan McCallum for always being on hand to help and not badgering us for making his life harder by buying dangerous chemicals, John Dobson for helping with everything in room 14, the audio visual team, especially Stephen Berry for being patient when helping to make a great pictorial description of the μSR technique, Budhika Mendes for help with the TEM (that destroyed my samples) and his suggestion that girls should wear skirts more often, Mark Raine for help with heat capacity and AC susceptibility measurements, Tom Lancaster for his helpful discussions about data, Gary Oswald (although from chemistry) for taking XRD data for me and lastly but by no means least Graham Cross for his entertainment and lessons on what it means being a man of the '70's'. Lastly I need to give my thanks to Sean Giblin for all his help through out my PhD with experiments helping with some of my rather simple questions on muons and for his general help with things such as simply hanging out in Dallas.

Lastly I would like to thank my friends and my family. Through out my PhD my friends have been a source of relief and there are a few that deserve mentioning: Proggy Dan, Matthew Thom for always taking the time, Valerio Ferracci, the Italian Stallion and Simon Titley for always having an open home. I would also like to thank Ross Colman for his teachings on Rietveld refinement.

My family not only show me huge amounts of support but also love. It saddens me that my Father and Aunty Eleanor could not be around to celebrate and enjoy this next step of my life with me. My brother Marc is a source of inspiration, has helped me out on many occasions and has always shared my passion for music. My sister Leila has always shown me a huge amount of love and has always been strong when she needed to be which has in turn given me strength. Finally I would like to thank my mother. I would not be here without the love and support of my mum, although life has had it's up and downs she has always been there for me and because of her selflessness I have managed to get to where I am. I owe everything I am to her. L'chayim!

Contents

List of Figures

List of Tables

Chapter 1

Introduction

Over the latter part of the last century the study of organic based magnetism has seen large amounts of interest as it provides a route to making new and novel magnetic materials. Organic molecules can show many remarkable properties such as electrical conductivity changes arising from excitation using radiation sources such as light or even simple polymerisation of organic units. In fact carbon is the only element with the energetics making it suitable for creating long chain carbon based structures [1].

(Cyclohexa-2,5-diene-1,4-diylidene)-dimalononitrile also known as 7,7,8,8-tetracyanoquinodimethane (TCNQ) was first discovered in the 1960's by Dupont researchers Acker and Hertler [1] who commented on the molecule's "exceptional" property to form a radical anion, which has a very low activation energy, where it essentially behaves as an $S = \frac{1}{2}$ (S is the spin angular momentum) system with a quenched orbital angular momentum ($L = 0$ and therefore $J = \frac{1}{2}$[2]) [2]. The structure of a neutral TCNQ molecule is shown in figure 1.1 which displays the symmetrical, flat arrangement of the electron accepting moieties and from the conjugated π-bonds, one can see why this is able to stabilise a radical so easily.

[1] The halides also provide some interest here such as the various polyiodides that are known

[2] J is the total angular momentum where $J = L \pm S$

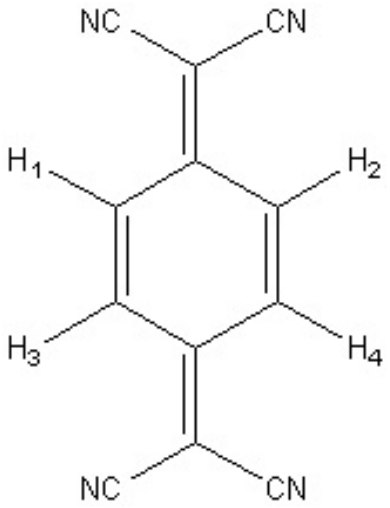

Figure 1.1: 7,7,8,8-Tetracyanoquinodimethane (TCNQ).

Another useful property of TCNQ is the ability to undergo displacement reactions where nucleophilic attack from an amine can substitute one or more of the cyano groups. Interestingly two cyano groups at one end of the TCNQ molecule can be substituted with amine groups however this then renders the other end inert and not susceptible to attack by a similar mechanism [3]. Molecules of this nature can also form zwitterions[3] and they can have large molecular hyperpolarisabilities due to their large dipole moments and conjugation which makes them of valuable interest in the field of non-linear optics [4].

Synthesising TCNQ based derivatives, where one can substitute hydrogens on the aromatic ring (i.e. H_1-H_4 on figure 1.1), is also possible but is a more involved process where the TCNQ is assembled from the starting materials specific to the desired product rather then a direct substitution of H_n, this ultimately results in a plethora of TCNQ derivatives being available such as $TCNQF_4$ (2, 3, 5, 6-tetrafluro-7, 7, 8, 8-tetracyanoquinodimethane) or $TCNQBr_2$ (2, 5-dibromo-7, 7, 8, 8-tetracyanoquinodimethane) [5].

One of the first organic metals to be discovered was TTF-TCNQ (TTF=tetrathiafulvalene

[3]A zwitterion is an ion that has both a positive and negative charge on the same group of atoms which can be formed from having both an acidic and basic group within the same molecule, such as an amino acid which has an overall net charge of 0

which is an electron donor) in which metallic conductivity was observed from room temperature down to ∼60 K [6]. The TCNQ molecules form 1D stacks within this system where the charges are evenly spaced along the stack at high temperatures. At low temperatures the system undergoes a structural phase change where the TCNQ molecules dimerise and the charges become localised on each dimer. The cause of the metal-insulator transition is this instability within the sample that causes a Peierls distortion where the TCNQ units dimerise leading to non-metallic conduction where the charges are localised on each TCNQ dimer rather then along the stack, which would lead to a low conductivity [7]. There are other more recent examples of metal-TCNQ charge transfer conductors such as CuTCNQ and AgTCNQ which show interesting properties with the conduction believed to be along the quasi-1D stacks of TCNQ [8, 9]. Both samples show electrical switching as a memory effect even in a thin film form [10].

TCNQ has also been used extensively within magnetic materials. Examples date back to the explosion of research that was coupled with the observation of electrical conductivity of TCNQ based materials. Alkali metal-TCNQ salts were shown to not only exhibit a Peierls distortion that impaired the electronic properties but also a spin-Peierls transition, the magnetism on TCNQ units couples antiferromagnetically causing a dimerisation of the spins [11]. Other examples of magnetic materials include the $[Fe(Cp^*)]_2[TCNQ]$ charge transfer salt where ferromagnetism has been observed at low temperatures and which will also be discussed later in subsequent chapters [12, 13]. It should also be noted that zwitterionic materials can also display magnetic properties and recently it has been reported that betaine derivatives display a strong local Heisenberg antiferromagnetically coupled spins [14].

One advantage of organic materials over inorganics is that organic molecules can undergo chemical reactions to alter their structure with relative ease which can create subtle changes in their physical properties. Organic based materials can also be made at room temperature where as inorganic magnetic materials such as ceramics often require extensive heat treatment using furnaces which also makes the synthetic procedure of organics much cheaper. From the above introduction it should

be clear that TCNQ itself has a wide range of interesting properties including optical, electrical conductivity and magnetism within new novel based organic materials, which it is hoped that one can combine these physical properties where the magnetism/electrical conductivity could be coupled with a change on absorbancy of optical radiation for example. The TCNQ moiety itself can be changed subtly though chemical reactions whereby these changes can lead to slight changes in the physical properties and ultimately lead to tuneable or 'designer' conductors/magnets.

Within this thesis various topics will be discussed that relate to TCNQ based materials. The first is a 'glassy' ferromagnetic Ni-TCNQ material originally synthesised by Cléarc *et al.* [15] where further studies using muon spin relaxation reveal more insight regarding the ferromagnetic transition. The second topic is the alkali-TCNQ spin-Peierls system, KTCNQ. Muon spin relaxation was used to study the transition as well as other derivatives being synthesised which show a shift in the critical temperature. The third is a compound composed of Ni nanoparticles in a metal-organic matrix containing TCNQ where the blocking temperature of the particles does not directly correspond to their size which means that the matrix has a significant dramatic effect on hardening the small nanoparticles. A further study of low moment metal-clusters is also included in this work which ties into the study of the nanoparticulate composite system.

1.1 Publication List

Below is a list of publications that are associated with the work within this thesis:

- A Sample Holder For Measuring The Magnetic Properties of Air Sensitive Compounds - A. Berlie, I. Terry and M. Szablewski. *Meas. Sci. Technol.* **22** (2011) 017002
- A Magnetic Study of Low Moment Nickel Clusters Formed From the Solid State Decomposition of Nickel Bis-1,5-cycloctadiene - A. Berlie, I. Terry and M. Szablewski. *to be submitted to Phys. Rev. B.* 2013

- Controlling Nickel Nanoparticle Size in an Organic/Metal-Organic Matrix Through the Use of Different Solvents - A. Berlie, I. Terry and M. Szablewski. *to be submitted to Advanced Materials* 2013

- A Muon Spin Relaxation Study of the Metal-Organic Magnet: $Ni(TCNQ)_2$ - A. Berlie, M. Szablewski, S. R. Giblin, T. Lancaster and I. Terry. *J. Appl. Phys.* Accepted for publication 2012

- Cluster Glass Behaviour Within the Metal-Organic Ferromagnet: $NiTCNQ_2$ - A. Berlie, M. Szablewski, I. Terry. *In preparation.* 2013

Bibliography

[1] D. S. Acker and W. R. Hertler. *J. Am. Chem. Soc.* **84** (1962) 3370

[2] L. R. Melby, R. J. Harder, W. R. Hertler, W. Mahler, R. E. Benson and W. Mochel. *J. Am. Chem. Soc.* **84** (1962) 3374

[3] W. R. Hertler, H. D. Hartzler, D. S. Acker and R. E. Benson. *J. Am. Chem. Soc.* **84** (1962) 3387

[4] M. Szablewski. *J. Org. Chem.* **59** (1994) 954

[5] R. C. Wheland and E. L. Martin. *J. Org. Chem.* **40** (1975) 3101

[6] J. Ferraris, D. O. Cowan, V. V. Valatka and J. H. Perlstein. *J. Am. Chem. Soc.* **95** (1973) 948

[7] L. B. Coleman, M. J. Cohen, D. J. Sandman, F. G. Yamagishi, A. F. Carito and A. J. Heeger. *Solid State Sommun.* **12** (1973) 1125

[8] R. S. Potember, T. O. Poeheler and D. O. Cowan. *App. Phys. Letts.* **34** (1979) 405

[9] S. A. O'Kane, R. Clérac, H. Zhao, X. Ouyang, J. R. Galan-Mascaros, R. Heintz and K. R. Dunbar. *J. Solid State Chem.* **152** (2000) 159

[10] R. S. Potember, T. O. Poeheler, and R. C. Benson. *App. Phys. Letts.* **41** (1982) 548

[11] Y. Takaoka and K. Motizuki. *J. Phys. Soc. Jpn.* **47** (1979) 1752

[12] A. H. Reis Jr., L. D. Preston, J. M. Williams, S. W. Peterson, G. A. Candela, L. J. Swartzendruber and J. S. Miller. *J. Am. Chem. Soc.* **101** (1979) 2756

[13] J. S. Miller, A. H. Reis Jr., E. Gebert, J. J. Ritski, W. R. Salaneck, L. Kovnat, T. W. Cape and R. P. V. Duyne. *J. Am. Chem. Soc.* **101** (1979) 7111

[14] W. A Shelton, E. Aprá, B. G. Sumpter, A. Saraiva-Souza, A. G. Souza Filho, J. Del Nero and V. Meunier. *Chem. Phys. Letts.* **511** (2011) 294

[15] R. Clérac, S. O'Kane, J. Cowen, X. Ouyang, R. Heintz, H. Zhao, M. J. Bazile and K. R. Dunbar. *Chem. Mater.* **15** (2003) 1840

Chapter 2

Theory of Magnetism

A form of magnetism is present in all materials whether it be diamagnetism, paramagnetism or a form of ferromagnetism. Both paramagnetism and ferromagnetism are a consequence of systems where there are unpaired electrons and within these regimes the total spin quantum number is non-zero ($S \neq 0$). These spins can interact with each other and when a magnetic field is applied, the magnetic dipoles can align. A measure of the alignment of the spins is from the magnetisation (M) which is the magnetic dipole per unit volume or mass. The volume magnetic susceptibility (χ) is a dimensionless figure where $\chi = \frac{M}{H}$, but alternatively, the magnetic molar susceptibility (χ_m) or the mass susceptibility (χ_g) in units of m^3kg^{-1} is given. This chapter will outline some of the basic concepts underlying magnetic materials much of which is covered in more detail in standard text books [1–3].

2.0.1 Diamagnetism

Diamagnetism is present in all atoms as a result of the orbital motion of the core electrons. Lenz's law states that when the flux through an electrical circuit is changed an induced current is set up to oppose the flux change. The effect of the electronic charges that orbit an atom within an applied field create a magnetic moment that opposes the field with an effect that is temperature independent. The diamagnetic

susceptibility can be described by the classical Langevin equation,

$$\chi = \frac{\mu_0 N \mu}{B} = -\frac{\mu_0 N Z e^2}{6m} \left\langle r^2 \right\rangle, \tag{2.1}$$

where B is the applied field flux density, N is the number of atoms or ions, Z is the number of electrons, m is the mass and r is the atomic/ionic radius.

Despite diamagnetism occurring in all materials it is normally overshadowed by other forms of magnetism where the magnetic moment of the atoms can align with the applied field.

2.0.2 Paramagnetism

If a system has a non-zero spin quantum number (where there are unpaired electrons) the magnetic moment of the electrons, in the absence of an applied field, will have random orientations and so the net magnetisation will be zero. When a magnetic field is applied these moments on the unpaired electrons can align with the field but are considered to be completely independent of one another. A paramagnetic material shows a positive magnetic susceptibility and for example, can be found in molecules with unpaired electrons such as organic free radicals (i.e. triphenylmethyl) as well as within defects in solid systems.

Quantum mechanics dictates that the orientation of an electrons spin can only occupy specific directions that are degenerate in the absence of a field. The magnetic moment of an atom in free space is given by

$$\mu = \gamma \hbar \mathbf{J} = -g \mu_B \mathbf{J}, \tag{2.2}$$

where the total angular momentum $\hbar\mathbf{J}$ is the summation of the orbital $\hbar\mathbf{L}$ and spin $\hbar\mathbf{S}$ angular momenta where this coupling of the spin and orbital angular momenta

is known as Russel Saunders Coupling. γ is the gyromagnetic ratio[1] and g is the *Landé g factor* defined by

$$g = 1 + \frac{J(J+1) + S(S+1) - L(L+1)}{2J(J+1)}. \tag{2.3}$$

The energy level of a system in a magnetic field is

$$U = -\mu \cdot \mathbf{B} = m_J g \mu_B B. \tag{2.4}$$

If a magnetic field is applied to an energy level there is splitting, i.e. if $S = \frac{1}{2}$ then the values of $m_s = \frac{1}{2}$ or $-\frac{1}{2}$. The lower energy level is where the moment of the electron is parallel with the applied field. When considering a single free electron $g = 2$ and $m_J = \pm\frac{1}{2}$ therefore $U = \pm\mu_B B$ where the negative value is parallel to the field. The population of the energy levels can be calculated using Boltzman statistics:

$$\frac{N_1}{N_{Tot}} = \frac{e^{\frac{\mu B}{k_B T}}}{e^{\frac{\mu B}{k_B T}} + e^{\frac{-\mu B}{k_B T}}}, \tag{2.5}$$

$$\frac{N_2}{N_{Tot}} = \frac{e^{\frac{-\mu B}{k_B T}}}{e^{\frac{\mu B}{k_B T}} + e^{\frac{-\mu B}{k_B T}}}, \tag{2.6}$$

where N_1 and N_2 are the populations of the lower and upper energy levels. From this one can derive the Brillouin function which is used to describe the magnetisation of an atom in an applied field, where the atom will have $2J + 1$ equally spaced energy levels.

$$M = NgJ\mu_B B_J(x) \text{ where } x = \frac{gJ\mu_B B}{k_B T}. \tag{2.7}$$

The Brillouin Function, B_J is defined as

[1] γ is the ratio of the magnetic moment to the angular momentum

$$B_J(x) = \frac{2J+1}{2J}\coth\left(\frac{(2J+1)x}{2J}\right) - \frac{1}{2J}\coth\left(\frac{x}{2J}\right). \tag{2.8}$$

For a system that has $J = \frac{1}{2}$ the Brillouin function reduces to

$$M = Ng\mu_B J\tanh(x). \tag{2.9}$$

The Brillouin Function can be used to model a system at values of $\frac{B}{T}$ where T can be held constant. This gives one a curve that describes the effect of scanning through values of applied magnetic field on the magnetisation.

By dividing the magnetisation by H one comes to Curie's Law which can be used to model the effect of changing the temperature of the material on the susceptibility, which, for a paramagnetic system, is positive in value as shown by Eqn 2.10

$$\frac{M}{H} = \mu_0\frac{M}{B} = \frac{\mu_0 NJ(J+1)g^2\mu_B}{3k_BT} = \frac{\mu_0 Np^2\mu_B^2}{3k_BT} = \frac{C}{T}, \tag{2.10}$$

where C is the Curie constant and p is the effective number of Bohr magnetons and defined as

$$p = g[J(J+1)]^{\frac{1}{2}}. \tag{2.11}$$

Hund Rules - (Russel Saunders Coupling)

The Hund Rules are applied to electrons in a shell within an atom that give the ground state term using the following:

I. The maximum value of the total spin, S, allowed by the exclusion principle.

II. The maximum value of the orbital angular momentum, L, consistent with the value of S.

III. The value of the total angular momentum, J, is equal to $|L - S|$ when the shell is less then half full and $L + S$ when the shell is more than half full.

2.0.3 Environments: The Crystal Field

The crystal field is an electric field that occurs due to the neighbouring ions within the crystal lattice. The surrounding ions will interact with a transition (or rare earth) metal centre and the magnitude of the field is largely due to symmetry of the local environment. When a transition metal ion is placed in the centre of this crystal field the degeneracy of the d-orbitals is removed and the orbital angular momentum is said to be quenched. When a metal ion is coordinated by either 4 ligands in a tetrahedral environment or by 6 in an octahedral environment the d-orbitals are split into two degenerate sets with symmetry t_{2g} and e_g. For the octahedral crystal field $E_{t_{2g}} < E_{e_g}$ and for the tetrahedral crystal field $E_{t_{2g}} > E_{e_g}$. The way the energy levels fill is now a play off between the energy gap between the t_{2g} and e_g levels versus the Coulomb energy cost of pairing 2 electrons in one orbital (known as the pairing energy). If one considers an Fe(II) ion ([Ar] $3d^6$) in an octahedral environment and the energy gap is the larger than the pairing energy the 6 d-electrons will occupy the t_{2_g} molecular orbital, a configuration known as the low spin state. However, if the energy gap is smaller then the pairing energy, the electrons will follow Hund's Rules and one will get 4 electrons in the t_{2_g} and 2 electrons in the e_g molecular orbitals, known as a high spin state.

Within a system such as the octahedral Fe(II) atom in a low spin state, there can be spin transitions between the Highest Occupied Atomic Orbital and Lowest Unoccupied Atomic Orbital or the t_{2g} and e_g molecular orbitals. This transition can occur over a few Kelvin (or a small energy) and is spontaneous where the fraction of low spin to high spin states may not be identical over the same range of temperatures as it depends on whether the sample is being heated or cooled and can lead to hysteretic effects.

Within an octahedral system it is possible for further splitting of the molecular

orbitals by a Jahn-Teller distortion where the cost of the increased elastic energy is balanced by resulting electronic configuration, which occurs in ions such as Mn(III).

2.0.4 Magnetic and Exchange Interactions

Magnetic moments within a solid can couple together and potentially produce long range magnetic order; this coupling is known as exchange. However it is also possible for magnetic dipoles to interact to couple moments together.

Magnetic Dipolar Interaction

A electron can be considered as a magnetic dipole and when you two dipoles are spaced at a distance $\vec{r}$ the energy will equal

$$E = \frac{\mu_0}{4\pi r^3}\left[\mu_{\mathbf{1}} \cdot \mu_{\mathbf{2}} - \frac{3}{r^2}(\mu_{\mathbf{1}} \cdot \tilde{\mathbf{r}})(\mu_{\mathbf{2}} \cdot \tilde{\mathbf{r}})\right]. \tag{2.12}$$

The above equation depends on the moments' separation and their degree of mutual alignment. In reality this effect is only relevant at very low temperatures in materials that order at milliKelvin temperatures as the effect is very small and is negligible in materials that order at high temperatures.

Direct Exchange

Exchange interactions play an important role in the long range order of magnetic materials and are an effect of electrostatic interactions. Two electrons that have spatial coordinates $\mathbf{r}_1$ and $\mathbf{r}_2$ respectively must have wavefunctions that are symmetrical or anti-symmetrical to obey Pauli's exclusion principle. This will mean the two electrons wavefunctions must be antisymmetric with respect to each other, which will either form an antisymmetric singlet state in the case of symmetric spatial state or a symmetrical triplet state if the spatial state is antisymmetric. These

two states can be written in the form of a Hamiltonian to describe the spin states dependence on the energy levels of the system

$$\widehat{H}^{spin} = -2J\mathbf{S_1} \cdot \mathbf{S_2}. \tag{2.13}$$

If $J > 0$ then $E_{\mathrm{S}} > E_{\mathrm{T}}$ and the triplet state is favoured. If $J < 0$ then $E_{\mathrm{S}} < E_{\mathrm{T}}$ and so the singlet state is favoured. Equation 2.13 can be expanded to a many body problem by summing from the i^{th} to j^{th} electron or overall electrons within the system

$$\widehat{H} = -\sum_{ij} J_{ij}\mathbf{S}_i \cdot \mathbf{S}_j. \tag{2.14}$$

This Hamiltonian is known as the Heisenberg Model and J_{ij} is the exchange constant between the i^{th} and j^{th} spins.

Direct exchange occurs if the electrons are on neighbouring atoms and can interact with each other through the exchange field. Generally there is insufficient overlap of the magnetic orbitals on the neighbouring atoms to control the magnetic properties of the material.

Indirect Exchange: Superexchange

This occurs in ionic solids since many have magnetic ground states, such as oxides and fluorides. MnO is the classic example that is antiferromagnetic at low temperatures, however this is unexpected as the Mn^{2+} ions are too far apart for direct overlap of the orbitals. Superexchange can be defined as an indirect exchange between two non-neighbouring magnetic ions by a non-magnetic ion placed between these two magnetic centres. The antiferromagnetism arises as there is a kinetic energy advantage to having the spins on the Mn ions pair anti-parallel. If both Mn ions are in an S=$\frac{5}{2}$ state and the O has a filled p-orbital that overlaps with the d-orbitals on the Mn centres then it is advantageous for the Mn(1) to have spin up

and Mn(2) with spin down mediated by the through the oxygens paired electrons and so the electrons can become delocalised over the whole structure. If Mn(2) was to pair ferromagnetically this would lead to an excited state.

Indirect Exchange: RKKY Interaction

The Ruderman, Kittel, Kasuya and Yosida (RKKY) Interaction occurs in metals and is mediated by the conduction electrons where a localised magnetic moment spin-polarises the conduction electrons which in turn couples another local environment. This does not involve direct coupling of the spins but an exchange that is over a distance that is dependent on the term r where the exchange interaction has the form

$$J_{RKKY}(r) \propto \frac{cos(2k_f r)}{r^3}, \tag{2.15}$$

where k_f is the Fermi wavevector.

2.1 Magnetic Ordering

2.1.1 Ferromagnetism

A ferromagnetic material shows a spontaneous magnetisation in the absence of an applied magnetic field where a simple schematic is shown in figure 2.1.

The energy of the i^{th} spin has an exchange part and a Zeeman term $g\mu_B \mathbf{S}_i \cdot \mathbf{B}$ where the total exchange interaction is similar to Eqn 2.14. The exchange interaction is replaced by an effective molecular field, $\mathbf{B_{mf}}$ produced by the neighbouring spins. The Hamiltonian can be written as

$$\widehat{H} = g\mu_B \sum_i \mathbf{S}_i \cdot (\mathbf{B} + \mathbf{B_{mf}}), \tag{2.16}$$

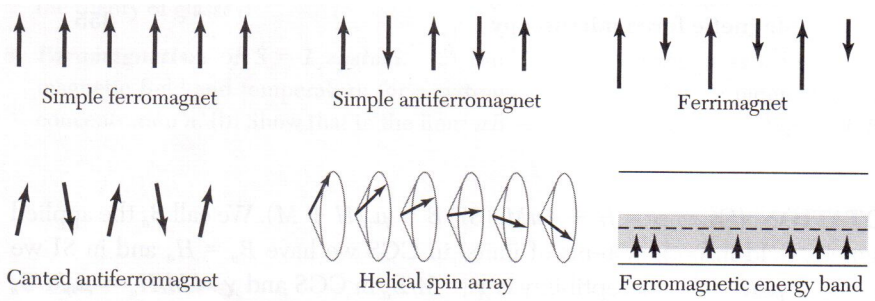

Figure 2.1: Examples of magnetic order within materials showing the more complex example such as canted and helical ferromagnetism. The ferromagnetic energy band is present within materials where there is a conduction band [1].

where

$$\mathbf{B_{mf}} = -\frac{2}{g\mu_B}\sum_j J_{ij}\mathbf{S}_j. \tag{2.17}$$

It is assumed that all magnetic ions experience the same molecular field and within a ferromagnet this acts to align the magnetic moments in one direction when the exchange constant is positive. At low temperatures the internal field is strong enough to align the moments and as the temperature is raised thermal fluctuations cause the magnetisation to decrease and above a specific temperature the order is destroyed. By applying a small magnetic field this can minimise the energy with respect to the alignment of spins parallel to the external field which can help promote ferromagnetic alignment of the internal magnetic moments.

The temperature dependence of a ferromagnet follows the Curie-Weiss law where θ is a measure of the interaction between magnetic moments. A positive value denotes a ferromagnet and a negative value an antiferromagnet (see figure 2.2)

$$\chi = \frac{C}{T-\theta}. \tag{2.18}$$

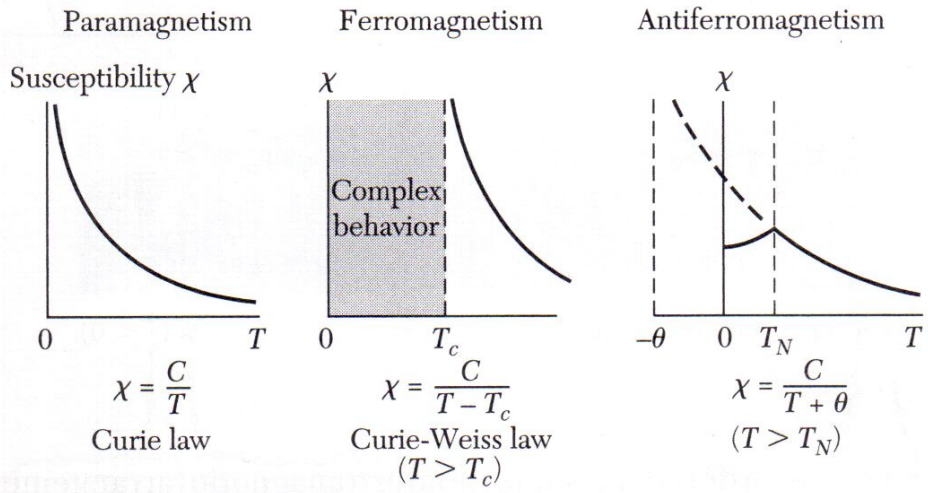

Figure 2.2: A diagram showing the temperature dependence of the susceptibility of a paramagnet, a ferromagnet and an antiferromagnet of a polycrystalline sample [1]. Below the critical temperature within a ferromagnet there are a whole variety of different responses depending on the ordering within the magnetic structure.

2.1.2 Antiferromagnetism

Within an antiferromagnet the exchange constant is negative, $J < 0$, and the neighbouring magnetic moments align antiparallel to one another. The result is a system where the net spontaneous magnetisation is equal to zero (see figure 2.1). A common case for an antiferromagnetic material is that it is split into two sublattices, one where the spins are pointing in one direction and another where the spins are in the opposite direction with the magnetisation of each sublattice proportional to one another. The magnetic ordering disappears above a transition temperature, known as the Néel Temperature (T_{N}). Above T_{N} the system behaves as a paramagnet.

The magnetic susceptibility of the system follows the Curie-Weiss law

$$\chi \propto \frac{1}{T + T_N}, \tag{2.19}$$

where θ, in this case T_N, is negative.

When a field is applied to an antiferromagnet the field direction is highly important

as there is no real energetic advantage for the magnetic moments to align with the field as the energy saving on one sub-lattice will be cancelled by the energy cost of the other aligning opposite to the field. At $T = 0$ an applied field parallel to one of the sub-lattices will cause one lattice to align with the field and another to oppose the field thus $\chi_{||} = 0$. If however a field is applied perpendicular to the magnetisation of the sub-lattices then the magnetisation of each sub-lattice will cant so that a component of the magnetisation will lie with the field so $\chi_{\perp} \neq 0$.

2.1.3 Ferrimagnetism

A similar case to antiferromagnetism is ferrimagnetism (see fig. 2.1). If there are two sub-lattices that do not have an equal and opposite magnetisation then when ordered there will be a net magnetisation in a specific direction as the sub-lattice components do not cancel out.

An example of a ferrimagnet is $Fe(II)O{\cdot}Fe(III)_2O_3$, known as magnetite (Fe_3O_4)[2] which has a spinel structure where there are two different types of lattice sites; one tetrahedral (A site) and two octahedral (B sites) per chemical formula unit.

2.2 Magnetic Frustration and Competing Interactions

Magnetic Frustration arises due to competing interactions on a lattice or within a material. The consequence is that there may be many degenerate magnetic ground-states within the system where the non-minimisation of the energy is shared throughout all the interacting magnetic moments. This can be visualised by considering an antiferromagnetically coupled square lattice compared to an antiferromagnetic coupled triangular lattice. On the square lattice all the moments can align anti-parallel

[2]Or indeed other ferrites with forumla $MO{\cdot}Fe_2O_3$ where M is a divalent cation (shown by the notation (II)) such as Zn, Fe, Co, Ni,Cu or Mn.

to their nearest neighbour. However on a triangular lattice, if two moments align anti-parallel, then the third moment is left 'frustrated' as if it aligns anti-parallel to one neighbouring spin it does not minimise its energy with respect to the other nearest neighbour.

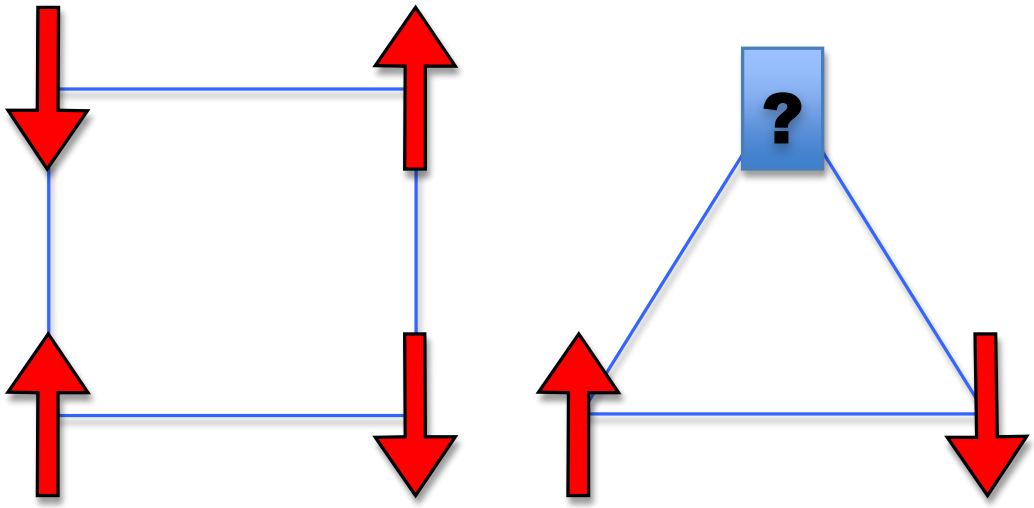

Figure 2.3: A schematic diagram showing antiferromagnetic alignment of spins on a square lattice and a triangular lattice. On the triangular lattice there is one spin that can not satisfy both antiferromagnetic interactions with its nearest neighbours and so is said to be frustrated.

From Fig 2.3 one can see that the geometry of the crystal lattice has an effect on the magnetic frustration within the system. A prominent example is the Kagome lattice (based on interlaced triangles) that was first reported in 1951 and has since seen much development and research [4, 5].

2.2.1 Spin Glasses

Spin glasses are more complex magnetic systems as they are based upon a non-magnetic lattice that is sparsely populated with magnetic atoms. Within a lattice, if there are x magnetic atoms that have a low concentration the exchange interaction between two magnetic atoms will vary depending on the proximity to one another. If

a nearest neighbour has a ferromagnetic interaction and the next-nearest neighbour an antiferromagnetic interaction generally there will be cases where moments will couple and align relative to each other however there may be instances of frustration of the magnetic moments where there are a mix of nearest neighbour and next nearest neighbour interactions so the frustrated moment will have a number of degenerate ground states that it may occupy at $T = 0$ [6].

In a transition metal alloy such as $Cu_{1-x}Mn_x$, if the concentration of Mn atoms is very low, a few atomic percent and therefore the Mn atoms are separated by such a distance that the only interaction is through RKKY exchange mediated by the conduction electrons in Cu. This leads to either ferromagnetic or antiferromagnetic interactions and so there is a degree of frustration within the system with no well defined ground state. At high temperatures, $k_B T$ is large enough to cause thermal fluctuations of the magnetic moments and as the material is cooled through the spin glass freezing temperature (T_f) the moments on the Mn will fall into one of their degenerate ground states [2].

The susceptibility of a simple spin glass (CuMn) is shown in figure 2.4 where both the zero-field (ZFC) and field cooled (FC) curves are shown. The applied field is low (6 G) so that there is no saturation of the magnetic system and the true susceptibility of the spin glass is probed. The cusp in the data is the freezing temperature and the deviation of the ZFC and FC curves illustrate the hysteretic behaviour of the system. On cooling the material in the absence of an applied field the system will fall into one of its many magnetic groundstates and so on warming in a 6 G field there is an increase in thermal energy causing the spins to align with the field direction. If the system is cooled in the presence of an applied field one observes an ordered magnetic groundstate dictated by the applied field. A spin glass system is extremely sensitive to its magnetic history.

An elegant example of how the magnetic properties change with dopant levels of the magnetic ions was shown by Morgownik and Mydosh in 1981 [8]. When fitting a Curie-Weiss behaviour to the reciprocal susceptibility, the order parameter increased with the dopant level of Mn. Thus one has a tuneable system where the magnetic

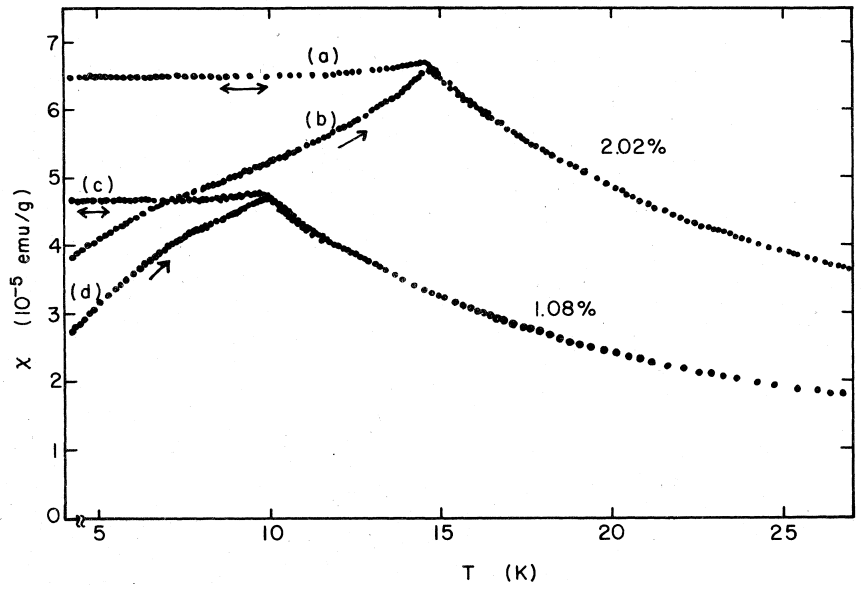

Figure 2.4: Zero-field (b and d) and field cooled (a and c) temperature dependent susceptibility of $Cu_{1-x}Mn_x$ at concentrations of x at both 1 and 2% taken from [7].

properties can be controlled by the concentration of the magnetic atom. In general the order paramter, θ, represents a sum of all the exchange interactions that are present within this random system:

$$\theta(x) = x\frac{S(S+1)}{3k_B}\sum_r J(r). \tag{2.20}$$

Here x is the concentration of the magnetic element and this shows that as x increases so to does the number of ferromagnetic interactions that is roughly a linear increase as shown in Fig 2.5

Within a material that is a semiconductor or insulator there are no RKKY interactions and so the coupling of spins originates from superexchange. This results from bond randomness where the exchange interactions will vary between +J or -J depending on the position of the magnetic atoms within a crystalline lattice where each bond between atoms can have different exchange constants as the bonds are randomly distributed through the sample.

Magnetic anisotropy can be another factor affecting spin glasses as each magnetic

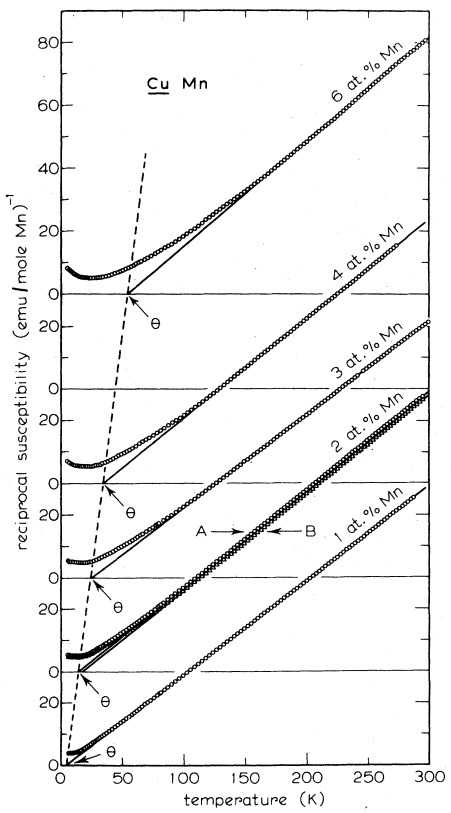

Figure 2.5: χ^{-1} as a function of temperature showing the Curie-Weiss fits and the evolution of the order parameter, θ, as the concentration of Mn increases. Taken from [8].

atom or area will posses an easy axis for the magnetisation. This creates a random anisotropy that has order only in local areas of the material. Ultimately the question of the spin glass is a paradoxical one, as J. A. Mydosh described it: "How can we achieve order out of randomness?" [6]

Cluster Glass

If the doping of magnetic impurities increases to the point where the concentration within localised areas increases this can lead to a situation where a cluster of magnetic atoms/ions forms. Within the canonical spin glasses, i.e. CuMn, increasing the concentration of Mn will lead to clusters of strongly correlated magnetic atoms. In this case the exchange is through the strong RKKY interaction and this is dependent on distance so that the interactions can be either ferromagnetic or an-

tiferromagnetic. These clusters will order over a short range and due to these local regions of order this greatly effects the overall magnetism of the material [6].

Within these clusters one will observe statistical fluctuations and ferromagnetic order where the moments can be large ranging from 20-20000 μ_B [6]. As the temperature is cooled these clusters will freeze into a random orientation where these clusters are locally ordered but there is still macroscopic randomness similar to a spin glass. The remanent behaviour of the sample becomes enhanced due to the presence of these large clusters within the frozen state which also allows for easy study of the temperature dependence of the material. One of the obvious signs of a cluster glass is displaced hysteresis loops as the system is incredibly sensitive to heating and cooling rates as well as magnetic field.

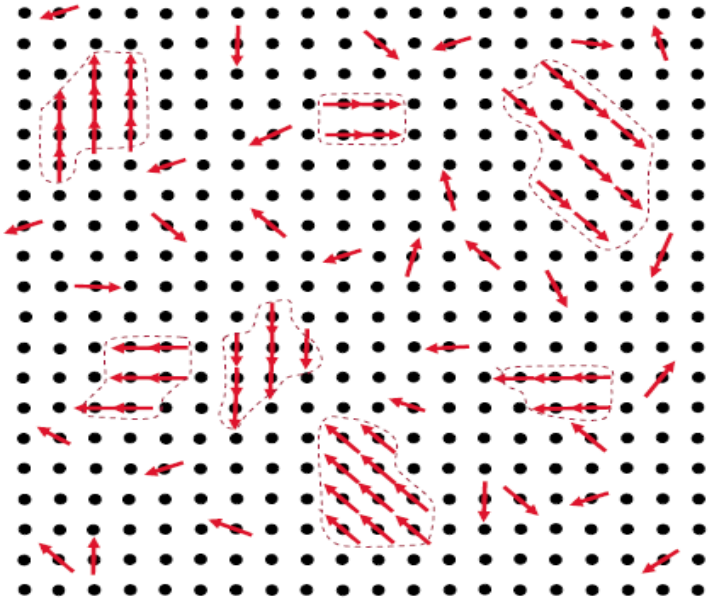

Figure 2.6: Diagram illustrating the concept of a cluster glass where randomly orientated locally ordered clusters cash be observed. Taken from [6].

Figure 2.6 shows the concept of a cluster glass. There are areas of local order where there is a high concentration of magnetic atoms/ions which have formed clusters. These clusters show a glassy behaviour with respect to each other and in that sense are similar to a spin glass however within the clusters themselves the moments are aligned ferromagnetically. There may be a case that the alignment may favour

antiferromagnetism if the neighbouring interactions favour that configuration.

2.2.2 Superparamagnetism

Within a material if there are clusters of magnetic nanoparticles these may also show some properties that can be confused with glassy behaviour. If a ferromagnetic particle is small enough then it is no longer energetically favourable to form a domain boundary and so the particle will effectively be a single-domain. The magnetisation of the particle is usually constrained to lie along a particular direction or opposite due to magnetocrystalline anisotropy or if the particle is elongated, a shape anisotropy may dictate the direction of magnetisation. To flip the direction of the spins through 180° an activation energy is needed that is proportional to the volume of the particle, $\Delta E = KV$ where V is the volume of the particle and K is a constant which quantifies the energy density associated with the anisotropy. If the particle is very small $k_{\mathrm{B}}T \gg KV$ and so thermal fluctuations can easily flip the spins.

If these particles are in a non-magnetic matrix and are far enough apart, interactions between each particle can be neglected. When $k_{\mathrm{B}}T \gg KV$ the system behaves like a superparamagnet and so will follow the form of the Langevin Function (see eqn. 2.21) as we are at the limit of the Brillouin function, where $J(S) \to \infty$,

$$M(y) = (N < \mu > \mu_B)\left\{ \coth\left(\frac{< \mu > \mu_B B}{k_B T}\right) - \frac{k_B T}{< \mu > \mu_B B}\right\}. \tag{2.21}$$

Below a specific temperature known as the blocking temperature (T_{B}) the magnetic moment will not be able to change orientation and the particles will show a remanent magnetisation. However T_{B} is dependent on the size of the particle and so generally the blocking of the particles is a gradual change because there is usually a particle size distribution. In the case of a particle size distribution the magnetisation can be modelled simply by addition of Langevin components such as

$$M(y) = (N_1 < \mu_1 > \mu_B)\left\{ \coth\left(\frac{< \mu_1 > \mu_B B}{k_B T}\right) - \frac{k_B T}{< \mu_1 > \mu_B B}\right\} + (N_2 < \mu_2 > \mu_B)\left\{ \coth\left(\frac{< \mu_2 > \mu_B B}{k_B T}\right) - \frac{k_B T}{< \mu_2 > \mu_B B}\right\} + ... \tag{2.22}$$

On cooling down the particles the fluctuations slow down and the system will appear static on the time scale of the magnetic measurements and therefore different measurements may probe different time scales. Generally when $\tau > \alpha t$ where τ is the fluctuation time, t is the time scale of the measurement and $\alpha = 100$ [2] when we go below T_B one will be within the static regime of the system. T_B can be defined as

$$T_B = \frac{KV}{k_B ln(\alpha t/\tau_0)}, \tag{2.23}$$

where K is the anisotropy constant and V is the volume of the particle. From eqn. 7.3 it is quite clear that $T_B \propto V$ and therefore the volume of the particle is an extremely important variable in controlling T_B.

2.3 Molecular Magnetism and Spin Transitions

The field of molecular magnetism is incredibly vast as it is a truly interdisciplinary topic. The goal is to create 'magnetic molecules' which requires a large amount of synthetic chemistry. The study of these systems can lead to magnetic properties being tuned by subtle changes to the reactants or reactions conditions. If one imagines a cluster of magnetic ions surround by ligands that are carbon based (diamagnetic) then one can create Single Molecule Magnets (SMM) where the main interaction governing the magnetism is from exchange within the magnetic cluster.

Within magnetic clusters the magnetic properties may not resemble that of the bulk metal or even nanoparticles. It is common within these materials for the Zeeman

energy levels to cross as the applied field is ramped. If one imagines an $S = \frac{1}{2}$ system then the energy levels will show Zeeman splitting in an applied magnetic field, where m_s = -1,0,+1. The splitting of these energy levels increases as the applied field increases. However, within certain molecular magnets this may not be the case and so crossing of the energy levels can be observed which leads to a level-crossing transition. Another common property is the transition from low spin to high spin states, this may be from thermal excitation or through pumping the system with resonant photons that promote the transition as well as the existence of Van Vleck paramagnetism within may molecular materials. An illustration of Van Vleck paramagnetism is if a molecule has a non-magnetic groundstate and if a second order perturbation on the energy level from thermal excitation is applied this causes the existence of excited unpaired electrons resulting in a paramagnetic state (see Fig 2.7). It should be noted that this concept is a common theme in molecular magnetism but is not restricted to this topic alone as many other purely inorganic compounds show transitions from diamagnetic low spin to paramagnetic/ferromagnetic high spin states.

This area of magnetism is incredibly vast and is covered in more detail within Kahn's "Molecular Magnetism" [9].

2.4 Muon Spin Rotation/Relaxation/Resonance

Muon Spin Rotation/Relaxation/Resonance (μSR) is an incredibly powerful tool that is sensitive to the local microscopic environment within the material. There are numerous uses for μSR such as studying magnetism, superconductivity, semiconductors or even chemical reaction rates. Muons were first discovered in 1936 by Neddermeyer and Anderson and the pioneering experiments were performed using cosmic muons with one muon hitting each square centimetre of the Earth's surface every minute [10]. For μSR experiments a much higher flux ($>10^4$) is needed and so these experiments can only be performed at particle accelerators such as ISIS, UK or TRIUMF, Canada. Although both positive and negatively charged muons

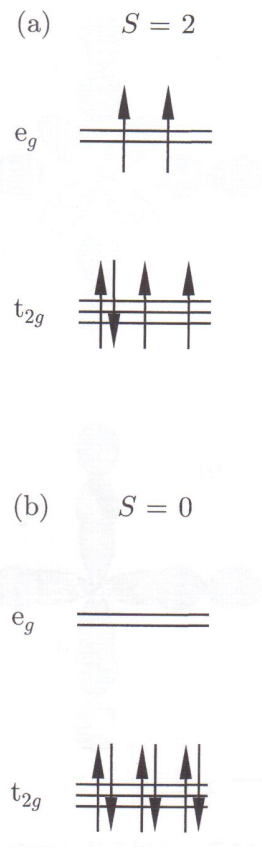

Figure 2.7: Electronic configuration for the Fe^{2+} $3d^6$ shell. The system is able to go from a non-magnetic ground state ($S = 0$), ***a***, to a thermally excited magnetic state (S=2), ***b***. Taken from [2].

exist, within this thesis we will be concerned with μSR experiments conducted with only μ^+. There are similarities between μSR and NMR or ESR; however, where the latter two are measured in frequency space, μSR is measured in time-space. There are other sources that will cover the following section in more detail [10, 11], but the basic principles behind μSR will be outlined here including the interpretation of collected data within the context of magnetic materials. The experimental set up will be described in Chapter 3.

The muon is a spin $\frac{1}{2}$ particle and, due to parity violation at the point of decay, the direction of the muons' spin is conserved. The muon particle is also extremely sensitive to local magnetic fields. Implantation of the muon into a material results in an interaction with the local fields and measuring the direction of the positron emitted

from muon decay, which has a half life of 2.2 μs, one can determine information regarding the magnetism of the host material. Equation 2.22 shows the decay of a muon into a positron and two neutrinos.

$$\mu^+ \rightarrow e^+ + \nu_e + \overline{\nu_\mu}. \tag{2.24}$$

Fig 2.8 shows the basic principles of μSR within a bulk ferromagnetic material. The muon is implanted into sites within the lattice and it will couple to the internal magnetic fields. Similar to other particles that experience applied magnetic fields, the muon magnetic moment (spin) precesses and since the muon decays maintaining the direction of its spin we can observe the muon precession frequency within the given material by measuring the asymmetry in the decay of the muon into a positron. One elegant advantage of μSR as a probe of magnetic materials is that true zero field (ZF) measurements can be observed thanks to the radioactive decay of the muon particle. Such a ZF probe is a significant advantage for studying materials such as spin glasses.

If no external field is applied and the muon is implanted into a magnetic material where the spins are static (on the time scale of the muon) then the muon responds by Larmor precessing around the internal field direction. The z component of the spin polarisation is given by:

$$\sigma_z(t) = \cos^2\theta + \sin^2\theta\cos(\gamma_\mu|H|t), \tag{2.25}$$

where

$$\gamma_\mu = \frac{g_\mu e}{2m_\mu}, \tag{2.26}$$

and γ_μ is the muon gyromagnetic ratio[3]. The first term is the time independent muon spin polarisation and the second term describes the asymmetry of the muon

[3] $135.54 \times 2\pi$ MHz/T

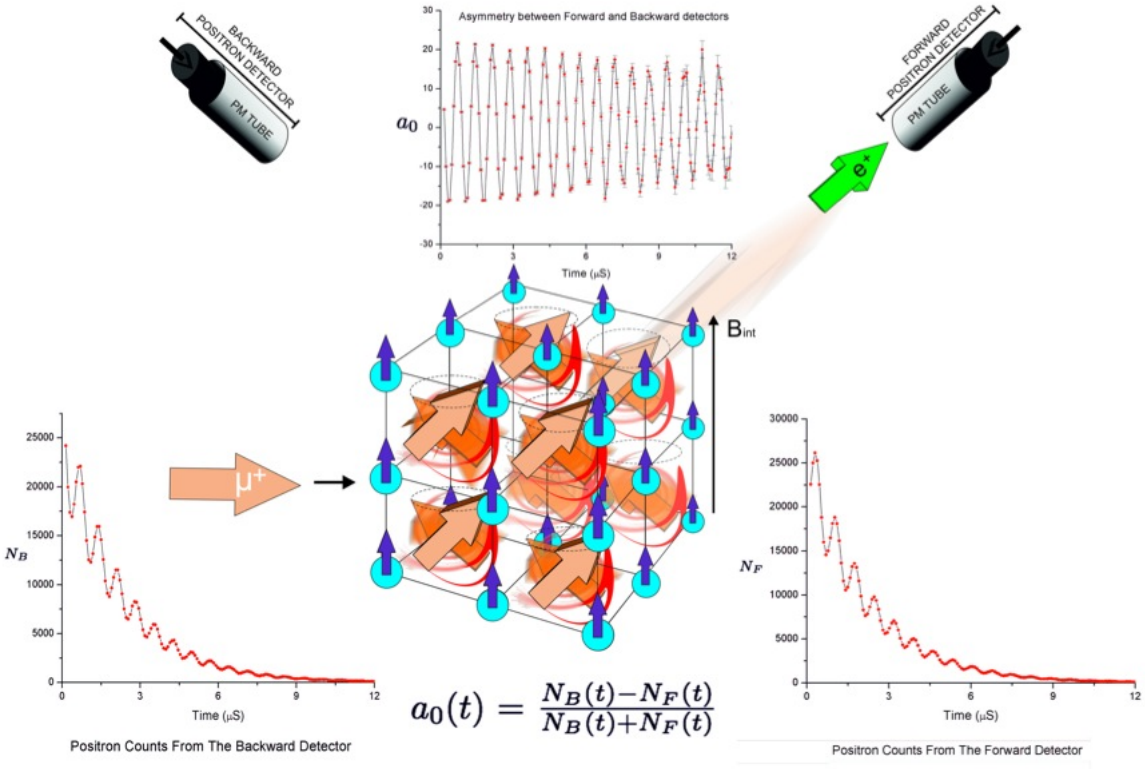

Figure 2.8: A schematic diagram showing the principle of μSR.

precession frequency. By taking the time average of $\sigma_z(t)$ over the field distributions we arrive at the directional averaged muon spin relaxation asymmetry ($G_z(t)$)

$$G_z(t) = \frac{1}{3} + \frac{2}{3}\cos(\gamma_\mu |H| t). \tag{2.27}$$

It is possible to take the above relaxation function and track the local critical transition within a material by following the evolution of the precession frequency as a function of temperature. In some materials where there are two sub-lattices it is possible to observe the response from both sub-lattices as they can appear in the frequency spectrum of the muon spin precession. It is then possible to track both transitions as a function of temperature. This is one of the only techniques capable of providing insight to this level within similar systems.

2.4.1 Muon Spin Relaxation Functions

When implanted into a material the muon may experience multiple stopping sites or magnetically inequivalent sites and so the average spin polarisation of the muon must be considered. In such cases one must use the probability distribution of the local fields ($P(H_i)$) ($i = x, y, z$). If the surrounding moments are random, as are nuclear dipoles or within spin glasses, and are at an equal distance from the muon stopping site, these can be defined using a Gaussian distribution;

$$P^G(H_i) = \frac{1}{\sqrt{2\pi}\Delta} \times \exp\left(\frac{-H_i^2}{2\Delta^2}\right), \tag{2.28}$$

where Δ is the field distribution. When considering the magnitude of the internal field, H:

$$P^G(|H|) = \left(\frac{1}{\sqrt{2\pi}\Delta}\right)^3 \times \exp\left(\frac{-H_i^2}{2\Delta^2}\right). \times 4\pi|H|^2 \tag{2.29}$$

The Gaussian form can be a good approximation of a concentrated spin system as well as a variable range of random local fields at a muon site.

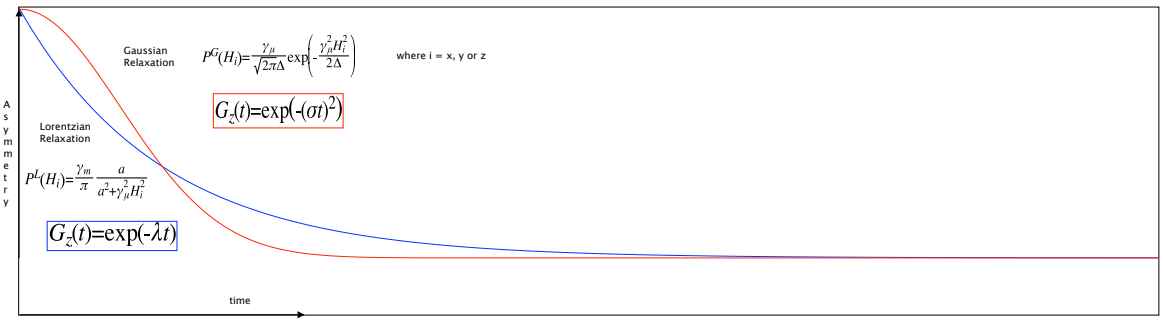

Figure 2.9: Gaussian and Lorentzian relaxation functions used to model the relaxation of the implanted muons.

In dilute spin systems the muon relaxation is much different and shows a Lorentzian distribution. Generally Lorentzian distributions have a wider range of $|H|$ and so one observes a shallower trough in the relaxation function (see Fig 2.9). Within a

system that has $\frac{1}{r^3}$ interactions, where r is the distance between magnetic moments, the Lorentzian distribution describes this very well where the amplitude parameter, a, is proportional to the concentration of the moments. The equation describing a Lorentzian distribution is seen below:

$$P^L(H_i) = \frac{\gamma_\mu}{\pi} \times \frac{a}{a^2 + \gamma_\mu^2 H_i^2}, \tag{2.30}$$

where:

$$P^L(H_i) = \frac{\gamma_\mu^3}{\pi^2} \times \left[\frac{a}{a^2 + \gamma_\mu^2 H_i^2}\right]^2 \times 4\pi|H|^2. \tag{2.31}$$

When averaging over equation 2.26 using a Gaussian distribution one arrives at the Kubo-Toyabe function:

$$G_z(t) = \frac{1}{3} + \frac{2}{3}(1 - \gamma_\mu^2\Delta^2 t^2)exp(-\frac{\gamma_\mu^2\Delta^2 t^2}{2}). \tag{2.32}$$

This function is defined by the persisting $\frac{1}{3}$ asymmetry and the $\frac{2}{3}$ component showing a damped oscillation where the width of the random fields Δ can be calculated (see Fig 2.10). A famous study was conducted on MnSi at room temperature where the Kubo-Toyabe function observed at ZF was due to nuclear dipolar fields from the Mn nuclei depolarising the muon spin. By applying a longitudinal field it was possible to 'decouple' the nuclear fields from the muon spin polarisation [12].

When a longitudinal field is applied this causes a perturbation on the Gaussian Kubo-Toyabe behaviour

$$\begin{aligned} G_z^G(t, H_L) = 1 - \left(\frac{2\gamma_\mu^2\Delta^2}{\omega_L^2}\right)\left[1 - \exp\left(-\frac{\gamma_\mu^2\Delta^2 t^2}{2}\right)\cos(\omega_L t)\right] \\ + \left(\frac{2\gamma_\mu^2\Delta^4}{\omega_L^3}\right)\int_0^t \exp\left(-\frac{\gamma_\mu^2\Delta^2 t^2}{2}\right)\sin(\omega_L\tau)d\tau, \end{aligned} \tag{2.33}$$

where H_L is the longitudinal field applied and $\omega_L = \gamma_\mu H_L$. For an electronic contribution to the muon depolarisation, this type of behaviour is caused by static

random distribution of moments within the sample where the field distribution (Δ) is comparable to ω_L.

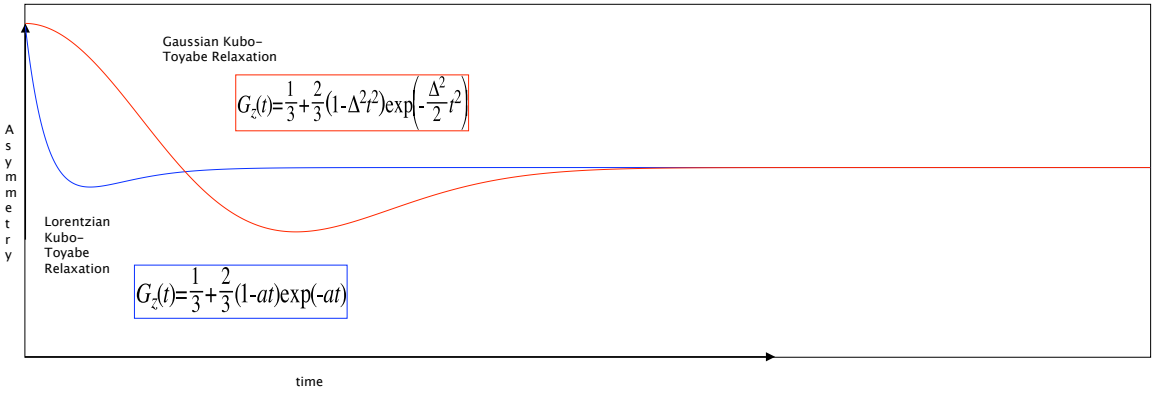

Figure 2.10: Gaussian and Lorentzian Kubo-Toyabe relaxation functions.

For Lorentzian local field distributions it is also possible to see a similar Kubo-Toyabe behaviour although the function has a shallower dip due to faster damping of the oscillation (see Fig 2.10) with the form:

$$G_z^L(t) = \frac{1}{3} + \frac{2}{3}(1 - at)\exp(-at). \tag{2.34}$$

When an LF is applied the Lorentzian KT function becomes:

$$\begin{aligned} G_z^L(t, H_L) = 1 - \left(\frac{a}{\omega_L}\right) j_1(\omega_L t)\exp(-at) - \left(\frac{a}{\omega_L}\right)^2 [j_0(\omega_L t)\exp(-at) - 1] \\ - \left[1 + \left(\frac{a}{\omega_L}\right)^2\right] a \int_0^t j_0(\omega_L \tau)\exp(-a\tau) d\tau, \end{aligned} \tag{2.35}$$

where j_1 and j_0 are spherical Bessel functions.

In many systems as well as a static field there may be a coexisting dynamical contribution where the $\frac{1}{3}$ asymmetry tail seen in the static KT function is not observed and so one sees a damped oscillation (related to the static component) on a relaxing background (related to the dynamic component). For this one needs the to use a dynamical Kubo-Toyabe function to describe the system. Here one must consider the

strong collision approximation for the muon within a sample where the local field is fluctuating and a change in direction of the moment is observed at time t. The local field experienced by the muon after a collision is random and not correlated to the local field before the collision. In general this dynamical KT function is comprised of a summation of: muons that don't collide up to time t + muons that undergo one collision + muons that undergo two collisions + ... For the muons that experience no collisions the polarisation function would follow a static KT however after the first collision, at time t_1, the the muon polarisation would decay following a KT function from $t = t_1$. This repeats for the second collision and so on.

The fraction of muons that do not undergo a collision up to time t is proportional to $\exp(-\nu t)$, where ν is the collision rate, and so for a Gaussian case, the mathematical description of the dynamical KT function includes this term and is shown below:

$$G_z^{\mathrm{G}}(t,\nu) = \exp(-\nu t)\Bigg(g_z(t) + \nu\int_0^t g_z(t_1)g_z(t-t_1)dt_1 + \nu^2\int_0^t\int_0^{t_2} g_z(t_1)g_z(t_2-t_1)g_z(t-t_2)dt_1dt_2 + \cdots\Bigg), \tag{2.36}$$

where $g_z(t)$ denotes the static relaxation function. There are a few features of the relaxation functions that should be noted; that the relaxation becomes slower as the number of collisions is increased corresponding to a larger ν and for the Gaussian case when $\nu/\Delta > 5$ (i.e. fast fluctuations) the relaxation can be modelled by a single exponential. The system is said to be in the fast fluctuating limit where there is substantial motional narrowing of the field distribution and in this case the strong collision approximation leads to a fitting function

$$G_z^{\mathrm{G}}(t,\nu) = \exp(\frac{-2\gamma_\mu^2\Delta^2 t}{\nu}). \tag{2.37}$$

From the respective ZF Kubo-Toyabe functions it is possible to simplify the Gaussian and Lorentzian relaxations (denoted by superscript G and L respectively) to the following terms by using a Taylor expansion on the exponential terms:

$$G^G(t) = \exp(-\sigma^2 t^2), \tag{2.38}$$

$$G^L(t) = \exp(-at). \tag{2.39}$$

It is these functions that will be used for a large amount of μSR data analysis where σ and a are related to the relaxation in μs^{-1} or MHz.

It is also worth mentioning the use of a stretched exponential function to analyse μSR data:

$$G(t) = \exp[-(\lambda t)^{\beta}]. \tag{2.40}$$

This function is particularly useful for spin glass systems as the value of β does approach $\frac{1}{3}$ near T_g [13]. It can also provide information on critical behaviour close to a transition and, more simply, demonstrate whether a relaxation is Gaussian or Lorentzian in character. The stretched exponential function is not without many flaws as it can fit most data and gives no real physical meaning of what is going on.

2.5 Basics of Neutron Scattering

Both neutron scattering and x-ray scattering are complementary techniques however using neutrons over x-rays does have many advantages. Neutrons interact with the atomic nuclei and x-rays (photons) with the electrons within an atom. The trend with x-rays, that the scattering strength of the atoms increase with Z^4, is not observed with neutrons. Lighter atoms (i.e. hydrogen, oxygen and nitrogen) can scatter neutrons strongly and so it is possible to possible to distinguish atoms of similar atomic number and even different isotopes. The wavelength of high energy x-rays is comparable to low energy neutrons which is similar to the scale of elementary

[4] Z = Atomic number

excitations within matter and so this makes neutrons suitable for studying dynamics of atoms or compounds. Since neutrons interact weakly with the sample there is very little perturbation from the equilibrium state of the material and the deep penetration depth make it ideal for studying bulk effects. Neutrons have a plethora of uses within the field of magnetism as the $S = \frac{1}{2}$ state of the neutron means that it interacts with magnetic dipoles associated with specific atoms.

This section will outline briefly both elastic and inelastic neutron scattering, however these topics and more are covered in many books on thermal neutron scattering [14–16].

The 1st Born Approximation assumes that each neutron is only scattered once by the sample which leads to the Kinematic Theory of scattering which depends on the scattering vector $\overline{Q}$ and the energy transfer ΔE. Since the neutron is considered a particle, the wavefunction in its initial state will be

$$\psi_i = Ae^{i\underline{k}_i \cdot \underline{r}}, \tag{2.41}$$

where A is the the complex amplitude, wavevector $\underline{k}$, position vector $\underline{r}$. The wavefunction of the final state, after scattering, will be the same except with subscript 'f'.

The neutron is scattered from an initial state to a final state (see figure 2.11) and since the energy must be conserved changes in the neutron must be balanced by the sample. The scattering vector $\overline{Q}$ and energy transfer ΔE is defined below

$$\hbar\overline{Q} = \hbar(\underline{k}_i - \underline{k}_f) \tag{2.42}$$

and

$$\Delta E = \frac{\hbar}{2m}(k_i^2 - k_f^2). \tag{2.43}$$

When $\Delta E = 0$ the triangle is isosceles as both k_i and k_f are equal and this is known as elastic scattering (see figure 2.12). When the wavevectors of the initial and final

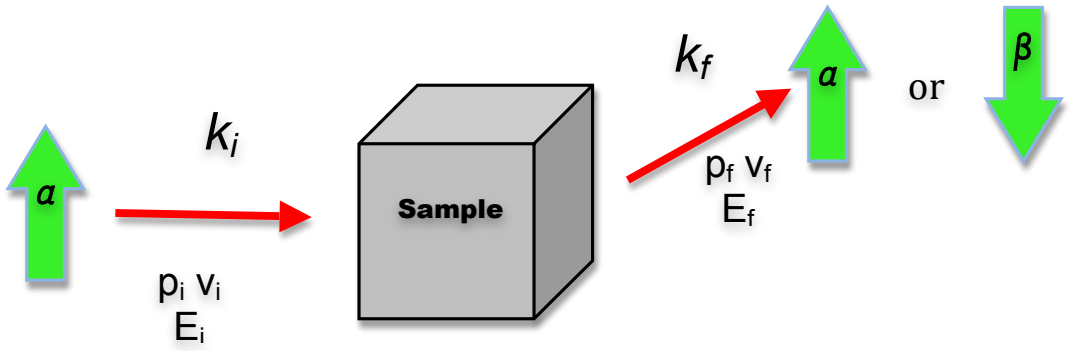

Figure 2.11: Neutron scattering processes where the neutron is scattered from state $|k_i\rangle$ to state $|k_f\rangle$ where p is the momentum, v is the velocity E is the energy and α or β are the different spin states.

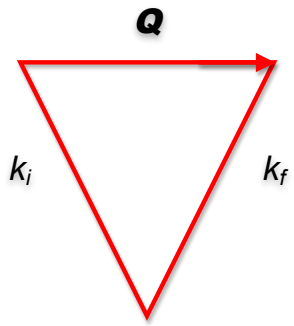

Figure 2.12: Neutron scattering Vectors.

states are not equal this leads to the situation $\Delta E \neq 0$ which is known as inelastic scattering.

The neutron scattering cross section is an important quantity defined as the number of neutrons scattered per second into a solid angle (Ω) with a range of energies (from E to E+dE) divided by the flux of incident neutrons. It is this quantity that most equations of neutron scattering seek to calculate. The formula to describe this quantity is shown below

$$\frac{d^2\sigma}{d\Omega d\omega} = \frac{k'}{k}\frac{1}{2\pi\hbar}\sum_{j,j'} b_j b_{j'} \int_{-\infty}^{\infty} \langle e^{-iQ\cdot\widehat{R}_{j'}(0)} | e^{iQ\cdot\widehat{R}_j(t)} \rangle e^{i\omega t} dt, \tag{2.44}$$

where b_j is the scattering length of atom j, $b_{j'}$ denotes the final state of the scattered neutron, Q is the scattering vector and the neutron is scattered from a nuclei at a fixed point, $\widehat{R}_j$. The scattering length has both real and complex parts; the real part is an energy independent term and the complex describes the energy dependent absorption. The imaginary part is large if the energy of the neutron corresponds to the energy of a nuclear excited state. Therefore the scattering lengths depend on both the isotope and nuclear spin quantum number, I. The coherent and incoherent scattering lengths can be described by

$$\sigma_{coh} = 4\pi\left(\frac{1}{N}\sum_j b_j\right)^2 = 4\pi\left\langle b\right\rangle^2 \tag{2.45}$$

and

$$\sigma_{inc} = 4\pi(< b^2 > - < b >^2). \tag{2.46}$$

The average scattering lengths are defined by

$$\langle b\rangle = \sum_j p_j b_j \tag{2.47}$$

and

$$\left\langle b^2\right\rangle = \sum_j p_j b_j^2, \tag{2.48}$$

where $\sum_j p_j = 1$. p_j denotes the probability that nucleus j has the scattering length b_j. The neutron can interact with the nuclear spin to give either an ortho $|+\rangle$ or para $|-\rangle$ state. This means that there will be a chance of a neutron-nuclei interaction resulting in a triplet or singlet state. The two different states will have different probabilities:

$$p^{+} = \frac{I+1}{2I+1}, p^{-} = \frac{I}{2I+1}. \tag{2.49}$$

The average scattering length can be calculated using equations 2.43 and 2.44. Hydrogen, for example, has a nuclear spin $I = \frac{1}{2}$ and is an excellent incoherent scatterer. The scattering length of the triplet state $|+\rangle$ is -1.085×10^{-12} cm and the singlet $|-\rangle$ state is -4.750×10^{-12} cm which are very different from each other. Therefore $\sigma_{inc} = 80.3$ barn $\gg \sigma_{coh} = 1.76$ barn. However for deuterium, $I = 1$, the scattering lengths are similar; $\sigma_{inc} = 2.05$ barn and $\sigma_{coh} = 5.59$ barn. Therefore in order to study organics using neutrons it is wise to swap the hydrogen atoms for deuterium to minimise the incoherent scattering process.

2.5.1 Elastic Scattering

From the definition of the scattering cross section it is possible to arrive at an expression to describe Bragg's law:

$$n\lambda = 2d \sin\theta. \tag{2.50}$$

This is the equation that governs coherent elastic diffraction of both neutrons and photons (i.e. x-rays); by measuring the intensity of the scattered wave from crystal planes from the lattice as a function of θ it is possible to get diffraction from allowed Bragg reflections within the material. Reflections with $n = 2, 3, ...$ are known as higher order reflections which correspond to the path length difference of 2,3,.... wavelengths. This elucidates a large amount of information on the structure (such as lattice parameters) and one can determine the symmetry of the unit cell as well as the location of atoms (in this case nuclei) by analysis of intensity of the Bragg peaks through the constant of the structure factor as well as information on the atomic displacements that is obtained from the **Q**-dependence of the Debye-Waller factor.

Within a polycrystalline material it is certain that some crystallites will always be orientated to fulfil conditions for Bragg reflection for a fixed wavelength, however this produces cones or rings similar to the Debye-Sherrer method where the information is 2 dimensional (i.e. Intensity vs. 2θ). This makes it harder to gain knowledge of the 3-dimensional crystal structure since the information is condensed into the afformentioned 2-dimensions though is possible to extract information on lattice parameters and atomic positions through analytical methods such as Rietveld refinement [17].

Magnetic Scattering

The scattering process involves interaction of the spin angular momentum of the neutron and the magnetic field associated with the atomic electronic moment. This interaction can be described by

$$\hat{U} = \hat{\mu} \cdot \mathbf{H} = -\gamma \mu_N \hat{\sigma} \cdot \mathbf{H}, \tag{2.51}$$

where $\hat{\mu}$ is the magnetic moment operator of the neutron, $\gamma = -1.91$ the gyromagnetic ratio, $\mu_N = 5.505079 \times 10^{-27}$ JT^{-1} and $\hat{\sigma}$ is a Pauli spin operator. $\mathbf{H}$ is the magnetic field generally associated with unpaired electrons where the field is produced by a combination of the spin of the electron and its orbiting motion.

For a system where the orbital angular momentum is zero or has been quenched by crystal field interactions the scattering cross section is described by:

$$\frac{d^2\sigma}{d\Omega d\omega} = (\gamma r_0)^2 \frac{k'}{k} F^2(\mathbf{Q}) e^{-2W(\mathbf{Q})} \sum_{\alpha,\beta} \left(\delta_{\alpha\beta} - \frac{Q_\alpha Q_\beta}{Q^2} \right) S^{\alpha\beta}(\mathbf{Q}, \omega). \tag{2.52}$$

Where $e^{-2W}(Q)$ is the Debye-Waller factor and $S^{\alpha\beta}(\mathbf{Q}, \omega)$ is the magnetic scattering function:

$$S^{\alpha\beta}(\mathbf{Q}, \omega) = \sum_{j,j'} e^{i\mathbf{Q}} \cdot (\mathbf{R}_j - \mathbf{R}_{j'}) \sum_{\lambda,\lambda'} p\lambda \langle \lambda | \hat{S}^\alpha_{j'} | \lambda' \rangle \langle \lambda' | \hat{S}^\beta_j | \lambda \rangle \times \delta(\hbar\omega + E_\lambda - E_{\lambda'}). \tag{2.53}$$

$F(\mathbf{Q})$ is the magnetic form factor and $\widehat{S}_j^{\alpha}$ $(\alpha = x, y, z)$ is the spin operator at the jth ion at site R_j [14]. The magnetic neutron scattering cross section is estimated to be similar to that of the nuclear cross section and so we see similar scattering effects from the magnetic structure of the compound. The magnetic form factor is defined as the fourier transform of the normalised spin density associated with the magnetic ions and decreases with increasing $|\hat{\mathbf{Q}}|$. For cases where the orbital angular momentum, $L \neq 0$, one must consider the total angular momentum, J, within the neutron scattering cross section formula instead of simply the spin of the electron.

Essentially the neutron is an effective magnetic probe as it is field dependent and is both frequency and wavevector dependent. The neutron detects a total magnetisation,

$$M^{\alpha}(\mathbf{Q}, \omega) = \chi^{\alpha\beta}(\mathbf{Q}, \omega) H^{\beta}(\mathbf{Q}, \omega), \tag{2.54}$$

where $\chi^{\alpha\beta}(\mathbf{Q}, \omega)$ is the magnetic susceptibility tensor.

To study the magnetic structure of a crystalline compound the material exhibits magnetic Bragg scattering that may be commensurate or incommensurate with the crystal structure. A discrimination between Bragg scattering and magnetic scattering can be achieved by simply observing the peak profiles. There is generally a strong temperature dependence where the magnetic scattering is proportional to the square of the zero-field magnetisation. As the material passes through a transition, the magnetic peaks can increase in intensity where there is both scattering from the crystal structure and the magnetic structure.

An example of the power of magnetic neutron scattering is if the material is an antiferromagnet then one observes incommensurate magnetic Bragg peaks below the transition temperature. A classic example of this was the discovery of the antiferromagnetic structure by Shull and Smart in 1949 [18].

From the emergence of the (111) peak in the diffraction pattern below the antiferromagnetic transition the magnetic structure was observed to be associated with the

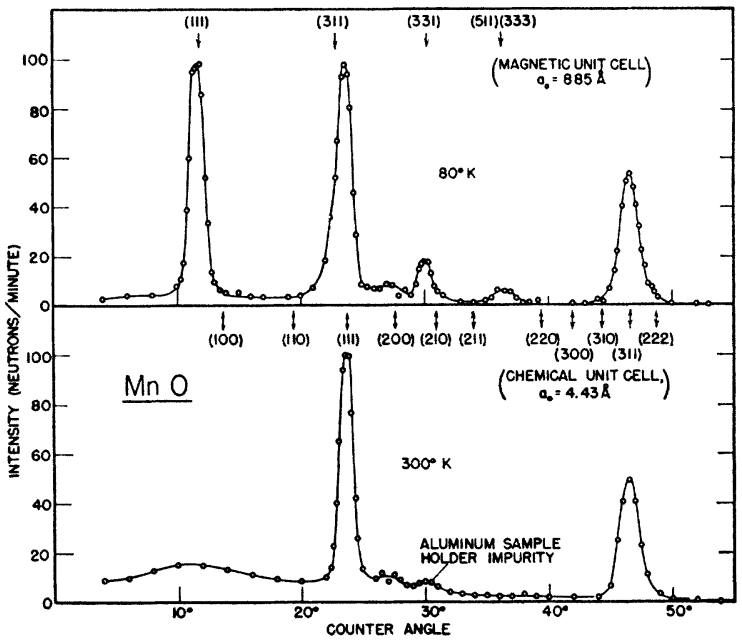

Figure 2.13: Neutron diffraction patterns for MnO at room temperature and 80 K [18].

(311) crystal plane where the magnetic unit cell is twice as large as the crystal unit cell.

2.5.2 Inelastic Scattering

We have so far considered the conditions where the initial and final energy of the neutron are the same, however it is possible for there to be energy transfer from the crystal to the neutron or vice versa resulting in a change in wavelength or energy of the incident neutron. This can be represented by Figure 2.12 where now $k_i \neq k_f$ however $\mathbf{Q}$ is still measurable. Neutrons are effective at measuring the change in energy as the excitations within the crystal (both phonon and magnon related) are of a similar magnitude of energy to the incident neutron energy.

By studying the spectrum of energy transfer of the scattered neutron one can study the dispersion relations of the crystal and magnetic excitations. This is an effective method for studying spin waves within ferromagnetic materials and their $\mathbf{Q}$

dependence.

Bibliography

[1] C. Kittel. *Introduction to Solid State Physics.* John Wiley and Sons, Inc, Hoboken, NJ. 8th Ed. (2005)

[2] S. Blundell. *Magnetism in Condensed Matter.* Oxford University Press, Oxford. (2007)

[3] D. Jiles. *Introduction to Magnetism and Magnetic Materials.* Chapman and Hall, CRC, Florence, KY. 2nd Ed. (1998)

[4] I. Syozi. *Progress of Theoretical Physics.* **6** (1951) 306-308

[5] B. Normand. *Contemporary Physics.* **50** (2009) 533-552

[6] J. A. Mydosh. *Spin Glasses: An Experimental Introduction* Taylor and Francis, London and Washington D.C (1993) 1-44

[7] S. Nagata, P. H. Keesom and H. R. Harrison. *Phys. Rev. B.* **19** (1979) 1633-1638

[8] A. F. J. Morgownik and J. A. Mydosh. *Phys. Rev. B.* **24** (1981) 5277-5283)

[9] O. Kahn. *Molecular Magnetism.* VCH Publishers, Cambridge. (1993)

[10] Editors: S. L. Lee, S. H. Kilcoyne and R. Cywinski. *Muon Science: Muons in Physics, Chemistry and Materials.* Institute of Physics Publishing, London. (1998)

[11] K. Nagamine. *Introductory Muon Science.* Cambridge University Press, Cambridge. (2003)

[12] R. S. Hayano, Y. J. Uemura, J. Imazato, N. Nishida, T. Yasuoka and Y. Ishikawa. *Phs. Rev. Letts.* **41** (1979) 1743

[13] I. A. Campbell, A. Amato, F. N. Gygax, D. Herlach, A. Schenk, R. Cywinski and S.H. Kilcoyne. *Phys. Rev. Letts.* **49** (1994) 1291

[14] A. Furrer, J. Mesot and T. Strässle. *Neutron Scattering in Condensed Matter Physics Series on Neutron Scattering Techniques and Applications - Vol. 4.* World Scientific, Singapore. (2009)

[15] G. L. Squires. *Introduction to the Theory of Thermal Neutron Scattering.* Dover Publications, Mineola. (1997)

[16] G. E. Bacon. *X-ray and Neutron Diffraction.* Pergamon Press, London. (1966)

[17] Editor: R.A. Young. *The Rietveld Method (International Union of Crystallography Monographs on Crystallography).* Oxford University Press, Oxford. (1995)

[18] C. G. Shull and J. S. Smart. *Phys. Rev.* **76** (1949) 1256

Chapter 3

Experimental Details and Set-up

This chapter will deal with the details of the experimental techniques that have been used to obtain data presented within this thesis. It is intended to give an outline of the experiments performed and instruments used throughout the research conducted within this thesis. The theory of neutron scattering and muon spin relaxation experiments is described in Chapter 2 but the instruments and different sources will be be described in this chapter.

3.1 Magnetometry

Within this section the equipment used for magnetic measurements will be described.

3.1.1 SQUID Magnetometer

For all magnetic measurements a Quantum Design (QD) MPMS 5XL magnetometer was used. This consists of a SQUID (Superconducting QUantum Interferenence Device) and a set of gradiometer coils to measure the magnetic moment through the change in magnet flux detected by the coils. The QD magnetometer can access temperatures between 1.9 K and 400 K and can apply a field of up to 5 T using a superconducting magnet; magnetic moments can be measured with a sensitivity of

1×10^{-11} JT^{-1} [1]. All measurements are conducted using a DC transport technique where the sample is moved through the gradiometer coils and the voltage changes measured. An oven option is available that increases the temperature range up to 800 K.

The concepts involved will be described in more detail below. An excellent review of SQUIDs was written by R. l. Fagaly detailing the instruments and applications [2]

3.1.2 The Josephson Junction and the SQUID

In 1962 Josephson predicted that when a superconducting wire loop has a resistive barrier inserted into it the Cooper pairs can tunnel through this potential from one superconducting region to another; most importantly, with no voltage drop [3]. A SQUID is a superconducting ring that consists of one (rf SQUID) or two (DC SQUID) Josephson Junctions and uses this tunnelling effect to measure very small changes in magnetic flux density.

Generally a bias current (I_b) is applied to the SQUID loop where I_b is a point on the I-V curve that is on the edge of both superconductivity and high resistive behaviour. When magnetic flux is coupled to the SQUID loop this creates a screening current that either shifts the critical current on the I-V curve to higher or lower values depending on the direction of the magnetic flux. If I_b is kept only slightly higher then the critical current then the coupling of the SQUID ring to the magnetic flux will either cause an increase or decrease of voltage across the Josephson Junction that is in a period of the flux quantum [1].

As the QD MPMS uses an rf SQUID this will be the focus of the following discussion. As mentioned the rf SQUID contains one Josephson Junction and when magnetic

[1] Only discrete amounts of magnetic flux can be trapped in a superconducting ring and therefore it is quantised where $\Phi = n\Phi_0$. The units of flux quanta is defined as $\Phi_0 = 2.068 \times 10^{15}$ Wb. Since 1 Wb/cm^2 = 0.1 mT in a superconducting ring of 1 cm^2 magnetic flux can only exist in quanta of 2.07×10^{-11} T

flux is inductively coupled to the SQUID ring this causes a change in current which is converted to voltage. The circuit is tuned to a specific radio frequency where the amplitude of the oscillations is at a critical level where there is little change in output voltage. This plateau is the prime operating condition for the SQUID therefore feedback circuitry is used to ensure this is maintained. Coupled flux to the SQUID coil will have both an ac and dc component and when the critical current is exceeded in the weak link, the oscillations in the rf coil are reduced by a single Φ_0 which then returns to normal as the weak link becomes superconducting again.

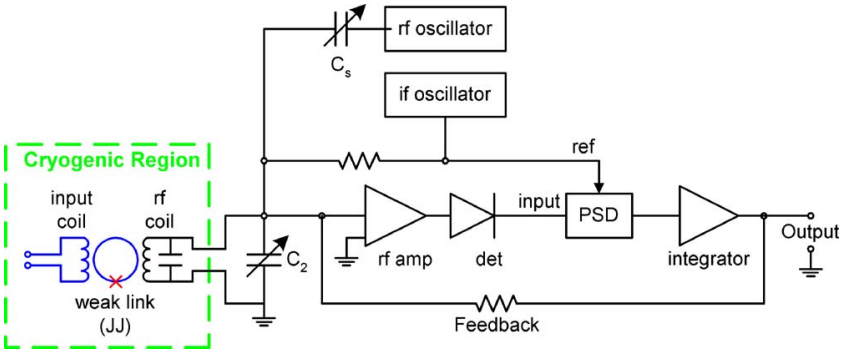

Figure 3.1: Block diagram of RF SQUID with locked loop operation. The input would be a detection coil (pickup), JJ means Josephson Junction and PSD is phase sensitive detection [2].

Using a SQUID loop as a detection coil is challenging due to its small area and the inductance can be small. A flux transformer is needed usually in the form of a pickup coil. Within systems detecting changes in magnetic flux using only a single coil would be very susceptible to stray field from external sources therefore generally most equipment uses two or more separate coils that usually are counter wound. The sample can be placed in the middle of one coil and the other coil will act as a separate compensating coil that will cancel out uniform stray magnetic fields. The response of a magnetic detection coil drops off as $\frac{1}{d^3}$, where d is the distance from the coil, therefore the sample's magnetic field will couple significantly to only one coil whereas external uniform magnetic fields will couple equally to both coils and therefore will cancel out. There are many types of different configurations for detection coils; the most commonly used are are a first order gradiometer where

two separate coils are counter wound and a second order gradiometer where there is a larger (two winds) middle coil with two smaller (single wind) coils above and below that are counter wound, which is found in the Quantum Design MPMS and an example is shown in figure 3.2.

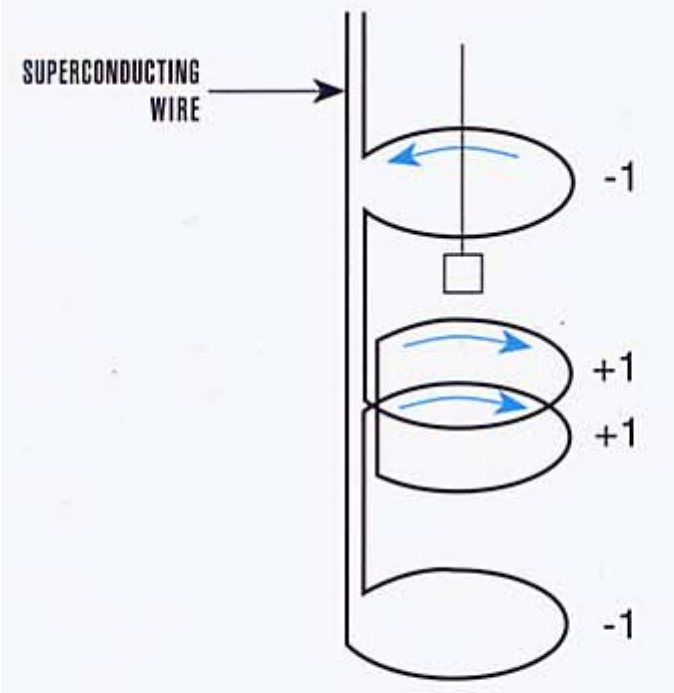

Figure 3.2: Second order gradiometer coils. The coils at the extremities are counter wound with respect to the middle coil which produces a flux change within the coil in the opposite direction. It is the signal produced from the middle and top/bottom counter wound coils that produce a curve that can be modelled as a dipole moment [4].

3.1.3 Quantum Design MPMS XL

The QD MPMs can be split into many sections that will be discussed below. A picture of the full length of the probe is shown in figure 3.3 with components labelled.

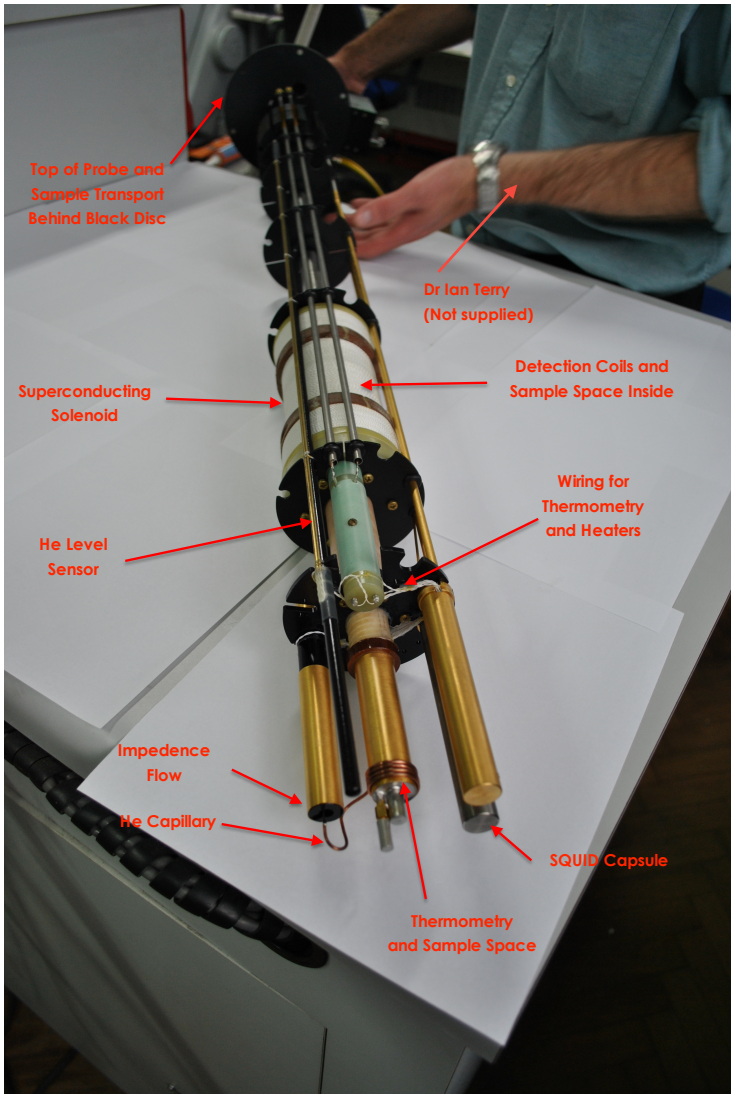

Figure 3.3: Probe of the QD MPMS with components labelled. The full probe would be completely immersed in a dewar of liquid He which keeps the superconducting components below their critical temperature.

Sample Space and Temperature Control

As previously mentioned the QD magnetometer can scan temperatures from 1.9 - 400 K within an applied field -5 T $\leqslant \mu_0 H \leqslant$ 5 T and was used for magnetic susceptibility measurements. Samples are located within the second order gradiometer coils, the central coil being positioned at the centre of the core of the superconducting solenoid. The other two gradiometer coils are positioned 1.5 cm above and below the central coil. The sample space itself has a diameter of 9 mm and the temperature is maintained by the use of a heater and He exchange gas. To access lower temperature regimes below that of approximately 5 K a small capillary filled with He is pumped on which reduces the vapour pressure and directly the temperature. Thermometers are located at both the base of the sample chamber and at the centre of the sample chamber that must be in agreement before measurements are taken. The quoted temperature stability is $\pm$5 mK [1]. Although the temperature facility of the QD MPMS is very stable (typically $\delta T \approx 0.01$ K), problems can be encountered when ice blockages arise in the system, especially when attempting to achieve temperatures below 4.2 K. This can block the impedance valve which prevents the capillary of He being able to be pumped on.

The SQUID

The SQUID itself is the most sensitive part of the piece of equipment and was discussed in more detail previously in section 3.1. The SQUID does not directly measure the changes in magnetic flux from the sample which is why detection coils are needed. As the sample is moved through the detection coils the change in current, which is inductivity coupled to the SQUID, produces a change in output voltage that is directly proportional to the current flowing through the SQUID coil. The SQUID is located in a superconducting shielded can 11 cm below the detection coils. The magnetic shielding is necessary as the SQUID is extremely sensitive to any magnetic fluctuations whether this is from within the laboratory, the superconducting solenoid or even the fluctuations in the Earths magnetic field.

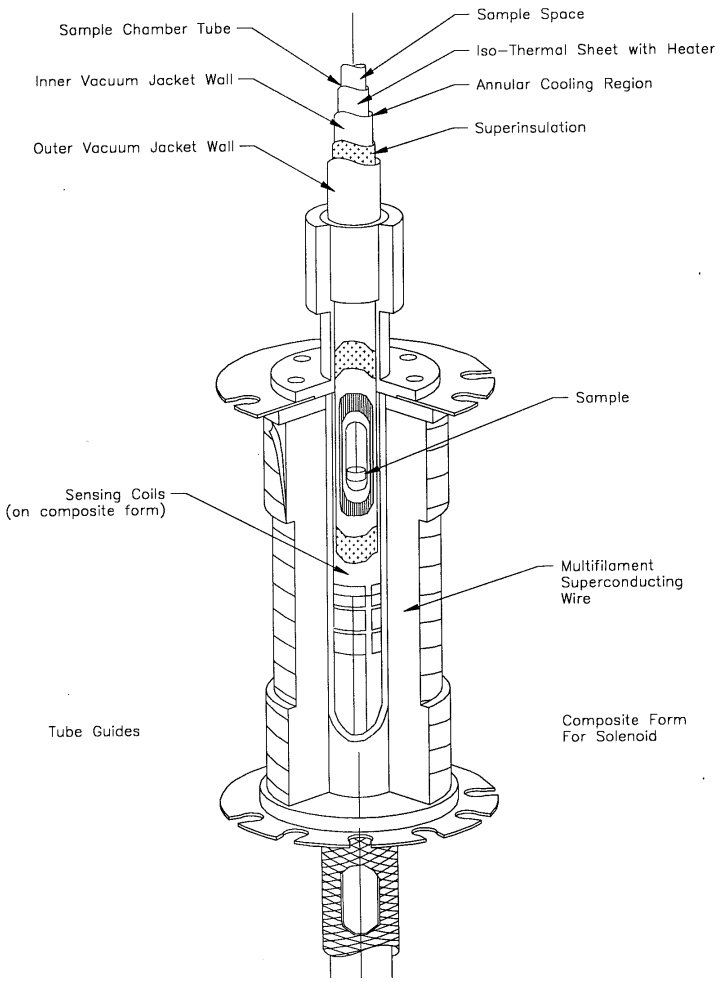

Figure 3.4: Schematic of QD MPMS sample space [5].

Detection Coils

As previously mentioned the QD MPMS employs a second order gradiometer set up for the detection coils as shown in figure 3.2 made from a superconducting wire. The upper and lower coils are a single turn that is counter wound to a double turn in the centre. The sample sits in the centre of the gradiometer coils and is moved through the entire range (4 cm) of these coils. As the sample is moved its magnetic field couples inductively to the coils which in turn couples to the SQUID.

The second gradiometer set up also acts to reduce noise and background drift as the flux change in the two centre coils will be balanced by the change in the upper and

lower single coil. Over time persistent currents can build up within the detection coils that can skew the measurement. This can be prevented by heating a small portion of the superconducting wire that causes a very small and localised quench [28].

5 T Superconducting Solenoid

The magnet within the MPMS acts as a closed loop. The magnet can be charged up during an experiment and will stabilise at a given field value without being coupled to an external current source. To charge the magnet a switch is used so that the closed circuit is broken and the current stored in the superconducting ring can be altered. When a desired field is reached the circuit is closed and the superconducting magnet returns to persistent mode. When the magnet is charging measurements using the SQUID cannot be made as the ramping of the magnetic field creates a lot of noise.

It is worth noting that after the current loop is closed and the magnet is returned to persistent mode, the magnetic field can further relax over time which is known as flux creep. This is due to magnetic forces acting upon the magnetic flux pinned in the superconducting wire. This means that even when set to zero-field there may still be residual trapped flux within the magnet. In fact one of the limitations of the QD MPMS and superconducting magnets in general is that it is difficult to obtain a true zero-field as residual flux can be trapped within the superconducting solenoid leading to stray fields of approximately 0.1 mT. Moreover the size of the trapped flux can depend upon the history of field settings in the magnetometer. One method to minimise trapped flux is by using a function that oscillates the field around 0 T while reducing its magnitude after every half period. However this is only effective in reducing the trapped field by about an order of magnitude. The oscillate function can also be used to set accurate fields at any value though it can have an adverse effect on samples that are sensitive to magnetization history such as spin glasses. Usually one uses the ‘no overshoot’ function for setting fields which increases/decreases the field value to that desired. These different ways of applying a field can have important effects on the sample and should not be neglected when planning an experiment.

The magnet can also be set to hysteresis mode whereby the switch to the superconducting solenoid is kept open and the current supply to the magnet is kept on. This means the field can be ramped or changed quickly which is of benefit when measuring the magnetic moment as a function of field. Although the field may not be as stable when the magnet is set using the oscillate or no overshoot function (ΔB = 1 - 2 G) the speed of the measurement can make up for this.

One thing that must be avoided is quenching of the superconducting magnet, this occurs when a small portion of the superconductor becomes normal and the resistance of the material increases rapidly. There is a resistive loss which is converted into heat which in turn heats the surrounding parts of the magnet. Quenching will occur if the current in the power supply is remarkably different to that in the magnet and when the closed superconducting circuit is opened this difference in current can lead to localised heating of the solenoid.

The Measurement

When conducting experiments using the QD MPMS powder samples are mounted in a gelatin capsule, which is small and has a low mass, and then secured in a clear plastic 14 cm long straw with either GE varnish or pieces of straw. Both gelatin and plastic have a very low moment, usually much smaller than that of the sample. Moreover, the straw itself is longer than the distance between the three detection coils (3 cm) and therefore it is present within all three coils during the measurement, thus minimising its impact on the samples' measured magnetic moment. The sample rod is made out of steel and brass with a plastic connector onto which the plastic straw is secured. The distance between the ideal sample position and the top of the sample rod should be 122 cm.

In DC transport mode, the sample is moved through the detection coils being driven by a motor where the step size can be varied. Changing the samples position with respect to the detection coils induced a change in magnetic flux and current within the coils and ultimately a change in output voltage of the SQUID. Generally one

takes an average of 3 scans over a 4 cm range with each scan containing 32 points. It is imperative to make sure the the sample is much smaller then the detection coils in order to get data that can be easily fit as a point magnetic dipole. If the sample is too long then there will be no observable change in the magnetic flux within the detection coils. It is for this reason that a long plastic straw is used to house the sample. When the sample is moved through the detection coils this results in a change in voltage within the SQUID ring where a trace similar to what is shown in figure 3.5A is obtained. The peaks and troughs are due to the sample being moved through each individual coil; top, middle and bottom. This trace can be treated as a magnetic dipole and by fitting to the curve one can calculate the magnetic moment of the sample.

The QD software detrends the data by removing the background which assumes a linear offset to achieve a 'symmetric' trace and then fits to the data to calculate the spatial response of the magnetic moment of the sample (see figure 3.5B). Information on the algorithim used in this process is in a technical note on the web site [7]. Note that the SQUID voltage to magnetic moment conversion is calibrated with a sample of palladium.

Another technique used with the QD MPMS for measuring the magnetic moment of a sample is the Reciprocating Sample Option (RSO). In this mode of operation the sample is oscillated around a fixed position, the amplitude of oscillation being small enough (typically 100 μm) so that in a very small region of the field one can create a perfectly homogenous sample environment. The corresponding SQUID voltage has an oscillatory component which results in a greater magnetic moment sensitivity. The sample is usually positioned at a point of greatest slope of the SQUID response shown in figure 3.5A .

3.1.4 AC Susceptibility

Using AC susceptibility one is able to measure the magnetic susceptibility using a small AC magnetic field with a frequency, ω. It should be noted that an applied ex-

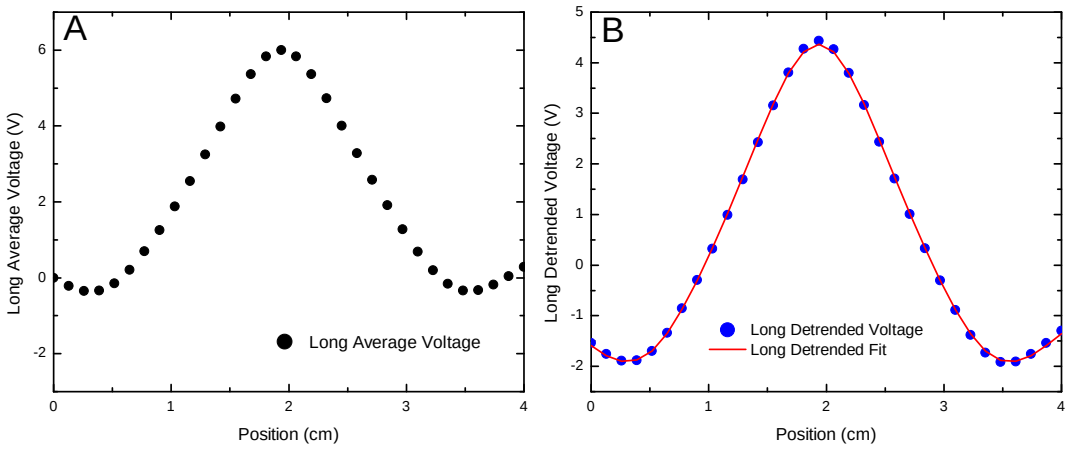

Figure 3.5: **A:** Typical response of moving a sample through the detection coils of the QD MPMS. The sample is centred at 2 cm shown by the maximum in the graph. **B:** Detrended data from A showing the fit of the QD software that calculates the magnetic moment (emu) from the voltage change measured. The data was taken at 10 K where B = 5 T on the sample $Mn(TCNQ\text{-}d_4)_2$.

ternal DC field can be applied while taking AC susceptibility measurements however for the purpose of this research no external field was applied. The main difference between what DC and AC susceptibility probes is that within a DC measurement the field can be considered static and so the response of the magnetization (M) will also correspond to a static state. Due to the fluctuating field within an AC measurement one can probe the magnetization dynamics on a time scale that is much faster than that accessible with a DC measurement.

At very low frequencies the AC susceptibility will follow the M(H) observed in the DC susceptibility and in small field the moment will be

$$m_{AC} = \chi \cdot H_{AC} sin(\omega t), \tag{3.1}$$

where H_{AC} is the amplitude of the AC field and ω is the frequency. As the frequency is increased the susceptibility will no longer follow the DC susceptibility and will

show a frequency dependence where the magnetization of the sample cannot keep up and follow the driving AC field. The resulting AC susceptibility can be thought of and separated into two components, the real part, $\chi'(\omega)$, and the imaginary part, $\chi''(\omega)$. Both parts of the susceptibility can be related to the static susceptibility by a phase shift,ϕ:

$$\chi' = \chi \cos \phi, \tag{3.2}$$

$$\chi'' = \chi \sin \phi. \tag{3.3}$$

χ can be defined as, $\chi = \sqrt{(\chi')^2 + (\chi'')^2}$ and $\phi = \arctan(\chi''/\chi')$. As mentioned, χ' will measure the real susceptibility where at high frequencies it will show a dependence. The imaginary part, χ'' provides information on the absorbance where hysteric and relaxation processes make this quantity non-zero. Essentially one is able to look at the decoupling of the moments from the oscillating field which can be related to freezing processes within the material.

3.1.5 Quantum Design Physical Properties Measurement System

Experiments were conducted on a QD PPMS with a 9 T superconducting solenoid, however as stated earlier no external DC field was applied. The AC Magnetometry System (ACMS) consists of a set of coils which provide the excitation field and a first order gradiometer detection coil where the set up is shown in figure 3.6. The copper coils are wound on sapphire coil forms as these have a low background but provide good thermal stability. The AC coil is wound around both detection coils as this allows for the background noise to be minimised by the compensation coil. To minimise the phase shift and contribution from the instrument itself, i.e. sample holder, magnet, cryostat, etc, there is a calibration coil at the centre of each detection coil which can determine the instrumental phase shift. The probe itself is placed within the sample space and the 12-pin connector at the bottom is connected

to the puck at the bottom of the sample space. This then connects the probe to the electronics and QD control system.

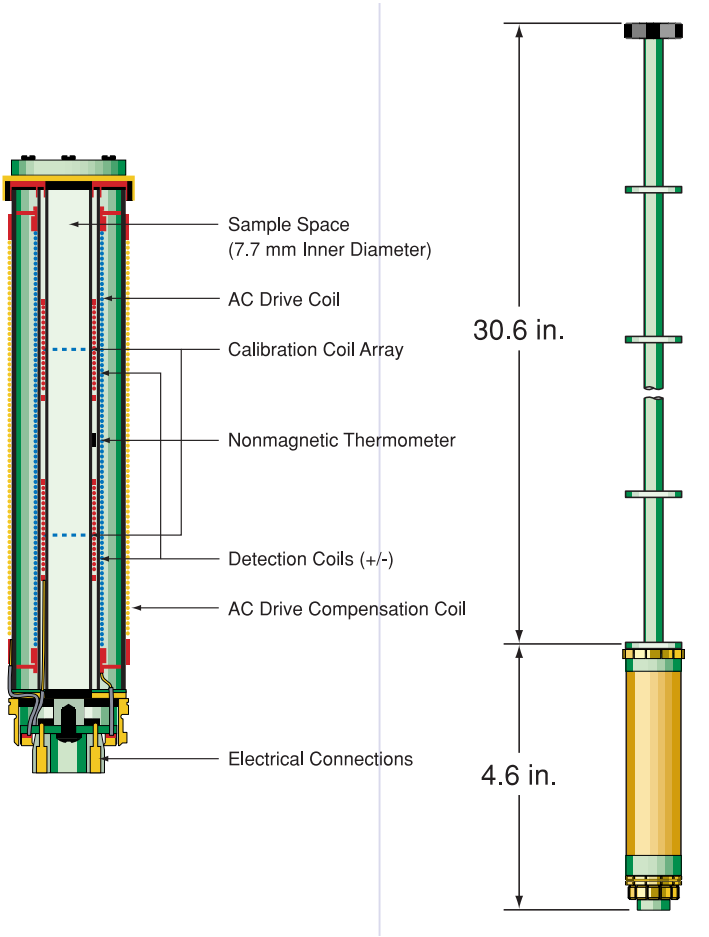

Figure 3.6: QD PPMS AC susceptibility probe.Taken from [8].

The measurement itself is performed by centring the sample in the second of the detection coils and the voltage changed induced in the coil by the change in magnetic flux within the sample is recorded. Multiple scans can be recorded to increase the signal to noise ratio. The calibration coils measure the amplitude of the AC magnetic field and also the response of the instrument and by subtracting this from the sample signal provides an accurate way of measuring the susceptibility.

Generally within samples that have a frequency dependent signal, a lock in amplifier is used to reduce signal to noise and can measure the phase shift in the output and return signal. With the QD PPMS a Digital Signal Processor (DSP) is used which improves the signal to noise ratio over that of an analog lock-in amplifier.

The specification of the ACMS probe are as follows [8]:

- Drive Coil Frequency: 10 Hz to 10 kHz
- Temeprature Range: 1.9 - 350 K
- Drive Amplitude: 2 mOe - 15 Oe
- Sensitivity: 2×10^{-8} emu

3.2 Microscopy

Due to the limited wavelength of visible light, one can only image objects down to a few hundred micrometers. This is due to the limited resolution of a system being related to the wavelength of the particles used in imaging by

$$d \approx \frac{\lambda}{2\beta}, \tag{3.4}$$

where λ is the wavelength of the particles and $\beta = sin(\theta)$, which is the numerical aperture therefore to image nanostructures particles with a small wavelength is needed. Using electrons which can have a much smaller wavelength it is possible to image objects with a resolution of approximately 1 nm or less. There are two main types of electron microscopy used that are briefly explained below.

3.2.1 Transmission Electron Microscopy

Transmission Electron Microscopy (TEM) is where a beam of electrons is accelerated by a potential difference and focused onto the sample using a magnetic lens. The electrons are transmitted through the sample and the contrast is what gives rise to the image as different thicknesses and sample densities will transmit a different amount of electrons. The basic set up of a TEM is shown in figure 3.7 where the resolving power is determined by the wavelength of the electrons. For typical voltages of 100 kV the resolving power is subatomic however other imperfections within the measurements can in reality, keep the resolving power above this limit [9].

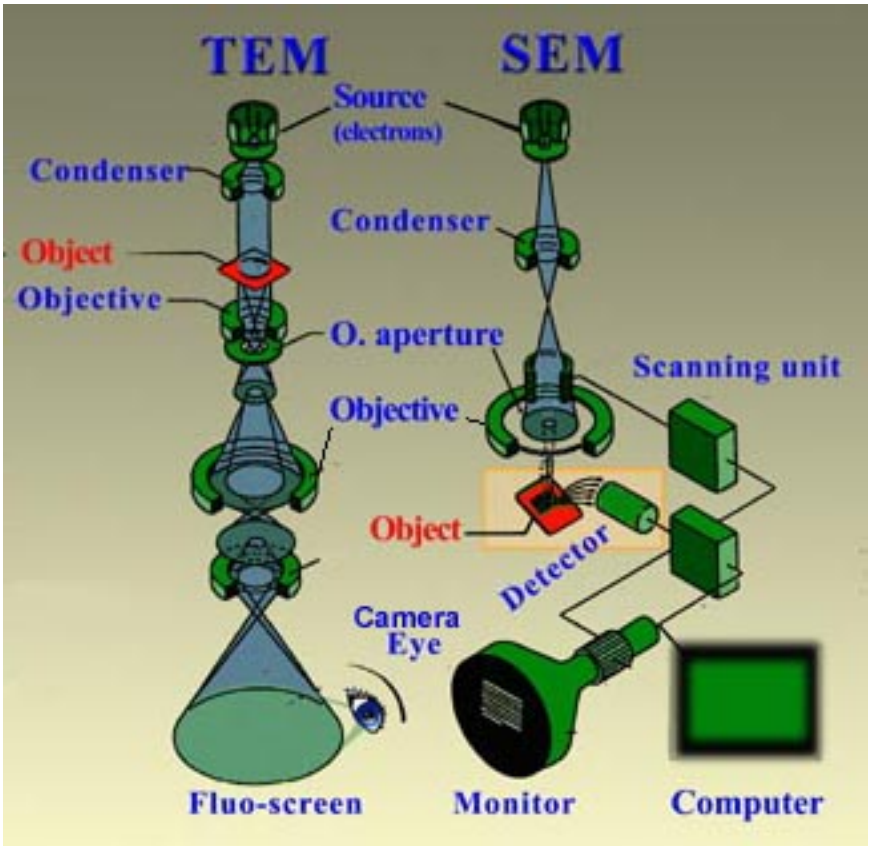

Figure 3.7: Basic set up of a TEM and SEM microscope which highlights the differences between the two techniques. Taken from [10].

Electron Energy Loss Spectroscopy

In Electron Energy Loss Spectroscopy (EELS) electrons with a narrow range of wavelengths are fired at a sample and are inelastically scattered. This loss in energy can be measured and corresponds to a particular cause of the scattering process. The incoming electrons can scatter off phonon excitations, intra and inter molecular transitions, plasmon excitations and inner-shell ionisation. Generally one considers the inner-shell ionisation energies which have specific values for specific atoms or elements. EELS can be used to provide information on the elements within the sample as well as their spatial distribution.

3.2.2 Scanning Electron Microscopy

Scanning Electron Microscopy (SEM) poses an advantage to TEM as the electrons do not have to penetrate the sample allowing thick samples to be measured. A beam of high energy electrons is fired at the sample and the back-scattered as well as secondary electrons are measured. The electron beam is highly localised and by moving the beam or scanning the sample one is able to build up a detailed picture of the material. One disadvantage is the trade off in resolution as typically TEM works at a much higher resolution than SEM [9].

3.3 Muon Spin Relaxation Experiments

μSR experiments were conducted on the EMU instrument at ISIS (Rutherford Appleton Labs, UK) and on the GPD (General Purpose Decay) instrument at PSI (Paul Scherrer Institut, Switzerland). ISIS is a pulsed source whereas PSI is a quasi-continuous beam, where the advantages of both will be discussed in more detail below. The theory of μSR was covered in Chapter 2 and this section will focus on the instrumentation and technique.

3.4 Muon Production and Facilities

Muons are produced from pion ($\pi^{\pm}$) decay where for the positive case (which is most commonly used for studying materials):

$$\pi^{+} \rightarrow \mu^{+} + \nu_{\mu}, \tag{3.5}$$

where $\pi^{\pm}$ has a lifetime of 26.04 ns. Although muons are constantly raining down upon us along with other cosmic particles a useful source for studying materials can only be realised at large scale facilities such as ISIS and PSI. Muons are created by a beam of protons impacting on a low Z (where Z = Atomic number) target,

where in the case of ISIS the target is pyrolytic graphite (5-10 mm thick). Muon production can be separated into two separate methods; surface and decay muons. Surface muons use low energy pions that decay in the target which results in low energy muons that are spin polarised in their direction of decay. Surface muons can be focused easily and since it relies on pions being stopped within a large target where the intensity of the beam is generally very high. A disadvantage is that only μ^+ can be produced via this method as π^- is captured by the graphite. Decay muons are created when the pion decays after it has escaped the target and in flight which results in the muons having a much higher energy than that of the surface muons. Decay muons can have energy ranging from 100-200 MeV whereas surface muons have lower energies $\sim$30 MeV [11]. Both μ^+ and μ^- can be produced via this method where the resultant muons can have a wide range of energies where the muon momentum can be selected using magnets. After the muons have been created they travel to the sample and are focused using quadrupole magnets as well as bending magnets for steering the beam. Using these magnets it is possible to select the muon momentum as the magnetic field that must be applied to deflect the muon is proportional to the muon momentum.

The specific muon sources at ISIS and PSI operate as follows. The ISIS synchrotron which accelerates the protons is a pulsed source with a frequency of 50 Hz that produces bunches of surface muons that are implanted into the sample at the same time. PSI is a quasi-continuous source which uses both surface and decay muons. The advantages to using a pulsed source is that the background is lower during the measurement and the time constant of the muon experiment can be increased by a factor of 3. Using a pulsed source one can also use the muons for more extreme experiments such as muon spin r.f resonance. The quasi-continuous source allows for a much shorter time scale to be probed which is a great advantage when dealing with very fast fluctuations, outside of the ISIS time window, and offers a greater time resolution. At PSI a range of muon energies can be achieved that allow for muon momentum to be selected which determines the implantation depth within the sample. Generally for a pulsed source the range of the muon within the sample is 110 mg cm^{-2} and at a continuous source the range is 150 - 110 mg cm^{-2} which is

related to the sample density [12]. Although there may be differences in the beam line the one similarity is that both beams produce 100% spin polarised muons.

3.5 The μSR Experiment

For all experiments performed we use μ^+ which decays into e^+ where, due to the asymmetry in the decay distribution from parity violation, the positron tends to be preferentially emitted along the direction of the spin of the muon at the point of decay. This means that simply by using the position or direction of the positron emission one can gain information on the relaxation of the spin of the muon within the sample. To detect a positron in muon experiments plastic scintillators connected to photomultiplier (PM) tubes are used. The positron causes light to be emitted from the sintillator materials that is converted to a voltage by the PM tube which can be detected by the electronics which essentially counts events and places each count in a bin associated to a specific time.

A standard μSR experiment will consist of forward (F), backward (B), Left (L), Right (R), Up (U) and down (D) detectors. For a continuous source, where only one muon is implanted at a time, one needs four detectors; F, B, U and D and a switch to start the measurement when the muon enters the sample. For a pulsed source there are a large number of muons that arrive in pulses with a clear time structure. This means that more detectors are needed at each location. At ISIS two forward and two backward detector banks are used which each contain an array of 32 scintillators and PM tubes in the case of the MuSR instrument and 96 scintillators in total (48 in each bank) in the case of EMU.

Within a μSR experiment with only two detector banks (F and B) what is essentially measured is simply the asymmetry in the decay of the muons within the F and B detectors which is described by

$$a_0(t) = \frac{N_B(t) - \alpha N_F(t)}{N_B(t) + \alpha N_F(t)}, \tag{3.6}$$

where N is the number of counts in each detector and α is an experimental parameter which accounts for any differences in detector efficiency. α can be calculated from performing a Transverse Field (TF) experiment on a sample that shows no relaxation, such as Ag, or from applying a TF to the material in question. For our experiments on Ni(TCNQ-d_4)$_2$ we applied a TF of 100 G where from a fit to the oscillations, as shown in figure 2.8, α could be calculated. For the data taken, α is then kept constant unless the sample is removed or changed.

When the muons are implanted into a material they will respond to the internal magnetic fields. In the case of a TF experiment this will be the applied field plus the internal magnetic fields. For a static distribution of magnetic moments in a TF field each muon will experience a field that causes it to undergo Larmor precession with a frequency that is proportional to the experienced magnetic field strength where $\nu = \gamma_\mu B$ where ν is the precession frequency and γ_μ is the muon gyromagnetic ratio, 135.5 MHz T^{-1}. Therefore for a field (either external or internal) of 1 mT this would correspond to a frequency of 0.135 MHz. The muons initially will begin to precess in phase but varying fields leading to a field distribution will cause a dephasing that is described by a Gaussian relaxation:

$$G_z(t) = A \exp(-\sigma^2 t^2). \tag{3.7}$$

Here σ is the rate that the muons will dephase and this parameter contains information on the local magnetic environment which is related to Δ, the distribution of internal fields. One of the advantages of μSR is that, since the muons sample on a local scale, zero-field measurements can also be conducted which, for instance, is sensitive to magnetic phase transitions where one can begin to detect bulk ordering of the magnetic moments. Longitudinal field measurements can also be performed where it is possible to decouple relaxation processes from one another as the applied field is increased. This is useful if the muon may be responding to nuclear moments as a small LF can decouple this relaxation signal while not being large enough to modify the electronic magnetism within the sample.

It should also be noted that implantation of muons into a sample can also lead to muonium formation where an incoming muon picks up and electron during thermalisation. This creates a hydrogenic muon-electron species where there is a hyperfine interaction observed with a hyperfine coupling constant, $A_0 = 4.46$ GHz in the vacuum state. It is possible for the hydrogen muonium to the form paramagnetic states within organic molecules from addition reactions across an unsaturated bond where a muonium radical state is formed. These states show a hyperfine coupling which can be studied using the application of an LF where the different values of hyperfine coupling constant can provide information on the distribution of electron density. Generally diffuse electron density spread across the molecule show a lower hyperfine coupling.

To analyse the data many programs can be used, however within the presented research, the WIMDA[2] program was used for data analysis [13]. WIMDA is a convenient Microsoft Windows based analysis software where one can view raw data files and fit the data using either user defined functions or functions that can be found in a library within the WIMDA program. The fits and data can be exported as text files which can then be imported into other plotting programs, such as Microcal Origin or Microsoft Excel.

3.6 μSR Instruments

3.6.1 EMU, ISIS

The experiments performed at ISIS on the EMU beamline. EMU is optimised for ZF and LF measurements and is comprised of 96 detectors which are separated into 6 axial banks, 3 forward and 3 backwards. The time resolution of the experiment can be changed between settings of 8, 16, 24, or 32 ns and the measurable frequency is from 0.1 to 10 MHz, the upper limit is due to the finite muon pulse width. LF of

[2]WIndows Muon Data Analysis

up to 5000 G can be applied and the experiments were performed using an Oxford Instruments (OI) orange 50 mm cryostat that is capable of temperatures between 2 K and 300 K [14].

Figure 3.8: The EMU spectrometer [14].

3.6.2 GPD, Paul Scherrer Institut

GPD is the General Purpose Decay spectrometer where the muons are produced from the decay of pions in flight which leads to a range of muon momenta being produced. The beamline can produce both μ^+ and μ^- with momenta of 60 - 120 MeV/c, where specific values of the muon momentum can be selected. The instrument consists of a single forward, single backward, and a pair of both up and down scintillator detectors with a time resolution of approximately 1 ns. The magnet is rotatable depending on whether LF or TF measurements want to be performed and are capable of an applied field of 0 - 6600 G [15].

As well as allowing the study of short times that are out of the time scale of ISIS instruments GPD can also be used for high pressure measurements due to the high momentum of the muon which can penetrate the pressure cell. A CuBe pressure cell was used where the maximum pressure obtainable is approximately 15 kbar. The sample is placed into the bottom of the CuBe cell where Daphne-7373 oil is used to create hydrostatic pressure and a PTFE gasket seals the tube and maintains the applied pressure. To measure the applied pressure a small sample of indium is also placed in the cell where the superconducting T_C is pressure dependent and when measured within the cell correlates to the applied pressure. When performing the experiment below 60 K the CuBe cell has a clear gaussian Kubo-Toyabe dependence that is temperature independent. The pressure cell was cooled in the Janis ^{4}He vaporiser cryostat which is capable of temperatures between 2.5 K and 300 K.

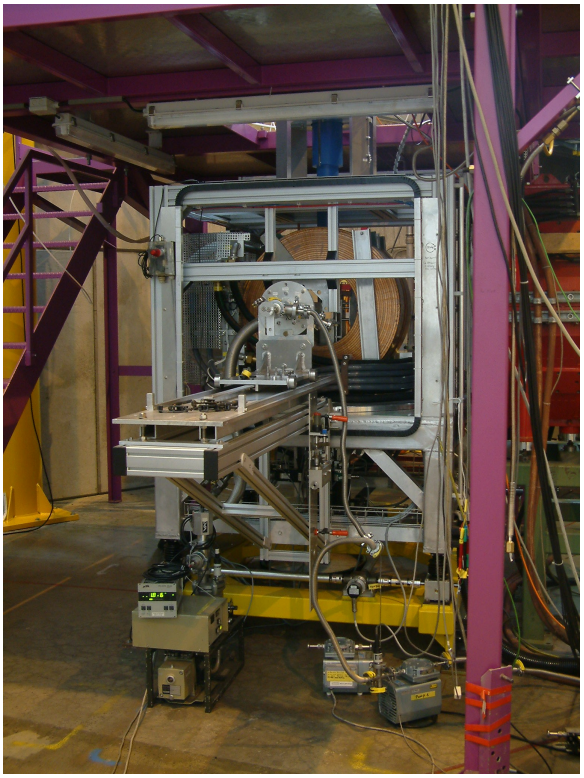

Figure 3.9: The GPD spectrometer [15].

3.7 Neutron Production and Experiments

Neutrons were initially discovered by James Chadwick in 1932 and subsequently neutron sources have emerged all over the world as they prove vital to many areas of research. They can be produced by two different methods; nuclear fission and spallation sources. Nuclear fission sources, such as the Insitiut Laue-Langevin (ILL), create a continuous beam of high energy neutrons through the capture of a slow neutron by ^{235}U. This reaction is effectively self sustaining as each individual reaction produces more neutrons than is needed to initiate the reaction.

Within a spallation source (such as ISIS, RAL) charged particles are fired at a target which results in neutrons 'evaporating' from the unstable nuclei. In order for spallation to occur, the incoming proton must have a wavelength comparable to that of the dimensions of the nucleus. The collisions with the nucleus cause energy to be transferred which is distributed over the entire nucleus resulting in it reaching a highly excited state which then 'evaporates' neutrons. The energies of the neutrons produced will have an energy distribution associated as energies up to that of the incoming proton can be occupied. At ISIS the spallation source is based on a pulsed proton synchroton that operates at 50 Hz, where the protons are guided towards a target that is made out of tungsten and tantalum.

Since both fission and spallation methods produce neutrons with a range of momenta with MeV energies and, as meV is needed for a scattering experiment, moderation is needed to retard the neutrons. These moderators are usually kept at room temperature and are filled with light elements/molecules such as H_2O or D_2O; the resultant moderated particles are known as thermal neutrons. Cold neutrons use colder moderators such as D_2 at $\sim$20 K whereas hot neutrons use a hot moderator such as graphite heated to 1000 K. When considering thermal neutrons, after leaving the moderator the neutron packet will have a log-normal distribution of momenta generally with a peak width wavelength of 1 Å.

To get monochromatic neutrons there are two methods, generally for time of flight experiments a chopper is used and for an experiment such as a triple axis spectrom-

eter a monochromator crystal is used. The chopper works by rotating a drum with slightly curved slits parallel to the incident beam at a set frequency that can filter out all but the desired neutron momentum. The monochromator crystal works by changing the angle of a specific orientation of the crystal with respect to the incident beam, specific wavelengths being selected using Bragg diffraction.

The detection of neutrons is indirect, in that generally one has to use the neutron to generate an electric charge that can be measured. There are a few different types of compounds that can be used for neutron detection however, for gas detectors, usually ^{3}He or $^{10}BF_4$ is used. Within these detectors an anode wire is run through a cylinder chamber of gas. When a neutron hits the gas it causes ionisation of the gas and the electrons produced are attracted towards the anode. Similar detectors can be used to calculate the position of the neutron when it hits the detector by measuring the voltage at both ends of a resistive wire run through the cylinder. From the voltage measured at each end one can calculate where on the length of cylinder the neutron hit. Another detector material is ^{6}Li which is used as a scintillator. The advantage of scintillator detectors is that they are very effective for high count rate but unlike the gas detectors they are sensitive to magnetic fields and gamma radiation.

Within this work only powder diffractometers have been used which can be separated into two methods; angular-dispersive (ADP) and energy-dispersive (EDP). In an ADP measurement monochromatic neutrons are used, with a large detector bank to measure the elastic diffraction angles (as opposed to a single detector that is moved through 2θ). The resolution for an ADP measurement is dependent on the monochromator angle, large monochromator angles will separate out overlapping Bragg peaks. EDP methods differ in that a pulsed source is used where the neutrons have a distribution of wavelengths and the sample is at a fixed scattering angle. Each d_{hkl} corresponds to a different time-of-flight and hence wavelength of the neutron. The resolution of these instruments generally depend on the pulse structure of the moderator, the length of flight path and scattering angle.

3.8 Neutron Scattering Instruments

3.8.1 D1B, ILL

D1B is a two-axis spectrometer that has a very high neutron flux, which makes it ideal for studying magnetic structures. A high spatial resolution can be achieved at small angles with a FWHM of 0.2°. A wavelength of 2.52 Å is attained using two pyrolytic graphite monochromators. Using a Ge monochromator allows the wavelength to be switched to 1.28 Å, though this reduces the flux by a factor of 16.

The instrument uses 1280 position sensitive detector cells filled with $^3He/CF_4$ with a height of 100 mm and a separation of 0.1° that covers angles ranging from 0.8 to 128.8° 2θ. A 50 mm OI orange cryostat was used in a temperature range of 1.7 and 300 K using liquid helium as the coolant. A 1 T magnet was also available to use, however for our studies it was not used. Due to the high flux of D1B very fast measurements can be done while scanning temperature, it is quoted as being able to scan through 1.5 - 300 K in 3-5 h [16].

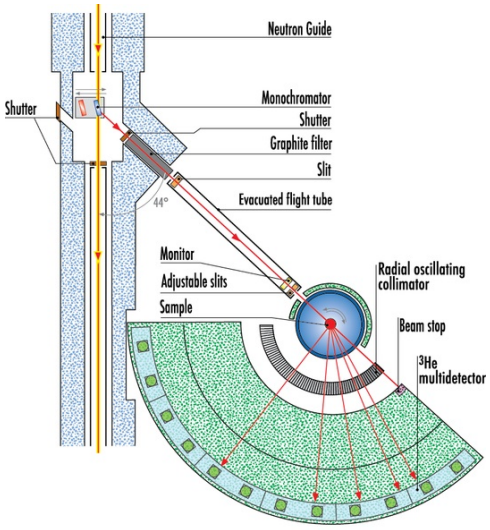

Figure 3.10: The D1B instrument [16].

3.8.2 D20, ILL

D20 [17] is a two axis diffractometer with a variable resolution and an extremely high flux. There are three different monochromators; pyrolytic graphite, Cu and Ge. Each monochromator gives different values of the neutron wavelengths with pyrolytic graphite giving a wavelength of 2.4 Å with a 70 % transmission. The Cu (200) monochromator provides wavelengths 0.82, 0.88, 0.94 Å at take-off angles from 26° to 30° where a second Cu (200) monochromator can be used to get a wavelength of 1.4 Å. Lastly the Ge monochromator can be used to access a wide range of wavelengths from 2.41 Å to 0.8 Å.

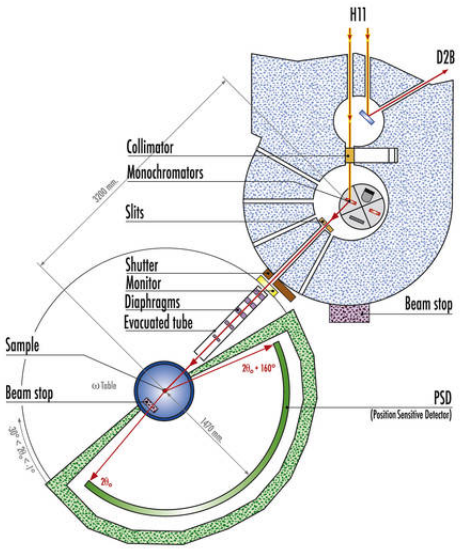

Figure 3.11: The D20 instrument [17].

Position sensitive detectors are used which are filled with $^3He/CF_4$ gas. Each detection plate has 32 cells of 0.1° where each plate covers 3.2°. In total the PSD detector bank covers 153.6°. A similar OI orange cryostat was used to that of D1B where temperatures between 1.7 and 300 K could be controlled. Overall the flux achieved on D20 is much higher than D1B and so diffraction patterns can be collected very quickly with a higher resolution.

3.8.3 D2B, ILL

D2B is a very high intensity two axis powder diffractometer that can also achieve high resolution although this is at the cost of intensity. A Ge monochromator is used with a high take off angle where wavelengths between 1 and 3 Å can be selected which makes this instrument suited to studying crystal structures of many different types of compounds. If the wavelength at the sample is 1.594 Å then one can select between high intensity or high resolution as switching between the two costs an order of magnitude in flux.

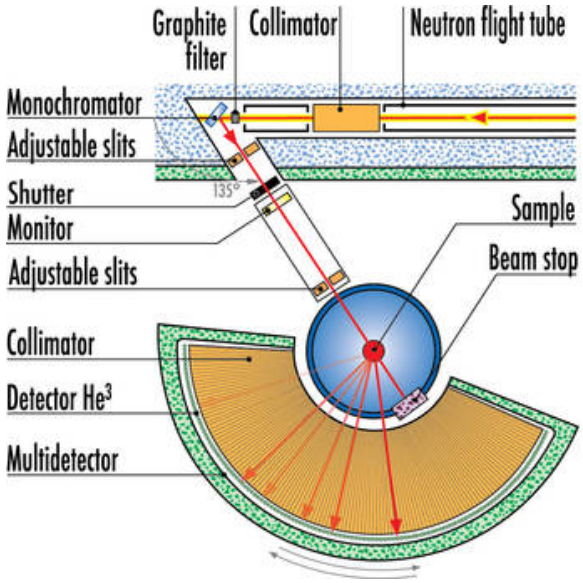

Figure 3.12: The D2B instrument [18].

The instrument uses a 2D detector array of 128 ^{3}He counting tubes where each tube is spaced 1.25° apart. It is possible to use a cryostat with the system however simply mounting the sample in a vanadium can, directly in the beam at room temperature leads to a much higher resolution avoiding scattering from the cryostat. It is also possible to use wavelengths up to 6 Å, at the cost of loss of flux, and makes the instrument ideal for looking at materials with a large d-spacing. A graphite filter can also be placed after the monochromator to give a 'cleaner' wavelength at 2.4 Å.

Bibliography

[1] Quantum Design MPMS Users Manual (2004)

[2] R. L. Fagaly. *Rev. Sci. Instrum.* **77** (2006) 101101

[3] B. D. Josephson. *Phys. Letts.* **1** (1962) 251

[4] www.mrl.ucsb.edu/mrl/centralfacilities/chemistry/quantum.html (July 2012)

[5] Magnetic Property Measurement System - Hardware Manuel. Quantum Design, San Diago. (1996)

[6] http://www.qdusa.com/techsupport/index.html - Fundamentals of Materials and Magnetic Measurements (July 2012)

[7] http://www.qdusa.com/sitedocs/appNotes/mpms/1014-214.pdf (July 2012)

[8] http://www.qdusa.com/sitedocs/productBrochures/mag3-07.pdf (July 2012)

[9] C. Kittel. *Introduction to Solid State Physics.* John Wiley and Sons, Inc, Hoboken, NJ. 8th Ed. (2005)

[10] http://www.vcbio.science.ru.nl/en/fesem/info/principe/ (August 2012)

[11] K. Nagamine Introductory Muon Science Cambridge University Press, UK (2003)

[12] S. L. Lee, S. H. Kilcoyne and R. Cywinski Muon Science: Muons in Physics, Chemistry and Materials Institute of Physics Publishing, UK (1998)

[13] F.L. Pratt *Physica B.* **710** (2000) 289

[14] www.isis.stfc.ac.uk/instruments/emu/ (Jan 2012)

[15] http://lmu.web.psi.ch/facilities/gpd/gpd.html (Jan 2012)

[16] www.ill.eu/en/html/instruments-support/instruments-groups/instruments/d1b/ (Jan 2012)

[17] www.ill.eu/en/html/instruments-support/instruments-groups/instruments/d20/ (Jan 2012)

[18] www.ill.eu/instruments-support/instruments-groups/instruments/d2b/ (Jan 2012)

Chapter 4

A Nickel-TCNQ Based Magnetic Material

4.1 Introduction

In recent years the field of organic based magnetism has attracted a great deal of interest, it combines areas of both chemistry and physics with the goal of creating tuneable magnets where the T_C can be altered by simple chemical changes to the organic moiety. By using a metal ion and creating a charge transfer salt with an organic radical, acting as the anion, the organic can act as an exchange pathway between magnetic ions [1, 2].

One of the first examples of charge transfer magnetic materials was the metallocene-TCNQ (7,7,8,8-tetracyanoquinodimethane) compounds, such as $[Fe(Cp^*)_2][TCNQ]$ ($Cp^* = C_5Me_5$, pentamethylcyclopentadienide), which produced alternating stacks of electron donors (metallocene) and acceptors (TCNQ) where there was no direct bonding between the two [3–5]. By making the anion smaller and thus creating a larger spin density, the magnetic properties of the metallocene compounds could be altered by exchanging TCNE (tetracyanoethylene) for TCNQ resulting in a shift of T_C from 2.55 K to 4.8 K for each respective compound [7, 8].

In fact, the salt [Fe(Cp*)$_2$][TCNQ] was found to exist in three different magnetic phases making it a more complex system perhaps than initially expected. The paramagnetic and metamagnetic phases were first synthesised by Miller *et al.* in 1979 [4, 5], however it was later found that by recrystallising the sample in acetonitrile at -20 °C resulted in a bulk 3D ferromagnet where T_C = 3.1 K [9]. The structure is similar to the metamagnetic product, with alternating chains of electron donor and acceptor along the *a*-axis. One subtle difference however is the conformation of the Cp rings, in the ferromagnetic product Cp cations are eclipsed and in the metamagnetic product the Cp cations are staggered. The TCNQ anions are arranged in a zig-zag formation along the b-axis and are aligned in the same direction for the respective products illustrating that simple conformational changes can have dramatic effects on the the magnetism within these samples.

Another factor that could greatly affect the magnetism within the [Fe(Cp*)$_2$][TCNE] form of the metallocene salt was solvent dependency. The un-solvated form has an orthorhombic unit cell where T_C = 4.8 K, however when a solvent is included in the structure this can severely alter the critical temperature [10]. If during the synthesis tetrahydrofuran (THF) is used, the unsolvated form is obtained, but if acetonitrile (MeCN) is used, which is a much better coordinating ligand, the product is; [Fe(Cp*)$_2$][TCNE]·S (where in this case S = acetonitrile). The solvated product has a monoclinic structure that is also composed of parallel alternating stacks of cations and anions where the intrachain Fe$\cdots$Fe distance is 10.451 Å compared to 10.621 Å in the unsolvated product [6]. Interestingly, the pure unsolvated product contained a sufficient amount of disorder so the location of the anion was not able to be exactly determined, however in the acetonitrile based product there was less disorder and so the location of the anion could be determined from XRD data. It was also possible to go from a solvated product to the pure product by removal of the solvent; once the solvent had been removed the T_C would shift back to a value of 4.96 K (except when S = 1-cyanopropane in which case T_C would shift to 5.12 K). This value is similar to that expected for a non-solvated product however it may be slightly higher due to less disorder being created which increases T_C. Within the AC susceptibility data there is a weak frequency dependence which can be characterised

by the parameter φ where

$$\varphi = \frac{\Delta T_f}{[T_f \Delta \log \omega]}. \tag{4.1}$$

T_f is the freezing temperature which is the cusp in the AC susceptibility and ω is the angular frequency of the AC experiment. Within disordered systems, $0.1 < \varphi < 0.01$ [11]. Within the [Fe(Cp)*][TCNE]·Solvent salts, φ ranges from 0.005 - 0.0085 (except for when S = 1-cyanopropane where $\varphi = 0.021$) and so the samples are believed to be weak spin glass materials [6].

It was found that the addition of different solvent molecules had a variable effect on the critical temperature and, for example, when S = MeCN, $T_C = 2.87$ K, while S = NCC_4H_8CN, $T_C = 4.83$ K. These solvent molecules disrupt the structure and from AC susceptibility measurements, there is evidence of increased magnetic glassiness. However, it is possible to include THF in the structure which shifts the T_C to a higher value of 5.5 K where the glassiness is reduced. The presence of THF is believed to increase the pressure of the sample where the shift in T_C corresponds to a pressure of 2.5 kbar as $[Fe(Cp^*)_2][TCNE]$ shows a pressure dependence of 0.22 K/kbar [12].

The field was further expanded by the discovery of a room temperature charge-transfer metal-organic magnet (T_c >350 K), $V(TCNE)_x \cdot yCH_2Cl_2$ where the vanadium ion and TCNE are believed to couple antiferromagnetically which results in the overall ferrimagnetism observed [13].

One of the major disadvantages to this discovery was that the material was amorphous and showed no evidence of crystallinity from x-ray diffraction studies. The idea of vanadium-organic magnets was recently extended by Harvey *et al.* where a series of salts of $V(EA)_2 \cdot yCH_2Cl_2$, where EA = Electron Acceptor, in this case a derivative of flurophyenltricyanoethylene. By subtle changes to the electron acceptor the critical temperature could be shifted within the region of 150 - 300 K [14].

Miller and Epstein further investigated the effect on solvent within the $V(TCNE)_x$

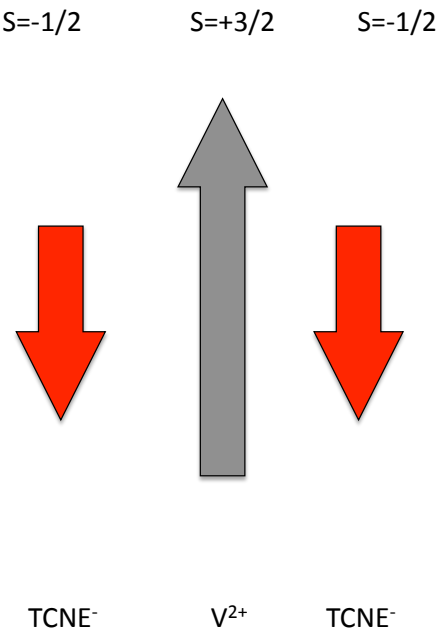

Figure 4.1: Example of the spin configuration within V[TCNE]$_x$ illustrating the antiferromagnetic coupling of the TCNE anions to the V^{2+} cation. The V ion has an $S = \frac{3}{2}$ ground state configuration and the TCNE anions an $S = -\frac{1}{2}$ as it opposes the direction of the moment on the V ion. Coupling of these spins lead to an $S_{Total} = \frac{1}{2}$.

system. They were able to produce a thin film of the sample using chemical vapour deposition which showed slightly different magnetic properties to the bulk (produced from a solvent wet chemical route) yet both samples had a similar T_C=410 K [15].

The solid lines of figure 4.2 show fits to Bloch's law for a ferromagnet:

$$M_s(T) = M_s(0)(1 - BT^{\frac{3}{2}}). \tag{4.2}$$

The values of $M_s(0)$ were calculated to be 14.2 emu Oe/g and 17.6 emu Oe/g [1] for the bulk and film samples respectively. The film sample exhibited a saturation

[1] It should be noted that these values are not SI nor cgs-emu, however the values have been quoted consistently with the data obtained from the original paper by Miller and Epstein [15]

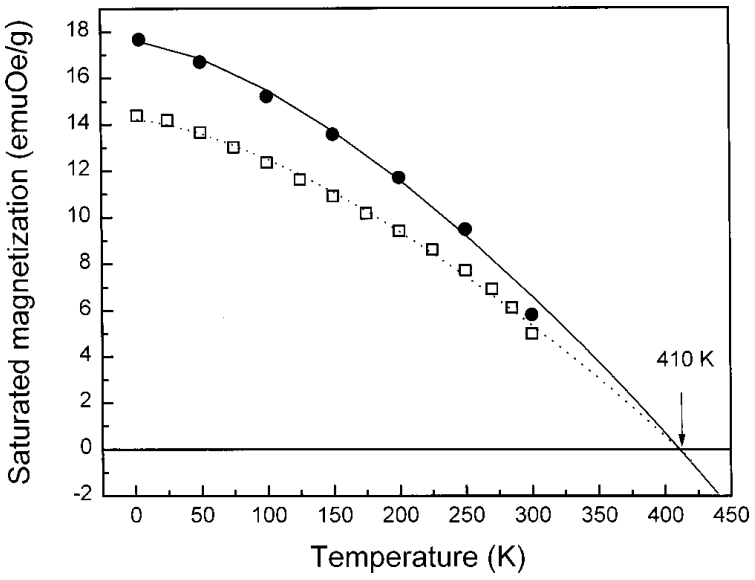

Figure 4.2: Temperature dependence of saturation magnetisation of both $V(TCNE)_2 \cdot y(CH_2Cl_2)$ (bulk sample, open squares) and $V(TCNE)_x$ (thin film sample, dark circles). The solid and dashed lines show fits to equation 4.2. Figure taken from [15].

magnetisation that was very close to what was expected (18.2 emu Oe/g) for a ferrimagnetic $S = \frac{1}{2}$ system whereas the bulk sample was not. This was attributed to more structural disorder present within the bulk material from a solvent synthesis. It was believed that including a solvent in the synthesis would create a non-magnetic spacer between magnetic ions and destroy the exchange pathway, such behaviour was also observed if other co-ordinating non-magnetic solvents were used [16,17]. At low temperatures the system showed characteristics of a correlated spin glass [15] where, in the bulk system, this was attributed to random atomic clusters. However, in the film the irreversibility shown by the ZFC and FC susceptibility curves was thought to be due to the freezing of magnetic domains where the authors drew parallels to the system $La_{0.7}Ca_{0.3}MnO_3$ (LCMO). Within the LCMO system an apparent spin glass state was due to competing interactions due to the pinning of magnetic domains by impurity particles within the crystallite grains where the interactions of these differently orientated domains lead to competing magnetic interactions [18].

A material that has been studied and is believed to show some similarities to $V(TCNE)_x$ is $[MnTPP]^+[TCNE]^- \cdot x(1,3\text{-}C_6H_4Cl_2)$ (TTP = tetraphenylprohphyrin) that shows characteristic 1D behaviour where the stacks are comprised of alternating donors and acceptor molecules with large interchain spacings (> 1.2 nm) that exhibits a T_C of 18 K [19,20]. The system is believed to show ferrimagnetic coupling between magnetic ions which is very strong however at low temperatures there is a level of magnetic disorder as the system falls into a spin glass regime where by varying the solvents the magnetic properties were seen to change. In fact on dehydration of the sample, this also showed a dramatic shift in T_C to higher temperatures [20]. The low temperature glassy phase was studied further and believed to be due to magnetic clusters forming within the structure where the frequency dependence of the AC susceptibility was similar to that of the canonical spin glasses [21–23]. The magnetic behaviour below 50 K was complex due to the glassy behaviour and the systems enters a viscous phase whereas $T \rightarrow 0$ K the interaction strength between the clusters grows as well as the level of disorder. At higher temperatures the system shows a 1D behaviour however using the changes in critical behaviour, it was shown that as $T \rightarrow T_g$ the clusters go from 1D to almost 2D where the magnetic clusters initially lie along the 1D chains but weaker interchain interactions begin to dominate leading to an increasing 2D regime [21–23].

A further advancement in metal-organic magnetism was reached with the synthesis of the $M(TCNQ)_2$ series, where M = Fe, Mn, Co and Ni [24]. Hydrated, crystalline $M(TCNQ)_2 \cdot 3H_2O$ compounds have been known for decades and behave as paramagnets [15]. More recently the $M(TCNQ)_2 \cdot (S)_x$ (where S = alcohol solvent) series has been synthesised, which also shows paramagnetic behaviour and single crystals can be easily grown [26, 27]. The main difference of the new compounds, $M(TCNQ)_2$, were that they were unsolvated, however there was clear evidence of crystallinity where the unit cell was indexed to be tetragonal and, in the case of the Ni compound, the lattice parameters $a = 17.029(5)$ Å and $c = 8.0508(2)$Å were obtained from x-ray diffraction data. For the $Ni(TCNQ)_2$ compound this showed a bulk ferromagnetic transition with a $T_C = 20.8$ K ($\theta = 37$ K) though it is believed that there is a glassy component associated with the magnetic transition.

The magnetic glassiness was suggested by both AC susceptibility data as well as a non-zero specific heat capacity as $T \rightarrow 0$ which points to residual entropy associated with the magnetism indicative of glassiness [11]. $Ni(TCNQ)_2$ was produced from a metathesis reaction of a metal-acetronitrile tetrafluroborate salt and an ammonium TCNQ salt. Vickers *et al.* used a similar method where they produced amorphous $M(TCNQ)_\gamma$ salts [28] and their Ni compound showed an elevated T_C of 31 K. The only difference between the two synthetic procedures was, instead of using a $[BF_4]^{2-}$ counter ion, Vickers *et al.* used a weaker binding anion of $[SbF_6]^{2-}$. In a similar vein to the $V(TCNE)_x$, the magnetic moments of the anion and cation were suggested to couple antiferromagnetically giving rise to a ferrimagnetic system.

$Mn(TCNQ)_2$ had previously been reported during the late 1970s by Thompson *et al.* where they produced both the protio and deutero products from a reaction of LiTCNQ with $MnCl_2$ or simply by dehydrating the hydrated product at 130 °C for 2 days [29, 30]. The TCNQ molecules in the unhydrated sample were believed to pair up and go from a triplet to an antiferromagnetically coupled singlet state where at low temperatures the reported magnetic moment is close to 5.92 μ_B which is the theoretical prediction if the magnetism is a result of the d-electrons located on the Mn (II) ion only. The pairing of the TCNQ occurs within the region of 200 K however they did not report any diffraction data to show a change in lattice structure as the sample goes through the transition.

Within this chapter an investigation to look at the origin of the underlying magnetism of $Ni(TCNQ)_2$ will be discussed as a representative of the $M(TCNQ)_2$ family of charge transfer ferrimagnets. Although neutron scattering experiments were undertaken, it proved difficult to extract useful information from the results. A more useful technique has proved to be muon spin relaxation which was introduced within Chapter 2 of this thesis. Also, the compound $Ni(TCNQ\text{-}H_4)_2$ has been synthesised using the same method as Clérac *et al.* [24] and magnetically characterised, but the main focus will be on the deuterated equivalent. Deuteration is one of the most subtle changes that can be made to an organic based magnet to see how functionalisation changes the intrinsic magnetic properties of the material. Since on deuteration

the mass of the proton is effectively doubled this will lead to different vibrational frequencies of the C-H bond. If the phonon couples to the electronic magnetism then subtle changes in the lattice phonon energies should result in changes to the electronic magnetism. Deuteration of samples has been shown to decrease the critical temperature when there is a hydrogen bonded network that mediates magnetic exchange as these exchange pathways are destroyed [31]. However when looking at samples where the hydrogen bonding is not an important magnetic exchange pathway, deuteration has been shown to increase the activation energy for magnetisation reversal in metal clusters surrounded by organic ligands and greatly effects the magnetisation dynamics within the system [32]. Although the structure of $Ni(TCNQ)_2$ had not been determined by Clérac *et al.* it is unlikely that there is any significant hydrogen bonding within the material; the negative charge on the TCNQ is stabilised by the delocalised electronic structure of the molecule which will mean a greater electron density on the aromatic ring which in turn will reduce the net positive charges on the protons. The material is also believed not to contain solvent so any interactions will be mainly from the positive Ni ions and the nitrile groups on the TCNQ which are the main locations of negative charge, much in the same way as within other transition metal - TCNQ based compounds such as AgTCNQ where the Ag ion is coordinated to four nitrile groups within the structure [33].

4.2 Experimental: Materials and Methods

The $NiTCNQ_2$ was synthesised using the same method as reported in the literature [24] and in freshly distilled acetonitrile from a solvent purification system that consists of columns of a porous zeolite that can remove both gases and water from the solvent. This involved firstly creating a [*n*-Bu_4N][TCNQ] salt from the reflux of LiTCNQ and [*n*-Bu_4N][BF_4] in 18 MΩ resistance water in a 1:1 ratio [15]. Secondly a [$Ni(CH_3CN)_6$][BF_4] salt was synthesised by the oxidation of the metal using $NOBF_4$ (see equation 4.3) [34]:

$$\mathrm{M} + \mathrm{NOBF_4} + x\mathrm{CH_3CN} \rightarrow [\mathrm{M}(\mathrm{CH_3CN})_x][\mathrm{BF_4}]_2 + \mathrm{NO} \tag{4.3}$$

The $NOBF_4$ was mixed with a molar excess of Ni powder and freshly distilled acetonitrile is added with stirring under argon and the reaction flask is placed under vacuum. When the solution begins to bubble vigorously the flask is backfilled with dry argon and the process repeated 3 times. The flask is then sealed under vacuum and stirred for 12 h where a light blue solution forms. The solution is then pumped on under vacuum to remove approximately half of the liquid. The blue solution is transferred to a flask under argon containing dry diethyl ether where a blue precipitate forms. To transfer the blue solution a filter stick was made so there was no transfer of any bulk Ni that was not reacted in the initial reaction. The diethyl ether/acetonitrile mixture could be removed using the filter stick under argon and the blue solid was washed with dry diethyl ether and dried under vacuum.

$$\begin{aligned}[\mathrm{Ni}(\mathrm{CH_3CN})_6][\mathrm{BF}]_4 + 2[n-\mathrm{Bu_4N}][\mathrm{TCNQ}] \\ \rightarrow \mathrm{Ni}(\mathrm{TCNQ})_2 + 2[n-\mathrm{Bu_4N}][\mathrm{BF_4}] + 6\mathrm{CH_3CN}\end{aligned} \tag{4.4}$$

Finally the $[Ni(CH_3CN)][BF_4]$ was redissolved in dry acetonitrile and a solution of [*n*-BuN][TCNQ] in dry acetonitrile was added. The reaction is shown in equation 4.4. A green precipitate formed immediately and with continuous stirring this changed to a dark purple solid. The solution was stirred for 3 hours and the powder was filtered and washed with dry diethyl ether. This yielded a dark purple powder with a typical yield of approximately 35%. Elemental analysis was performed on a sample where the composition was: C: 53.41%, H: 3.94% and N: 20.50%, which was consistent with the results of Clérac *et al.* [24]. It should be noted that the sample gained weight while on the balance indicating that sample is absorbing a component from the ambient atmosphere.

$Ni(TCNQ\text{-}D_4)_2$ was synthesised using the same route detailed above however TCNQ-D_4 was used in place of TCNQ and water that was used in the reflux reaction to make [*n*-BuN][TCNQ] was replaced with D_2O. TCNQ-D_4 was synthesised using the

method of Dolphin *et al.* [35] which will not be discussed in detail in this thesis. To confirm the product UV-Vis spectroscopy was used which showed a spectrum similar to that of the protio-TCNQ where the data collected are shown in figure 4.3 [36]. A typical percentage yield of the deuterated product was 40%.

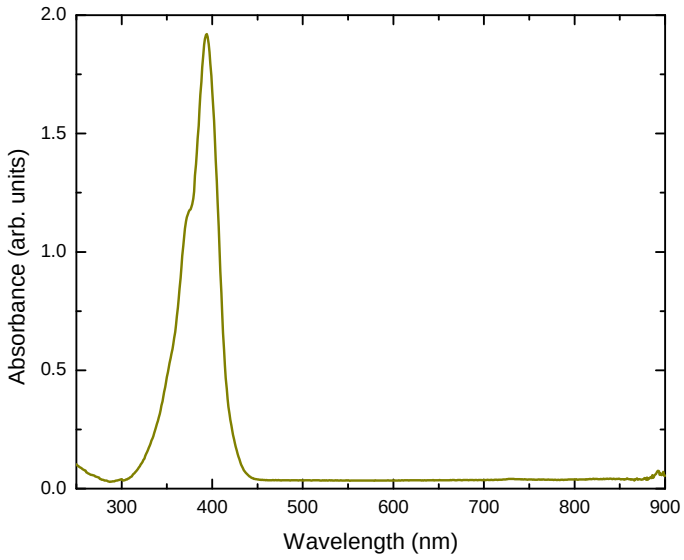

Figure 4.3: UV-Vis spectra of TCNQ-D_4 in acetonitrile.

Carbon NMR was also used where 12 carbon environments were detected that again was similar to that expected from protio-TCNQ. D_2O was purchased from Goss Scientific, the $NOBF_4$ from Acros Organics and all of the other reagents from Sigma Aldrich. All the solvents were from a solvent purification still within the Durham Chemistry Department and were kept sealed under nitrogen or argon. All reactions were performed using a Schlenk line under an inert atmosphere of dry argon. It should also be noted that in order to pass through the green intermediate stage, produced on mixing, both the Ni-acetonitrile salt and the *n*-butylammonium TCNQ salt a small amount of heating was needed. A small hot air heater was placed in the lab to warm the ambient temperature and the reaction proceeded with relative ease to a purple powder.

UV-Vis spectroscopy was also used to confirm that only the reduced form of TCNQ was used in the final step of the reaction to produce Ni(TCNQ-D_4)$_2$ where the spec-

trum agreed with previously measured data and can be seen in figure 4.4 [15]. This confirmed that all the TCNQ added was in its reduced form with no dimerised, decomposed or neutral TCNQ present as no peaks associated with the aforementioned products was observed.

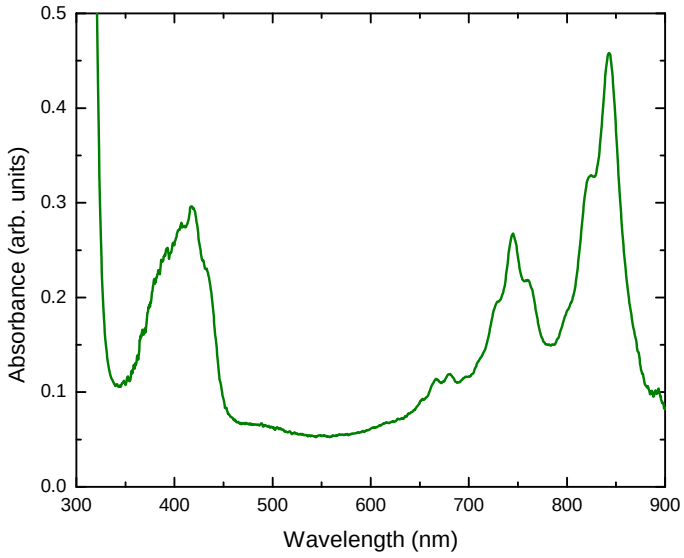

Figure 4.4: UV-Vis spectrum of [n-Bu_4N][TCNQ-D_4] in acetonitrile.

Many different samples have been made using the same procedure however they have been listed below with their preparation dates.

The magnetic characterisation of the samples was performed using a Quantum Design MPMS with a 5 T superconducting magnet. More information on this can be found in Chapter 3.

Neutron experiments were conducted on the D1B and D20 beamline at the Institut Laue Langevin (ILL) (See Chapter 3) where the sample was mounted in a vanadium can under an inert atmosphere. A He flow cryostat was used to control the temperature and cool the sample.

All experiments on the structure and magnetic data were performed on AB1 and AB2, however the for the AC susceptibility AB4 and AB5 were used.

Sample Name	Sample Code	Preparation Date
$Ni(TCNQ\text{-}H_4)_2$	AB1	June 2010
$Ni(TCNQ\text{-}D_4)_2$	AB2	June 2010
$Ni(TCNQ\text{-}D_4)_2$	AB3	Nov 2011
$Ni(TCNQ\text{-}D_4)_2$	AB4	Sept 2012
$Ni(TCNQ\text{-}D_4)_2$	AB5	Sept 2012
$Ni(TCNQ\text{-}D_4)_2{\cdot}3D_2O$	AB6	June 2010
$Mn(TCNQ\text{-}D_4)_2$	AB7	Sept 2011

Table 4.1: List of synthesised $Ni(TCNQ)_2$ samples and codes. Within the following chapters the samples will be referred to using these codes.

4.3 Structure

From the Scanning Electron Microscopy (SEM) that was conducted on both the protio (AB1) and deutero (AB2) samples one can gain a clear comparison on the morphology of the samples. There were slight differences in the reaction during the last step where the deutero product required heating to pass the intermediate and reach the thermodynamic product. The fact that this was not required with the protio sample indicates that the energetics of the reaction differ between the two samples.

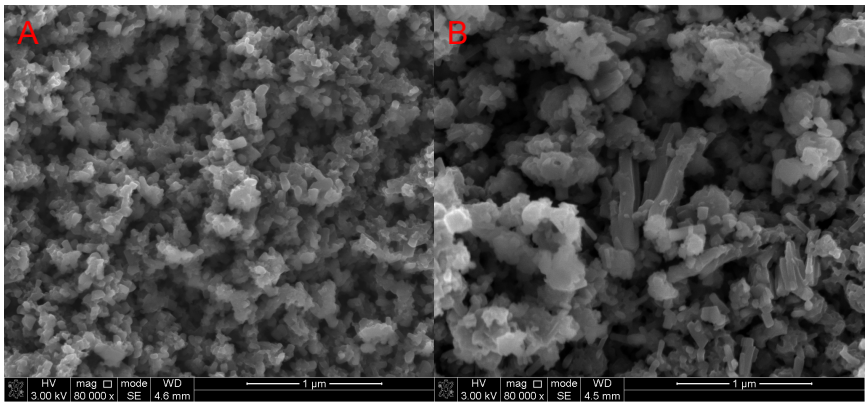

Figure 4.5: SEM images of both the protio (A) and deutero (B) forms of $Ni(TCNQ)_2$.

The images in figure 4.5 show that for both samples there is a range of particle sizes

and both samples are made of tiny crystallites. However on average the crystallites within the deuterated sample are larger. As deuterating the TCNQ appeared to have a dramatic effect on the reaction kinetics, it may have also caused slower growth of the crystals which would lead to larger particles sizes. The protio sample precipitated out of solution almost immediately upon mixing the reagents which is conducive to resulting in small particles.

Clérac *et al.* [24] could not grow a sample that was sufficient to gain detailed knowledge of the crystal structure, however from their data they concluded that the unit cell was tetragonal where a=17.029(5) Å and c=8.508(2) Å. From our laboratory powder x-ray diffraction measurements we obtained qualitatively similar results to that of Clérac *et al.* however the quality of the data was insufficient to obtain detailed structural information.

Experiments were performed on the diffractometers D1A and D20 at the ILL to study the crystal structure of the Ni(TCNQ-D_4)$_2$ sample (see Chapter 3). Deuterating the sample also improved the neutron diffraction measurements as it eliminated the incoherent scattering from the interaction of the neutron with the nuclear spin on the protons. Powder X-ray diffraction data was also collected on the I11 beamline at the Diamond Light Source[2] to attempt to pin down information on the structure.

The powder diffraction data from the I11 beamline was collected over an hour, at room temperature, and are shown in figure 4.6 and 4.7. In order to get a decent resolution the bin size was set at 0.05°, any smaller resulted in a significant broadening of the diffraction peaks. To analyse the data, the Treor90 program from the Fullprof Suite was used [37–39]. Treor90 is a trial and error program for indexing powder diffraction patterns which outputs the unit cell parameters and a suggested space group. The only structural information that was possible to gain from the data was that the unit cell is tetragonal where a = 18.11 Å and c = 8.51Å, which is similar to the results by Clérac *et al.*. Powder diffraction data was also collected on a Siemens D5 diffractometer with a Cu source (λ = 1.54 Å). The diffraction pattern can be

[2]Access was through a rapid access proposal and experiment performed by Julia Parker

seen in figure 4.6. The data sets show similar peaks and since both were collected at room temperature there should be little or no shift in the data. It is worth noting that the laboratory diffractometer/detector can have an zero-shift associated with it which may mean the diffraction patterns are not perfectly aligned.

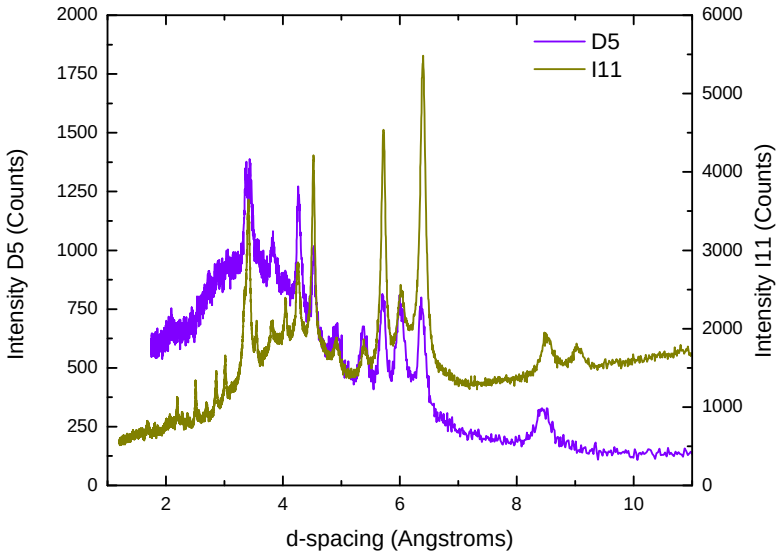

Figure 4.6: Powder X-ray diffraction data for Ni(TCNQ-D_4)$_2$ taken on a both a laboratory (D5) and synchrotron (I11) diffractometer/beamline. The data is shown to be similar, although more peaks are present in the high intensity synchrotron data.

For the laboratory XRD data one can use the Scherrer equation [41] to relate the peak width to particle size, the results have been tabulated in table 4.4 where the results suggest that the large particles observed in the SEM data may actually be made up of nanoparticles that have a size of approximately 30 nm.

Peak d-spacing (Å)	Particle Size (nm)
4.5	29.3
4.2	33.2

Table 4.2: Particle sizes calculated for Ni(TCNQ-D_4)$_2$ using PXRD data from a laboratory source diffractometer.

From the neutron data similar results were obtained. The clear difference between the XRD and ND data may be due to the difference in scattering strengths of the atoms for each respective technique. For the XRD experiment the D, N and C atoms have a very low scattering strength and so we expect to see the main contribution from the Ni as this contains the highest electron density [3]. For ND, there is no real trend similar to XRD and so light elements also scatter neutrons strongly. However if water has been absorbed by the sample, the hydrogen present would lead to a background of incoherent scattering which could hide any peaks that have a weak intensity. This means that the XRD data will show peaks that correspond to the planes associated with the Ni atoms whereas the ND data will show peaks for both the light elements and Ni so the diffraction patterns may differ between the two techniques. The theoretical structure between 3.2 and 4.8 Å was calculated using the lattice parameters and space group from the I11 XRD data. The data, which is shown in the appendix (figure A.1), does not match the structure and there is a large number of missing/unaccounted for peaks. What is also striking is that the peaks in the experimental data are extremely broad and may be, in reality multiple peaks. Nevertheless what is shown is that the experimental data do not match the calculated space group however this does not mean that the unit cell parameters are far off what they may be in reality.

Neutron powder diffraction measurements were conducted on both the D1A and D20 beamlines at the ILL. As shown in figure 4.7, one can see that there are a few overlapping peaks between the x-ray and neutron data. Any slight discrepancies in peak position are due to thermal expansion/contraction of the sample as the data were collected at different temperatures. The most detail is in the XRD data. Using the neutron data it is possible to confirm the tetragonal unit cell however no other information is elucidated.

[3]For XRD, the scattering strength of the atom increases with the atomic number (Z) as Z^4

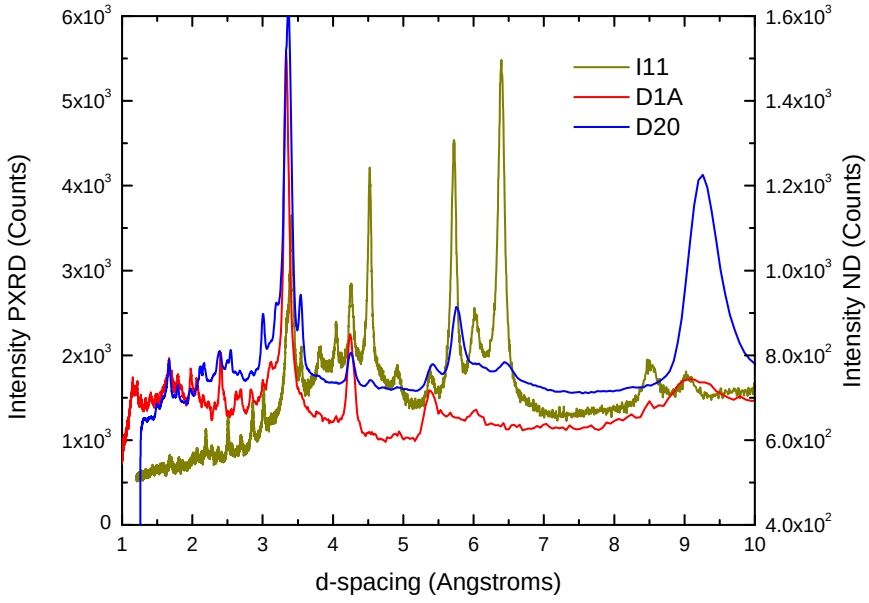

Figure 4.7: X-ray powder diffraction, I11, (XRD) and Neutron Diffraction (ND) data, D1A and D20, from Ni(TCNQ-D_4)$_2$. The XRD data were collected at room temperature, however both sets of ND data were collected at 60 K.

4.3.1 Magnetic Structure

Our neutron experiments also attempted to gain information on the magnetic structure of the metal-organic compound where the D1B diffractometer at the ILL (see Chapter 3) was used. Despite the high flux obtained from the instrument, long counting times were required of approximately 24 hours per temperature. Two temperatures were chosen above and below the magnetic transition of 60 K and 1.5 K (cryostat base temperature).

It was not possible to get any structural information from the data given the low angular resolution and the broad diffraction peaks. However, there was evidence for very weak magnetic peaks at approximately $2\theta = 10°$ and $32°$ as shown in the difference plot of figure 4.8. These weak peaks do not have the typical shape that corresponds to thermal expansion/contraction of the sample (see $2\theta = 43°$) and so it may be possible that we are observing magnetism that has a very short coherence

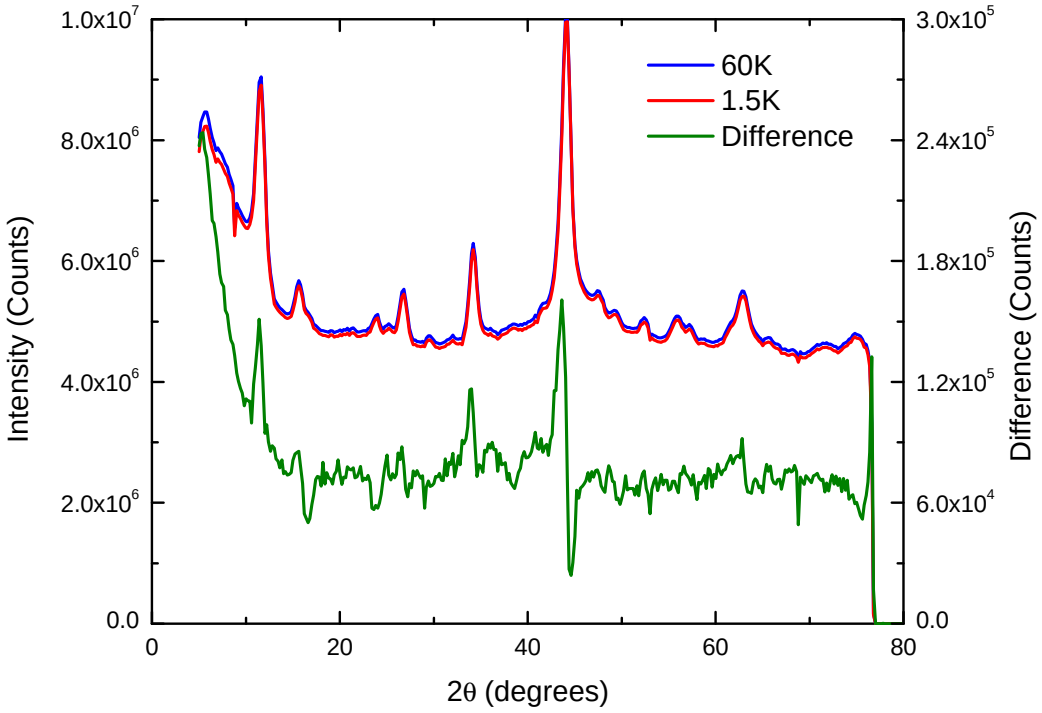

Figure 4.8: Neutron diffraction data for Ni(TCNQ-D_4)$_2$ where weak magnetic peaks were seen in the difference plot at approximately $2\theta = 10°$ and 32°.

length [42]. The *d*-spacing that the magnetic peaks correspond to are 11.0 Å and 3.5 Å respectively, which indicates that these magnetic ions are not located at the corners of the unit cell otherwise these higher order reflections would be a factor of the unit cell parameters. However at 3.5 Å, this peak is observed in the XRD data indicating the corresponding moment is likely to be situated on a Ni ion. From a simulated structure between 3.2 and 4.7 Å as shown in the appendix (figure A.1) the magnetic peak within this region cannot be assigned to one reflection however it could be either from the (3 0 2) or (2 2 2) plane. The 11.0 Å peak may sit on a Ni reflection as it might be present in x-ray data however the resolution for the data within the d-spacing range from figure 4.7 was either to low to be able to see peaks or the detector bank did not extend to the low angle needed to observe the peaks. In order to explore this weak magnetism in more depth a probe that is sensitive is required such as μSR which will be discussed later within this chapter.

4.3.2 Mn(TCNQ-D_4)$_2$

The manganese analogue of Ni(TCNQ-D_4)$_2$ was also synthesised and investigated with neutron diffraction experiments conducted on D2B at the ILL, Grenoble. This was done as a further attempt to gain insight into the crystal structure as, from Clérac *et al.*'s work, the compound is isostructural with the Ni, Fe and Cr variants with only the unit cell parameters differing slightly [24]. From the SEM images in Clérac *et al.*'s work the Mn compound had the largest crystallite size and so it was hoped that we would be able to reproduce this effect. From our SEM images of the protio versus the deutero sample (Fig 4.5) the deutero sample had a larger crystallite size. Combining the results from both ours and Clérac *et al.*'s it was predicted that creating a deuterated Mn compound would lead to large crystallites which would be ideal for a diffraction experiment.

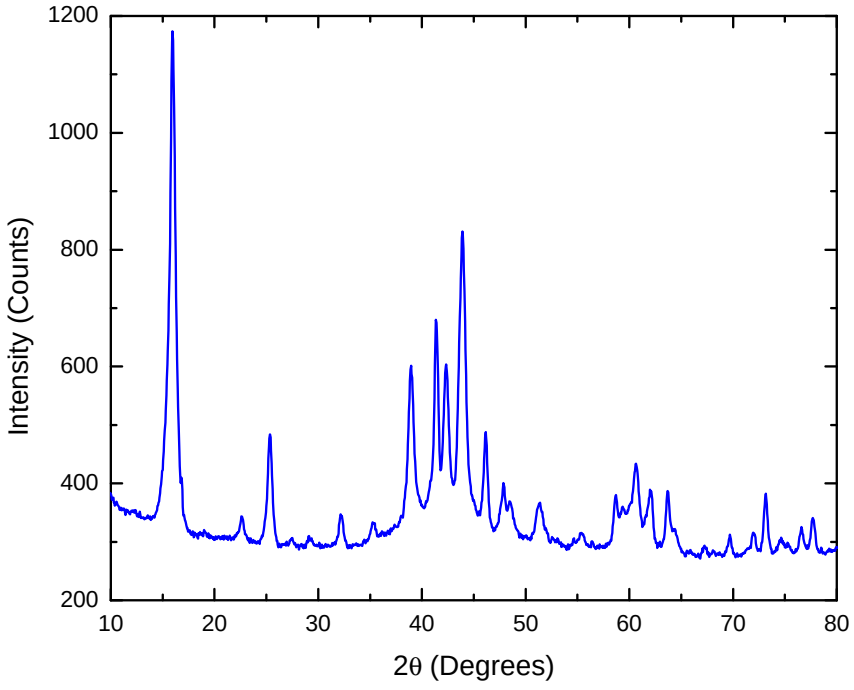

Figure 4.9: Neutron diffraction pattern for Mn(TCNQ-D_4)$_2$.

The neutron diffraction data are shown in figure 4.9 and there appears to be more structure in the diffraction pattern than for that observed for Ni(TCNQ-D_4)$_2$. How-

ever it was not possible to get any unambiguous results when determining the structure using Treor90. An alternative analysis was attempted using Dicvol04 [40] but the results were questionable as it was repeatedly indexed as a monoclinic unit cell where $a = 12.51$ Å, $b = 17.33$ Å, $c = 10.77$ Å and $\beta = 112.73°$. Dicvol04 works in a similar way to Treor90 however the parameters are varied by successive dichotomy whereby the diffraction pattern is split where the program attempts to result in a space group/unit cell by varying the d-spacing range that includes more peaks as the calculation progresses. By doing this the program works from a simple cubic unit cell and by the addition of more peaks will approach the less symmetric triclinic unit cell as a solution.

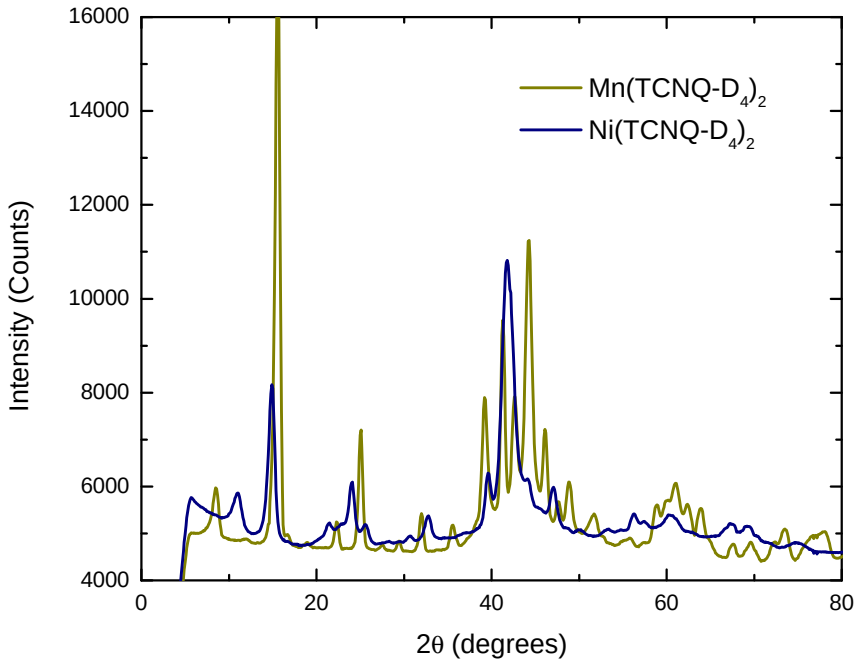

Figure 4.10: Neutron diffraction data for both $Mn(TCNQ\text{-}D_4)_2$ and $Ni(TCNQ\text{-}D_4)_2$ collected on the D20 diffractometer, ILL, Grenoble.

However when comparing the diffraction data of the Ni and Mn compound the peaks at $2\theta \approx 43°$ may be from the same reflections (see figure 4.10). If the diffraction patterns of $Mn(TCNQ\text{-}D_4)_2$ and $Ni(TCNQ\text{-}D_4)_2$ are similar it may be concluded that the large amount of detail that is missing from the diffraction data in figure 4.7 is

probably due to overlapping peaks as well as poor crystallinity. Using deuteration it is possible to synthesise a sample of $Mn(TCNQ\text{-}D_4)_2$ that is of a much better quality then that originally produced by Clérac *et al.* and our $Ni(TCNQ\text{-}D_4)_2$ samples. It may be possible that we have created a more crystalline structure of an $M(TCNQ)_2$ salt where the unit cell was indexed to be monoclinic which could better represent the real structure of the charge transfer compounds where previous measurements did not have the detail to allow for this conclusion. Another observation is the reduced peak widths in the Mn compound which would again suggest the presence of larger crystallites.

However the $Mn(TCNQ\text{-}D_4)_2$ diffraction pattern obtained is of insufficient quality to allow a detailed investigation of the crystal structure and, consequently, these data cannot be used to support both Clérac *et al.*'s conclusions or our findings from the $Ni(TCNQ\text{-}D_4)_2$ results. Overall, the results suggest that, without the possibility of growing a single crystal, little can be done to solve the crystal structure of the $M(TCNQ)_2$ system.

4.4 Magnetic Characterisation

Both the protio and deutero samples were magnetically characterised to determine whether such a subtle change in the molecular structure could impact upon the bulk magnetic properties. It is worth noting that both samples were fresh when measured as the samples do age, which will be discussed later in this chapter.

The data from the protio and deutero samples are shown in figure 4.11. The most significant change is an increase in T_C of approximately 3 K when the protons are swapped for deuterons. The respective critical temperatures are 17 K and 20 K for the protio and deutero product, the Curie temperatures being determined by differentiating the curve within the critical region where a Gaussian peak could be fit to the data to determine accurately the T_C which is essentially defined as the steepest part of the slope in an M vs. T plot.

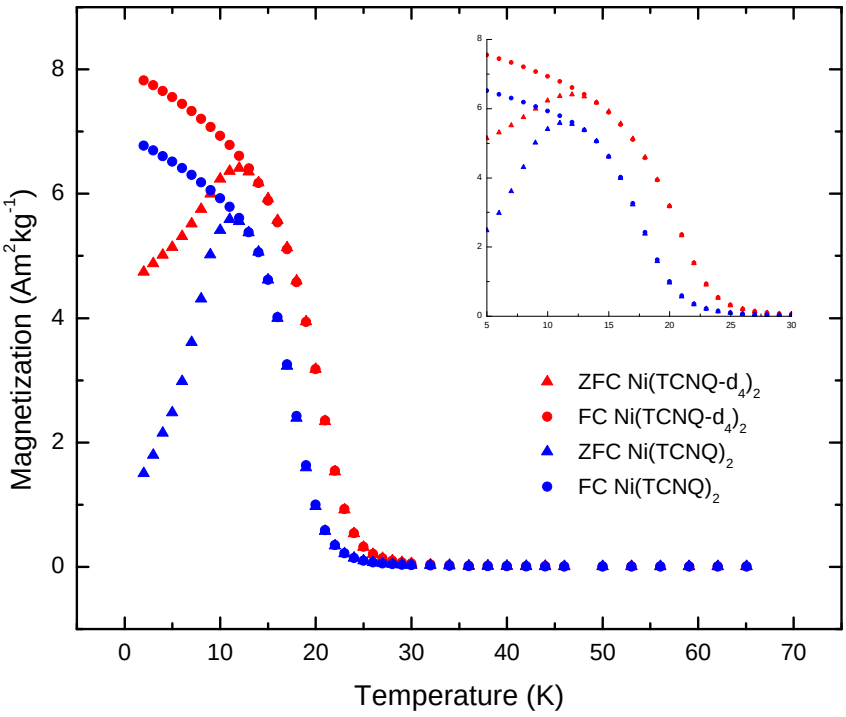

Figure 4.11: Magnetisation vs. temperature for both Ni(TCNQ-H_4)$_2$ and Ni(TCNQ-D_4)$_2$ in a field of 2.5 mT (ZFC = Zero-field cooled and FC= Field Cooled).

Another striking difference is the low temperature area of the ZFC curves where at the lowest temperatures the difference between the ZFC and FC curves is much greater for the protio sample. This may be due to the glassy component of the magnetism which was pointed out by Clérac *et al.* in their original paper [24] where the magnetic ground state may not be well defined and, due to competing interactions, different configurations of the magnetic ground state can be obtained when the sample is cooled. However, the data supports the conclusion that both samples are indeed ferromagnetic or ferrimagnetic materials where, at 2.5 mT, hysteretic behaviour is observed. The temperature at where the hysteresis is introduced in the system (T_{Div}) also scales with the change in T_C between the protio and deutero samples where the divergence of the ZFC/FC curves occurs at 11 and 13 K respectively.

Figure 4.12 shows the inverse magnetic susceptibility which, at high temperatures

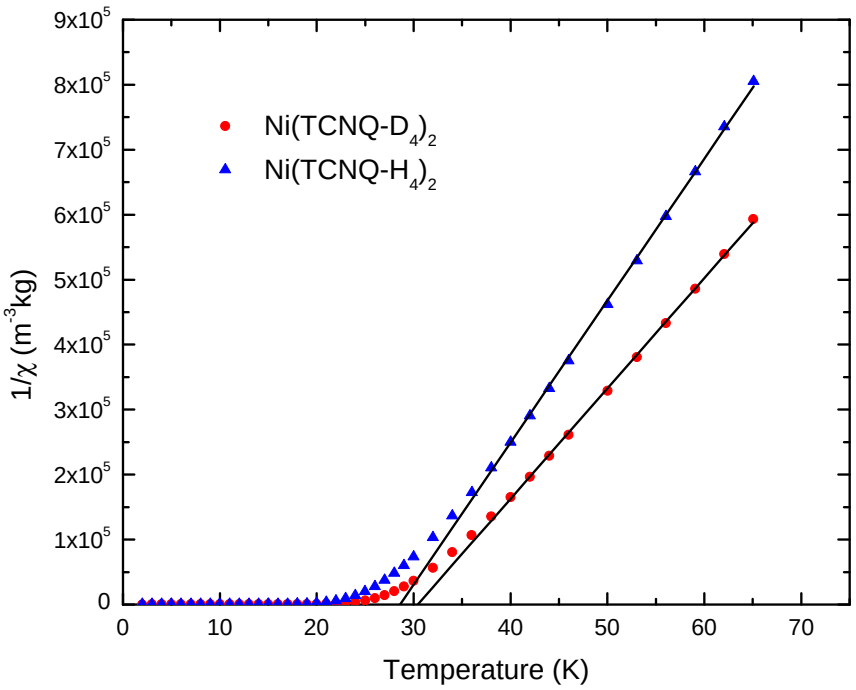

Figure 4.12: Inverse magnetic susceptibility (field cooled where B = 25 mT) vs. temperature for both the protio and deutero samples of $Ni(TCNQ)_2$. Solid lines are Curie-Weiss Fits to the high temperature data.

follows Curie-Weiss behaviour where θ = 30.4 K and 28.6 K for the deutero and protio samples respectively. The Curie-Weiss behaviour supports the ferromagnetic behaviour of the compound where there is a clear difference in the observed θ parameters which is plotted out as black lines in figure 4.12. The change in slope suggests that either or both the effective moment and/or the number of magnetic formula units per unit mass has changed. From the exchange of hydrogen for deuterium, this unit per mass or number density (N) will change as deuterium is twice as heavy as hydrogen. If one assumes a molecular formula unit of $Ni(TCNQ)_2$ the effective moments are calculated to be 4.21 and 3.68 μ_B for the deutero and protio samples respectively. These values are very similar suggesting that the change in slope is most likely due to the aforementioned change in masses of the protons for deuterons.

The ZFC magnetic susceptibility was measured in an applied field of 1000 G which

Parameter	$Ni(TCNQ\text{-}H_4)_2$	$Ni(TCNQ\text{-}D_4)_2$
T_C (K)	17.42(7)	20.17(9)
θ (K)	28.6(1)	30.4(2)
C ($mKkg^{-1}$)	$4.57(3)\times10^{-5}$	$5.89(4)\times10^{-5}$
μ_{eff} (μ_B)	3.7(3)	4.2(2)
T_{Div} (K)	13	11

Table 4.3: Parameters for $Ni(TCNQ)_2$ from the magnetic data collated for reference where C = Curie Constant. Errors are given in brackets.

greatly reduced any hysteretic behaviour however the sample still behaved as a ferromagnetic material (see figure 4.13). This illustrates that the hysteretic behaviour is a very weak effect and it may be due to a small component within the material. From a Curie-Weiss fit to the data θ = 30.6(1) K and $C = 3.97(3)\times10^{-5}$ $mKkg^{-1}$ which gives a moment of 3.4(2) μ_B.

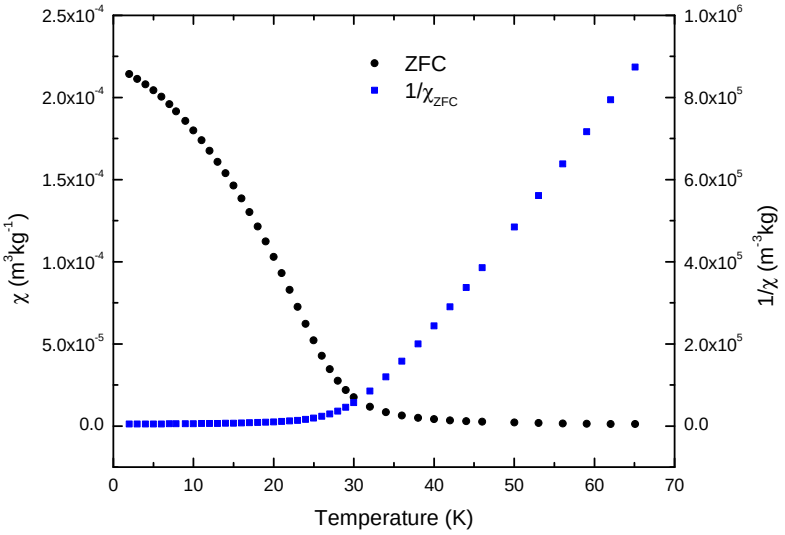

Figure 4.13: ZFC magnetic susceptibility and inverse susceptibility as a function of temperature where B = 1000 G. The solid line is a fit to Curie-Weiss law at high temperatures at $T > 30$ K.

At low temperatures it is possible to analyse the data using Bloch's Law

$$\frac{M(T)}{M_0} = 1 - D\left(\frac{T}{T_C}\right)^{\frac{3}{2}} \tag{4.5}$$

where M_0 is the spontaneous magnetisation at $T = 0$ K in an applied field of 1000 G (in this case) and D is a constant. The magnetisation is seen to have a $T^{\frac{3}{2}}$ dependence which decreases as T increases due to excitation of 3D spin waves within the material. It is possible to rearrange the equation to give

$$M = M_0 - M_0 D\left(\frac{T}{T_C}\right)^{\frac{3}{2}}, \tag{4.6}$$

which can be plotted as a straight line. For the ZFC 1000 G data seen in figure 4.13 it is possible to fit the above equation to the data at very low temperature up to 6 K at which the curves begin to diverge as shown in figure 4.14

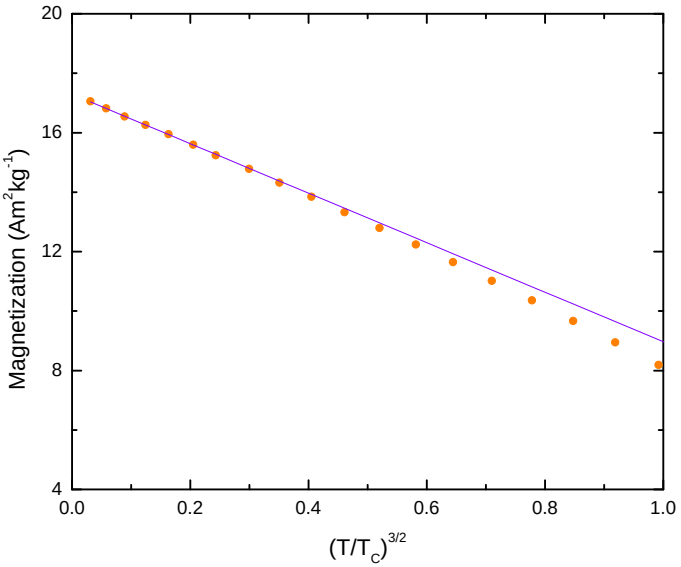

Figure 4.14: Low temperature data for Ni(TCNQ-D_4)$_2$, which can be fitted to Bloch's law (equation 4.6).

From the fit to the data M_0=17.3 Am^{2}kg^{-1} and D=-0.48. The fact that the data can be fit using this straight line equation, although way below T_C is evidence that the material is falling into a 3D ordered magnetic system at low temperatures.

Magnetisation data was also taken as a function of applied field to study the field dependent behaviour above and below the transition (see figure 4.15). It is clear that as the sample is taken below the transition temperature the response to an applied magnetic field is radically different. The sharp increase in the magnetisation as a small field is applied below T_C is consistent with the behaviour of a ferromagnetic or ferrimagnetic material indicating the presence of a spontaneous magnetic moment. See table 4.4 for a summary of parameters at the lowest temperature accessible, 1.8 K. Moreover, the approximately linear response of the magnetisation with applied field, for $T < T_c$, is indicative of a ferrimagnetic response [2] .

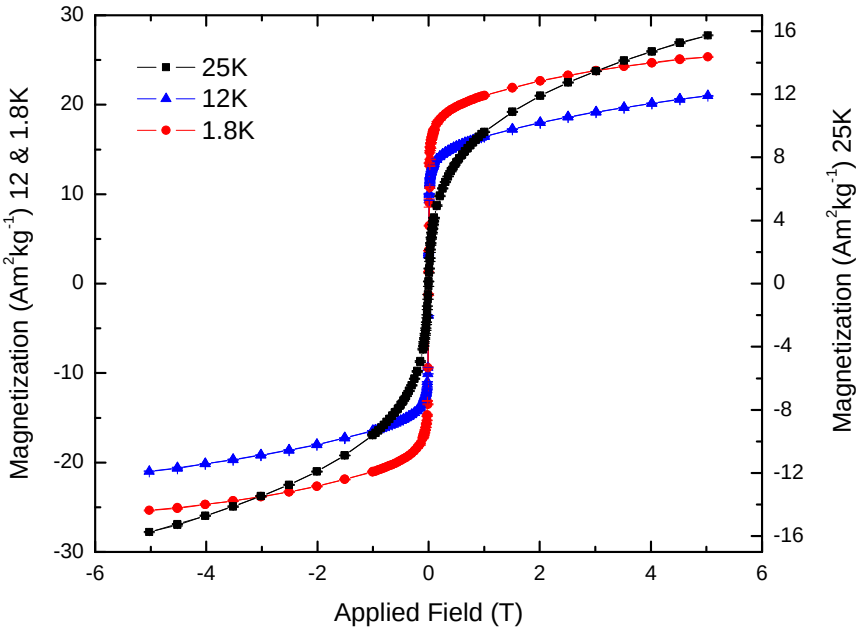

Figure 4.15: Magnetisation vs. applied field for the Ni(TCNQ-d4)$_2$ compound.

From the magnetisation data as a function of field, measured at the lowest temperatures, the magnetic moment per formula unit at 5 T is 2.12 μ_B when considering a Ni(TCNQ-D$_4$)$_2$ stoichiometry. If one considers a Ni^{2+} ion (5.59 μ_B) and two TCNQ anions (1.73 μ_B each) subtraction of the two (see equation 4.7) result in a net moment of 2.1 μ_B which agrees with the measured magnetic moment and a ferrimagnetic arrangement however this contradicts the inverse susceptibility data which closely resembles that of a ferromagnet and not a ferrimagnet [43].

Parameter	Value
M_{Spont} (Am^2kg^{-1})	21.4(1)
M_{5T} (Am^2kg^{-1})	25.35(7)
μ_{Spont} (μ_B)	1.8
μ_{5T} (μ_B)	2.1
H_C (G)	10

Table 4.4: Parameters for $Ni(TCNQ)_2$ from the magnetisation as a function of applied field at 1.8 K collated for reference. The subscript *Spont* indicates spontaneous magnetisation and *5T* indicates the values at a field value of 5 T. Errors are given in brackets.

$$\mu_{Tot} = \mu_{Ni^{2+}} - \mu_{TCNQ^-} - \mu_{TCNQ^-} = 2.13\ \mu_B \tag{4.7}$$

The samples do show hysteretic behaviour at all three temperatures (see figure 4.16) where the difference in magnetisation depending on the direction of the ramped field is not accounted for by the error in the measurement. Again, one can clearly see the differences in behaviour with an applied field between all three temperatures. The hysteretic behaviour present at 12 K is typical of a ferromagnetic material, however more data points are needed at low field in order to study the coercive field, however an estimate is in the order of 10 G. At the lowest temperature, 1.8 K, the magnetisation is different at the first quadrant of the measurement and the overall curve is asymmetric where perhaps there is a time dependence associated with the sweeping of the magnetic field however more data is needed to probe this. Within a superparamagnet the moments are easy to polarise however in a spin glass system below the T_f the sweep rate of the applied field plays a role where creep of the magnetisation can be present [11]. This is due to the glassy nature of the magnetism at low temperatures where the sample has been frozen into a metastable ground state as it was effectively cooled in the absence of an applied field. The application of a modest field ($\sim$70 mT) was enough to overcome the hysteretic behaviour, even at the lowest temperature, and suggests that this weakly

magnetically glassy ground state may be simply due to the interaction of magnetic clusters within the material. Within a strongly interacting spin glass the moments will be pinned along specific directions which is due to both magnetocrystalline anisotropy as well as magnetic interactions, where this could be purely dipolar or through more complex exchange interactions such as RKKY (see chapter 2 for a brief definition of the RKKY interaction). This leads to clusters that are randomly orientated each with a local anisotropy with a specific direction that may not be along the same vector. An application of an external field has to overcome the magnetic interactions of these clusters on a local scale to rotate the moments away from their pinned orientation. Within a spin glass this energy barrier to reorientate the moments is randomly distributed and will be of different heights (as there are different and competing exchange pathways). Below T_{f} when sweeping a magnetic field the sample will respond showing a complex magnetisation versus applied field behaviour where at different field values the Zeeman energy of each individual cluster will favour reorientation of the moment to align with the external field [11].

An additional observation is that hysteresis is present even at 25 K, albeit very small. Although at 25 K the sample is right on the edge of the critical region this hysteresis is dominant which may indicate that we are beginning to see magnetic clusters forming within the sample. However since the critical region is broad we may have a particle size distribution where the larger particles have a higher T_{C} and so we are observing the behaviour of the larger ferromagnetic particles.

4.4.1 AC Susceptibility Measurements

To further probe the glassy state of the material an AC susceptibility experiment was performed. The AC field was held constant at 0.1 G and no external DC field was applied where the frequency of the AC field was varied to probe both the real (χ') and imaginary (χ'') components of the susceptibility. The material was aged and corresponds to the 20 month old sample. The real component of the susceptibility for AB4 is shown in figure 4.17 where the transition temperature corresponds to

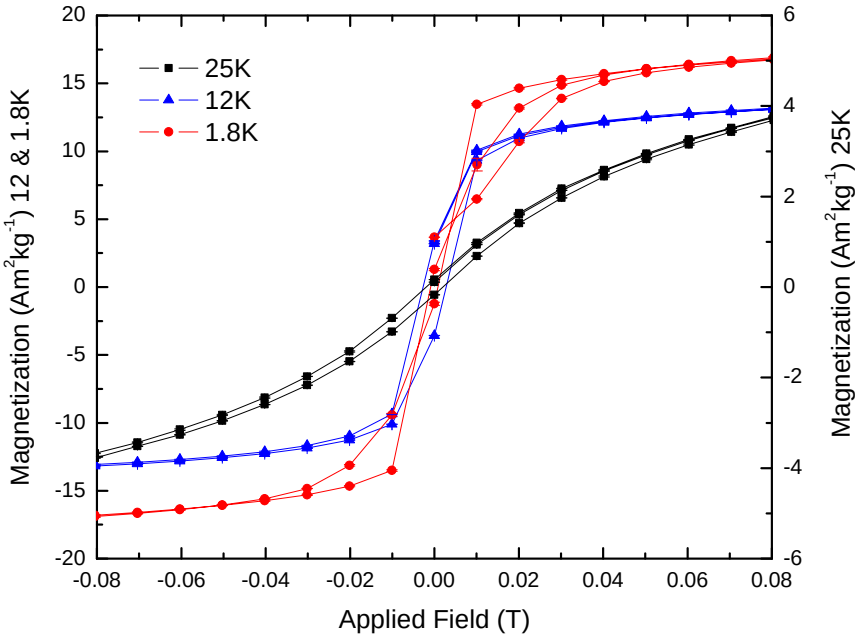

Figure 4.16: Low field magnetisation vs. applied field data of figure 4.15 for $Ni(TCNQ\text{-}D_4)_2$ showing the hysteresis present at all temperatures. Error bars are included however they are smaller then the data points.

that observed in the DC transport measurements shown in figure 4.23 although it does show a frequency dependence.

One of the advantages of AC susceptibility experiments is that one can probe the response of the sample not only as a function of a frequency dependent applied field but also work at very small fields, in this case 0.1 G. This is advantageous when probing a spin glass state, however it should be noted that separating out a superparamagnetic system from a spin glass state can be difficult [11].

Using the 'Mydosh' criterion for a spin glass as outlined in equation 4.1 this can essentially become an equation that governs a straight line where

$$T_f(\omega) = T_{f0}\varphi \log(\omega) + T_{f0}. \tag{4.8}$$

T_f denotes the freezing temperature of the spin glass which is attributed to the cusp

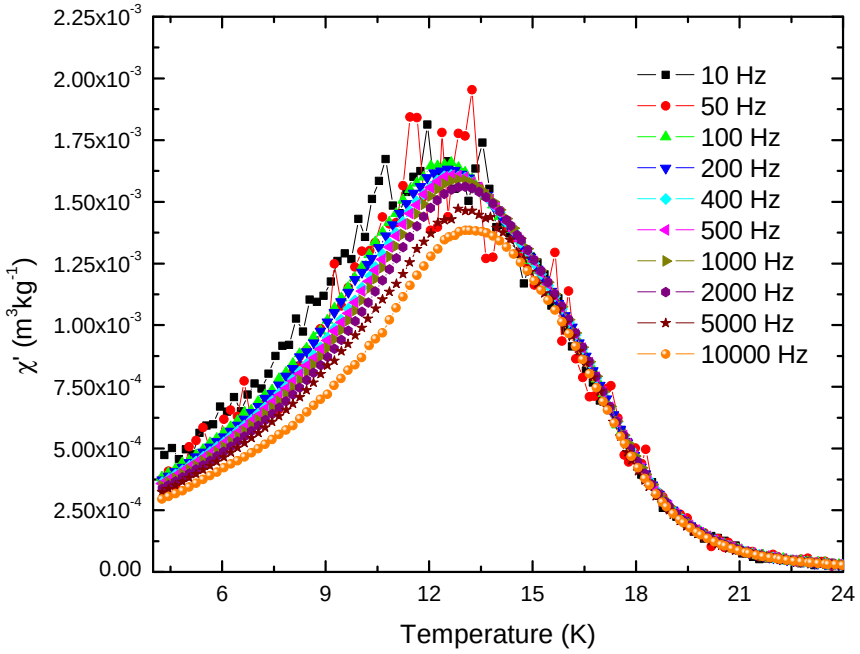

Figure 4.17: χ' vs. temperature for a fresh sample of AB4 showing the frequency dependence of the transition.

in the χ' vs. T data shown in figure 4.17. A plot of T_{f} vs $\log(\omega)$ yields a straight line where $T_{f0} = 11.52 \pm 0.04$ K and $\varphi = 0.0315 \pm 4{\times}10^{-4}$. The value of φ is small which suggests there is a very weak frequency dependence consistent with that observed for the canonical spin glass systems [4] [11].

Using the value of T_{f0} which approximately corresponds to T_{f}, or the cusp, in a static field one can feed this into equations to work out the energy barrier associated with the transition. Using the Arrhenius law which generally governs an activated process which can be used for superparamagnetic behaviour can be fit to the data where

$$\omega = \omega_0 \exp\left(\frac{-E_a}{k_B T_f}\right). \tag{4.9}$$

If one takes the natural log of the equation this describes a straight line where

[4] $\varphi = 0.0315$ is typical for canonical spin glasses such as CuMn

$$\ln(\omega) = \ln(\omega_0) - \frac{E_a}{k_B T_f}. \tag{4.10}$$

A fit to the data gives results of $\omega_0 = 1.25 \times 10^{38}$ Hz and $\frac{E_a}{k_B} = 1018$ K which are clearly unphysical values. This result supports the fact that the sample does not behave like a superparamagnet and so the low temperature behaviour can be attributed to a spin glass or super spin glass state by process of elimination.

Using a Vogel-Fulcher type analysis, shown in figure 4.18, which is also used and has an analogy with real glasses a new parameter is used, T_0, which one can take from the above analysis using the Mydosh Parameter, φ. The data was fit within the midrange where the 10, 5000 and 10000 Hz points were not included.

$$\omega = \omega_0 \exp\left(\frac{-E_a}{k_B(T_f - T_0)}\right) \tag{4.11}$$

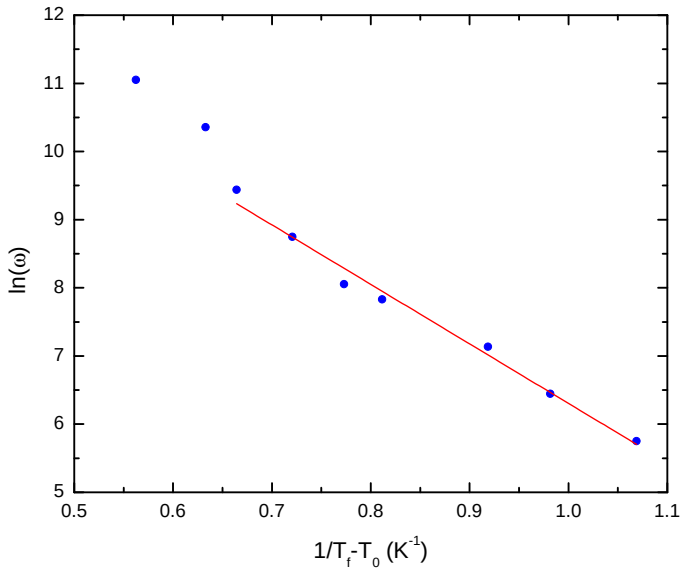

Figure 4.18: Vogel-Fulcher analysis of the frequency dependence of the cusp in the real susceptibility for AB4. The line is a fit to the data using the Vogel-Fulcher law (equation 4.11).

Using the value for T_0 that was obtained from using equation 4.8 this can be input into the equation allowing both ω_0 and $\frac{E_a}{k_B}$ to be calculated. It is found that $\frac{E_a}{k_B} =$

8.7 ± 0.4 K and $\omega_0 = 3.381 \times 10^6$ rads s^{-1} which corresponds to a frequency of 0.53 MHz. This frequency describes the fluctuation rate of the dynamical component within the system which is of a value that is similar to that observed in the μSR data for the fresh sample which will be discussed in chapter 5.

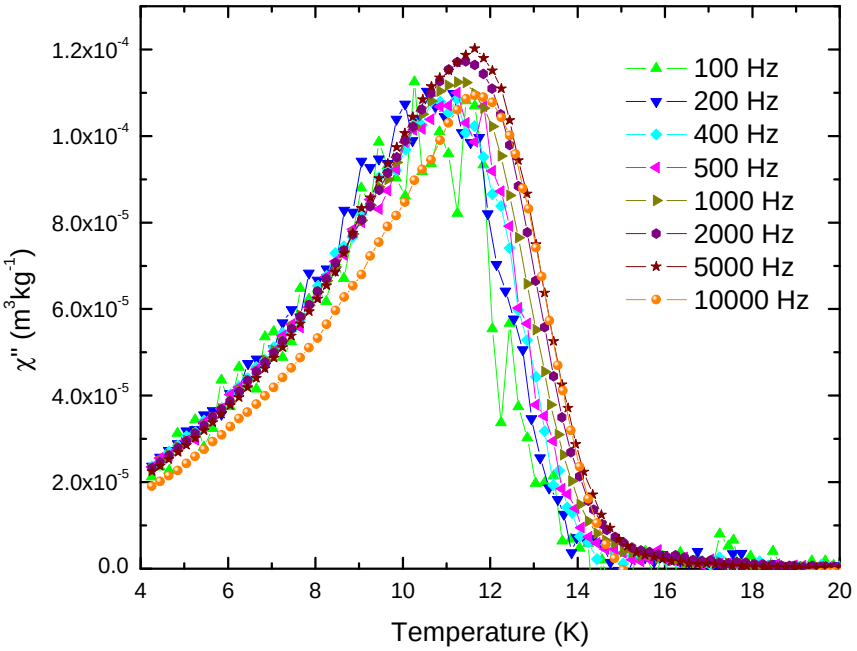

Figure 4.19: χ'' vs. temperature for the a fresh sample of Ni(TCNQ-D_4)$_2$.

The imaginary component of the susceptibility, as shown in figure 4.19, generally appears as a very weak effect only in systems where the relaxation process can decouple the spins from the lattice, such as with hysteresis [11]. The imaginary susceptibility shows a very weak/little, if any, frequency dependence and the broadness of the transition may suggest that there is a distribution of relaxation times.

From the data in both figure 4.17 and 4.19, one can see a frequency dependence in the value of both χ' and χ'' where the 10 kHz data undershoots that of the lower frequencies. At the high frequencies (0.5 and 10 kHz), one can see in figure 4.18 that the data deviates from the Vogel-Fulcher law and so the dynamics within the system cannot be described strictly using this relationship. Within a spin glass, there is a wide distribution of relaxation times, which is why a stretched exponential is used

to describe the auto-correlation function within the system [11, 44]. Peaks in both χ' and χ'' vs. frequency are also seen in nanoparticulate systems where there is a broad distribution of particle sizes and thus relaxation times. When these are frozen out one observes a drop in the susceptibility, both real and complex, as a function of frequency [45–47]. Within the Ni(TCNQ-D_4)$_2$ system we may be seeing something similar where we have phase separated magnetic clusters that have a broad size distribution and a peak in the susceptibility shows that we are sensitive also to a cluster size distribution that is within the distribution of relaxation time scales of the order of the AC susceptibility measurements.

A separate sample of Ni(TCNQ-D_4)$_2$, was synthesised and the AC susceptibility measured to compare with the previously discussed data (data not shown here). These samples were made using the larger batch of deuterated-TCNQ synthesised. The results were analysed in a similar method to the sample discussed above and summarised in table 4.5.

Parameter	Result
$T_f(0)$ (K)	13.94(4)
φ	0.023(2)
E_a/k_B (K)	8.5(5)
ω_0 (rads s^{-1})	6.63×10^6
$f(0)$ (MHz)	1.05

Table 4.5: Parameters calculated from the AC susceptibility of the AB5 sample.

These results are different from the previously discussed sample which is very striking as it means that from the same method a sample with slightly different properties was made. One significant result is the reduction in φ which is not accounted for by the error as this means that this sample shows a weaker frequency dependence and thus can be considered a weaker spin glass. When a spin glass orders there must be order formed out of randomness however if the frequency dependence (φ) is changing this implies the two different samples have different degrees of disorder. The two samples also differ in $T_f(0)$ where the previous sample has a lower value

for the freezing temperature which again supports the idea that the samples are not entirely reproducible.

The two samples (AB4 and AB5) also show different time scales for the spin dynamics with the second sample having a much slower dynamical component in the time domain, however this may be a result of the shift in T_f. The fact that it has not been possible to reproduce samples with a similar T_f illustrates that the sample may be inhomogeneous and that the synthetic method does not produce an exact stochiometric material every time.

4.4.2 Heat Capacity

Heat capacity was conducted on AB2 and the data show that there is no significant peak associated with the bulk transition at 20 K as one might expect from a ferromagnetic material. This may be due to the magnetic ordering being a local phenomenon or the transition is significantly broadened from a particle size distribution.

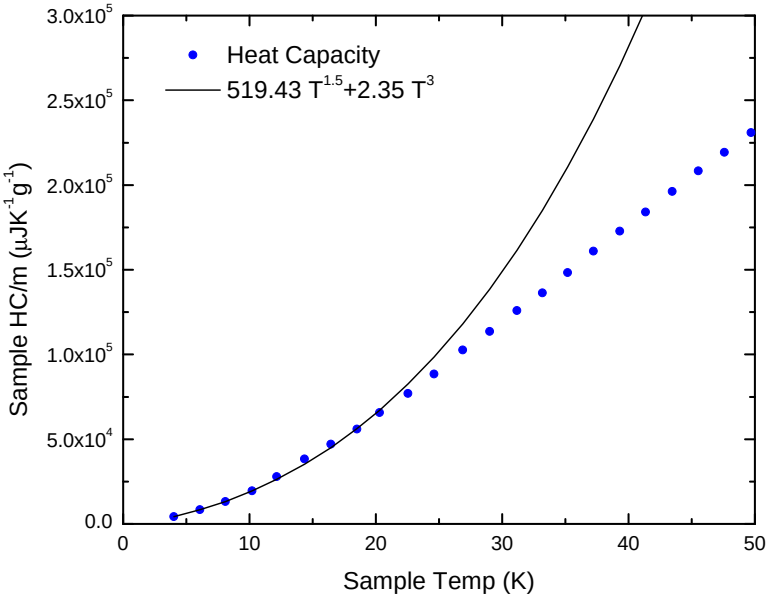

Figure 4.20: Heat capacity of Ni(TCNQ-D_4)$_2$.

At low temperatures where the glassy behaviour is expected to dominate there is a change in the data where the non-zero heat capacity signifies that there is residual entropy within the system, probably from magnetic disorder. This may support the conclusion that, at low temperature there is a glassy magnetic component that may not be directly associated with the bulk transition.

The heat capacity of a 3D lattice is proportional to T^3 however to work out the lattice contribution and the Debye temperature one normally measures the heat capacity of a non-magnetic analogue of the system of interest. Since this lattice heat capacity is unknown it is impossible to separate out the two from our data. To fit the data a phenomenological function was used

$$C = \alpha T^{1.5} + \beta T^3 \tag{4.12}$$

which described the observed heat capacity well only at very low temperatures ($2 < T < 12$) where $\alpha = 519 \pm 7$ and $\beta = 2.3 \pm 3$. It should be noted that the fit did not work if a T^2 was used instead of $T^{1.5}$ where a T^2 dependence would indicate 2D behaviour. The T^3 behaviour describes the lattice contribution and the $T^{1.5}$ accounts for the magnetic heat capacity where the power law of 1.5 corresponds to a 3D spin wave system as

$$C \propto T^{d/n}. \tag{4.13}$$

Where d is the dimensionality and $n = 2$ for a ferromagnet and 1 for an antiferromagnet there for arriving a value where d=3 and n=2 which gives a value of $T^{\frac{3}{2}}$ [48]. This supports the conclusion that the sample undergoes a 3D ferromagnetic ordering at the transition temperature similar to the analysis of the magnetic data using Bloch's law which also has a $T^{\frac{3}{2}}$ dependence.

4.4.3 Mn(TCNQ-D_4)$_2$ - Magnetic Data

The structure of Mn(TCNQ-D_4)$_2$, AB7, was briefly discussed earlier in section 4.3.2 as a comparison to the Ni(TCNQ-D_4)$_2$ sample. We were able to create a sample with more structural detail by using Mn instead of Ni where the data collected was superior to that of Clérac *et al.*. From the neutron diffraction data interesting comparisons can be made between the Ni and Mn sample where it is clear that the peak width of the Mn sample is smaller, suggesting more crystalline particles.

The magnetism of the Mn sample is shown in figure 4.21 where both χ and χT are plotted against T.

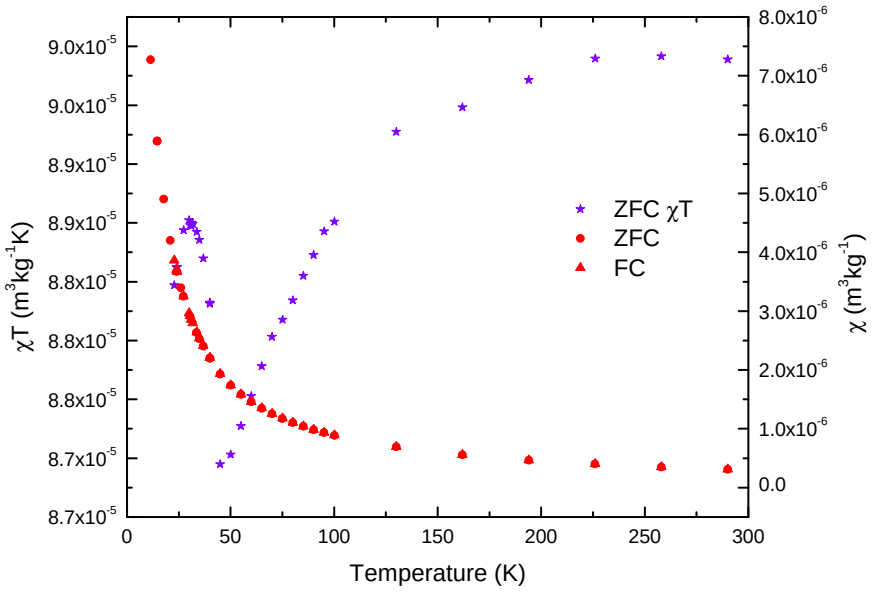

Figure 4.21: Magnetic data for Mn(TCNQ-D_4)$_2$.

When plotted as χ vs. T there is no evidence of any real hysteretic behaviour such as a cusp in the ZFC data similar to the Ni sample. This illustrates that there is a large difference between samples in reality. The fact the the coherence length of the crystallinity within the Mn sample is longer then the Ni sample suggests that increased order may destroy the magnetism within the sample. This would mean that as the crystallinity of a M(TCNQ)$_2$ salt is increased one might expect a shift in T_C to lower temperatures coinciding with increasing order. When plotted out as χT

vs. T one can see the complexity in the magnetic behaviour. If one was observing a truly paramagnetic system there would be little deviation from a straight line in the plot. The decrease with a minimum at ≈40 K suggests the presence of an antiferromagnetic phase and at low temperatures there is a cusp which may be where the sample falls into a ground state with competing interactions. Clérac *et al.* [24] quote a critical temperature of 44 K which coincides with the minimum in the χT vs. T data. They also see a freezing temperature at 21 K which again, is similar to our cusp in the data. These effects are very weak which is likely due to the increased order within our system.

4.5 Aged Sample

The deuterated sample of $Ni(TCNQ)_2$, AB2, that was used for the magnetic and μSR experiments was stored under an inert atmosphere and the bulk magnetic properties were measured at later dates to study whether the sample ages and to what extent.

4.5.1 Structure

A neutron diffraction study was conducted on an aged sample of AB2 (17 months) to attempt to pin down the structure and gain more evidence of magnetic Bragg peaks for $Ni(TCNQ\text{-}D_4)_2$ using a higher flux neutron diffractometer, D20, ILL, Grenoble. It was apparent that the structure was similar however it had undergone a change where new peaks appeared which could correspond to a new phase.

From figure 4.22 the difference in the diffraction patterns between the aged and fresh sample is apparent with obvious peaks appearing in the aged sample at d = 4.6, 5.7 and 6.4 Å. Although there are changes at low d-spacing these are less obvious however there are slight shifts. Dominant peaks appearing at larger d-spacing are suggesting that the change is increasing the size of the unit cell or stretching the overall structure of the compound. A comparison can be made with a diffraction pattern of $Ni(TCNQ\text{-}D_4)_2{\cdot}3D_2O$, AB6, which was taken on D1A at the

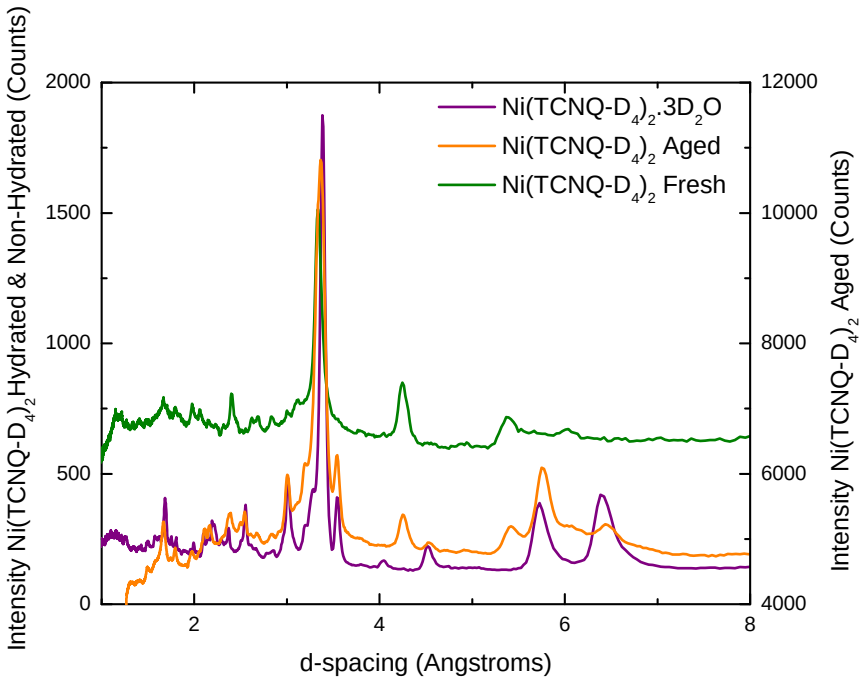

Figure 4.22: Neutron diffraction data for AB2 both fresh and aged and for AB6.

ILL, Grenoble at the same time as the fresh sample as a control. Clearly the fresh sample differs from the hydrated sample however in the aged sample the new peaks correspond to peaks seen in the diffraction pattern of the hydrated system. This may confirm the hygroscopic nature of the fresh sample of AB2 where over time the material absorbs water which induces a change in structure consistent with that of the hydrated sample. It should be noted that for the fresh and aged sample the data were collected at low temperatures (< 60 K) however the hydrated sample data was collected at 200 K and so there may be slight shifts in the peak positions due to thermal expansion. Experiments were also attempted on the WISH diffractometer at ISIS on the aged sample (20 months) however it was not possible to collect data due to a large background due to incoherent scattering which was suggested to be from absorption of water by the sample [49].

4.5.2 Magnetisation Measurements

Results from the magnetic measurements are shown in figure 4.23 and it is clear that the sample changes over time, with the value of T_C being substantially reduced. Moreover, the magnitude of the susceptibility, measured at 2.5 mT, appears to decrease with increasing time. Note that the diamagnetic susceptibility was calculated by a fit to Curie-Weiss law with a diamagnetic term added where χ_D = -2.420 $\times 10^{-8}$ cm^{3}g^{-1} which was subtracted from each data set to give the magnetic susceptibility shown in the figure. The diamagnetic susceptibility is not expected to change over time if there is no change in the sample however this will not be true if the changes of the sample over time are induced by absorption of water. However, the diamagnetic susceptibility is a good approximation of the actual diamagnetic susceptibility as can be seen from figure 4.23 as at high temperatures the curves overlap at a value that is roughly $\chi = 0$ and keeps the analysis consistent. It is also not clear why the magnitude of the susceptibility changes at the maximum of the ZFC curve however the sharpness of the transition is greater in the aged sample than the fresh sample suggesting that there may be a smaller particle (magnetic cluster) size distribution in the aged sample.

Inverse magnetic susceptibility versus temperature plots show that the samples as they age still behave as ferromagnetic materials over time, as shown in figure 4.24. If one assumes that N does not change, the change in slope is due to changes in the effective moment within the Curie-Weiss law expression (see chapter 2).

Age (months)	T_C (K)	θ (K)	C (mKkg^{-1})	μ_{eff} (μ_B)
0	20.17(9)	30.4(2)	5.88(5)$\times 10^{-5}$	3.7(1)
6	15.48(6)	27.5(2)	4.19(4)$\times 10^{-5}$	3.55(3)
17	10.6(1)	21.11(9)	2.819(9)$\times 10^{-5}$	2.92(3)
20	7.84(1)	18.39(5)	2.817(7)$\times 10^{-5}$	2.91(2)

Table 4.6: Parameters for the aged sample of AB2 from the magnetic data collated for reference where C = Curie Constant. Errors are given in brackets.

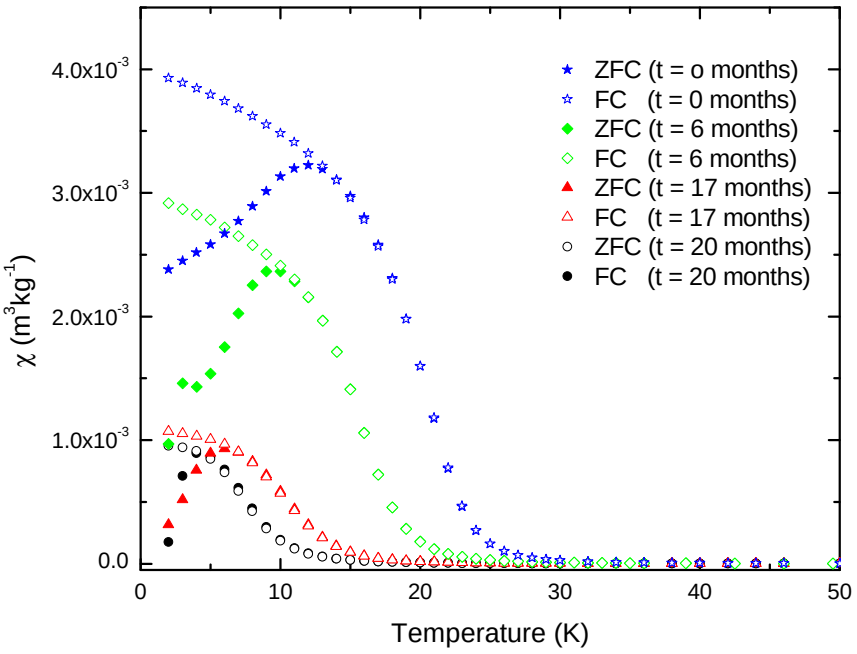

Figure 4.23: Magnetic susceptibility vs. temperature data for AB2 after set periods of time.

All parameters associated with Curie-Weiss behaviour decrease however the change in slope may be due to a change in N rather than moment if as the sample absorbs water where molecular formula units are becoming magnetically inactive and show no ferromagnetic response. If this was the case at 20 months $N = 6.71 \times 10^{23}$ kg^{-1} where a loss of 6.0×10^{23} kg^{-1} molecular units had taken place.

Since the material is hygroscopic [24] the sample may have absorbed some ambient moisture even though precautions were taken to avoid this problem. In absorbing moisture the sample structure changes which could destroy exchange pathways and thus decrease the overall coherence length of the ferromagnetic behaviour. These smaller magnetic clusters may then order at a lower temperature which accounts for the decrease in T_C [50, 51]. The sample has been shown that by absorbing water the structure changes which corresponds to changes in the diffraction pattern shown in the previous section. As more water is absorbed the material will approach the Ni(TCNQ-D_4)$_2$·3H_2O compound which is likely to be paramagnetic, similar to its

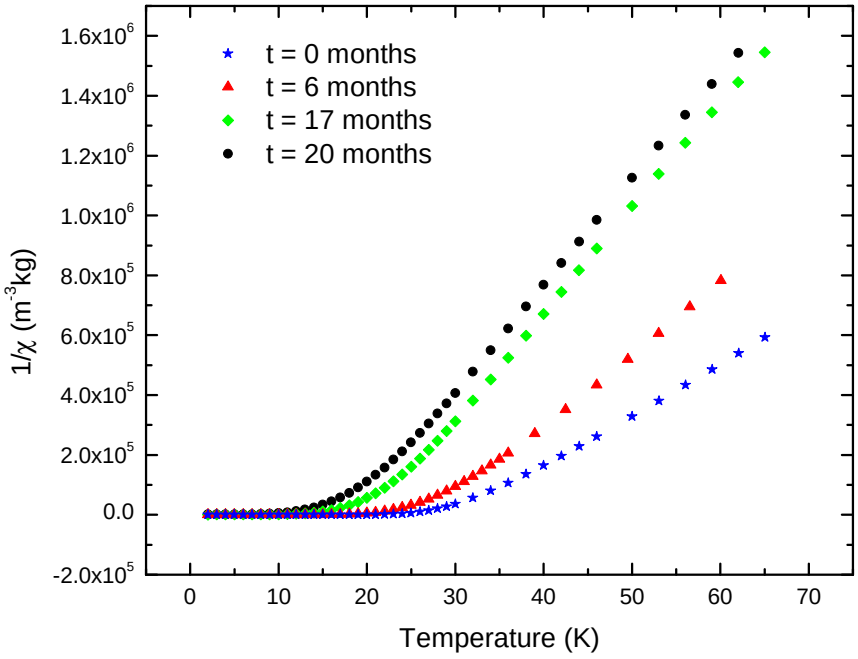

Figure 4.24: Inverse magnetic susceptibility of the aged AB2 sample.

protio counterpart [15].

The magnetisation of the sample as a function of field was measured after 17 months and is shown in figure 4.25. The behaviour is completely different to the data previously measured on the fresh sample (see figure 4.15) where the spontaneous magnetisation has disappeared and instead the curves show a larger paramagnetic component where now saturation is not observed.

This dramatic change in the material complements the data that supports the absorption of water as the disappearance of the ferromagnetic behaviour when compared to the fresh sample is accompanied by a large increase in a paramagnetic fraction which may be due to the hydrated product being present. There is also no evidence of hysteretic behaviour, however more data points at low field are needed to confirm this.

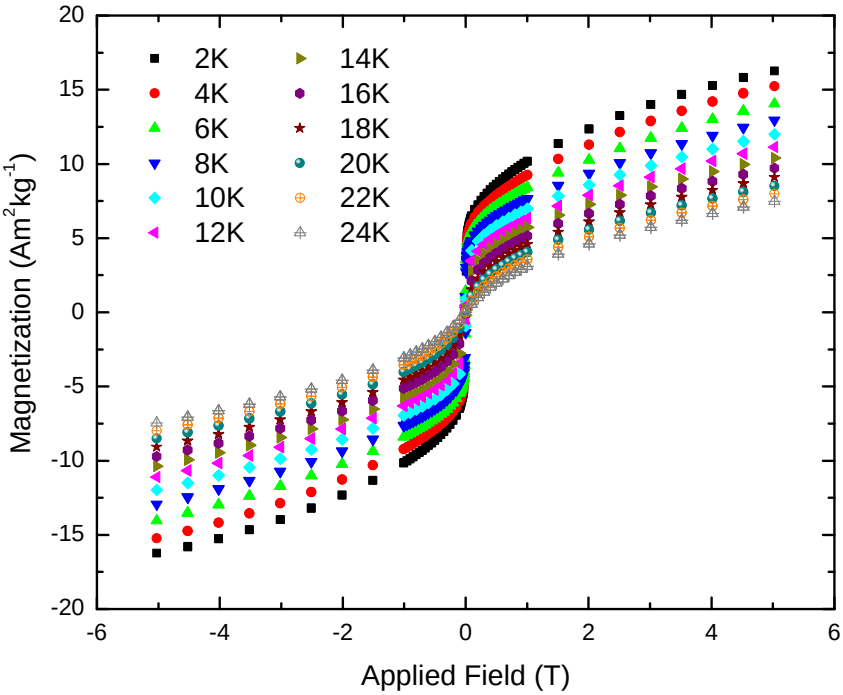

Figure 4.25: Magnetisation vs. applied Field for AB2 after 17 months.

4.5.3 AC Susceptibility Measurements

AC susceptibility was also performed on the aged sample to further compare the behaviour of a fresh and aged sample. The AC field was held constant at 0.1 G and no external DC field was applied where the frequency of the AC field was varied to probe both the real (χ') and imaginary (χ'') components of the susceptibility. The material was aged and corresponds to the 20 month old sample. The real component of the susceptibility is shown in figure 4.26 where the transition temperature corresponds to that observed in the DC transport measurements shown in figure 4.23 although it does show a frequency dependence similar to the fresh sample but just shifted down to lower temperature.

Using a similar analysis as for the fresh sample one arrives at a similar conclusion where a Vogel-Fulcher law is used to describe the data indicating inter cluster/particle interactions. The results are collated in table 4.7.

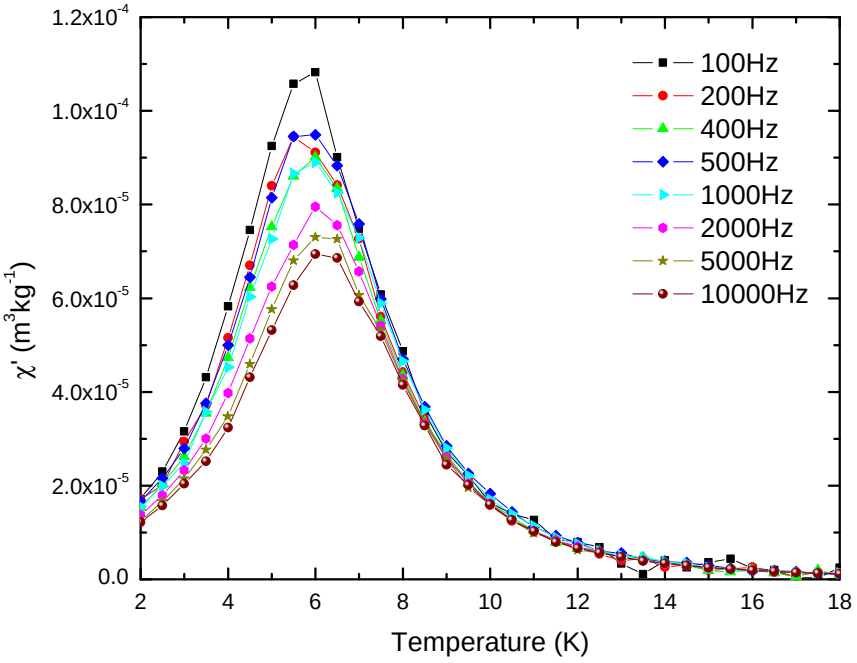

Figure 4.26: χ' vs. temperature for the aged sample of AB2 showing the frequency dependence of the transition.

When fitting using the Arrhenius law, similar to the fresh sample, the values obtained were unphysical which again points to the system not behaving like a superparamagnet and the Vogel-Fulcher law was used to analyse the data. The value of $f(0) = 0.8$ MHz which again is of a similar magnitude to the relaxation observed in the muon spin relaxation experiment. The values from the Vogel-Fulcher fit to the data are lower than that observed for the fresh sample showing that the absorption of water into the structure is creating a magnetic state with a lower activation energy within the magnetic state. The dynamical component has a value in between the two fresh samples measured and therefore one can assume the fluctuations associated with the reduced T_C magnetic state are similar to that observed within the fresh sample. The imaginary susceptibility shows little frequency dependence and is shown in the appendix (figure A.4).

Parameter	Result
$T_f(0)$ (K)	5.17(2)
φ	0.0184(4)
E_a/k_B (K)	5.6(2)
ω_0 (rads s^{-1})	5.28×10^6
$f(0)$ (MHz)	0.8

Table 4.7: Parameters calculated from the AC susceptibility the aged sample of AB2.

4.6 Discussion

The $M(TCNQ)_2$ samples were believed to be crystalline materials and in the case where M = Ni and Mn we have shown that the deuterated analogues show diffraction peaks that correspond to the existence of an ordered crystal. For the Ni sample the diffraction data has not yielded any firm conclusions on the atomic structure and the crystallinity appears to be weak and have a short coherence length. The SEM images show that micron-size particles are synthesised within the deuterated sample however this does not match up with the particle sizes calculated using the Scherrer equation which on average result in crystallites of approximately 30 nm. One however must separate out the two results and what we may be observing in the SEM is the size of a crystal that includes many defects where each defect may impose a grain boundary which is pinned and the individual grains are of the order of 30 nm.

The magnetic data show some very interesting results where the sample is shown to behave like a ferromagnetic material which at low temperatures enters an ordered phase that can be described by a Bloch's law indicating the existence of a classical 3D spin wave system. The resulting $T^{\frac{3}{2}}$ dependence of the magnetisation as a function of temperature only occurs well below the transition. This is supported by the heat capacity data where again the low temperature data can be shown to also follow a $T^{\frac{3}{2}}$ function as well as a small contribution from the lattice which goes as T^3.

From work conducted by Goddard *et al.* [31] where they observed a decrease of T_N of 4% on deuteration of a metal-organic magnetic material, $CuF_2(pyx)(H_2O)_2$ (pyz=paradiazine). When only the ring of the pyz molecule was deuterated there was not a dramatic decrease in T_N, however when D_2O was substituted for H_2O this caused a dramatic shift as it affected the hydrogen bonding within the structure. The exchange mechanism between magnetic centres was thought to be through the hydrogen bonds and substituting the hydrogen for deuterium reduced the effective size of D in the bond. The increased mass of D also leads to a smaller zero point vibrational energy and a reduction in electron wave function overlap which reduces J, the exchange interaction strength. Since this behaviour of a decrease in the T_C of $Ni(TCNQ)_2$ on deuteration of the ring the mechanism described by Goddard *et al.* is likely not to be present or relevant to the studied TCNQ based magnetic material. It may be the increase in T_C observed within $Ni(TCNQ)_2$ is due to the deuteration creating larger ferromagnetic clusters which may push the T_C higher. From the SEM data the increased size of the crystallites supports this idea of deuteration leading to larger grains which may also mean larger ferromagnetic clusters.

Analysis of the AC susceptibility data shows that the sample is likely to have a glassy component associated with the transition where the values of φ do not agree with that of a superparamagnet and are closer to the values of the canonical spin glasses [11]. The ferromagnetic transition in the magnetisation data however does not show any resemblance to a spin glass where one expects the FC curve to flatten out where the moments freeze into one of the metastable ground states which suggests that the transition and the glassy nature of the material may be due to different things.

From the DC transport data and heat capacity, one can see that the sample behaves as a 3D ferromagnetic material, however the frequency dependence of the real component of the AC susceptibility shows that there is a glassiness associated with the transition. The comparison with $Mn(TCNQ\text{-}D_4)_2$ shows that by creating an isostructural, more crystalline sample the dominant ferromagnetism is greatly reduced, although evidence suggests that it is not completely gone. It may be that within the Ni sample there is a short range interaction which is mediated by the

inhomogeneity, where we are observing disorder driven magnetism similar to that observed in $V(TCNE)_x$ [13]. This may lead to magnetic clusters of the order of 30 nm, the observed particle size from PXRD, where there is a percolative transition to a ferromagnetic phase as $T \rightarrow 0$. As T decreases through T_C the coherence length of these magnetic clusters grows and ultimately interaction between these clusters leads to a glassy ferromagnetic state which can lead to a complex magnetic ground state. It should be noted that this infinite cluster formed at T=0 K is effectively made up of many randomly frozen smaller clusters.

This idea is similar to that observed in the inorganic disordered perovskite, $La_{1-x}Sr_xCoO_3$ (LSCO). In the undoped form $LaCoO_3$ undergoes a temperature driven metal-insulator transition which is due to a spin state transition of the Co^{3+} ion, however there is some ambiguity as to whether at high temperatures this shows an $S = 1$ (intermediate) or $S = 2$ (High Spin) state [52]. Doping with Sr^{2+} ions not only creates holes but also induces disorder within the system. Hole doping the material induces an insulator-to-metal transition with increasing x. At low doping, the magnetism of the insulating phase shows characteristic spin glass behaviour, however when $x > 0.18$ this magnetism shows characteristics of a 3D ferromagnetic metal. The insulator-metal transition is believed to be percolative and is associated with magneto-electronic phase separated regions [53]. At low x the magnetism is dominated by the Co^{3+} antiferromagnetic superexchange interactions, however increased doping lead to an increased number of Co^{4+} ions which drives the local interactions into a double exchange ferromagnetic state leading to the aforementioned magnetic clusters. The spin glass behaviour is due to the competing ferromagnetic and anitferromagnetic interactions within the systems where irreversibility is also observed in the ZFC/FC data. The AC susceptibility data also show a frequency dependence of the transition even in the ferromagnetic phase which is clear evidence of spin glass freezing.

The LSCO system may be a parallel to the studied $Ni(TCNQ\text{-}D_4)_2$ samples where we are also observing very strong evidence for ferromagnetic behaviour in both the magnetisation and heat capacity measurements. However the AC susceptibility appears

to show characteristic spin glass behaviour and may be due to superparamagnetic particles. The SEM images shows that the sample is made of small crystallites however these are larger then the estimated cluster size from the PXRD peak width and so these small crystallites are likely made of smaller clusters with a short crystalline coherence length or nanocrystalline grains. This would lead to a disordered state within the crystal where, if each of these clusters was inhomogeneous yet had a strong magneto-crystalline anisotropy would lead to a cluster-glass type behaviour where the ferromagnetism is a consequence of a percolative transition. As $T \rightarrow 0$ K the ferromagnetic clusters would minimise their magnetocrystalline energy by aligning with each other causing an overall increase in the ferromagnetism where at $T = 0$ K one would observe a large infinite magnetic material where these individual magnetic clusters join together leading to an overall ferromagnetic behaviour.

4.7 Conclusion

In summary a $Ni(TCNQ)_2$ sample similar to that produced by Clérac *et al.* [24] was synthesised where the main difference was the deuteration of the TCNQ unit. The new material was characterised both structurally and magnetically and both protio and deutero samples were compared. It was found that on deuteration of the TCNQ this shifted the Curie temperature to a higher value, where $\Delta T_c = 3$ K, and from the M vs. H curves (figure 4.15) there is possible evidence for ferromagnetic coupling of the TCNQ and Ni ions.

The structure of the deuterated sample was studied using an SEM where it was found that by deuterating the TCNQ this leads to on average larger crystallites than the protio counterpart. This was thought to be down to the kinetics of the reaction where the formation of $Ni(TCNQ\text{-}D_4)_2$ was slower and therefore able to grow larger crystals. However the precipitation reaction is very fast and so it would be hard to grow substantial crystals using this method. Using X-ray diffraction it was possible to confirm that the unit cell is tetragonal with dimensions similar those determined in a previous study [24]. However, diffraction peak broadening was substantial and

it prevented a detailed analysis of the crystal structure of Ni(TCNQ-D_4)$_2$.

Since the sample was deuterated this was conducive to performing neutron scattering and muon spin relaxation experiments to study the material further. Neutron scattering studies showed that the structure is complex and no additional structural information could be gained from the data beyond confirming the results of Clérac *et al.* [24]. From a study of Mn(TCNQ-D_4)$_2$ we showed that the diffraction pattern is more complex and, although there are reflections in common with diffraction pattern of the Ni compound, the unit cell was indexed as monoclinic which did not agree with our results from Ni(TCNQ-D_4)$_2$ or indeed the structure of Mn(TCNQ)$_2$ deduced by Clérac *et al.* [24]. The D1B neutron diffraction experiment provided some evidence of very weak magnetic Bragg peaks which suggests that the ferrimagnetism within the sample is commensurate with the crystal structure and may not be due to, say, any form of amorphous ferromagnetism.

Results from magnetic data for the Mn(TCNQ-D_4)$_2$, AB7, sample was briefly discussed where when the susceptibility was plotted as χ vs. T, there seemed to be no real evidence of a cusp in the ZFC or FC data. However when looking for small changes in the susceptibility by plotting as χT vs. T, it was clear that there was evidence for the material undergoing a transition to an antiferromagnetic state (40 K) and a more complex magnetic state at low temperatures. The fact that this was not obvious in the χ vs. T plot may mean it is a very weak effect which and as the sample is more crystalline (as shown by the diffraction data) it may be that the ferromagnetism observed is increased by increasing levels of disorder within the system.

The magnetism of the $NiTCNQ_2$ sample is of great interest as the moments measured in an applied field of 5 T do not match those obtained from a Curie-Weiss fit to the data. When considering the AC susceptibility data, the cusp in the data, which is attributed to a ferromagnetic transition and shows a frequency dependence, is suggested to be a spin glass as it does not follow an Arrhenius type activated behaviour, which would be seen in a superparamagnetic system and instead can be modelled using the Vogel-Fulcher law. This results in the fluctuating component of

the magnetism in no applied AC field being equal to approximately 0.3 MHz which will also be discussed in the following chapter. From analysis using the Mydosh Criterion the frequency dependence of the transition, or T dependent cusp in the data, is similar to that of the canonical spin glasses such as CuMn or AuMn.

Within the aged sample of AB2 the magnetisation data shows that the magnetic moment is reduced which implies that there is a breakdown of magnetic exchange paths within the sample. This is put down to the hygroscopic nature of the material where water is being absorbed over time which leads to a change of phase from a non-hydrated to hydrated form of Ni(TCNQ-D_4)$_2$. AC susceptibility data proved useful where the frequency dependence of the transition has decreased illustrating that as water is absorbed and the sample ages it become a weaker spin glass although still within the realms of the weak canonical spin glasses such as NiMn.

Overall we have shown that Ni(TCNQ-D_4)$_2$ undergoes a magnetic phase transition to a ferromagnetic phase at 20 K where the reported glassy behaviour [24] may be associated directly with T_C. Although the material undergoes a ferromagnetic transition, possibly to a ferrimagnetic state, there is evidence of both a static magnetic component and also a dynamic contribution is present. However from the data presented one cannot rule out that within this metal-organic system the magnetism is due primarily to disorder and that a purely crystalline system may not show magnetic phase transition but behave paramagnetically or even undergo dimerisation of the TCNQ units.

Bibliography

[1] S. J. Blundell and F. L. Pratt. *J. Phys. :Condens. Matter* **16** (2004) R771

[2] J. S. Miller. *Chem. Soc. Rev.* **40** (2011) 3266

[3] J. S. Miller, J. H. Zhang, W. M. Reiff, D. A. Dixon, L. D. Preston, A. H. R. Jr., E. Gebert, M. Extine, J. Troup, A. J. Epstein and M. D. Ward *J. Phys. Chem.* **91** (1987) 4344

[4] A. H. R. Jr., L. D. Preston, J. M. Williams, S. W. Peterson, G. A. Candela, L. J. Swartzendruber and J. S. Miller. *J. Am. Chem. Soc.* **101** (1979) 2756

[5] J. S. Miller, A. H. R. Jr., E. Gebert, J. J. Ritski, W. R. Salaneck, L. Kovnat, T. W. Cape and R. P. V. Duyne. *J. Am. Chem. Soc.* **101** (1979) 7111

[6] J. S. Miller, J. C. Calabrese, H. Rommelmann, S. Chittipeddi, J.H. Zhang, W.M Reiff and A. J. Epstein. *J. Am. Chem. Soc* **109** (1987) 769

[7] J. S. Miller and A. J. Epsteinn. *Angew. Chem. Int. Ed.* **33** (1994) 385

[8] J. S. Miller. *Pramana - J. Phys.* **67** (2006) 1

[9] W. E. Broderick, D. M. Eichhorn, X. Liu, P. J. Toscano, S. M. Owens and B. M. Hoffman. *J. Am. Chem. Soc.* **117** (1995) 3641

[10] M. L. Taliaferro, T. D. Selby and J. S. Miller. *Chem. Mater.* **15** (2003) 3602

[11] J. A. Mydosh. *Spin Glasses: An Experimental Introduction*, 1st ed. (Taylor and Francis, London, 1993)

[12] Z. J. Huang, F. Cheng, Y. T. Ren, Y. Y. Xue, C. W. Chu and J. S. Miller. *J. Appl. Phys.* **73** (1993) 6563

[13] J. M. Manriquez, J. S. Miller and A. Epstein. *Science* **252** (1991) 1415

[14] M. D. Harvey, T. D. Crawford and G. T. Yee. *Inorg. Chem.* **47** (2008) 5649

[15] K. I. Pokhodnya, D. Pejakovic, A. J. Epstein and J. S. Miller. *Phys. Rev. B.* **63** (2001) 174408

[16] P. Zhou, B. G. Morin, J. S. Miller and A. J. Epstein. *Phys. Rev. B* **48** (1993) 1325

[17] B. G. Morin, P. Zhou, C. Hahm, A. J. Epstein and J. S. Miller. *J. Appl. Phys.* **73** (1993) 5648

[18] X.L. Wang, J. Horvat, H.K. Liu and S.X. Dou. *Solid State Commun.* **108** (1998) 661

[19] J. S. Miller, J. C. Calbrese, R. S. Mclean and A. J. Epstein. *Adv. Mater.* **4** (1992) 498

[20] W. Hibbs, D. K. Rittenburg, K.-I. Sugiura, B. M. Burkhart, B. G. Morin, A. M. Arif, L. Liable-Sands, A. L. Rheingold, M. Sundaralingam, A. J. Epstein and J. S. Miller. *Inorg. Chem.* **40** (2001) 1915

[21] S. J. Etzkorn, W. Hibbs, J. S. Miller and A. J. Epstein. *Phys. Rev. Letts.* **89** (2002) 207201

[22] S. J. Etzkorn, W. Hibbs, J. S. Miller and A. J. Epstein. *Polyhedron.* **22** (2003) 1751

[23] S. J. Etzkorn, W. Hibbs, J. S. Miller and A. J. Epstein. *Phys. Rev. B.* **70** (2004) 134419

[24] R. Clérac, S. O'Kane, J. Cowen, X. Ouyang, R. Heintz, H. Zhao, M. J. Bazile and K. R. Dunbar. *Chem. Mater.* **15** (2003) 1840

[25] L. R. Melby, R. J. Harder, W. R. Hertler, W. Mahler, R. E. Benson and W. E. Mochel. *J. Am. Chem. Soc.* **84** (1962) 3374

[26] H. Zhao, R. A. Heintz, X. Ouyang, K. R. Dunbar, C. F. Campana and R. D. Rogers. *Chem. Mater.* **11** (1999) 736

[27] H. Zhao, R. A. Heintz, K. R. Dunbar and R. D. Rogers. *J. Am. Chem. Soc.* **118** (1996) 12844

[28] E. B. Vickers, I. D. Giles and J. S. Miller. *Chem. Mater.* **17** (2005) 1667

[29] R. C. Thompson, Y. Hoyano and C. F. Schwerdtfeger. *Solid State Commun.* **23** (1977) 633

[30] R. C. Thompson, V. K. Gujral, H. J. Wagner and C. F. Schwerdtfeger. *Phys. Stat. Sol.* **53** (1979) 181

[31] P. A. Goddard, J. Singleton, C. Maitland, S. J. Blundell, T. Lancaster, P. J. Baker, R. D. McDonald, S. Cox, P. Sengupta, J. L. Manson, K. A. Funk, J. A. Schlueter. *Phys. Rev. B.* **78** (2008) 052408

[32] R. Blinc, B. Zalar, A. Gregorovic, D. Arcon, Z. Kutnjak, C. Filipic, A. Levstick, R. M. Archey and N. S. Dalal. *Phys. Rev. B.* **67** (2003) 094401

[33] L. Shields. *J. Chem. Soc., Faraday Trans. 2.* **81** (1985) 1

[34] R. A. Heintz, J. A. Smith, P. s. Szalay, A. Weisgerber and K. R. Dunbar. *Inorg. Synth.* **33** (2002) 75

[35] D. Dolphin, W. Pegg and P. Wirz. *Can. J. Chem.* **52** (1974) 4078

[36] H. T. Jonkman and J. Kommandeur. *Chem. Phys. Letts.* **15** (1972) 496

[37] J. Rodriguez-Carvajal. *Physica B.* **192** (1993) 55

[38] www.ill.eu/sites/fullprof/php/programsdccc.html?pagina=Treor90 (July 2012)

[39] P.-E. Werner, L. Eriksson and M. Westdahl. *J. Appl. Cryst.* **18** (1985) 367

[40] A. Boultif and D. Louer. *J. Appl. Cryst.* **34** (2004) 724

[41] A. L. Patterson. *Phys. Rev* **56** (1939) 978-982

[42] A. Furrer, J. Mesot and T. Strässle. *Neutron Scattering in Condensed Matter Physics Series on Neutron Scattering Techniques and Applications - Vol. 4.* World Scientific, Singapore. (2009)

[43] C. Kittel. *Introduction to Solid State Physics.* John Wiley and Sons, Inc, Hoboken, NJ. 8th Ed. (2005)

[44] I. A. Campbell, A. Amato, F. N. Gygax, D. Herlach, A. Schenck, R. Cywinkski and S. H. Kilcoyne. *Phys. Rev. Lett.* **72** (1994) 1291

[45] P. C. Fannin, B. K. P. Scaife and S. W. Charles. *J. Phys. D: Appl. Phys.* **21** (1988) 533

[46] P. C. Fannin, L. Choen-Tannoudji, E. Bertrand, A. T. Giannitsis, C. Mac Oireachtaigh and J. Bibette. *J. Magn. Magn. Mater.* **303** (2006) 147

[47] F. Ludwig, A. Guillaume, M. Schilling, N. Frickel and A. M. Schmidt. *J. Appl. Phys.* **108** (2010) 033918

[48] P. M. Lahti. *Magnetic Properties of Organic Materials.* Marcel Dekker, Inc. New York. (1999)

[49] Personal communication Pascal Manuel. Beam line Scientist on WISH, ISIS.

[50] P. V. Henriksen, P.-A. Lindgård and S. Linderoth. *Phys. Rev. B.* **48** (1993) 7259

[51] J. P. Chen, C. M. Sorensen, K. J. Klabunde, G. C. Hadjipanayis, E. Devil and A. Kostikas. *Phys. Rev. B.* **54** (1996) 9288

[52] M. Imada, A. Fujimori and Y. Tokura. *Rev. Mod. Phys.* **70** (1998) 1039

[53] J. Wu and C. Leighton. *Phys. Rev. B.* **67** (2003) 174408

Chapter 5

A Muon Spin Relaxation Study of a Nickel - TCNQ Based Magnetic Material

Muon Spin Relaxation (μSR) is a technique that is sensitive to weak magnetism and magnetic order on a local scale ($\sim$2 nm) as well as long range (static fields) [1]; see Chapter 2 for an introduction to the technique. μSR experiments were performed on Ni(TCNQ-D_4)$_2$ where the deuteration of the compound was of an advantage as it decreased the coupling of the muon to the nuclear spins on the protons [1]. This meant that the only important nuclear spin that would contribute to the depolarisation of the muon was on the nitrogen atoms. Neutral TCNQ has been studied using muon spectroscopy where an 80 MHz radical was observed which corresponds to coupling of the muon to the nitrogens at the end of the molecule. In reduced TCNQ it may be possible to observe bonding of the muon to the aromatic ring which would have a higher hyperfine coupling [2, 3]. Thus although deuterium has a nuclear magnetic moment, because it is smaller than that of N-14 and, given the suspected stopping site of the muon, it can be ignored. Since positive muons are implanted into the material one expects the muon to stop next to areas of negative charge which, within

[1] Deuterium also has a moment however this is small when compared to that of a proton

our sample, would be sites close the TCNQ where the anion radical is stabilised, i.e. the cyano groups at one end of the TCNQ molecule. However, the magnetic environment of the muon is complicated as the muon will be sensitive to both the nuclear magnetism on the nitrogen atoms and also the electronic magnetism below T_c. From figure 5.1 one can see that the electron density is spread across the ring and so it may be possible to have paramagnetic muonium formed from bonding to the ring. However from the positions at (0.65,0) and (0.9,0.5) one can see there is a larger electron density within this tertiary carbon which supports a large amount of electron density from the radical anion being located on the NC-C-CN part of the molecule. The data within the figure were collected using powder x-ray diffraction and a Rietveld refinement of the data resulted in an electron density map (see chapter 6 for more information on the KTCNQ salts).

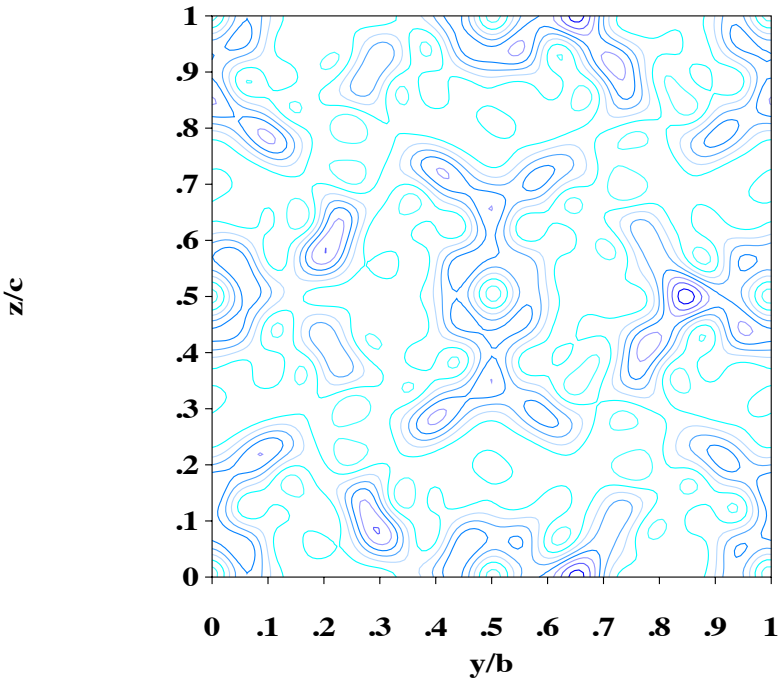

Figure 5.1: Fourier map from an x-ray diffraction experiment for KTCNQ-D_4 showing the electron density of TCNQ anions that are aligned along the a-axis.

One of the advantages of μSR as an experimental technique is the ability to look at magnetic transitions in a true Zero Field (ZF) environment and where the bulk

magnetic susceptibility will track the ZFC curve (e.g. figure 4.11), one can follow the susceptibility on a local scale. All data were fit and analysed using the Wimda program [4].

For the muon spin relaxation experiments, which were on the EMU spectrometer at ISIS, an Oxford He flow cryostat was used to cool the sample. The sample was mounted on a silver backing plate with a mylar cover. The silver shows no relaxation signal and so any muons that are stopped in the silver have no contribution to the muon relaxation and results in a constant baseline. Extra μSR measurements were taken on the GPD spectrometer at the Paul Scherrer Insitut (PSI) where the sample could be put under an applied pressure where the results will be briefly touched upon within this chapter.

5.0.1 Zero Field μSR

ZF experiments were conducted on a fresh ($<$ 1 month old) sample of Ni(TCNQ-D_4)$_2$. The same sample was used for the neutron diffraction experiment on D1B and so since there is evidence of weak magnetic Bragg peaks one would expect the muons to be sensitive to this magnetism.

The raw data from the ZF experiment at selected temperatures are shown in figure 5.2 and it is clear that the relaxations are qualitatively different above and below the Curie temperature. At 50 K (i.e. $T > T_{\mathrm{C}}$) the data must be fit using a sum of two Gaussian functions (see equation 5.1) which is likely describing the relaxation due to the nuclear magnetism of the nitrogen atoms for both components 1 and 2.

$$G(t) = A_1 \exp(-\sigma_1^2 t^2) + A_2 \exp(-\sigma_2^2 t^2) + A_{\mathrm{Bg}}, \tag{5.1}$$

where A_i is the asymmetry associated with the ith muon stopping site, A_{Bg} is the baseline which accounts for muons that are relaxing in the silver sample holder or cryostat and σ_i is the relaxation parameter that is dependent on the local magnetic field at the ith muon stopping site.

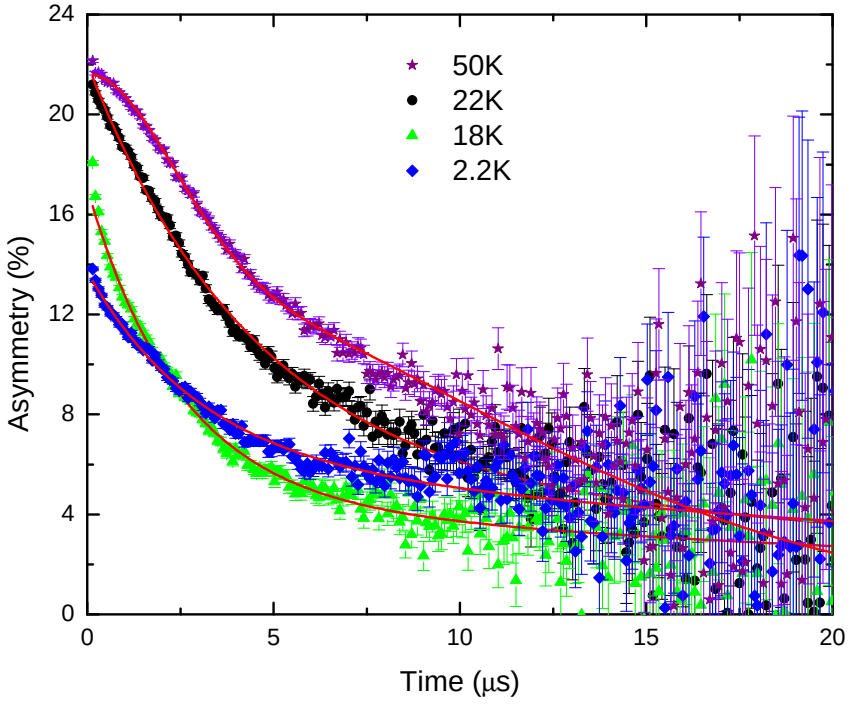

Figure 5.2: ZF μSR raw data at selected temperatures above and below T_C.

The fact that the relaxation at 50 K cannot be modelled simply using a single Gaussian (see table 5.1 for values of fitting parameters) suggests that there are at least 2 muon stopping sites within the sample. These may be next to the negative charge on the cyano groups at the end of the TCNQ moiety and also above or below the aromatic ring on a TCNQ molecule where there is significant π-electron density. At these different stopping sites the magnitude of internal nuclear field strength will be different as it depends on the distance from the nuclear moments and so each muon will experience a different net local field and their relaxations will differ corresponding to different values of σ. This results in the data showing a summation of relaxation similar to what we observe. Since $\sigma_1 < \sigma_2$ this means that the field distribution experienced by μ_2^+ is larger then that for μ_1^+. At the site where the muon is coupled to the nitrogen the distribution of nuclear fields will be larger than if the muon was coupled to the aromatic ring, therefore we may have a case where muons are coupled to both the ring and the cyano groups. However it could be that two different muons are implanting to two different sites where the magnetic

Parameter	Value
A_1 (%)	11.44
A_2 (%)	7.69
σ_1 (μs^{-1})	0.081
σ_2 (μs^{-1})	0.327

Table 5.1: Parameters from a fit to the high temperature μSR data.

behaviour differs, i.e. in the centre and edge of a magnetic cluster, which will be discussed in more detail later.

As T approaches T_C from below the relaxation has an increasingly non-Gaussian form and is closer to a simple exponential for $T < T_C$. One assumes that the electronic magnetism has a larger contribution to the muon relaxation as they become quasi-static and so when going through T_C the overall magnetism of the material dominates the muon relaxation signal. In fact, in this regime the data were fitted using a summation of two single exponential relaxations,

$$G(t) = A_1 \exp(-\lambda_1 t) + A_2 \exp(-\lambda_2 t) + A_{Bg}. \tag{5.2}$$

Here λ_i is the relaxation parameter that again is proportional to the local internal magnetic field experienced by the muon at the ith site. Following the analysis of the 50 K ZF μSR data the two relaxations observed close to or below T_C are from the different muon stopping sites. The baseline (A_{Bg})was kept fixed at 2.5% as it is not expected to change as a function of temperature. The data could only be fitted using equation 5.2 and not a single exponential as λ_2 accounted for a very slow relaxation. The value of λ_2 was kept fixed at 0.03 μs^{-1} which was seen to be a reasonable description of the relaxation rate where this slow relaxation is believed to be the tail of a relaxation that is outside of the time window of the measurement and not accounted for in the baseline. If there is indeed a relaxation that is outside of the EMU time window this may imply that at one muon stopping site the internal fields are at such a high value the implanted muons are dephased very quickly and we

cannot detect their relaxation. It should be noted that equation 5.2 was used to fit to the higher temperature data as this allowed some form of parameterisation however above the critical region this may not be the most physically relevant description.

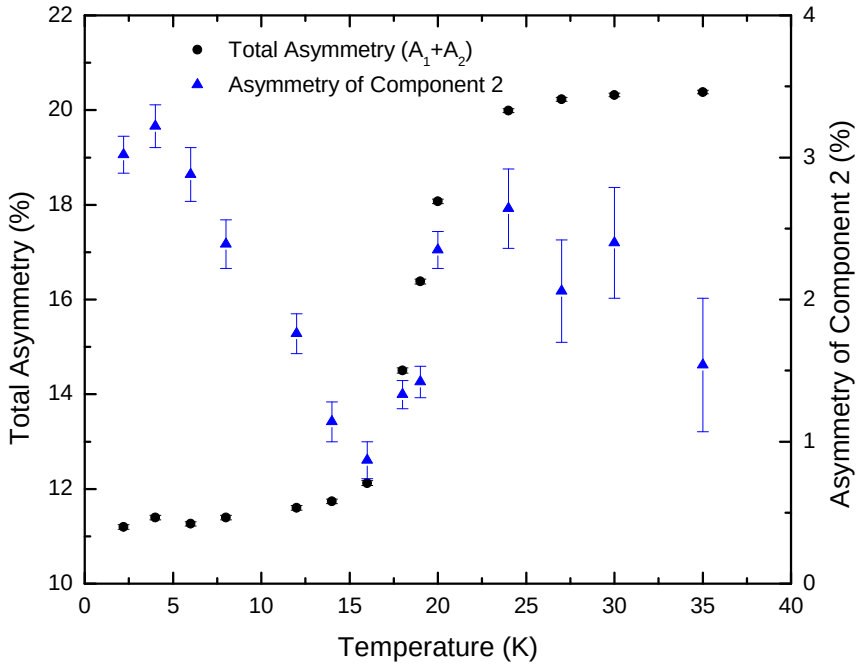

Figure 5.3: ZF total asymmetry and the 2nd component asymmetry (A_2).

The asymmetries of components 1 and 2 (A_1 and A_2 respectively) are shown in figure 5.3 where A_2 (blue triangles) is showing a dramatic change at 19 K that corresponds to the ferromagnetic transition. As the sample approaches the magnetic phase transition from a higher temperature the fluctuating spins begin to order and the magnitude of the internal field increases. If the muons experience a high field then they are dephased very quickly and thus one sees a missing fraction on entering the ordered phase where the static field is large enough to depolarise the muons outside of the EMU instrument's time window. The asymmetry of component 2 is well coupled to the transition which suggests that it has a relationship to the electronic magnetism within the sample. As $T \rightarrow 0$ this contribution increases which again suggests that it is due to the increased magnetic order within the material as the fluctuations will freeze out below T_C, however the exact nature of this relaxation

cannot be determined from our data.

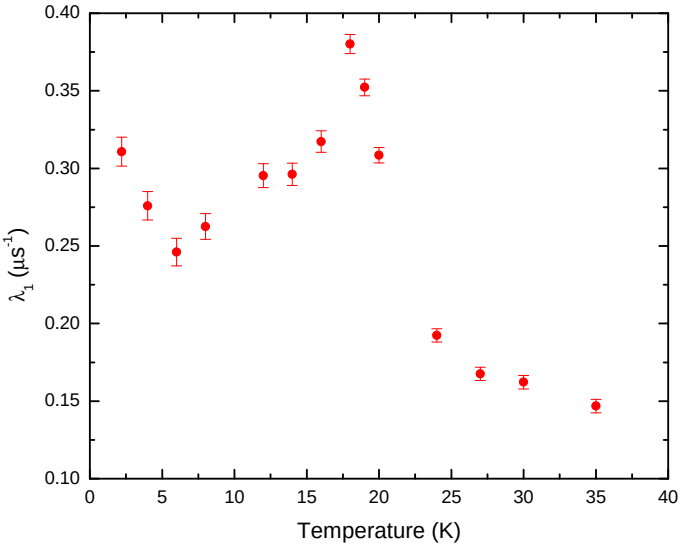

Figure 5.4: ZF relaxation parameter of component 1 from fits to the raw data using equation 5.2.

The ZF relaxation parameter, λ_1 of the first component, shown in figure 5.4, is related to the spread of internal fields and the fluctuating electronic moments as in the fast fluctuating limit $\lambda \propto \Delta^2/\nu$. From the data it is clear that the sample goes through a transition at $\sim$19 K where the fluctuating magnetic moments slow down and the system enters an ordered phase (on the time scale of the muon). The apparent plateau at 14 K may be real and indicates that there is a more complex magnetic behaviour (i.e. another peak in λ_1) present however more data is needed to confirm this and to draw any conclusions.

Below 6 K the value of λ_1 begins to increase rapidly, which is denoted henceforth as T_f but should not be confused with the AC susceptibility data in the previous chapter. From the magnetization data shown in figure 4.11 one can see that at low temperatures the ZFC curve changes slope which may coincide with the material cooling into a glassy ground state where the field distribution will change which in turn will alter the muon relaxation spectrum. The increase in the muon relaxation may be due to the response to this glassy component within the material where a

glassy temperature is present (T_g) that may be below 2 K, our accessible temperature range. Below this temperature the relative motion of magnetic clusters will freeze out. However one can not rule out the possibility of another exchange mechanism becoming influential at very low temperatures; for example TCNQ - TCNQ interactions, which are known to be present in other 1:2 TCNQ based materials [5] which would again change the field distribution and electronic fluctuations thus leading to observable changes in λ_1. However this may be unusual as the system has already ordered.

5.0.2 Longitudinal Field μSR

Longitudinal field measurements allow decoupling of the components within the muon relaxation, i.e. by application of a field one can repolarise muons that are dephased by the nuclear moments on the N atoms. It is also possible to decouple static magnetism and to study the dynamics within a system.

Although the sample was deuterated, minimising the possibility of muon hyperfine coupling to the protons on the TCNQ ring, coupling between the muon and the nuclear moment on the nitrogen nuclei is likely as suggested by ZF measurements at 50 K. To decouple this nuclear contribution a longitudinal field (LF) ($\leq$4500 G) was applied which acts to repolarise muon spins. We find that an optimal LF for decoupling the nuclear component is 50 G which will be discussed in more detail later. At high fields one might expect to repolarise all the muons spins, including those relaxed by static local fields which are electronic in origin, so a full fraction is recovered. However, this was not the case up to 20 K where the effect is more extreme at lower temperatures. At 2 and 6 K, and 4500 G LF a 21% total asymmetry was reached (a full fraction on the EMU instrument being taken as $\sim$23%) which suggests that even at these high LF values there is a significant dynamical contribution to the magnetism within the system. In fact at a LF above 100 G a single exponential relaxation function was fit to the data where $\lambda_{LF} = 0.146 \pm 0.018$ μs^{-1} for all temperatures and at all field values, the raw data is shown in figure 5.5 at 6 K .

There is little difference between the relaxation at different temperatures except for the asymmetry as the LF is ramped.

Since the of λ_{LF} value could be fixed it means that the same relaxation process is dominant at all temperatures and supports there being significant dynamical fields within the system. The fact that there is a dramatic change in the LF data at $\sim$100 G indicates that the spread of internal fields in the sample, which acts to depolarise the muon spins, is around this magnitude.

When a smaller LF is applied (0-100 G) the muon relaxation is different to the high field data in that the relaxation cannot be modelled by a single exponential and is more suited overall to a dynamical Kubo-Toyabe (KT) function; see chapter 2 section 2.4.1. Fitting the data using this function takes into account the fluctuations of the magnetic moments as these rapidly changing moments cause the muon to experience different internal fields that broaden the relaxation and so an oscillation can be heavily damped. For the dynamical KT fits to the data Δ, the distribution of internal fields, was fixed at 2.1 MHz and held constant at all temperatures and only the fluctuation rate was allowed to float as one does not expect the field distribution to change, only the fluctuation rate. The data were fitted between 0-5 $\mu\mathrm{s}^{-1}$ as at low fields, and from the ZF μSR data, the relaxation is complex with there being at least two relaxation processes. Considering only short times it is possible to use a KT function to describe the fast relaxing component which dominates the data. The fluctuation rate is plotted out in figure 5.7 and shows the parameter as a function of both applied field and temperature.

Although the data points in ZF are sparse it is clear that there is a peak in the fluctuation rate at approximately 12 K, which does not correspond to the peak in λ_1 at 20 K for the ZF temperature dependent data (see figure 5.4). This, however, is of interest as, from the ZFC and FC magnetization data (see figure 4.11) 12 K is approximately the point of irreversibility of the temperature dependent magnetization with a coercive field beginning to dominate at low fields. With the ZF μSR data when fitting to a KT function, and at short times, it shows that the relaxation is sensitive to the freezing of the magnetization of the bulk sample, however this

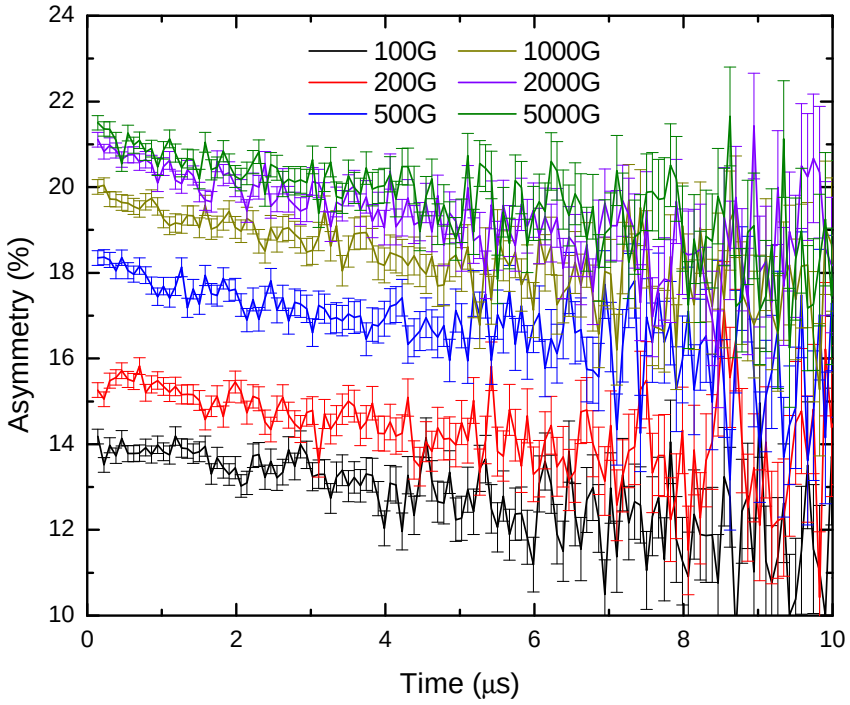

Figure 5.5: The asymmetry at 6 K at different LF values. From the data one can see the relaxation is very small and is essentially the same at each LF and only the asymmetry is changing.

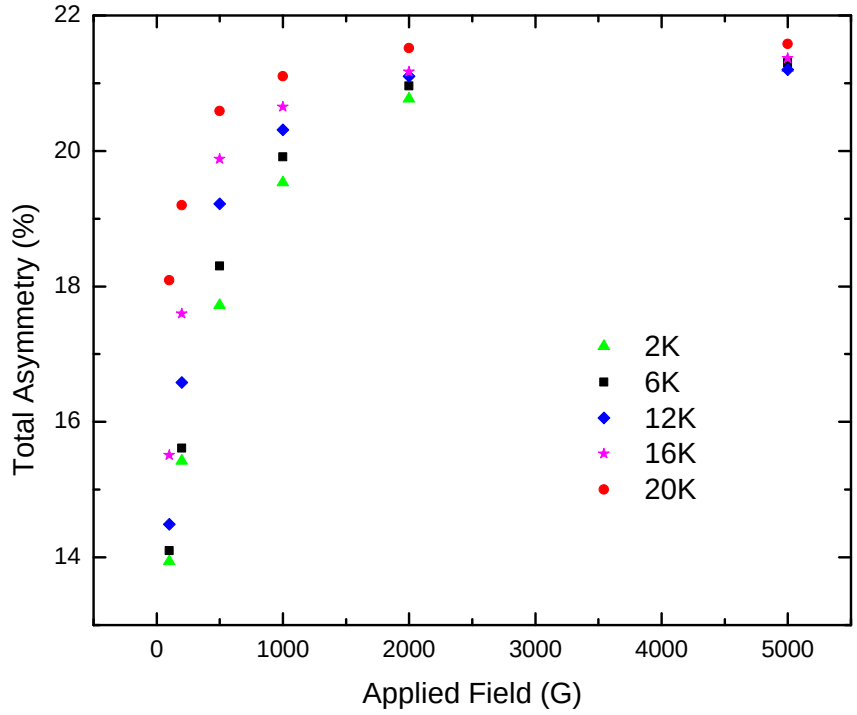

Figure 5.6: Total asymmetry as a function of applied LF where $B \geqslant 100$ G.

was only done for the temperatures where LF measurements were conducted. This is to parameterise and compare the ZF with the LF data as the KT fits may not be the best description and in reality a summation of single exponentials is best to describe the physics.

Figure 5.7 demonstrates that, at all temperatures, the LF relaxation data show what may be expected, that as a higher field is applied, magnetic fluctuations present in the sample are suppressed. When at $B_{LF} = 50$ G these fluctuations at all temperatures are of a similar rate and close to zero. At 25 G the fluctuation rate varies where there is some evidence of it being related to the transition, though for the lower temperatures <20 K, these values are essentially the same within the error. At 20 K and above, the values for the fluctuation rate are lower, presumably because the fluctuation rate of the majority of magnetic clusters are out of the EMU instrument time window when in the transition region and at higher temperatures (i.e. in the paramagnetic phase). The lower fluctuation rate observed at T >20 K may there-

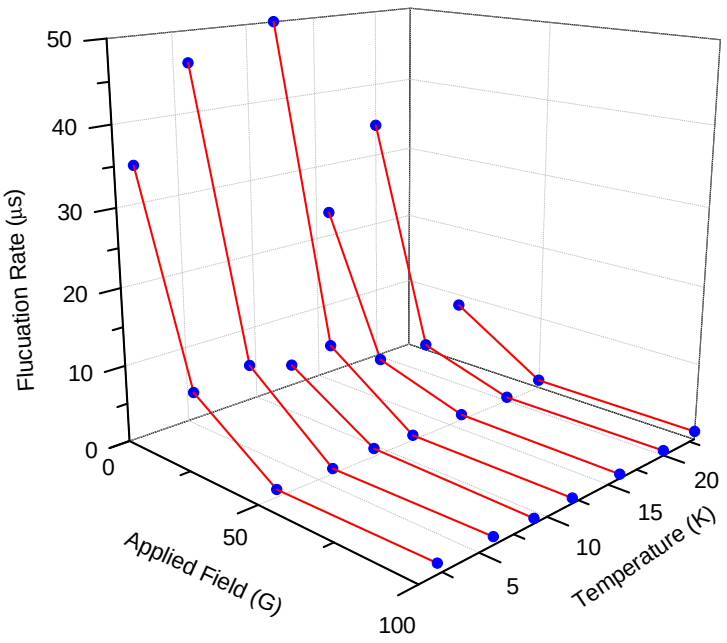

Figure 5.7: Low Field (<100 G) LF parameters from fits to a dynamical KT function. Note that at 9 K and 23 K there are no zero field data.

fore be due to larger clusters having T_C 's greater than 20 K or strong interactions between magnetic clusters pointing to a magnetic cluster size distribution.

The asymmetry was linear within error at each temperature where, at the low temperatures (2-16 K), this was within the values of 14-16%. However at the higher temperatures (20-23 K) the asymmetry had increased to 21% which is approaching a full fraction following the ZF asymmetry seen in figure 5.3 where a magnetic phase transition is observed.

At all field values it is clear that, when plotted as a function of temperature (figure 5.8), the asymmetry of the KT dynamical contribution increases as the temperature increases and exhibits a magnetic transition similar to what was observed in the ZF data (figure 5.3). The asymmetries of the ZF data do not have the same values or follow the trends of figure 5.3 suggesting that at short times the muon relaxation is more complex where, within this time scale, the KT function is capturing the initial drop in asymmetry as a function of time slightly better then the ZF fitting function

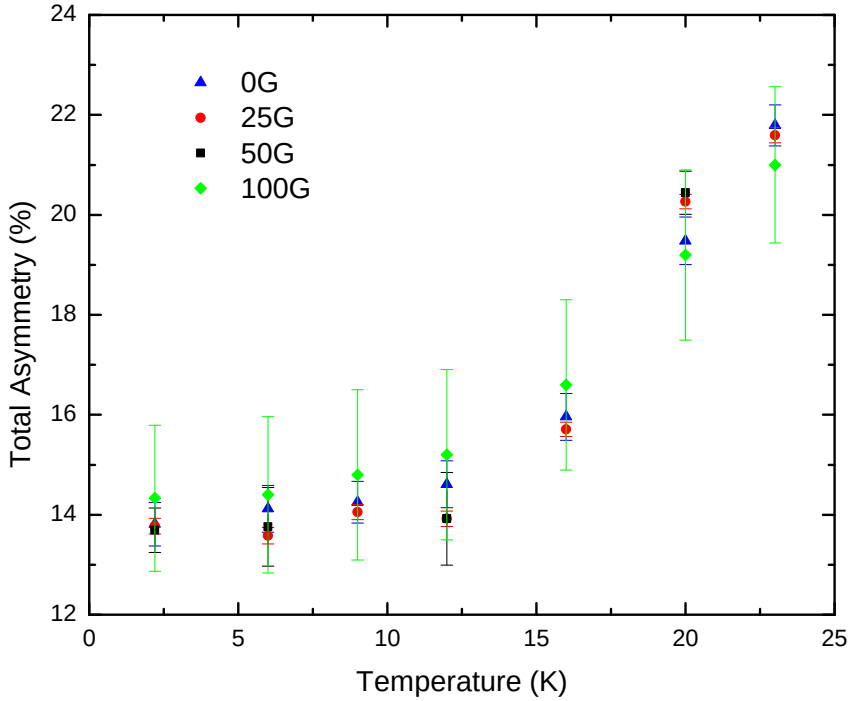

Figure 5.8: Total asymmetry of the low field (<100 G) dependent data as a function of temperature showing the sensitivity to the magnetic transition.

and results in an increased muon asymmetry. At short times if there is a very strong internal field there may be a very fast relaxation (outside of the time window of EMU) which will distort the relaxation slightly and increase the complexity of the data. With this in mind a temperature sweep in an applied field of 50 G was performed which will be discussed in the following section.

5.0.3 Temperature Sweep in 50 G Longitudinal Field

In an LF of 50 G a markedly different relaxation was observed to that of the ZF measurements as shown in figure 5.9. We found that the best fits to the data were obtained using a heavily damped oscillatory function that captured the behaviour at very short times:

$$G(t) = A_1 \exp(\lambda_1 t) \cos(\omega t + \phi) + A_2 \exp(\lambda_2 t) + A_{\mathrm{bg}} \tag{5.3}$$

where ϕ (fixed at 0.12) is the phase component. Similar to the ZF fits, the value of λ_2 was fixed at 0.03 μs^{-1} and the background asymmetry was set at 2.5%. The oscillation frequency was also fixed at 0.6 MHz ($\sim$ 44 G) which is related to the field experienced by the muon by $\omega = \gamma_\mu |\mathbf{B}|$, where γ_μ is the gyromagnetic ratio of the muon [2]. The damped oscillation is an indication that there are internal fields, larger than the applied LF, that are transverse to the initial muon spin polarisation. The value that is obtained for the frequency will be a vector sum of the internal fields experienced by the muon, explaining why the value of $\mathbf{B_{int}}$ is lower then the applied LF. The frequency calculated may relate more to the distribution of the internal static fields, where the applied LF has slowed down some of the dominant fluctuations within the material allowing the muons to sense a disordered static arrangement of spins. The fact that the oscillation is dephased quickly (i.e. is heavily damped) suggests that the muon is experiencing a significant distribution of static fields.

The values of λ_1 for the LF data shown in figure 5.10 are an order of magnitude larger then those of the ZF results indicating a very fast relaxation of the muon spins. However, what is striking is that, although the low temperature feature (T_{f}) is still present, the higher temperature peak is at 12-13 K, which a similar temperature to the divergence of the ZFC/FC magnetization curves shown in figure 4.11. It is therefore likely that, in an LF of 50 G, the muons are sensitive to a different relaxation process which may be due to the ferrimagnetic particles that have a coercive field larger than 50 G but smaller then 100 G as the evidence of an oscillation is not present in the LF 100 G spectra. The peak in λ_1 at 25 K may not be physically meaningful as we are above T_{C} and what this relaxation is capturing is the very fast relaxation at very short times. When looking at the magnetization data within the previous chapter there is nothing to suggest that we should observe

[2] It should be noted that $\omega = 2\pi\nu$ so if working with angular frequency, ω, γ_μ should contain the conversion to frequency

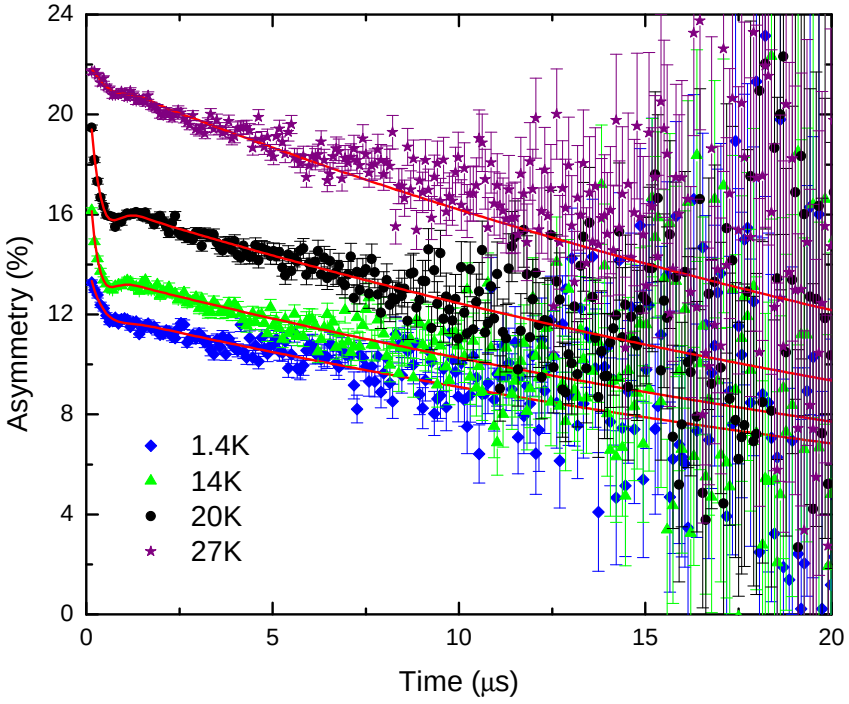

Figure 5.9: Time dependent μSR spectra with a 50 G LF where there is a complete decoupling of the nuclear component and the emergence of a heavily damped oscillation as T_C is approached. The lines are fits to the data using equation 5.3.

a feature above T_C. In fact what we might be observing is the external applied field magnetising the sample within the critical region which would distort the field distribution and fluctuation rates.

This again supports the conclusion for the LF data that the internal fields are approximately 100 G. The value of 0.6 MHz is not realistic for the response of the muon to a purely electronic component as it corresponds to a low precession frequency and thus rotation field, it may be that this fit is more empirical with the slow frequency capturing the dip in the data and the two Lorentzian relaxations describing the two distinct magnetic components. The total asymmetry (see figure 5.11) also shows a large change at approximately 12 K though A_2, for 50 G LF, shows a coupling to the ZF magnetic transition (20 K) indicating that this component has also undergone a change with a small applied field (see figure 5.3 for comparison).

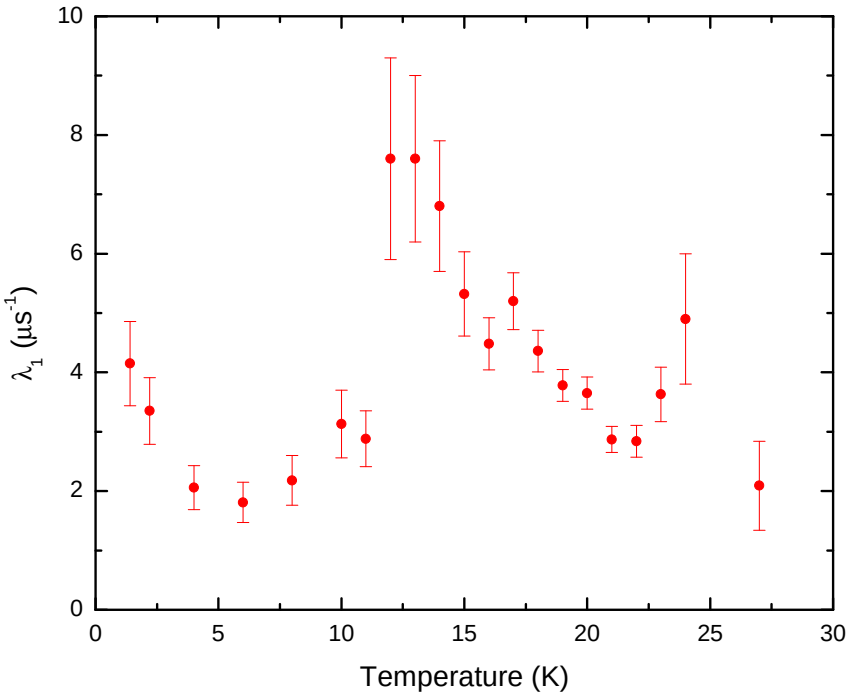

Figure 5.10: 50 G LF relaxation parameter λ_1, obtained from figure 5.9, as a function of temperature.

With an applied field of 50 G we are not only repolarising muons that are dephased by the nuclear magnetic fields but we are also perturbing the magnetism of the sample. Therefore this is why λ_1 is sensitive to the hysteretic behaviour of the material where, at 12 K we are observing a freezing out of magnetic fluctuations associated with the ferromagnetism. It should be noted that the sample was cooled in the absence of an applied field and this is supported by our ZFC magnetization data where we see a divergence of the ZFC/FC curves that correspond to hysteretic behaviour at approximately 15 K.

5.0.4 Discussion

An interpretation of the different muon stopping sites and the ferromagnetic glassy behaviour is that we are observing a relaxation from one muon that is stopping in

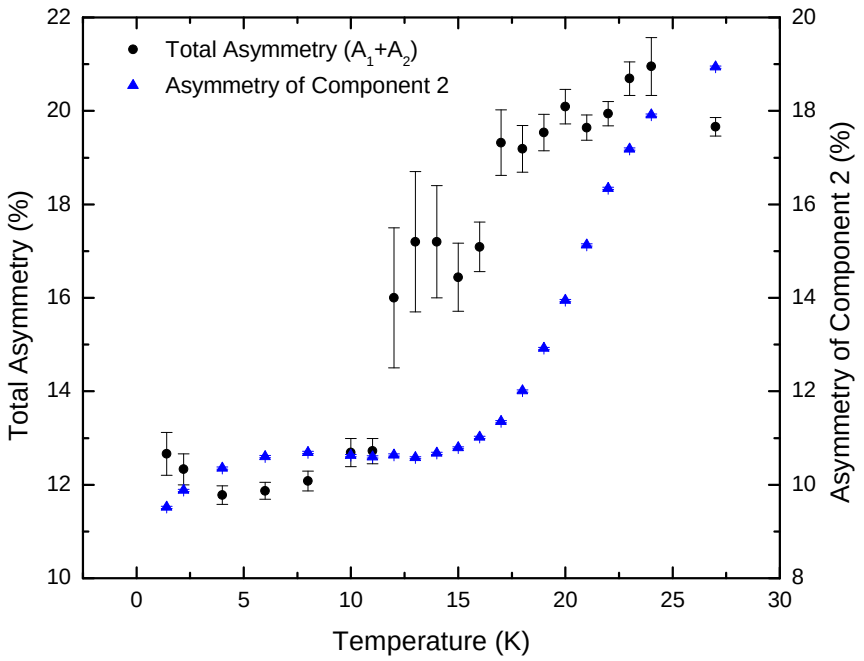

Figure 5.11: 50 G LF relaxing asymmetry and 2nd component asymmetry (A_2). Both parameters were obtained from figure 5.9.

the centre of a large particle and another that may be sensitive to the surface or walls between the particles in a system like a cluster glass (see section 2.2.1). If a muon were to stop in the centre of a particle the internal fields may be very large which would depolarise the muon too quickly and outside of the measurable time window at ISIS. If this were the case we would expect to see a $\frac{1}{3}$ tail in the asymmetry that would correspond to the magnetic component aligned along the z-direction, or initial muon polarisation. Ultimately the fixed λ_2 values may be the late time of this relaxation from the muons experiencing a very large internal field. A $\frac{1}{3}$ tail is not present in the raw data and hence another relaxation process dominates. These may be from muons that are stopped close to the surface or wall of the particles where the internal fields may be much weaker. The fact that λ_1 peaks at T_C in ZF shows that these muons are sensitive to the bulk magnetization of the ferromagnetic component when the material is entering an ordered magnetic phase. However, the LF sweeps show that there is a significant dynamical component present and the

muons are likely to experience motional narrowing by these fast fluctuating fields with no applied field.

Note that Clerac *et al.*. [24] concluded that the M[TCNQ]$_2$ system exhibited a magnetically glassy state below T_C. However, this μSR investigation suggests that the magnetic glassiness (at $T = 5$ K) may be due to the interaction of the magnetic particles where the system is behaving similar to a super spin glass [6] or a cluster glass where the dipolar fields from each individual magnetic cluster attempts to align its neighbours to minimise the energy, which may also lead to an element of frustration as can be seen in spin glasses. With the ferromagnetic transition at $\sim$20 K there is no evidence from the μSR data that there is a glassiness associated. A characteristic decay was not observed with Ni(TCNQ-D4)$_2$ where a stretched exponential could be fit to the data suggesting a range of time scales of the relaxation of the magnetism similar to that observed in spin glasses [7]. Therefore there are two distinct temperatures, a ferromagnetic transition ($T_C = 20$ K) and possibly a magnetic freezing temperature ($T_f = 5$ K) that can be attributed to the sample but the latter is unlikely to be related to magnetic frustration at an atomic level.

Application of a field of 50 G results in a heavily damped oscillation being observed, where the nuclear field component of the muon relaxation has been decoupled. These oscillations may be revealing the underlying magnetic ordering but since a standard KT function does not describe the data it is likely that the application of a 50 G field is actually affecting the sample itself and disturbing the internal magnetism. This may act to slow the magnetic fluctuations within the material where the two stopping sites described for ZF still exist. In fact applying a field would also be expected to align the large spins of the clusters and also the magnetic moments within the walls between these clusters/particles. The increase in the values of λ_1 indicates that the relaxation that the muon is sensitive to is very fast and that the application of the field has suppressed a slow relaxation. This fast relaxation is sensitive to a transition with a peak at 15 K, similar to the divergence of the ZFC/FC magnetization curves as well as a freezing temperature (5 K) which seems unaffected by the 50 G field.

An explanation of the μSR results presented so far may be obtained by considering the inorganic system, $GdPO_4$. A bulk sample was studied using μSR where a static component was observed that shows a T_C of approximately 1 K. However when nanoparticles are made of $GdPO_4$ the muon relaxation observed has both a static and dynamical component to it. The static component shows a reduced T_C which is expected with nanoparticulate systems [8] and is modelled by a static KT function. The dynamic component persists down to 40 mK and is best described by a single exponential relaxation where below 0.7 K bulk magnetic ordering is observed. The main difference is that there is another peak in λ at a lower temperature where the parameter increases at 0.4 K which Evangelisti *et al.*. have attributed to a spin freezing effect where the nanoparticulate system moves into a quasi-static regime from inter particle interactions [9]. $GdVO_4$ nanoparticles were also synthesised where similar behaviour was observed, however the spin freezing peak in λ was much less pronounced which is suggested to be due to more magnetic disorder within this quasi-static regime [9]. This may support the similar behaviour seen within the Ni(TCNQ-D_4)$_2$ system where the increase in the ZF λ_1 parameter is attributed to a spin freezing temperature or the material entering a quasi-static regime. However from the SEM images it is likely that the Ni(TCNQ-D_4)$_2$ material may not strictly be nanoparticulate.

Another comparable inorganic system is that of $La_{0.7}Pb_{0.3}(Mn_{1-x}Fe_x)O_3$ (LPMFO) where $0 \leqslant x \leqslant 0.2$ [10]. Within this system there are two forms of exchange that compete and as x increases this increases the disorder within the material which pushes down the critical temperature. When $x = 0.2$ the FC magnetization data shows a flat top below T_C which is consistent with a spin glass or in this case a cluster glass. μSR measurements on an undoped sample show changes in the relaxation and asymmetry as the sample goes through T_C. However, when doped with Fe the behaviour changes and not only is a peak that is associated with the transition observed but a second peak appears at lower temperatures which is attributed to spin freezing of magnetic clusters. As the disorder is increased within the system both T_C and the spin freezing peak shift to lower temperatures and ΔT between them increases. Below this spin freezing temperature the moments go from

a dynamic to a static disordered regime where ferromagnetism is observed through a percolation type behaviour. This model fits in more with the picture of our sample where we believe disorder may play an important role in producing the magnetic properties of the system. If the impurities within $Ni(TCNQ)_2$ are essentially defects which act to pin domain boundaries then we may be observing the bulk magnetic transition in the centre of these domains or magnetic clusters. The ferromagnetism is then induced in the whole material by a percolation transition and below 5 K the material enters a static disordered regime whereby the magnetic clusters can interact as the spin fluctuations, which are measured in ZF by λ_1, freeze out. Similar spin freezing effects are seen within $Ca_3Co_{2-x}Mn_xO_6$ with $x = 1$, which behaves like a cluster glass and the value of λ increases rapidly as the temperature is cooled through the spin freezing transition where the magnetic clusters lock into a random configuration and the moments become quasi-static [11].

5.1 Aged Sample

5.1.1 ZF Muon Spin Relaxation Measurements

μSR experiments were conducted on the sample after it aged for 20 months to study the effect on the magnetic transition in the material. The sample behaves in a similar way to the fresh sample (see section 4.5), but we will show that the data support the observation of a decrease in the critical temperature along with a transition region that has become sharper, where the width of the peak in λ is approximately 4 K, see figure 5.13. The raw data are shown in figure 5.12 where above the T_c the data can be fit using two Gaussian relaxations, similar to the fresh sample, which indicates that there are at least two muon stopping sites.

Below the T_c the data are described well by an addition of two single exponential relaxations with a baseline of 2.5%. Once again, a fixed value of $\lambda_2 = 0.03\ \mu s^{-1}$ was used to describe the missing asymmetry from strong internal fields that dephase the muon spins out of the time window of the measurements and where we are possibly

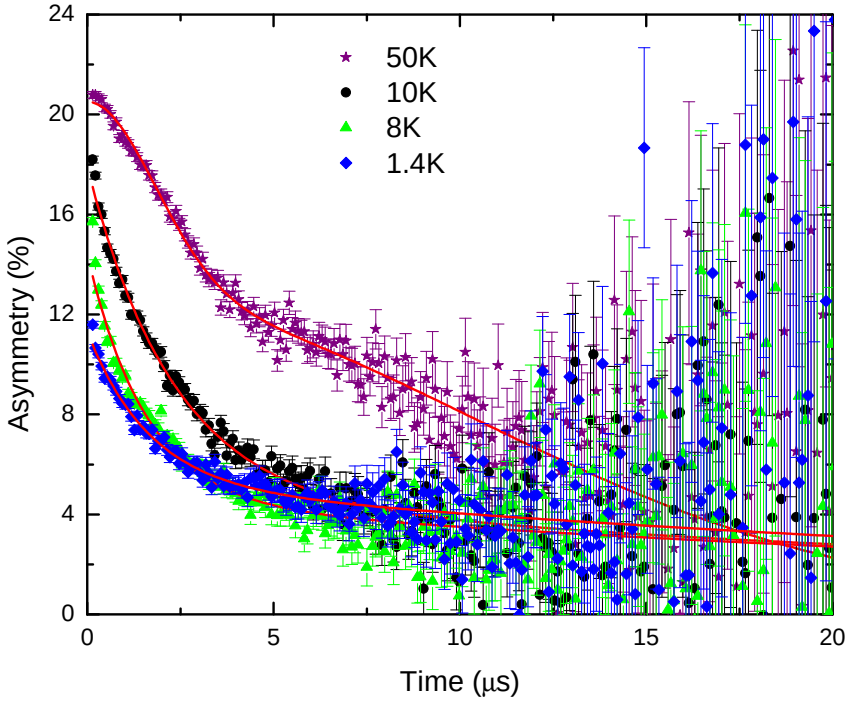

Figure 5.12: ZF μSR raw data at selected temperatures above and below T_C for a Ni(TCNQ-d4)2 sample aged for 20 months.

detecting the end of this relaxing component. λ_1 is shown in figure 5.13 where the reduction in T_c can be clearly seen and the sharpening of the transition occurs also on the local length scale probed by the muons.

Figure 5.13 shows that, although the magnetic transition has changed, the freezing temperature at approximately 5 K, which was discussed in the previous section, has not been affected over time. In the fresh sample the freezing temperature was attributed to freezing out of the magnetic clusters from interparticle or inter-cluster interactions which have not changed in the aged sample. Since there is no change, the possible dipole-dipole interaction between magnetic clusters that leads to frustration and a glassy groundstate must suggest that these clusters still exist. However, due to the absorption of water by the sample, these clusters may not be the same size. It is worth noting that if the magnetic clusters were simply reduced in size by the absorption of water this would be accompanied by a decrease in moment and thus

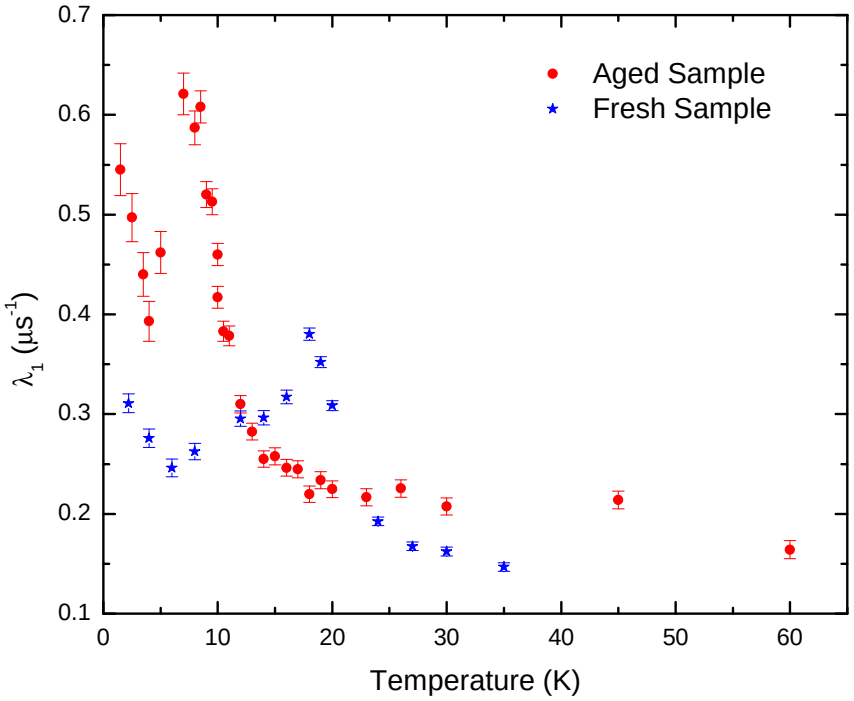

Figure 5.13: ZF λ_1 vs. temperature comparing results for the fresh sample and after it had aged for 20 months.

a decrease in the dipolar interactions. For this reason the data at low temperatures are hard to interpret but could mean that the muons are sensitive to areas that have perhaps not absorbed a significant amount of water, i.e. being located next to sites that show dynamic behaviour within the centre of a crystallite.

5.1.2 Longitudinal Field μSR Experiment on the Aged Sample

A LF was applied to assess whether the sample, aged for 20 months, behaved in a similar fashion to the fresh sample. The data could be separated, in a similar way to the fresh sample, into two regimes; above 100 G LF and below/equal to 100 G LF. Above 100 G LF the raw data could be described by a single exponential relaxation with an average value of $\lambda = 0.25 \pm 0.02$ μs^{-1}, with the total asymmetry increasing

with LF; see figure 5.14 (the raw data can be seen in figure A.2 for 6 K) . Although the errors are large, it appears that a full fraction is not reached even at 4500 G, which suggests that a significant dynamical contribution to the depolarization is still present within this system. If the relaxation rates can be assumed to be proportional to the inverse of the fluctuation rate of the moments within the sample, the increase for the aged sample implies that these fluctuations in an applied field are slower then in the fresh sample. If the paramagnetic fraction of the sample has increased dramatically then these paramagnetic moments will also have a larger dynamical component within an applied field than within a ferromagnetically ordered solid (akin to the fresh sample).

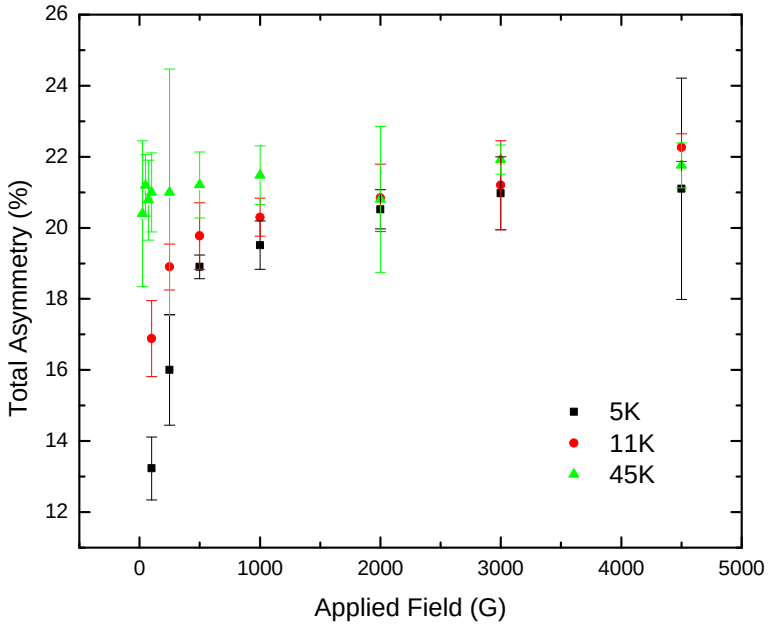

Figure 5.14: Total asymmetry vs. applied LF for the aged sample where LF$\geqslant$100 G.

The low field (LF$\leqslant$100 G) raw data at 5 and 11 K could not be fit using a single exponential and so a dynamical KT function was used, similar to the fresh sample (see section 4.5.2), where the electronic fluctuations were able to be determined when fitting between 0 - 5 μs. Though the fluctuations generally show similar behaviour with temperature, the aged sample exhibits a fluctuation rate is that lower than the fresh sample. This suggests that by the sample aging these fluctuations are becoming

suppressed and the material may be more ordered which constrains behaviour of the magnetic moments and their associated dynamics.

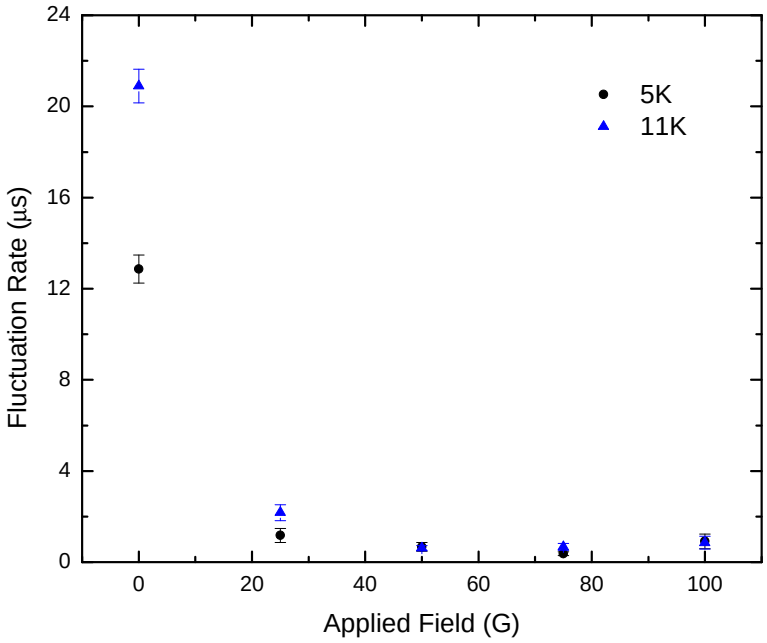

Figure 5.15: Low Field (<100 G) LF fluctuation rate from fits to a dynamical KT function for the aged sample.

5.1.3 50 G Longitudinal Field Temperature Dependence

When a 50 G LF was applied to the aged sample a heavily damped oscillation was present within the transition region (see figure 5.16), similar to that observed in the fresh sample.

The data were fit to the same function as the fresh sample (equation 5.3) with ν=0.6 MHz, A_{Bg}=2.5% however λ_2=0.06 μs^{-1}. This difference in the λ_2 value is possibly attributed to the ageing of the sample and may be due to the increased paramagnetic fraction (from water absorption) within the sample. However, this relaxation itself is likely to be outside of the EMU instrument's time window and there is little information we can gain from it.

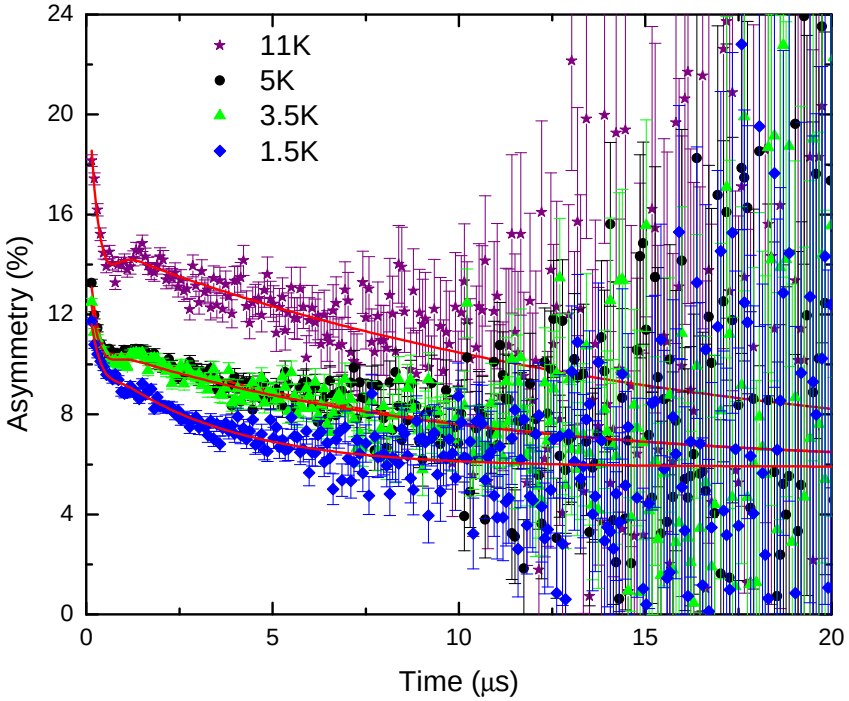

Figure 5.16: Time dependent spectra of the relaxation with an applied 50 G LF at temperatures above and below T_C.

At 11 K there may be evidence of an oscillation that is not damped after the first peak, however it is very weak. This would point to increased ordering or less of a spread of fields/damping compared to the fresh sample. The fact that we still observe this heavily damped oscillation suggests the muon relaxation mechanism is similar to the fresh sample and at 50 G we decouple any relaxation due to the nuclear moments. We do not have enough data points to draw conclusions from the values of λ_1 (see figure B.2) as one cannot pick out the transition region thus more data are needed. The asymmetry shows that the muons are sensitive to the magnetic transition which is at a lower temperature than in the fresh sample with a 50 G LF applied (see figure 5.17). Note that the asymmetry of component 2 is coupled to the transition and is of the same order of magnitude as the fresh sample where this relaxation begins to dominate as the temperature increases, however as pointed out more data are needed within the transition region to probe this further and draw conclusions.

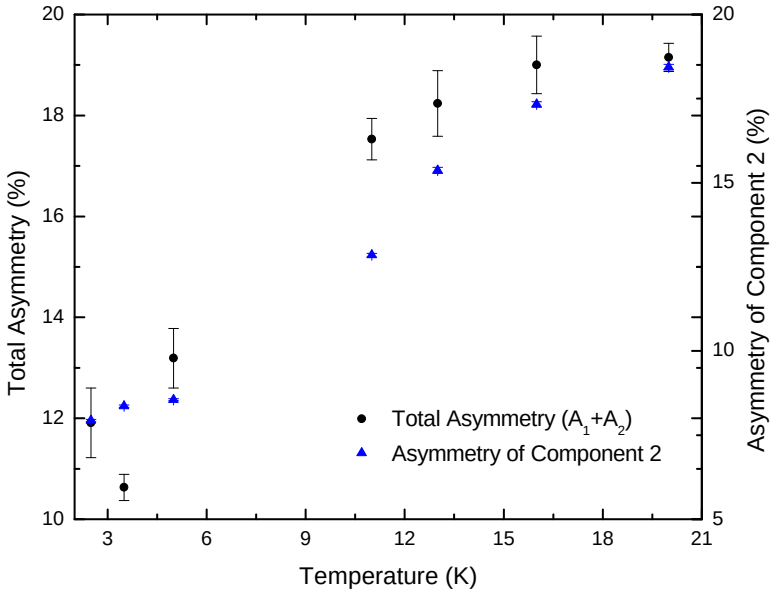

Figure 5.17: Total relaxing asymmetry and the asymmetry of the 2nd component with an applied LF of 50 G.

5.1.4 Discussion

From the evidence presented above, it appears that the aged sample behaves in a similar manner to the fresh sample, however the T_C has shifted significantly as the sample ages. This is most likely due to magnetic exchange pathways being altered or broken leading to a decrease in T_C which has been shown in the previous chapter to be due to absorption of water into the structure where the hydrated salt is paramagnetic and shows no bulk ordering. The sample is similar to the fresh sample in that there are at least two muon stopping sites where the value or spread of internal field will differ. This leads to the complex relaxation seen in ZF where an addition of two single exponential relaxations are needed to describe the data. The interpretation of two muon stopping sites, proposed for the fresh sample, still stands as λ_1 again describes a muon decaying in the wall of a magnetic cluster. At that position there is a significant dynamical component to the local magnetism and the magnetic glassy freezing temperature remains the same for both the fresh and aged sample and in both cases this is attributable to the interaction of these magnetic

clusters/particles.

For the ZF data the value for λ_2 is similar to that of the fresh sample suggesting that, if this is from the same relaxation with a muon located at the centre of the magnetic cluster, the large internal field is still present that dephases the muons outside of the experimental time window and we only detect the end of this very fast relaxation. We also observe no $\frac{1}{3}$ tail which means that there is evidence for fluctuations of the magnetic moments that are depolarizing the muon spins.

When an LF is applied, again we see that at 4500 G a full fraction is almost reached ($\sim$21%), although the uncertainties are large (errors are 4% at high T and 15% at 5 K of the total values) preventing firm conclusions. It is likely however that a significant dynamical magnetic component is still present in the sample even in the presence of a high LF. When applying an LF of 50 G a heavily damped oscillation is observed that is consistent with the results from the fresh sample and similar parameters can be used to fit the data in both cases. Also, the muons are sensitive to the magnetic transition in the material, regardless of age. However, in the aged sample there may be evidence of an oscillation at 11 K that is not observed in the fresh sample and though the data are not good enough to be able to get a decent fit a rough estimate of the period of oscillation suggests an internal field of approximately 37 G. The interpretation of the 50 G LF data is similar to the fresh sample where applying the field is having an effect on the electronic magnetism of the sample itself and the muons are detecting the ordering of the magnetic clusters with respect to each other. Since when LF = 50 G a very slow relaxation is needed to fit the data, this means that λ_2 is still present and the values of 0.06 μs^{-1} are twice as large as those of the fresh sample. This difference may be due to the absorption of water by the sample which leads to a higher paramagnetic fraction and we assume that the fluctuation rate should be the same for both samples and it is Δ (see chapter 2 for the theory behind μSR), the field distribution, that must change. For the aged sample this value of Δ will be smaller than for the fresh sample suggesting that the spread of internal fields is decreasing. We also observe no $\frac{1}{3}$ tail which means that, once again, there is evidence for fluctuations of the magnetic moments which

are depolarising the muon spins, however this may be expected if there are more paramagnetic species within the sample and so the muons will detect a motionally narrowed paramagnetic state.

5.2 Pressure Dependence

Preliminary measurements were conducted on the GPD spectrometer at PSI where a Ni(TCNQ-D_4)$_2$ sample was put under an applied pressure up to 11 kbar. TCNQ salts are well known for interactions between the TCNQ anions themselves through $\pi - \pi$ overlap [5, 12, 13]. Within Ni(TCNQ)$_2$ if there are TCNQ-TCNQ interactions then applying pressure may force these units closer together, which can have dramatic effects on the magnetism where ferromagnetic interactions can become antiferromagnetic or change to more exotic forms of magnetism [14–16].The aim of the experiment was to explore whether we could increase the interactions between the TCNQ molecules and create changes in the magnetism within the sample.

The ZF raw data obtained from these pressure measurements on Ni(TCNQ-D_4)$_2$ were fitted with a sum of a Gaussian Kubo-Toyabe function and a single exponential:

$$G(t) = A_1\left(\frac{1}{3} + \frac{2}{3}(1-\Delta^2 t^2)\exp(-\Delta^2 t^2)\right) + A_2\exp(-\lambda t) \tag{5.4}$$

and the temperature dependence of relaxation parameter, λ, is shown in figure 5.18. The Kubo-Toyabe function is sued to describe the CuBe pressure cell where Δ=0.33 MHz, samples of raw data can be found within the appendix.

The asymmetry values (not shown here) are unphysical and within error are very similar at each temperature and pressure of approximately 35-40%, for GPD a full fraction would be 28%. The reason for these unphysical values may be due to the relaxation of the muons being a convolution of both the background and the sample itself. The background was a CuBe cell which should have a well defined relaxation below approximately 40 K that can be described by a Kubo-Toyabe function due to

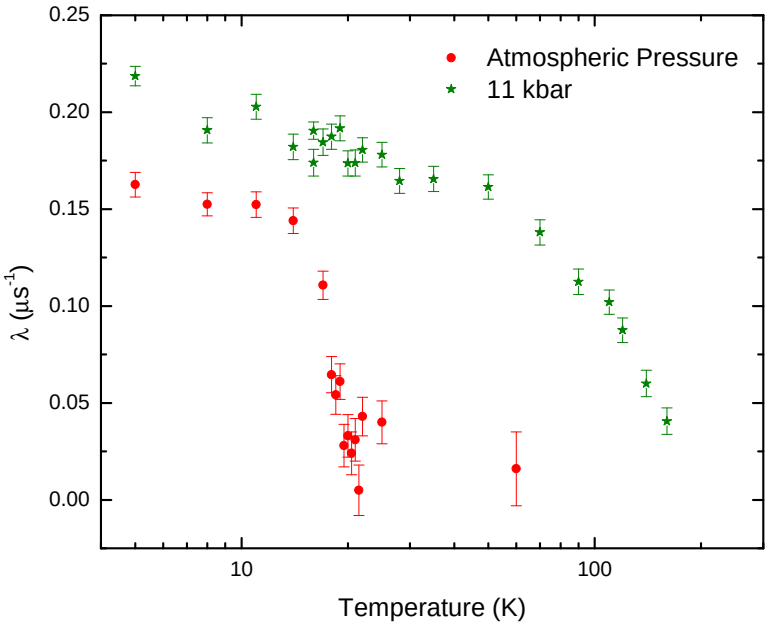

Figure 5.18: ZF λ vs. temperature at atmospheric (green triangles) and with an applied pressure of 11 kbar (red circles) for a fresh sample of Ni(TCNQ-d4)$_2$.

the relaxation of muons from the nuclear spins on the Cu. However, the background does display a temperature dependence at higher temperatures which is shown in figure B.5. This signal does change as a function of temperature but, at low temperatures, the electronic magnetism within the sample was enough to dominate the muon relaxation. However the λ parameter is showing a relaxation that is half of the rate measured in the experiments on EMU at ISIS when compared with the data in figure 5.4. Within the GPD experiment, where the muons implant is dependent on their momentum; too much or too little momentum and they may miss the sample and implant in the CuBe cell. For the Ni(TCNQ-D$_4$)$_2$ experiment, this may have been the case where the muons were implanting in the sample holder, even though their momentum was adjusted to optimise relaxation from the sample. Nevertheless, the largest contribution to their depolarisation was from the dipolar fields present within the Ni(TCNQ-D$_4$)$_2$, which is why a transition is observed in ZF and with no applied pressure. However when 11 kbar pressure was applied the temperature dependence of the relaxation parameter became qualitatively different (see figure

5.18) and although λ is of the same magnitude as the zero applied pressure experiment, there is some evidence of an anomaly at a much higher temperatures. As the temperature increases the background becomes harder to model as it is a convolution of sample plus background. The trend in the data matches what is observed in the background which suggests that by applying pressure the sample has changed either to a paramagnet or the transition temperature is pushed to low temperatures outside of what we can measure. To support any conclusions more information is needed from additional experiments which takes into account the large background and also any centring issues with the sample.

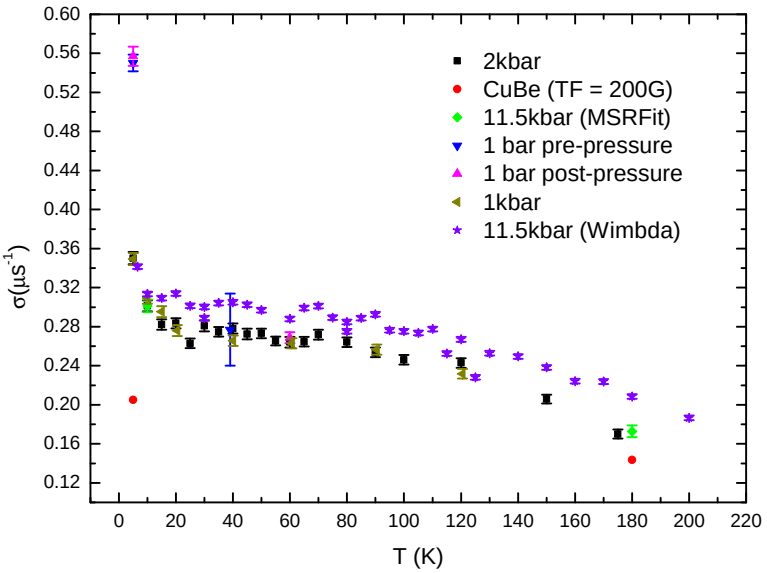

Figure 5.19: TF relaxation vs. temperature at different applied pressures for a fresh sample of Ni(TCNQ-d4)$_2$.

A further experiment was conducted under an applied transverse field where the results can be seen in figure 5.19. To fit the data a oscillatory component with a Gaussian relaxation with an added background term was used. The data under an applied pressure of 2 kbar and 11.5 kbar follow the same trend where there is a decrease in the relaxation rate as the temperature increases which is likely due to the change in the relaxation within the sample holder. At low temperatures the data show no evidence of a transition and instead the material looks more like a

paramagnet. The data were fit using different programs which have been labelled in brackets in the legend of the graph, MuSR is the PSI data analysis software and Wimda is used at ISIS. As a pressure is applied the large relaxation occurring at the lowest temperatures is suppressed suggesting that the sample losing its ferromagnetic properties. However, pressure-dependent magnetic and diffraction experiments are needed to confirm this result as it may be that application of pressure can induce crystalline order within the system which in turn cause a loss in the magnetic properties of the sample.

The sample seems very robust as magnetization data was collected after the pressure-dependent μSR experiment which showed that the ferromagnetic transition had not been significantly affected as is shown in figure 5.20. The sample used was different to previous μSR experiments as a fresh sample was synthesised using the same method. The slight shift in T_C and the absence of a cusp in the ZFC data is unlikely to be due to the implantation of muons but may be a consequence of the application of pressure which could increase the order within the system and so there is less of a glassy component.

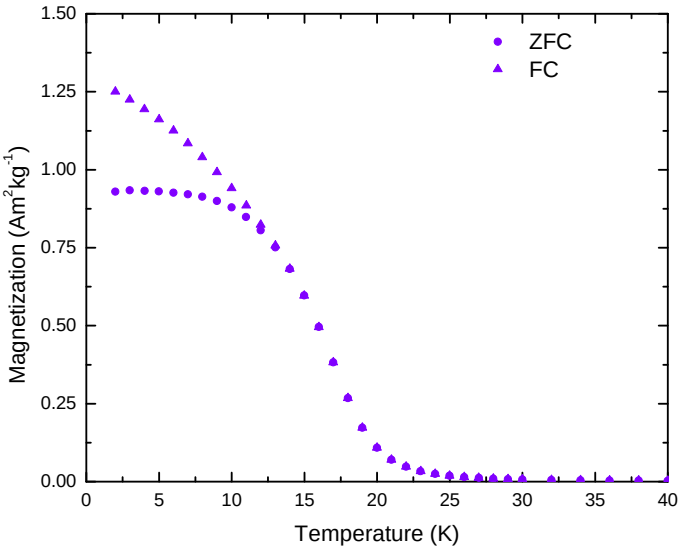

Figure 5.20: Magnetization vs. temperature for a Ni(TCNQ-D_4)$_2$ sample after exposure to a muon beam and applied pressure of 11 kbar where B_{app} = 25 G.

5.3 Conclusion

A sample of Ni(TCNQ-D_4)$_2$ was studied using μSR where both fresh and aged samples were measured. The sample is shown to undergo a magnetic transition to a ferromagnetic state under no applied field which is accompanied by a dramatic drop in the muon asymmetry, however we do not see the value fall to $\frac{1}{3}$ suggesting that there may still be some dynamical processes present and contributing to the decay of the muon spin polarisation. The ZF raw data can be separated into two relaxations, a faster dynamic component, λ_1, and a longer, slow relaxation, λ_2, which is attributed to muons implanting in a region of higher magnetic homogeneity leading to an internal field that dephases the muon outside of the time window for the experiment. The dynamic relaxation, λ_1, shows a peak associated with the bulk transition, however the relaxation also begins to diverge at 5 K which is suggested to be a due to a spin freezing effect from the interaction of magnetic clusters created by inhomgeneities within the sample. λ_2 is also shown to be coupled to the transition as the associated asymmetry shows a temperature dependence that correlates to the transition region.

Applying a longitudinal field decouples the nuclear moments of the nitrogen atoms and at fields above 100 G there is a dramatic change where the relaxation becomes very small. However, since a full fraction is not completely recovered up to 4500 G this highlights that there are significant dynamics within the system. On application of a 50 G LF the nuclear component is completely decouple which reveals a small, heavily damped oscillation where the corresponding internal field, transverse to the initial muon polarisation, is estimated to be approximately 44 G. The relaxation rate changes dramatically, increasing by an order of magnitude, suggesting that the muons are sensitive to a different relaxation mechanism which peaks at the divergence of the ZFC/FC magnetization curves and so one can assume that by applying the field we are sensitive to the hysteric magnetic behaviour of the sample. Not only this, but the application of the applied field may also be effecting the sample itself. However what is clear is that there are both static and dynamic fields at both zero-field and with an applied LF.

The aged sample also behaves in a similar manner to the fresh sample, however the long, slow relaxation, λ_2 has changed which may be due to the increased paramagnetic fraction from the absorbance of water leading to the formation of the hydrated sample. λ_1 shows the transition has shifted to a lower temperature consistent with the magnetic data. The LF data suggests a similar conclusion of both static and dynamic fields within the sample.

From preliminary experiments at PSI, where pressure was applied to the sample, there is evidence that the critical region may be pressure sensitive with a shift to either low temperatures or a change in magnetism to a paramagnetic phase. There were issues with the experiment itself as the background is large compared to the relaxation of muons inside the sample itself and so more detailed scans are needed in order to tune the momentum and height to make sure the majority of muons are implanted within the sample and not the CuBe pressure cell. The values of the relaxation is smaller at PSI suggesting that perhaps experiments are needed at ISIS where we can access longer times rather then studying the short time scale.

Overall the studied metal-organic magnet shows that deuteration has proved a powerful tool in changing the magnetism within the sample. The interaction of the muon with the nuclear spins on the organic molecule is believed to be reduced as deuterium has a much smaller moment then hydrogen and we were able to observe the bulk magnetic transition which appears to be second order on a local scale where there is no evidence of any first order transitions associated with dimerisation with the TCNQ anions [17]. Using μSR we have shown that there is both a static and dynamic component to the magnetism where at low temperatures (5 K) another relaxation process is observed which is believed to be a spin freezing effect which may be the cause of the glassy magnetic behaviour within the material. The freezing may be due to the dipolar interaction of magnetic clusters which are created from inhomogenities within the sample.

Bibliography

[1] S. L. Lee, S. H. Kilcoyne, and R. Cywinski, eds., *Muon Science: Muons in Physics, Chemistry and Materials* (Institute of Physics Publishing, London, 1998)

[2] Personal communication with Francis Pratt, ISIS, RAL

[3] F. L. Pratt, S. J. Blundell, Th. Jestädt, B. W. Lovett, R. M. Macrae and W. Hayes. *Magn. Reson. Chem.* **38** (2000) S27

[4] F.L. Pratt *Physica B.* **710** (2000) 289

[5] B. W. Lovett, S. J. Blundell, F. L. Pratt, Th. Jestädt, W. Hayes, S. Tagaki and M. Kurmoo. *Phys. Rev. B.* **61** (2000) 12241

[6] M. Ulrich, J. Garcia-Otero, J. Rivas, and A. Bunde. *Phys. Rev. B.* **67** (2003) 024416

[7] I. A. Campbell, A. Amato, F. N. Gygax, D. Herlach, A. Schenk, R. Cywinski, and S. H. Kilcoyne. *Phys. Rev. Letts.* **72** (1994) 1291

[8] J. Park, E. Lee, N. Hwang, M. Kang, S. C. Kim, Y. Hwang, J. Park, H. Noh, J. Kim, J. Park, T. Hyeon. *Angew. Chem. Int. Ed.* **44** (2005) 2872

[9] M. Evangelisti, T. G. Sorop, O. N. Bakharev, D. Visser, A. D. Hillier, J. J. Alonso, M. Haase, L. A. Boatner and L. Jos de Jongh. *Phys. Rev. B.* **84** (2011) 094408

[10] J. Gutiérrez, F. J. Bermejo, J. M. Barandiarán, S. P. Cottrell, P. Romano, C. Mondelli, J. R. Stewart, L. Fernández Barquín and A. Peña. *Phys. Rev. B.* **73** (2006) 054433

[11] T. Lancaster, S. J. Blundell, P. J. Baker, H. J. Lewtas, W. Hayes, F. L. Pratt, H. T. Yi and S. W. Cheong. *Phys. Rev. B.* **80** (2009) 020409

[12] Y. Leprine, A. Caille and V. Larochelle. *Phys. Rev. B.* **18** (1978) 3585

[13] J. S. Pedersen, K. Carneiro and M. Almeida. *J. Phys. C: Solid State Phys.* **20** (1987) 1781

[14] K. Takeda, M. Mito, K. Kinoshita, M. A. Novak, J. L. Tholence and A. Rassat. *Polyhedron* **22** (2003) 2287

[15] G. Levchenko, V. N. Varyukhin, L. V. Berezhnaya and V. F. Rusakov. *J. Phys.: Condnes. Matter.* **24** (2012) 166002

[16] Z. J. Huang, F. Chen, Y. T. Ren, Y. Y. Xue, C. w. Chu and J. S. Miller. *J. Appl. Phys.* **73** (1998) 6563

[17] S. J. Blundell, F. L. Pratt, P. A. Pattenden, M. Kurmoo, K. H. Chow, S. Takagi, Th. Jestädt and W. Hayes. *J. Phys.: Condens. Matter* **9** (1997) L119

Chapter 6

KTCNQ - A Further Study of an Organic Based Spin Peierls System

6.1 Introduction

A brief introduction to metal-organic magnetism was given in Chapter 4 which discussed the magnetism of a nickel-TCNQ based compound. This chapter will briefly explore a preliminary study of a TCNQ based spin-Peierls system with the inclusion of some magnetic susceptibility measurements and μSR studies.

A Peierls transition is a lattice distortion in one dimension where the uniform ordering atoms or molecular units within the crystal structure distort, which can result in a dimerisation of units with two distances created; an intra-dimer spacing and an inter-dimer spacing. This transition is linked to the energy gained by the pairing up of the dimers and also the electron-phonon coupling where $T_p \sim \frac{E_F}{k_B} \exp(-1/\lambda_{e-ph})$ where λ_{e-ph} is the electron-phonon coupling constant and E_F is the Fermi energy. A spin-Peierls (SP) transition is a magneto-elastic effect where the spins of magnetic units (in this case dimers) in a Heisenburg 1D chain are antiferromagnetically coupled in their groundstate where $T_{sp} \sim \frac{|J|}{k_B} \exp(-1/\lambda_{s-ph})$ where J is the magnetic exchange coupling between adjacent spins and λ_{s-ph} is the spin-phonon coupling constant. This will lead to a second order phase transition that should be detectable in

the magnetic susceptibility.

For a simple chain of magnetic ions ($S = \frac{1}{2}$) where the ions are equally spaced and antiferromagnetically coupled in one dimension the Hamiltonian to describe the interaction in zero field is

$$\mathbf{H} = -J \sum_{i=1}^{n-1} \mathbf{S}_{Ai} \cdot \mathbf{S}_{Ai+1}, \tag{6.1}$$

where the summation is over the n-sites in the chain. Bonner and Fisher [1] addressed this problem and obtained a numerical form of the susceptibility. Their results were subsequently fitted by Estes *et al.* [2] with the expression:

$$\chi = \frac{Ng^2\mu_B^2}{k_BT} \frac{0.25 + 0.074975x + 0.075235x^2}{1 + 0.9931x + 0.172135x^2 + 0.757825x^3}, \tag{6.2}$$

where

$$x = \frac{|J|}{k_BT}. \tag{6.3}$$

Bonner and Fisher also demonstrated that the calculated susceptibility will have a low temperature limit as within a chain system with a singlet groundstate when n is an odd number there will exist $S = \frac{1}{2}$ doublets that will cause the susceptibility to diverge as $T \rightarrow 0$ [1].

Below an SP transition the magnetic ions are no longer equally spaced and a situation with alternating exchange constants arises. The spin Hamiltonian now becomes

$$\mathbf{H} = -J \sum_{i=1}^{\frac{n}{2}} [\mathbf{S}_{A_{2i}} \cdot \mathbf{S}_{A_{2i-1}} + \alpha \mathbf{S}_{A_{2i}} \cdot \mathbf{S}_{A_{2i+1}}], \tag{6.4}$$

where α is a parameter to describe the degree of dimerisation of the singlet-triplet state; for $\alpha = 1$ this corresponds to a uniform chain where as when $\alpha = 0$ this corresponds to isolated pairs in a singlet groundstate. As $T \rightarrow 0$, $\chi \rightarrow 0$ in this

low temperature regime where a gap in the magnetic excitation spectrum opens up which is at its maximum when $T = 0$ K [3].

Below T_{SP} Bulaevskii derived a formula to simulate the susceptibility of the sample in its dimerised state [4]:

$$\chi(T) = \frac{Ng^2\mu_B^2}{k_B}\frac{\alpha(T)}{T}\exp\left(-\frac{2[1+d(T)]J\beta(T)}{T}\right), \tag{6.5}$$

where

$$d(T) = \frac{\delta(T)}{2pJ} \tag{6.6}$$

and $p \approx 1 + \frac{2}{\pi}$. α and β are tabulated in Bulaevskii's original paper [4]. The result stems from calculations involving a system with a different degree of dimerisation, as T increases the degree of dimerisation decreases as the system moves into a state of uniform distant magnetic chains.

One of the first compounds documented to exhibit an SP transition is the donor-acceptor compound $[\mathrm{TTF}]^+[\mathrm{CuS_4C_4(CF_3)_4}]^-$ (where $\mathrm{TTF}^+ = $ tetrathiafulvalene) [5]. Below 12 K the sample undergoes a second order phase transition where the TTF cations ($S = \frac{1}{2}$) interact to form dimers in a singlet groundstate. This occurs along the c-axis within the sample and essentially creates a quasi 1D chain of magnetic ions. It is believed that antiferromagnetic (AF) interaction of the TTF cations is mediated through superexchange via the diamagnetic anion. From a fit to the data above T_{SP} using the method derived by Bonner and Fisher [1], $J/k_B = -77 \pm 2$ K and using a method described by Pytte [6] the gap in the magnetic excitation spectrum at T=0 K is estimated to be 21 K [5]. Another organic based conventional Peierls system was discovered in 1989 by Obertelli *et al.et al.*, α'-$(\mathrm{BEDT\text{-}TTF})_2X$, where $X = \mathrm{AuBr_2}$, $\mathrm{CuCl_2}$ or $\mathrm{Ag(CN)_2}$ [7] and BEDT-TTF = bis(ethylenedithio)tetrathiafulvalene. However below 7 K the $\mathrm{Ag(CN)_2}$ sample showed a sharp decrease in its magnetic susceptibility that was thought to be associated with an SP transition where there is a dimerisation of dimers formed in the

conventional Peierls transition, creating a spin coupled tetramer.

Of interest to the research within this thesis are systems involving magnetism of TCNQ based materials. Another class of interesting SP compounds are the alkali-TCNQ salts which are stoichiometric and each TCNQ molecule has the charge of $-|e|$. Na, K and RbTCNQ show phase transitions at 348, 395 and 381 K respectivly where a dimerisation of the radical bearing TCNQ units occurs which leads to a singlet groundstate [8,9]. The crystal structure of KTCNQ has been solved at both high and low temperatures, which in both cases is monoclinic, where the structure undergoes a first order phase transition where displacement of the TCNQ anions is observed leading to a dimerisation. The TCNQ molecules stack along the a-axis where in the high temperature phase there is an equal interspacing distance of 3.479 Å that changes to alternating spacing of 3.237 Å and 3.567 Å through the phase transition [10]. Lépine *et al.* [11] studied the SP transition in the KTCNQ salt further where they analysed the data using a method derived by Bonner and Fisher [1] and Bulaevskii [4]. The temperature dependent susceptibility of KTCNQ, measured by Lépine *et al.* [11] and Vetger *et al.* [8], is shown in figure 6.1.

In the high temperature phase the data were fit using a method similar to Pytte [6] where the exchange integral is a function of temperature so

$$J(T) = J'(T)[1 \pm \delta(T)] \tag{6.7}$$

The change in J is a result of the lattice distortion and depends on the thermal expansion/contraction of the TCNQ stacks. Lépine *et al.* calculated that when $T =$ 460 K, $J' = -1950$ K and at 396 K $J' = -2280$ K indicating the exchange constant is also a variable in a system where one observes a singlet to triplet gap opening up.

Below T_{SP} the TCNQ anions are inclined at angles of 15.8° and 11.3° to the (100) plane where as at high temperatures they are both at an angle of 8.9°. The structural transition is first order, however the magnetic transition from the dimerisation of the spins is second order [9]. For the average position of the TCNQ anions there are two potential wells that can be occupied, at high temperatures this is a sharp and

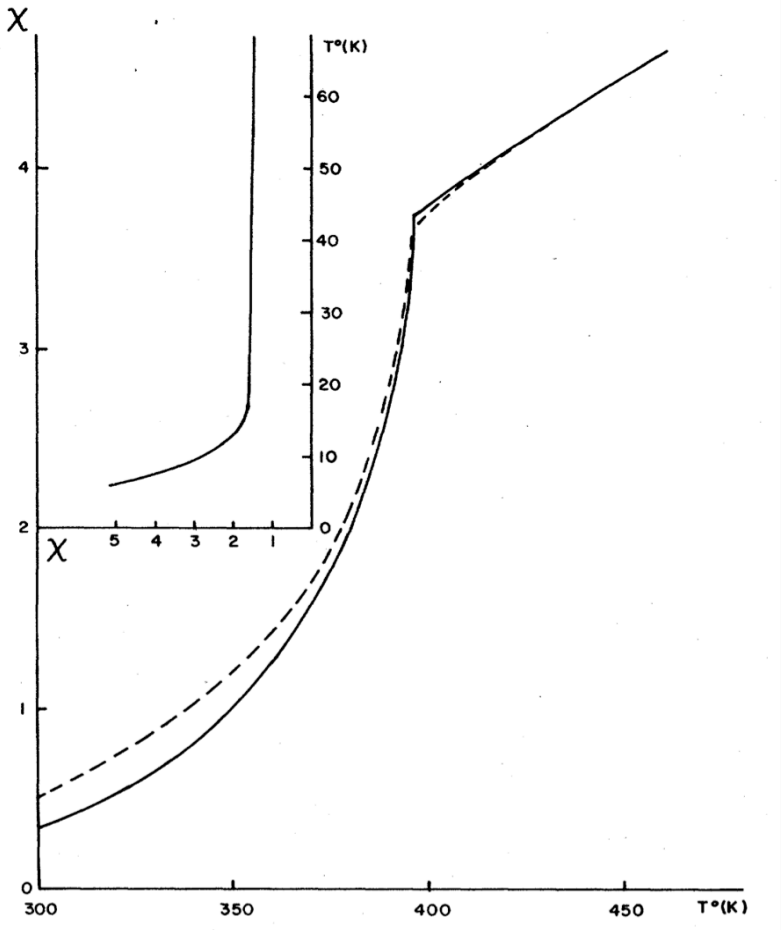

Figure 6.1: Paramagnetic susceptibility per spin (χ) as a function of temperature for KTCNQ. The solid line is the result from Lépine *et al.* [11] and the dotted line from Vetger *et al.* [8]. The inset shows the low temperature Curie tail that is due to uncompensated TCNQ spins.

deep well, however as the T is lowered the TCNQ anion falls into a very wide well which leads to a more deformable structure. From fitting to the low T data using a the theory derived by Pytte [6], $J' = -1800$ K, $\delta(0) = 0.427$ which in this case is the degree of dimerisation.

More attention has been given over the past few decades to methyl-ethyl-morpholinium di-7,7,8,8-tetracyanoquinodimethanide (MEM(TCNQ)$_2$) which is an interesting material that crystallises with a triclinic unit cell and forms stacks of planar TCNQ molecules each with a charge of -$\frac{1}{2}|e|$ [12]. At 335 K this compound undergoes a structural phase transition where two TCNQ molecules dimerise. This is a structural

Peierls transition above which the conductivity is metallic where the half filled one dimension band collapses and an electron becomes localised on a TCNQ dimer as the temperature decreases [13]. At ∼20 K another phase transition occurs whereby there is a dimerisation of TCNQ dimers, which is the spin-Peierls transition (T_{SP}). This is due to antiferromagnetic coupling of the adjacent spins on separate TCNQ dimers which is coupled to a decrease in the magnetic susceptibility and x-ray measurements below T_{SP} show that the unit cell doubles in size which is consistent with a tetramerisation of TCNQ molecules [13]. Above the spin-Peierls transition the data was fit using the Bonner-Fisher (BF) Model [1] where $J = 53$ K, below T_{SP} the susceptibility drops below the BF curve and a new model is needed to fit the data. Using a model devised by Bulaevskii [4], Huzinga *et al.* were able to fit the data using equation 6.5 where they found $\delta(T) = 0.16$ and the magnetic excitation gap $2\Delta(0) = 56$ K which is related to J as this the energy needed excite the dimer into a triplet state. It should be noted that the calculated value of χ had to be scaled by a factor of 0.84 to the BF model at $T = T_{\mathrm{C}}$. To fit the data fully another paramagnetic Curie tail was needed where $\chi_{\mathrm{para}} = \frac{0.75\times10^{-3}}{T}$ mKmol^{-1} which accounted for the divergence of the susceptibility as $T \to 0$ due to impurity spins.

Muon Spin Relaxation (μSR) measurements were conducted on a sample of MEM(TCNQ)$_2$ by Lovett *et al.* [14, 15]. Magnetic susceptibility data showed the existence of an SP transition in the sample and, due to the advances in technology, the actual magnetic moment of the sample could be measured more accurately[1]. They found similar results from magnetic susceptibility data to Huizinga *et al.* [13] where from a fit to the BF model, $J = -50.3$ K and at low temperature $\delta(0) = 21.3(1)$ K [15].

For the μSR experiment a clear difference between the relaxation at high and low temperatures was observed. Since there is no recovery of muon asymmetry to $\frac{1}{3}$ it was concluded that there was a significant dynamical component of the magnetism within the sample. At high temperatures the data is well described by a Gaussian relaxation which is due to the random static nuclear spins that depolarise the muons.

[1] Huizinga *et al.* used a vibrating sample magnetometer where as Lovett *et al.* used SQUID magnetometry

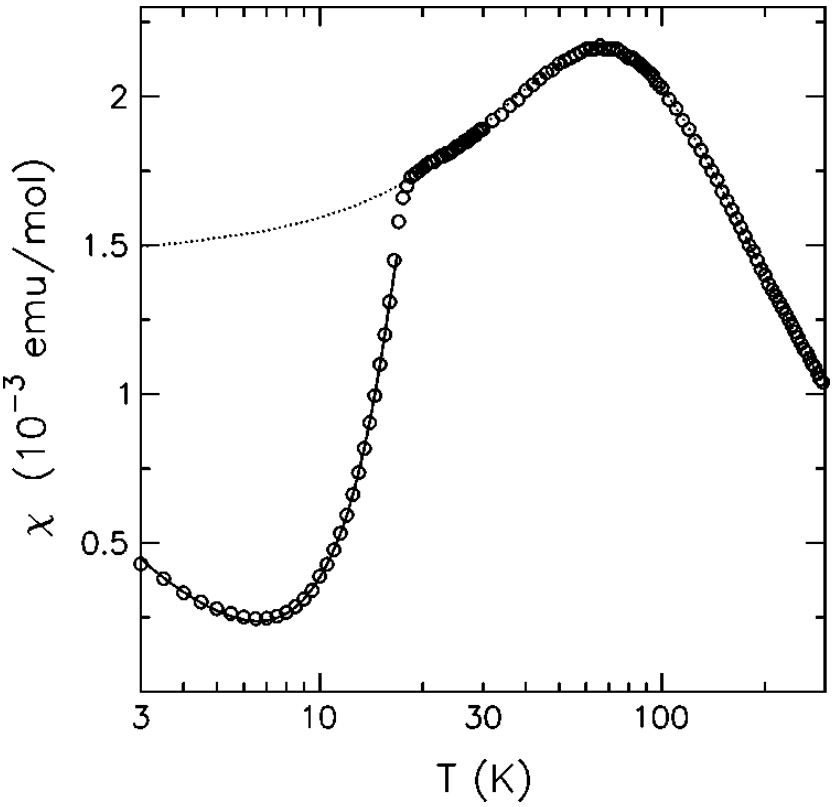

Figure 6.2: Magnetic susceptibility for $MEM(TCNQ)_2$. The dotted line is a fit to a BF expression and the solid line is a combination of both a SP state and a Curie tail. Taken from [15].

At high temperature the electronic field distribution is motionally narrowed by the high fluctuation rate that falls outside of the muon time scale and hence we expect the muon relaxation to only be sensitive to the nuclear magnetism in this high temperature state. At low temperatures however the relaxation is exponential which can be attributed to fluctuating moments or a dilute spin system. It is most likely that the relaxation is due to the muon being within the motional narrowed limit where for fast fluctuations one can treat the muon polarisation as:

$$P_z^{\mathrm{dyn}}(\Delta,\nu) = \exp\left(\frac{-2\Delta^2 t}{\nu}\right). \tag{6.8}$$

However at ultra low temperatures of 39 mK the data are still described using an exponential relaxation. At this temperature one would expect the fast fluctuations

to be frozen out as well as the singlet-triplet excitation gap to be large (∼21 K) so it is assumed that the mechanism for depolarising the muon ensemble is due to dilute spins or a low concentration of magnetic defects which would give rise to a Lorentzian Kubo-Toyabe function:

$$P_z(t,a) = \frac{1}{3} + \frac{2}{3}(1-at)\exp(-at). \tag{6.9}$$

To parameterise the data, Lovett *et al.* fitted the entire data set with the phenomenological function

$$P_z(t,\lambda,\beta) = \frac{1}{3} + \frac{2}{3}(1-(\lambda t)^{\beta})\exp(-\lambda t)^{\beta}, \tag{6.10}$$

that essentially is a power law Kubo-Toyabe function as first suggested by Crook and Cywinkski [16].

Lovett *et al.* fitted the data up to 5 μs where the static component was expected to dominate and they observed that as the sample was warmed through the transition temperature the value of β changed from approximately 1 at low temperatures to 2 at high temperatures (see figure 6.3).

The value of λ was fixed at 0.25 MHz and the transition occurs over a width of 5 K. One major difference between the μSR data and the magnetic susceptibility data is the transition occurs at different temperatures, which is lower for the μSR technique. This is evidence that the magnetic fluctuations do not slow down even below the apparent T_{SP} when the magnetic excitation gap becomes very large [14, 15].

Within this chapter are reported the preliminary measurements of two KTCNQ salts: KTCNQ-H_4, KTCNQ-F_x ($x = 2, 4$) as well as KTCNQ-Br_2. The idea was to study the change in TCNQ-TCNQ interactions in a simple spin-Peierls system and what effect changes to the TCNQ moiety would have on the magnetic properties of the material. Magnetic susceptibility measurements are reported as well as μSR experiments, although μSR was only conducted on the H_4 and F_4 products. The

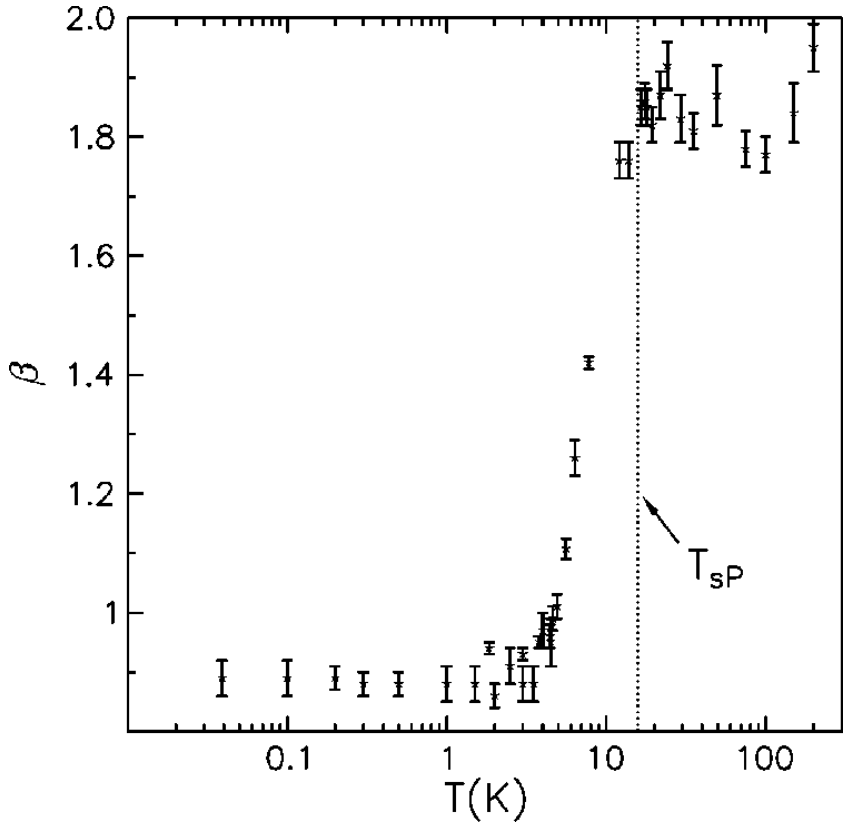

Figure 6.3: Temperature dependence of the line shape parameter, β from equation 6.10 for MEM(TCNQ)$_2$ taken from [15].

data however represents only a preliminary study and more work is needed before a complete picture is built up. However, the initial observations suggest this proves to be a simpler system then MEM(TCNQ)$_2$ as both the conventional Peierls and spin-Peierls transitions are linked as it is a dimerisation of TCNQ units rather then a tetramerisation as seen in MEM(TCNQ)$_2$.

6.2 Experimental: Materials and Methods

The KTCNQ was synthesised according to Melby *et al.* [20] in a solution of dry acetonitrile:

$$3\mathrm{KI} + 2\mathrm{TCNQ} \rightarrow 2\mathrm{KTCNQ}(s) + \mathrm{KI}_3(aq). \tag{6.11}$$

A stoichiometric amount of potassium iodide (KI) was added to a solution of TCNQ in acetonitrile under reflux which then produced a dark purple precipitate, KTCNQ. The precipitate was filtered under vacuum and washed with diethyl ether until the colour of the filtrate solution ran through clear and not yellow/brown. Once dry the purple solid was stored in air and at a glance small crystallites could be observed.

The TCNQ-D_4 was made using a method reported by Dolphin *et al.* [21] (see chapter 4 experimental section for more details). The anhydrous potassium iodide and TCNQ were purchased from Sigma Aldrich [22]. $TCNQF_4$ and $TCNQF_2$ were purchased from the Tokyo Chemical Industry [23]. Dry acetonitrile and diethyl ether was purchased from the Durham University Chemistry department solvent purification system. The percentage yields for each product are shown in Table 6.1. Since the H_4 and D_4 TCNQ derivatives are expected to behave in a similar way within a reaction the high percentage yield of KTCNQ-D_4 may be due to unreacted KI. If one assumes that the percentage yield should be similar for KTCNQ-H_4 and KTCNQ-D_4 then the level of the KI impurity within the entire sample may be approximately 30%.

Product	% Yield
KTCNQ-H_4	50
KTCNQ-D_4	83
KTCNQ-F_2	89
KTCNQ-F_4	75
KTCNQ-Br_2	39

Table 6.1: Percentage yields of the KTCNQ derivative products.

X-ray diffraction measurements were performed on a Siemens D9 diffractometer with a Cu source where there was both $Cu_{k\alpha}$ and $Cu_{k\beta}$ radiation. Magnetic measurements were conducted on a Quantum Design MPMS with a 5 T superconducting magnet. More information can be found in the experimental chapter of this thesis (chapter 3).

Muon spin relaxation experiments were conducted on the EMU spectrometer at ISIS (see chapter 3). A closed cycle refrigerator (CCR) was used to both heat and cool the samples where the samples were mounted on a titanium sample holder and backing plate. Three mylar sheets were used to cover the sample and degrade the muon momentum so the muons would stop within the sample. To measure the background contribution to the signal hematite was first placed within the sample holder in a similar set up to that used with the KTCNQ and the sample holder within the CCR. From a transverse field (B=100 G) measurement the resulting 4.5% asymmetry was due to the muons relaxing in the sample holder/CCR and makes up the background of the measurement. Fitting of the raw μSR data was done using the WIMDA program [24].

6.3 Structural Data

X-ray diffraction experiments were performed on a sample of KTCNQ-D_4 when it was in the low temperature phase below T_{SP}. The diffraction pattern was refined using FullProf and the results can be seen in figure 6.4. XRD data were used to attempt to identify the purity of the sample and to also see whether there was full transformation from the high temperature phase to low temperature phase. The data were refined using cell parameters and atomic positions that were previously discovered by Konno *et al.* [10] where the goodness of fit figure of merit, $\chi^2 = 5.79$. In order to achieve a low χ^2 value a potassium iodide phase was needed to also account for peaks not due to the KTCNQ-D_4.

The cell parameters for the KTCNQ-D_4 sample were calculated to be $a = 7.0902(6)$Å, $b = 17.807(2)$Å, $c = 17.873(3)$Å and $\beta = 94.927(5)^\circ$ which are very close to the parameters measured by Konno *et al.* [10]. The slight discrepancies may be due to the poor data quality; broad peaks affected the quality of the refinement that could be achieved. The occupation and atomic positions were not refined and an average thermal isotropic temperature ($U_{\text{iso}} = 0.300$) was used that was also held constant.

A small potassium iodide impurity was detected where some peaks overlapped with

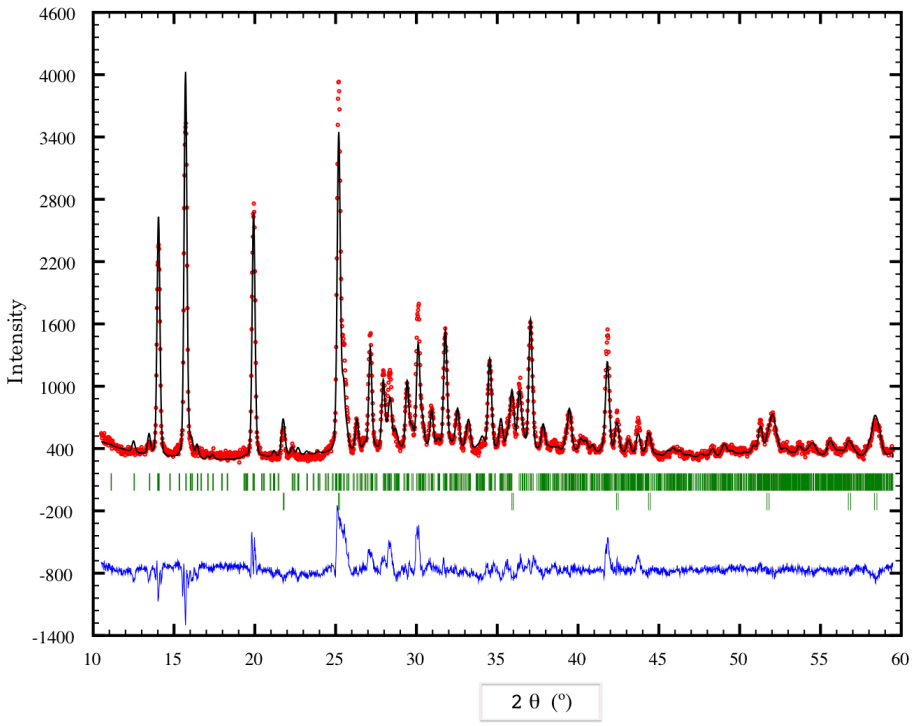

Figure 6.4: Refined XRD data for KTCNQ-D_4 below T_{SP}. The red curve = raw data, black curve = calculated pattern, blue curve = difference and the green ticks are predicted peaks, the lower tier is for the KI phase.

the KTCNQ-D_4 pattern, however it did not impact the data significantly and, as already stated, is taken into account within the refinement. However the presence of KI will pose a huge problem for μSR experiments as it is well documented that there is significant muonium formation when muons are implanted in alkyl halides [17, 18, 38]. One issue that was highlighted in the experimental section of Chapter 4 was that in order to bypass the reaction intermediate an additional external heat source was needed, which suggests that simply changing the protons for deuterons greatly affects the energetics and kinetics of the reaction. The same case may be true for the reaction of TCNQ-D_4 with KI, although since the reactants are under reflux it would be hard to measure whether more heat is needed to cause the reaction to progress more fully. If the energetics of the reaction are significantly changed then this would imply that more KI would be present within the KTCNQ-D_4 sample.

6.4 Magnetic Measurements

Magnetic measurements were performed on the synthesised KTCNQ and its derivatives. Due to the low moment and low density of the sample this made the measurements particularly challenging. The low density meant that it was hard to pack enough sample into a capsule to conduct the experiment, where an average amount of sample used was between 10 and 20 mg. The sample had a low moment within the paramagnetic limit and below T_{SP} the only signal should be from the diamagnetism, as the spins are locked out until at very low temperatures were a paramagnetic Curie tail was observed. The KTCNQ-D_4 could not be measured accurately and no high quality data could be obtained to support the transition temperature of the sample.

6.4.1 KTCNQ-H_4

Results from the magnetic experiments on KTCNQ-H_4 are shown in figure 6.5 and demonstrated that the transition was within a temperature region that was similar to previously reported [11]. We observed a transition between 300 and 400 K that appears to be second order in nature[2]. It was not possible to calculate the corrected susceptibility of the sample since the diamagnetic susceptibility could not be determined as there was no region where the slope was essentially zero resulting in a negative susceptibility. Moreover, positive background susceptibility suggests a temperature independent paramagnetic component to the magnetism or an impurity.

A Curie-Weiss law was fitted to the 2nd sample ZFC curve. χ_D was calculated using Pascal constants [25] and equated to - 9.34×10^{-8} m^3kg^{-1} however despite the subtraction of this diamagnetic term there was a temperature independent positive susceptibility that needed to be included in the fit. The values of the parameters are shown in table 6.2. Assuming that for a TCNQ anion, $S = \frac{1}{2}$ and $g = 2.002$

[2]The data is plotted as magnetisation rather then χ vs. T as it is clear that at both samples have different values for χ_D

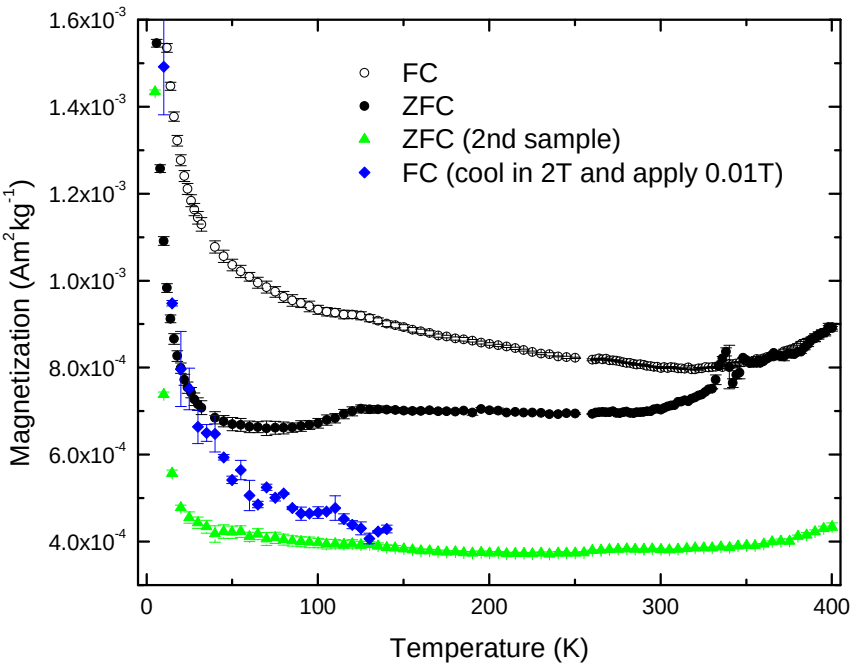

Figure 6.5: Magnetisation vs. temperature for KTCNQ-H_4 where **B = 100** G (0.01 T). A separate sample was measured due to the anomalous behaviour observed at 100 K.

for an orbitally quenched system one can calculated N, which is the number of uncompensated TCNQ spins that are responsible for the Curie tail at low temperatures. Standard Curie's law cannot fit the data and an exchange term (θ) is needed suggesting that the behaviour at low temperature is not strictly due to non-interacting, paramagnetic TCNQ anion species. The percentage of defects accounts for an impurity phase of 0.052%, which is very small, however there is a temperature independent paramagnetic susceptibility that is not understood and not accounted for within the subtraction of the diamagnetic susceptibility. The fact that an exchange term is needed within the low temperature fit to the data is not surprising as it has been shown that within the inorganic spin-Peierls system, $CuGeO_3$, there is long range ordering of the defects that occurs below a critical temperature (approximately 2 K) [26]. However this exchange term should be negative implying antiferromagnetic 3D ordering of the defect spins and on a higher doping of defects

(i.e. $> 1.5\%$) this has dramatic effect on the magnetic susceptibility. The defects, or breaks in the 1D chains, can be thought of as clusters where there is varying overlap of the wave function with other clusters which leads to various exchange interaction energies and in this sense the order parameter can be inhomogeneous within the sample [27]. The percentage of defects within the sample is very low when compared with work on other systems [26–28], which are of the order of a few percent, and for this reason we may not see any dominate effects within our data.

Parameter	Value
C ($\mathrm{mKkg^{-1}}$)	$3.06(9) \times 10^{-8}$
θ (K)	2.71(9)
χ_p ($\mathrm{m^3kg^{-1}}$)	$9.80(4) \times 10^{-8}$
% Defects	0.052

Table 6.2: Values for from Curie-Weiss fit to the Sample 2 ZFC data with errors given in brackets. The % of defects was calculated assuming that these are single uncompensated $S = \frac{1}{2}$ TCNQ anions.

What is striking about the data is the the anomalous behaviour at low temperatures where a step is observed at ∼100 K. Also, there appears to also be hysteresis within the sample which is not expected in a simple SP system such as this. Additionally the step in the data shows that the magnetic behaviour of the sample is changing where the slight increase as the temperature increases, at ∼100 K, suggests that moments are becoming unfrozen and so can contribute to the net observed moment. This may be due to the magnetic history of the sample where a large field needed to be applied in order to centre the sample within the detection coils. The application of a large field may have frozen in a magnetic state were the TCNQ molecules are not locked in their dimerised AF state. A second sample was measured in the same field and no dramatic change was seen at ∼100 K on heating the sample. To further study the anomaly a large field of 2 T was applied on cooling the sample and a lower field of 0.01 T was applied on heating. Although the errors are large, a small change is seen within the same region (100 K) however there is a decrease in the moment.

This supports the idea that the application of a large magnetic field on cooling may have a dramatic effect on the sample, however the physical picture which can be used to describe this is unclear. The fact that there is an observed Curie tail is due to paramagnetic uncompensated TCNQ moments where the spin is not coupled within a dimer. Application of a large field may cause these uncompensated moments, which act as bound defects, to fall into a polarised state where the moments freeze. There may also be a glassy component to this 'impurity' magnetism which would mean that the response would change slightly as the groundstate will be metastable. However it may be that regions of the TCNQ stacks are altered so the moments may be frozen into a glassy uncompensated state rather than it being based solely on the defect magnetism.

6.4.2 KTCNQ Derivatives

On substitution of the protons on the aromatic ring of the TCNQ with other elements shows a dramatic change in the SP transition and ultimately the exchange interaction between the TCNQ dimers. Figure 6.6 shows the magnetic susceptibility of KTCNQ-F_4, KTCNQ-F_2 and KTCNQ-Br_2. Simply by the substitution of fluorine for hydrogen on the TCNQ molecule this has shifted T_{SP} to approximately 160 K, however there is little difference between the transition temperatures whether there are two fluorines or four fluorines substituted on the ring except that within KTCNQ-F_2 the transition region is broadened out. This broadness may be due to additional disorder created as the TCNQ-F_2 molecules can overlap and there will be two orientations of the TCNQ molecule with respect to dimer.

It was possible to fit Curie-Weiss law to the low temperature data where χ_D was calculated to be - 2.37(8)$\times 10^{-8}$ m^3kg^{-1} for the F_2 and - 2.23(2)$\times 10^{-8}$ m^3kg^{-1} for the F_4 product. The values from the fits to the FC curves can be seen in table 6.3. A fit of Curie-Weiss law gave a slightly higher R^2 value and so it meant that the best description of the data also needed an exchange term, however this was small.

The percentage of defects, or uncompensated TCNQ spins is small, similar to the H_4

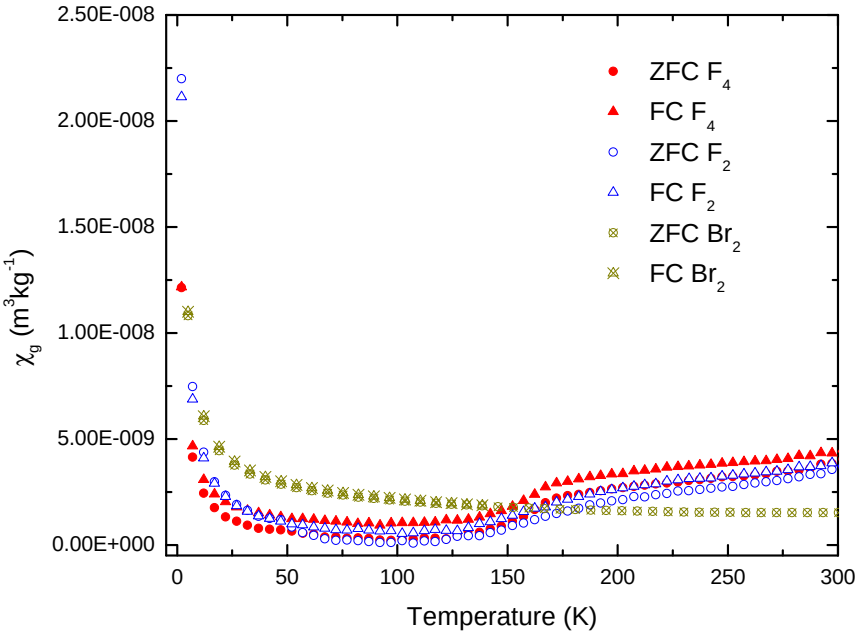

Figure 6.6: Magnetisation vs. temperature for other KTCNQ derivatives where $B = 1000$ G. It is clear that there is a dramatic shift in transition temperature on substation of the H atoms.

product however the exchange constant, θ is much smaller and negative. The error in the fit also does not account for a change from negative to positive θ and so it may be that within both the fluorinated systems there is antiferromagnetic exchange coupling between these spin defects, which is expected for the 3D ordering of these defects however, within this system, the mechanism for this exchange is unclear [26]. Again the number of defects is very low and so there may not be direct coupling of all the clusters through a perculative pathway as seen in $CuGeO_3$ which occurs through the defects pinned within structural defect created domain boundaries [28].

When using the organic acceptor TCNQ-Br_2, the product created shows an even greater deviation from the protio product where there is no evidence of any transition temperature. To the data shown in figure 6.6 one can fit Curie-Weiss law, again Curies law simply does not have as high an R^2 value and so the fit is not as good. The parameters from the fit are shown in table 6.4.

Sample	C ($mKkg^{-1}$)	θ (K)	% Defects
KTCNQ-F_4	2.98(5) $\times 10^{-8}$	-0.60(4)	0.17
KTCNQ-F_2	4.86(8) $\times 10^{-8}$	-0.31(4)	0.25

Table 6.3: Values for from Curie-Weiss fit to the KTCNQ-F_x FC data with errors given in brackets. The % of defects was calculated assuming that these are single uncompensated $S = \frac{1}{2}$ TCNQ anions.

Parameter	Value
C ($mKkg^{-1}$)	6.9(2) $\times 10^{-8}$
θ (K)	-2.4(4)
χ_p (m^3kg^{-1})	1.32(2)$\times 10^{-9}$

Table 6.4: Values for from Curie-Weiss fit to the KTCNQ-Br_2 ZFC data with errors given in brackets.

Assuming that the magnetism is not similar to the other samples and not due to a magnetic impurity (uncompensated TCNQ spins) the effective moment derived from the Curie constant, C, of the magnetic atoms/ions/particles are approximately 4.21$\pm$0.06 μ_B where for an uncompensated TCNQ anion we expect 1.73 μ_B. This difference is not accounted for by the error and is large, which suggests that we are observing a cluster of TCNQ spins interacting. It should be noted that for the previous KTCNQ salts since the number density (N) is not directly known one cannot calculate both N and μ_{eff} so it is assumed that the the moment of the magnetic impurity is simply that of a TCNQ anion, $S = \frac{1}{2}$. The negative nature of θ also means that the magnetic species responsible for the Curie tail are coupled antiferromagnetically .

For both the KTCNQ-F_x samples it has not been possible to fit the data above the transition or on the transition itself as it does not show a behaviour similar to other SP systems as shown in figure 6.2. Ideally to get better data the sample should be pressed into a pellet and the magnetisation measured which would increase the density of the sample and allow for a measurement with a larger change in moment.

What is clear from the above data is that simply changing the substituents on the TCNQ ring can have huge effects on the magnetic coupling along the stacks. It has been shown previously that the election affinity of the TCNQ molecule can be tuned by changing substituents on the ring. Thus TCNQ-F_4 has a greater electron affinity then TCNQ-H_4 [29]. The changes in electron affinity and the ability of the TCNQ derivative to form a salt with a distinct structure can be related to both steric and electronic properties [30]. The addition of fluorine can increase the π-donation of the substituent (in this case F) onto the aromatic ring and conjugated system thus helping to stabilise the radical anion across the whole molecule and shifting the molecular orbital energy so there may be greater overlap with that of the metal ion thus increasing the exchange interaction. However the addition of Br to a structure can create steric effects as the size of the atom can alter the packing of the molecules where within the neutral TCNQ-Br_2 there is slight molecular distortion [31]. If there are changes in the TCNQ-Br_2 configuration this may alter the magnetic exchange and π-overlap between TCNQ molecules however to confirm this structural data are needed. Since there will be little interaction with the K ions within the material the changes in magnetism will be due purely too changes in the TCNQ-TCNQ interactions. Although TCNQ-F_x ions may not show molecular distortion, the resulting changes in electronic structure may lead to the dramatic changes in the energy levels of the HOMO and LUMO which will in turn lead to changes in the coupling strength within the TCNQ dimers.

6.5 Muon Spin Relaxation Experiment

Muon spin relaxation experiments were conducted on the samples to complement the magnetic measurements where the KTCNQ-H_4 and KTCNQ-F_4 samples have been measured. Within this section it will be shown that using μSR one is able to study the SP transition and due to the muons acting as a shorter time scale probe the fluctuations and dissolving of the SP state occurs at a lower temperature then measured using conventional DC susceptibility. Blundell and Lovett *et al.* also

found that the lineshape parameter, β, from the fit to the raw μSR data that it increased from 1 to 2 through T_{SP} which they stated was a feature of an SP system [14, 15]. From our results we were able to test on a similar chemical system but with stoichiometric and structural differences whether behaviour of an exponential to Gaussian relaxation is generic for other SP TCNQ systems.

6.5.1 KTCNQ-H_4

The sample was studied in Zero Field (ZF), Longitudinal Field (LF) and Transverse Field (TF) which allowed a variety of relaxation processes to be probed.

6.5.2 ZF μSR

Raw data from the ZF study of KTCNQ are shown in figure 6.7 and it is clear that the muons are sensitive to the SP transition where, as the sample is heated, the relaxation of the muon changes dramatically. We observe a behaviour similar to that observed in the MEM$(TCNQ)_2$ system where below T_{SP} the spatial distribution can be best described by a Lorentzian curve, however at above T_{SP} the relaxation distinctly Gaussian. At low temperatures ($T \ll T_{SP}$) the relaxation changes again which is most likely not related to the SP behaviour as fluctuations are expected to be frozen out.

Since there is a change in relaxation function with temperature the data are best described using a stretched exponential function where:

$$G(t) = A\exp(-\lambda t)^{\beta} \tag{6.12}$$

where λ is the relaxation parameter, A is the asymmetry and β describes the power dependence of the relaxation. When $\beta = 1$ the relaxation is a single exponential and when $\beta = 2$ the relaxation is Gaussian.

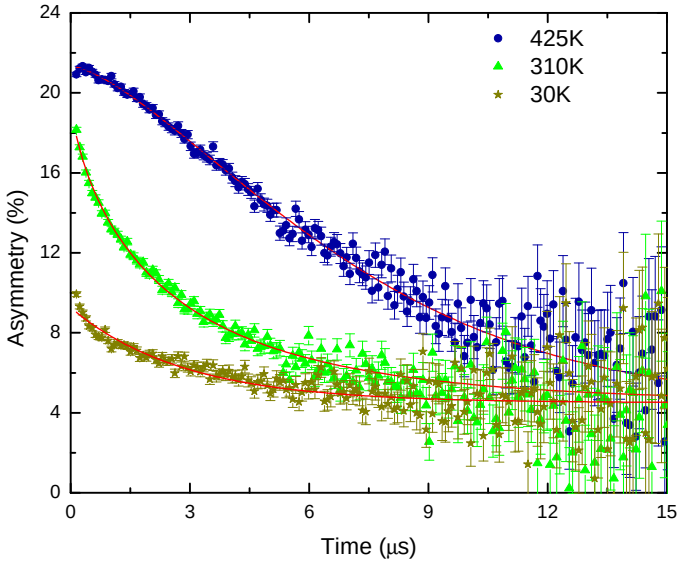

Figure 6.7: KTCNQ-H_4 ZF raw data at temperatures above and below T_{SP}.

From a plot of the asymmetry (see figure 6.8) within the transition region one can see that the unfreezing of the dimerised state occurs at 300 K and at 350 K the asymmetry levels off with slight fluctuations.

Both λ and β are shown in figure 6.9 where it is clear that there is a dramatic change as the sample is heated through T_{SP}. Within this system the most likely physical meaning of λ is that it describes the dynamics of the system and as λ decreases the fluctuations are becoming faster as $\lambda \propto 1/\nu$. This makes sense when considering that the system goes from a quasi-static dimerised state to a uniformly spaced paramagnetic state where the fluctuations will eventually become motionally narrowed and outside of the time window of the muon relaxation. Within the paramagnetic state the field distribution that the muon experiences becomes smaller due to rapid fluctuating moments where the fluctuations are too fast for the muons to be sensitive to, it is when this field distribution collapses to a small value that the muon is within the notionally narrowed limit.

The parameter, β, displays the curious behaviour of increasing through the transition however the value starts off below 1 and never reaches 2 (figure 6.9), which

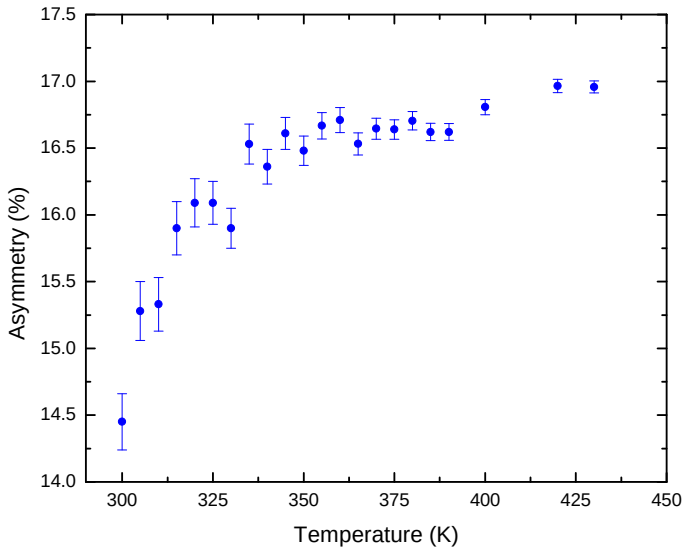

Figure 6.8: ZF asymmetry for KTCNQ-H_4 within the SP transition region.

would describe both a perfect single exponential and Gaussian relaxation perfectly respectively. The value below 1 may be due to a convolution of relaxations and the system cannot be perfectly described by a single relaxation. This may be the case if the the muons have multiple stopping sites where each site was sensitive to a different field distribution when the system is within the static limits. As the temperature increases, so does β where the fluctuation rate increases and the static nuclear fields on the N and H atoms start to dominate the relaxation. Indeed at high temperatures above the SP transition the fluctuations are moving to the limit of the μSR experiment and so the main component of the muon relaxation is from the nuclear moments within the TCNQ molecules. However the fact that the relaxation is never described simply by a Gaussian is due to the presence of some dynamics associated with the electronic magnetism.

When considering the stopping sites within a system such as KTCNQ, there may be sites where the muon will couple to the negative charges on the end of the TCNQ molecule by the cyano groups. However when in the dimerised state the electron density is localised across the dimer and more specifically within the π-orbitals which couples the two TCNQ molecules together. Therefore it may be desirable for the

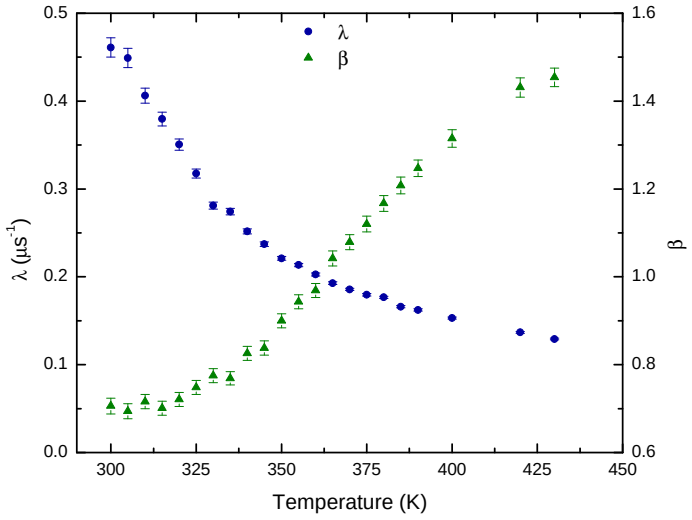

Figure 6.9: Values for λ and β for the KTCNQ-H_4 system in ZF.

muon to locate itself near or within this region of high electron density. As the dimerisation is destroyed through heating this site may no longer be favourable and so the muon site may change where there may be direct bonding to the ring or coupling to the electron rich cyano groups.

6.5.3 Low Temperature ZF μSR

At low temperatures (< 300 K) the relaxation is different when compared to temperatures > 300 K and so the system cannot be described using a similar stretched exponential function and is best described purely as a single exponential. It should be noted that the single exponential does not fully capture the behaviour at short times suggesting there are two different relaxations, one that is just outside of the EMU time window and thus very fast and another that we can measure. As the temperature increases, this fast relaxation decreases and is eventually lost. The trend in the asymmetry shows that at low temperatures there is a significant missing fraction that begins to decrease at 150 K.

The increase in asymmetry in figure 6.10 also coincides with an increase in the relaxation, λ where a cusp is observed at 250 K. The exact origins of this cusp are

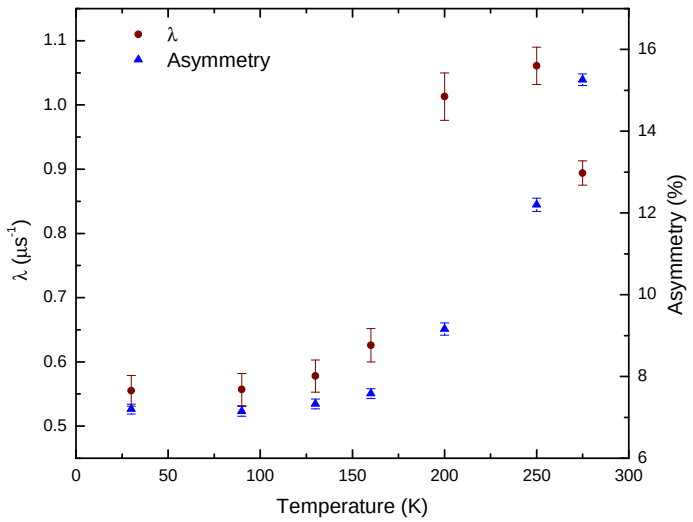

Figure 6.10: Low temperature muon relaxation parameters for KTCNQ-H_4.

not obvious however if continuing with the idea of the unfreezing and break down of the quasi-static SP state it may be that the dynamics or fluctuations enter the muon time scale at this temperature. Below 250 K the system may behave like a static arrangement of atoms however there will still be excited dimers at a low frequency along the quasi-1D chain. At these low temperatures the muon relaxation may be sensitive to these slow excitations of the dimer which increase in frequency as T increases. However at 250 K the structural order within the system begins to change, i.e. it is no longer in the static limit, and so the muon becomes sensitive to the fluctuations related to the closing of the spin gap.

Although there is a fast relaxing component that cannot be modelled this could be due to presence of muonium, which generally has a fast relaxation or, more likely, a muon which is located within a region of large internal fields which causes the muon ensemble to dephase rapidly. It should be noted that this internal field does not have to be polarised on a macroscopic scale and what the muon may be experiencing is large internal quasi-static fields that show a degree of disorder.

6.5.4 Transverse Field μSR

Applying a transverse field can be used to measure T_2 processes within the sample, i.e. decoupling of the spins from the magnetic lattice as $\lambda \propto 1/T_2$. What is most noticeable about the TF spectra (figure 6.11) is that at low temperatures there is a large missing fraction where the data could be described throughout the entire temperature range by the fitting function

$$G(t) = A_1 \exp(-\lambda t) \cos(\gamma_\mu \mathbf{B} t + \phi) + \mathrm{Bg}, \tag{6.13}$$

where

$$\mathrm{Bg} = A_{\mathrm{Bg}} \cos(\gamma_\mu \mathbf{B}_{\mathrm{Bg}} t + \phi). \tag{6.14}$$

The Bg term accounts for the muons stopping in the sample holder and the asymmetry (A_{Bg}) was fixed at 4.5%. The background term could be fixed from data collected using hematite placed in the sample holder with an applied TF of 100 G where $\mathbf{B}_{\mathrm{Bg}}$ could be fixed at 102.5 G. The phase (ϕ) was fixed globally at 7.87. Both the total asymmetry and the relaxation rate are shown in figure 6.12. The rotational field for the sample showed little variation and was approximately 103 G where all deviation was accounted for within the error and so one can keep the field fixed throughout the fits.

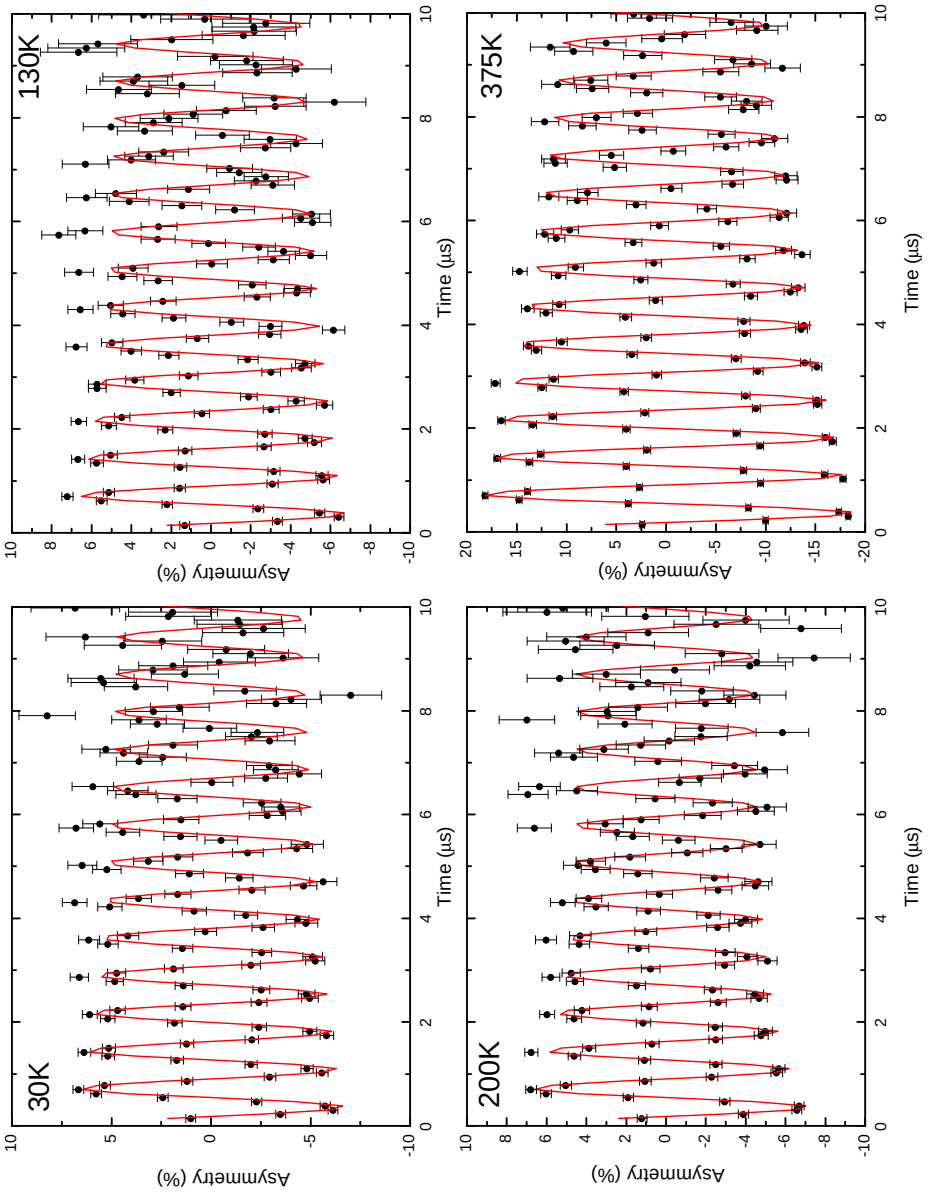

Figure 6.11: TF spectra at temperatures both below and above T_{SP} for KTCNQ-H_4. The solid lines correspond to the fits to the data.

It is clear from the data that the asymmetry is coupled to the transition and increases between 200 and 400 K. As previously mentioned there is a substantial missing fraction of approximately 15% at 30 K where on application of a TF one would expect there to be a significant recovery of any missing fractions observed in ZF. Since this missing fraction is not recovered when a TF is applied this may point to a significant fraction of muonium present at low temperatures where the muon is physically bonding to an electron rich area within the sample creating a paramagnetic state.

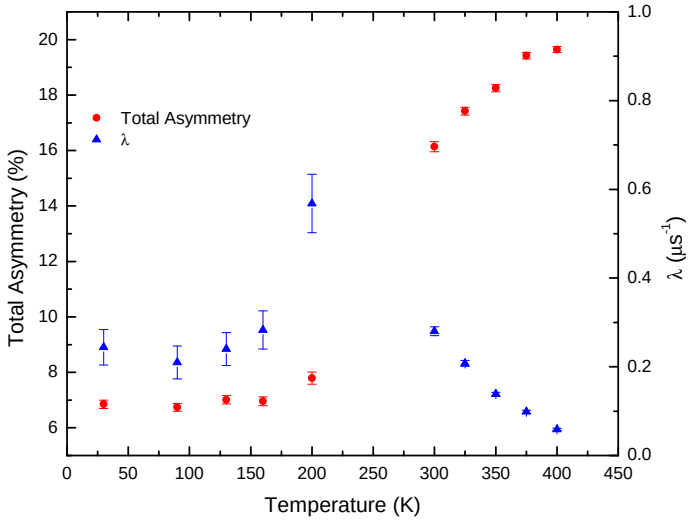

Figure 6.12: Asymmetry and relaxation rate for KTCNQ-H_4 where TF = 100 G.

The relaxation rate shows a temperature dependence however the changes in λ are small. At low temperatures the data is essentially a flat line with little change however at 200 K there is a peak observed. This peak may be where the fluctuations begin to enter the muon time scale and the system begins to unfreeze from the SP state. The higher temperature data ($>$ 300 K) shows the speeding up of the dynamical electronic fluctuation which is similar to the relaxation rate observed in ZF.

Applying a TF at low temperatures ($<$ 300 K) might have no effect on the system as the magnetic intra-exchange coupling within the TCNQ dimers will be strong and the system locked into a local antiferromagnetic state. However as the temperature increases and the fluctuations begin to dominate, the application of a field may

slow these down to the point where they may be quasi-static on the muon time scale. The muon would then experience a vector sum of internal and external fields which would give rise to small changes in muon precession frequency however we did not have the statistics to detect any changes within our experiment. At higher temperatures (> 300 K), above T_{SP}, the sample will be approaching the behaviour of a paramagnet and the fluctuations may not be slowed by the applied 100 G TF. The missing fraction at low temperatures may indicate the presence of muonium however this behaviour has not been observed in other systems [14, 15] or even within the $Ni(TCNQ)_2$ sample discussed in the previous chapter.

6.5.5 Longitudinal Field μSR

LF sweeps within this system may be able to decouple components in a similar way to the $Ni(TCNQ)_2$ sample where application of a 50 G LF decoupled the nuclear component from the relaxation. To decouple a component means the depolarisation of muons along the z-axis or initial polarisation by the application of an LF. By applying an LF of different magnitudes it is possible to overcome the coupling of the muon to different internal field environments within the sample. The data can be fitted using a single exponential relaxation however the value of λ_{LF} can be fixed for temperatures of 30, 340 and 410 K however at 225 K this relaxation changes. The raw data can be found in the appendix.

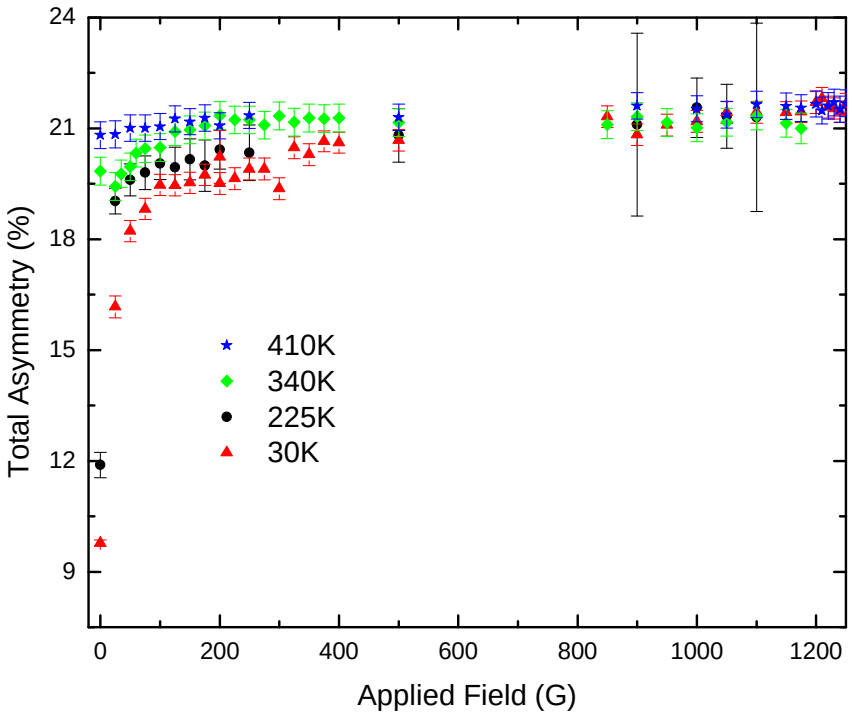

Figure 6.13: Asymmetry as a function of LF for KTCNQ-H_4.

Figure 6.13 shows that at low temperatures the system is within the dimerised state and a relatively large field of ~500 G LF is needed to decouple what may be an electronic component. The nuclear component is expected to be decoupled at low fields (50 G). At 410 K the asymmetry is constant within error suggesting

that within this high temperature limit there is little electronic magnetism that the muons are sensitive to. However since a full fraction is considered to be ∼23%[3], the fact that this value is not reached may mean that there is still a significant dynamical component that dephases the muon ensemble. At low temperatures the system will be closer to a static state and the recovery of the asymmetry may be due to decoupling the muon from an internal field of approximately 500 G. As the temperature increases, the dynamical component will also increase and so too the coupling within the TCNQ dimers. The fact that all temperatures show a recovery to the same value indicates that at all temperatures there may be a dynamical component that is significant and cannot be fully repolarized.

The values used for λ_{LF} are shown in table 6.5 and these were kept constant at each field value. These values were chosen as rough values of λ_{LF} and may not be exact, however they described the data sufficiently well. A constant λ means that the same relaxation process is dominating the muon decay however it is the asymmetry that is important in this case. At 225 K the relaxation cannot be modelled using a single value and so the relaxation process is changing.

Temperature (K)	λ_{LF} ($\mu\mathrm{s}^{-1}$)
410	0.2
340	0.25
30	0.5

Table 6.5: Values for λ_{LF} used for the LF sweeps.

The fact that for 225 K, λ_{LF} cannot be fixed at a set value, points to this temperature being of importance. Figure 6.14 shows the response of the relaxation as the applied LF is increased where there is a rapid decrease and then the value essentially becomes constant. The LF value (∼200 G) where the relaxation flattens out is too high for simply a nuclear component and therefore it must be having an effect on the electronic magnetism or muons responding to it. When looking at the ZF data

[3]This is true only if α is correct.

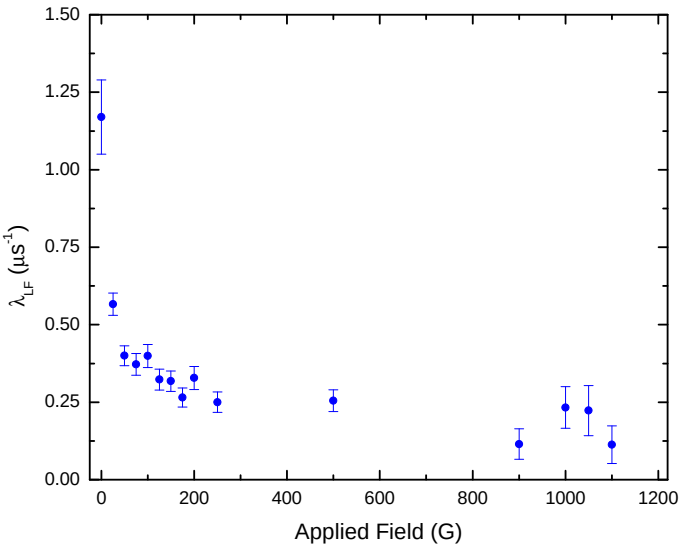

Figure 6.14: λ as a function of LF for KTCNQ-H_4 when $T = 225$ K.

shown in the previous section (6.5.3) the peak in λ is approximately at 225 K the peak has been attributed to a damping in the muon hopping or a increase in excitation frequency along the 1D stacks of TCNQ. If the muon is hopping at this temperature then application of an LF would decouple the relaxation from the distribution of fields that the muon couples to as it hops from site to site within its lifetime. However it may be that the applied field at this temperature is able to decrease the existence of fluctuations along the TCNQ stacks which would also lead to a decrease in λ_{LF}.

6.5.6 Summary

To summarise briefly the μSR experiments performed on KTCNQ-H_4 it has been shown that the muon relaxation is sensitive to the SP transition where, due to the shorter time scale of the experiment, the dynamics associated with the opening/closing of the spin gap is visible at lower temperatures then when using a static DC measurement. The relaxation below 300 K cannot be described by a stretched exponential and from fitting using a single exponential a peak in λ suggests that we are seeing a dynamical component dominate between 200 - 250 K. With the appli-

cation of a TF there is a substantial missing fraction that is observed and at 300 K there is a dramatic drop in λ at both long and short times which corresponds to the SP transition. From LF experiments at 225 K the relaxation changes as a field is applied suggesting that this is effecting the fluctuation rate within the sample however at 30 K the material is within a quasi-static state and at 340 and 410 K the fluctuations cannot be calmed by the application of a field and so the relaxation does not change.

6.5.7 KTCNQ-F_4

From the section on magnetic data (6.4) it is clear that substitution of the protons for fluorine atoms causes a dramatic shift in the SP transition. The temperature dependence has also been probed using μSR.

6.5.8 ZF μSR

A ZF μSR study was conducted on the KTCNQ-F_4 sample within the region of T_{SP}. The data could be best modelled using a stretched exponential in a similar way to the KTCNQ-H_4 sample where an increase in β coincided with the transition and indicating a change in relaxation from a single exponential to Gaussian, which is shown in figure 6.15. The raw data can be found in the appendix (figure C.5).

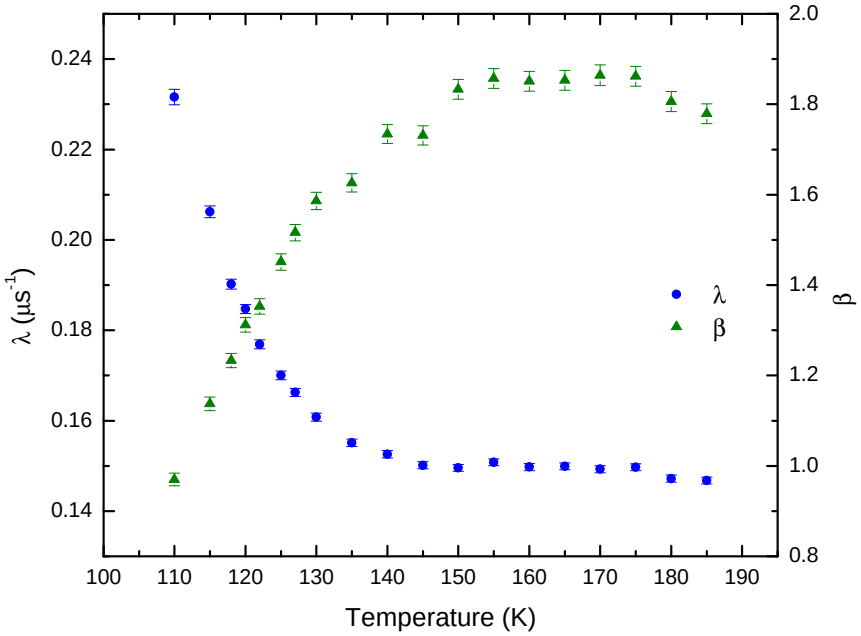

Figure 6.15: λ and β as a function of temperature for KTCNQ-F_4.

The decrease in λ is due to the increase in fluctuation rate as the sample changes to the paramagnetic state. The sample follows the same behaviour as the KTCNQ-H_4 sample and the value of λ settles off in both cases at $\sim$0.15 μs^{-1}. The asymmetry

shows an almost linear increase through the transition from 19.4 to 20.4% where the data can be seen in the appendix (figure C.6). The very small change in asymmetry shows that the majority of muons are deposed within the time scale of the measurement where above the transition a full fraction is recovered.

It should be noted that the baseline was fixed at 2.5% for this sample which is different to the H_4 experiment. This may have been due to a different sample holder being used which may have had a significantly lower baseline. It was not possible to perform a background run using hematite and so the value was estimated from fits to the ZF μSR spectra at high temperatures.

6.5.9 Low Temperature ZF μSR

The low temperature (< 100 K) data showed a more complex relaxation that could not be best described by a stretched exponential relaxation. Instead the data is better described a sum of two exponential relaxations similar to equation 5.2 shown in the previous chapter. The asymmetry remains constant within error at all temperatures except at 90 K where it diverges. Although there is a small missing fraction, this is not as significant as with the H_4 sample but it may indicate that some muons dephased outside of the EMU time window, possibly by strong internal fields.

The relaxation parameters, λ, are shown in figure 6.16 where the fact that there are two parameters points to two distinct muon sites. One component, λ_2, shows a very fast relaxation and the other, λ_1, a relaxation that is slow and of the order of the KTCNQ-H_4 sample. Both values are constant at low temperatures (to within error) and, in a similar manner to the asymmetry, increases at 90 K. This temperature is much lower than the transition temperature and so it may be that the muon is sensitive to fluctuations along the entire $TCNQF_4$ stack. It could also be the same case as before where the muon may be hopping and what we are seeing is a change in the overall Δ where the muon itself is mobile at 90 K.

Since one relaxation is very fast, we are seeing the tail end of the relaxation and it may be just outside of the EMU time window. If $\lambda \propto \Delta^2/\nu$ then there may

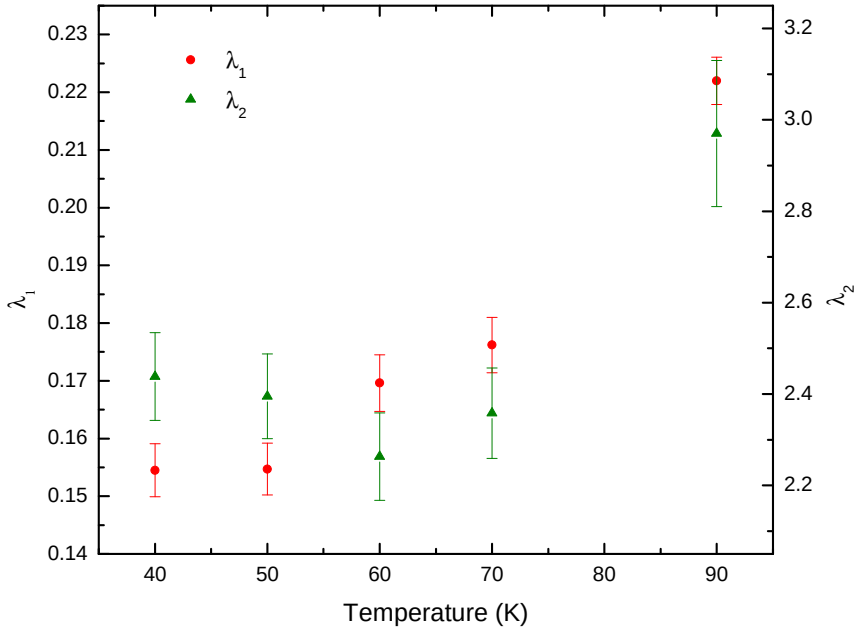

Figure 6.16: Low temperature λ vs. temperature for KTCNQ-F_4.

be a dramatic difference between the internal field distribution that the muon is experiencing between the two sites.

More detail can be observed at very short times where a damped oscillation is seen in the spectra (see figure 6.17). Due to the electronegativity and nuclear moment of the fluorine atoms this makes a muon site located near to the atom(s) considerably favourable. This effect has been observed in a few systems where the μ^+ is observed to couple to either one or two F atoms creating either an F-μ^+ or F-μ^+-F state [32–35]. Within the alkali halides the F-μ^+-F state is formed by 'pulling' together two F^- ions creating a hydrogen bond between the muon and F^- ion which causes a local lattice distortion where the separation is approximately the ionic radii of F^- [32]. When dealing within molecular systems the behaviour of the muon can be more complex [33].

It was found that for the data, the best fit was for the F-μ^+-F state, where there are two muon sites rather then simply an F-μ^+ interaction. The data were fit using the equation

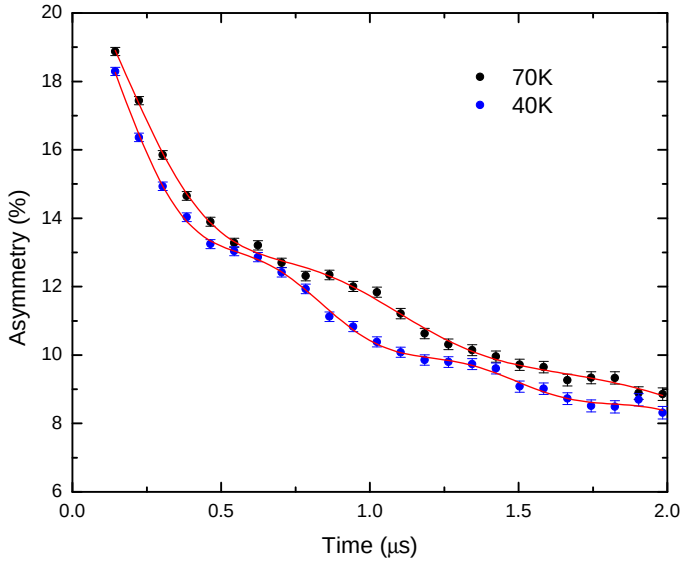

Figure 6.17: Low temperature raw data at short times showing the existence of oscillations. The solid lines correspond to a fit for the F-μ^+-F state.

$$G(t) = A_1 D_1(\omega_1, t)\exp(-\lambda_1 t) + A_2 D_2(\omega_2, t)\exp(-\lambda_2 t) + A_3\exp(-\lambda_3 t), \qquad (6.15)$$

where the 3rd component account for the strong relaxing background which may be due to muons being weakly dephased by random fields. The polarisation function, $D(\omega_i, t)$ describes the entanglement of the muon with the fluorine ions where

$$\begin{aligned} D(\omega_i, t) = \frac{1}{6}\Bigg[3 + \cos(\sqrt{3}\omega_i t) \\ + \left(1 - \frac{1}{\sqrt{3}}\right)\cos\left(\frac{3-\sqrt{3}}{2}\omega_i t\right) \\ + \left(1 + \frac{1}{\sqrt{3}}\right)\cos\left(\frac{3+\sqrt{3}}{2}\omega_i t\right)\Bigg]. \end{aligned} \qquad (6.16)$$

From the value of ω_i it is possible to calculate the distance between the muon and F atom using the relationship

$$\omega_i = \frac{\mu_0 \gamma_\mu \gamma_F \hbar}{4\pi r_i^3}, \tag{6.17}$$

where r_i^3 is the F-μ^+ distance, γ_{mu} is the gyromagnetic ratio of the muon and γ_F is the gyromagnetic ratio of the fluorine atoms. Since we have used a summation involving two separate values of ω_i, which provided the best fit to the data, this suggests that there are two different F-μ^+-F states within the sample at low temperatures when the sample is within the dimerised state. For site 1 the frequency of the oscillations shows a temperature dependence. For site 2, within error, the frequency is the same and the F-μ^+ distance is calculated to be 0.128±0.004 nm. The temperature dependence of site 1 is shown in figure 6.18.

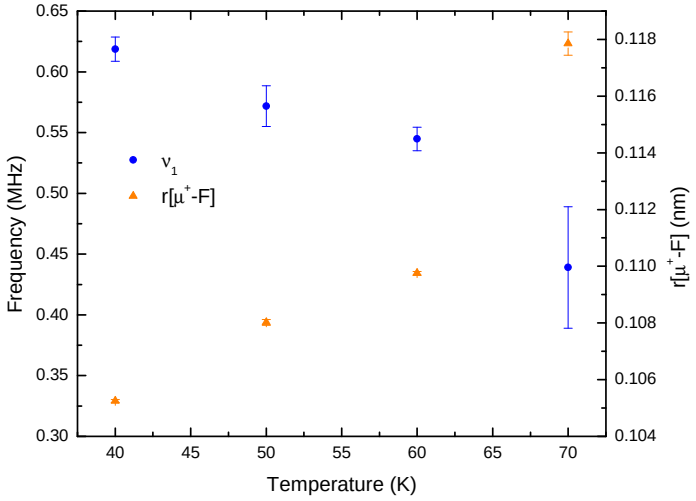

Figure 6.18: Temperature dependence of the frequency and F-μ^+ distance for site 1.

All other parameters associated with the fit are similar within error and so averages have been taken which are tabulated below (table 6.6).

Although the errors are large for the values of the parameters the values fit to the data it is clear that there is a strong relaxing component (3) that dominates the overall relaxation. The asymmetry for the two other components that correspond to the F-μ^+ coupling the asymmetry of component 2 is slightly higher however the relaxation rate between the two sites are roughly the same. From previous data

Fitting Component	Asymmetry (%)	λ_n (μs^{-1})
1	0.6(1)	1.0(2)
2	1.4(4)	1.4(4)
3	15.2(7)	0.29(3)

Table 6.6: Parameters for fits from equation 6.15 to the KTCNQ-F_4 data.

collected on KTCNQ crystal structure and neutral TCNQ the distance between the F atoms on a ring is likely to be of the order of 0.3 nm [10, 36]. It should be stressed that this is an assumption based on the KTCNQ-H_4 crystal structure as the crystal structure of KTCNQ-F_4 is unknown. Each distance for site 1 and 2 does not correspond to the bond distances between F atoms on the same TCNQ molecule or between F atoms on the TCNQ dimer and so no firm conclusions can be drawn. The implantation of a muon will distort the local environment and so it is no surprise that the calculated bond distances do not match the F-μ^+ distances [34]. However it would seem reasonable that these would be the two muon stopping sites as they would both produce different values of the field distribution and are thus inequivalent sites. These possible sites are shown in figure 6.19.

It is hard to distinguish which component corresponds to site 1 and site 2 as the distances calculated suggest that it could be either. However if the TCNQ-F_4 molecule is rigid then the temperature independent component may correspond to coupling between F atoms on the same TCNQ molecule and the temperature dependence of component 1 may be due to the increasing distance between dimers as T increases and thus the F-μ^+ distance will also increase.

The 3rd component which dominates the relaxation is relatively slow and means that the majority of muons are located at a site where there is a field distribution which is the cause of the muon dephasing. This site may not show coupling to the F atoms which may point to the muons coupling to the negative charge on the cyano groups at the end of a TCNQ molecule.

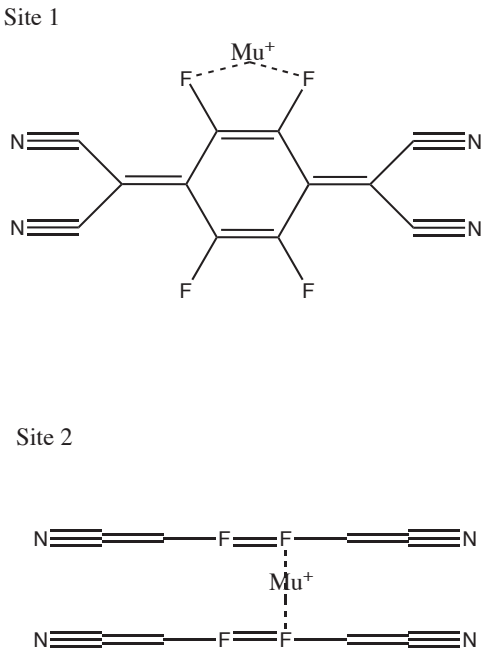

Figure 6.19: Possible muons stopping sites that give rise to the F-μ^+-F state observed. Site 2 shows coupling between TCNQ molecules within a dimer.

6.5.10 TF μSR

Experiments were performed in a TF of 100 G where the data could be split into two regimes; low temperature (< 100 K) and high temperature (> 100 K). Within this sample it is more clear from the raw data that there are at least two components to the TF muon spectra which can be seen in figure 6.20 at low temperature.

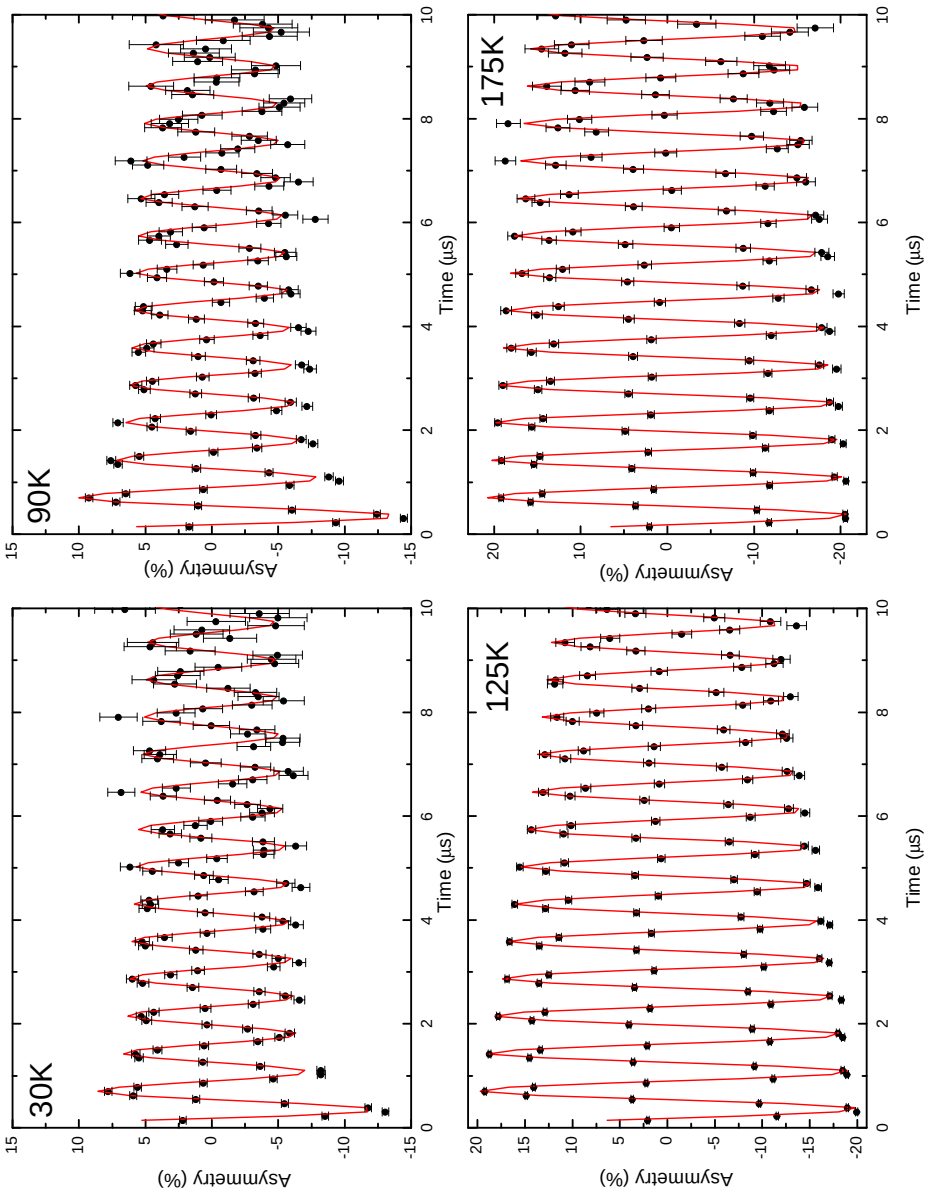

Figure 6.20: TF spectra for temperatures above and below T_{SP} for KTCNQ-F_4. The solid lines are fits to the data.

At high temperatures the data could be described in a similar way to the KTCNQ-H_4 TF data using equation 6.13. The rotational field could be fixed at 103 G where the only parameter that varied was the relaxation rate where the total asymmetry and λ can be seen in figure 6.21. The data show an increase in the total asymmetry going through the transition from below as well as a decrease in λ where the electronic fluctuations are increasing and the systems moves from a static to a paramagnetic state.

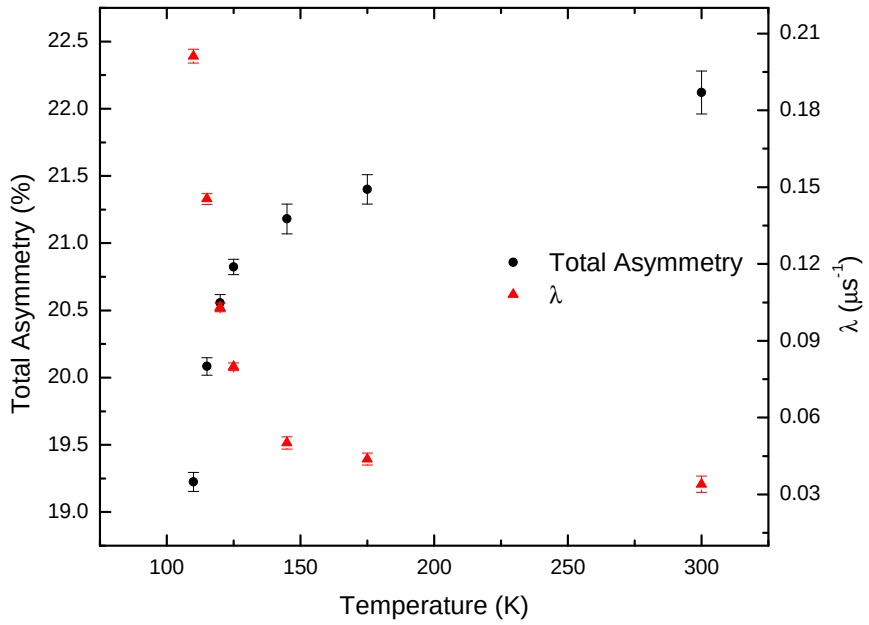

Figure 6.21: λ and asymmetry vs. temperature in an applied TF of 100 G at high temperatures.

One difference between the behaviour of the fluorinated sample to the protio sample is the absence of a substantial missing fraction at low temperatures. This may be due to a muonium species not being favourably formed due to the changes in electronic structure of the TCNQ anion from the substitution of F for H atoms.

The low temperature TF data is more complex and it is clear that there is at least two different relaxations, one which may be due to the formation of F-μ^+-F states as well as coupling of muon to the quasi-static electronic moment. Since the relaxation complicated a summation of oscillatory terms was used to describe the data where

all the total asymmetry and respective amplitudes of each component had to be fixed:

$$G(t) = A_1 \exp(-\lambda t) \cos(\gamma_\mu \mathbf{B}_{\mathrm{TF}} + \phi) + A_2 \exp(-\sigma t)^2 \cos(\gamma_\mu \mathbf{B}_{\mathrm{TF}} + \phi) + \mathrm{Bg}, \quad (6.18)$$

where Bg was defined previously for the KTCNQ-H_4 sample. The total asymmetry and phase was fixed at 22.5% and 8.37 respectively. The amplitudes of the individual components had to be fixed in order to produce a good fit to the data where $A_1 = 16\%$ and $A_2 = 2\%$, the value of sigma was also fixed at 0.14 μs^{-1} which provided an improved fit to the data. This Gaussian component was added to approximately describe the coupling of the muon to the F atoms within the sample although the majority of the muons are dephased by the fast relaxing exponential component. The rotational field could be fixed to 103 G and showed little variation with temperature that was not accounted for within the error.

The dependence of λ as a function of temperature is shown in figure 6.22 where the increase between 30 and 40 K may be due to fluctuations entering the time scale of the muon where a gradual decrease is observed as T is increased further however one cannot neglect changes to the F-μ^+-F state. The values for the relaxation show a very fast dependence and there is a large drop between the low and high temperature regime. This is likely to be due to the convolution of F-μ^+-F and electronic fluctuations that cause the muons to dephase where it is hard to unravel these components.

It is known that the F-μ^+-F state shows a temperature dependence and in fluorinated polymers the change is due to movement of the F atoms through lattice excitations such as rotational motion [33]. We may be observing something similar where the uniform lattice structure will start to break down and the system will change phase from the dimerised state to a paramagnetic, equally spaced, $TCNQF_4$ unit system. At low temperatures the muon may be located between two F atoms on separate TCNQ molecules within the dimer, however as this structure begins to break down, the spacing will change and it may no longer be favourable for this state to exist.

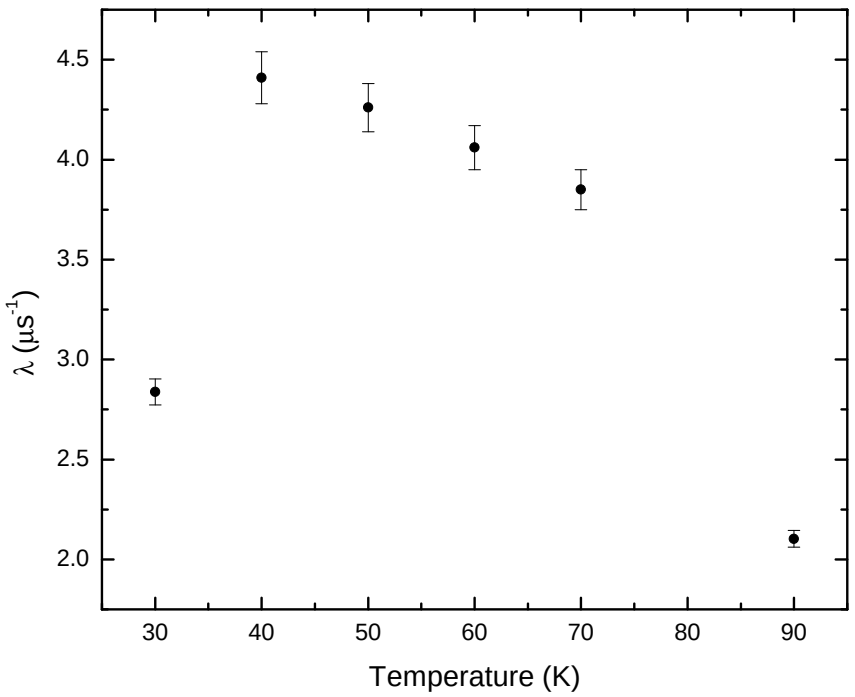

Figure 6.22: λ vs. temperature in an applied TF of 100 G at low temperatures.

However the F-μ^+-F state may be present up to much higher temperatures as these states have been shown to exist well above the critical transition [37].

Although the data are not fully understood at present, it is clear that there is no similarity to the magnetic data and so all the low temperature effects seen within this sample must be due to muon induced changes or states within the material. It is likely that the F-μ^+-F state is observed in the TF experiments as well as in ZF however recovery of a missing fraction can be due to changes in internal field distributions, slowing down of fluctuation rates or even the thermal ionization of muonium. Generally with an applied TF at small values, muons that form paramagnetic muonium are dephased very rapidly and so they relax outside of our measurable time scale.

6.5.11 LF Sweep at 30 K

Data were collected at 30 K where there is clear evidence that the relaxation is complex as there will be an electronic contribution from the quasi-static spins on the TCNQF4 anions where there may be multiple stopping sites, and coupling of the muon to fluorine atoms, again which has two stopping sites. Raw data are shown within the appendix (figure C.8). The data are hard to fit for this reason but the most reasonable fitting function was found to be a single exponential. In ZF this does not completely capture the fast relaxation however in an applied field the slower relaxation is damped and so the fitting function can model the fast relaxation better, which is why an increase in λ_{LF} is observed. The increase shows there are at least two components in ZF however there is a dramatic change at 100 G LF which may be decoupling of the F-μ^+-F state.

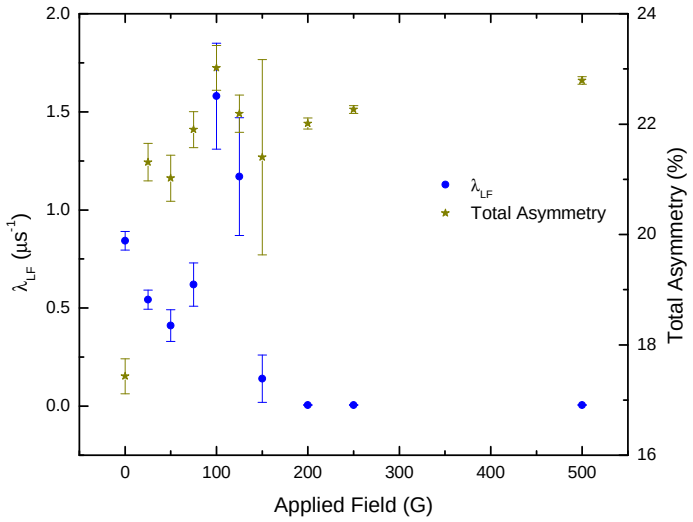

Figure 6.23: Parameters for the 30 K LF sweep for KTCNQ-F_4.

Above 200 G the relaxation is damped and almost a full asymmetry is recovered. This would mean that there is little dynamics associated with the magnetism and the TCNQ dimers are essentially quasi-static within the time scale of the muon experiment. The fact that a relatively weak field is needed to recover a full asymmetry also suggests that there is not a strong coupling between the muon and the

electronic magnetism of the sample.

6.6 Summary and Conclusion

In the course of this preliminary work we have made a variety of KTCNQ salts : KTCNQ-H_4, KTCNQ-D_4, KTCNQ-F_x ($x = 2, 4$) and KTCNQ-Br_2 salts. Both magnetometry and μSR experiments were performed on selected samples. Although KTCNQ-D_4 was made it has not been possible to get any magnetic measurements on the sample. In fact a μSR experiment was attempted on the material but, due to the relatively large impurity of KI, this meant that a large fraction of the muons formed muonium which is common within the alkali halides [38]. This meant that there was very little muon relaxation and, therefore, information that could be gained from the data.

Within this chapter preliminary results on previously unknown TCNQ based compounds were presented where changing the substituent on the TCNQ ring to a more electronegative atom has shifted the SP transition to a much lower temperature. Within the previous chapters on $NiTCNQ_2$ the change from hydrogen to deuterium caused a change in T_C which may be due to changes in electron phonon coupling. This may be similar in KTCNQ-F_x where the phonon energies will be expected to change, however since there is little difference between the response of the F_4 and F_2 variants it suggests that the shift may be due to changes in the electronic structure of the TCNQ molecule. Using Br as a substituent changes the properties of the system dramatically where there is no evidence of a SP transition within the T range we have measured. The magnetic data for all samples are relatively poor and the Bonner-Fisher expression could not be fit to the high temperature data. It may be that, within the SP state, the moment is zero and there is a small diamagnetic background that is being measured which is close to the limit of the sensitivity of the magnetometer. Also the Quantum Design software can have trouble fitting the magnetic dipole moment when the moment is close to zero or going through zero. To improve the measurement the density of the sample must be increased to give a larger moment, possibly by compressing into pellets.

Curiously there is a dramatic effect that cannot be explained at this time within the

KTCNQ-H_4 magnetic results where, at approximately 100 K, a step in the data is observed. It is thought that this is due to the magnetic history of the sample where application of a large field and cooling leads to a frozen state of spins. These spins may arise from uncompensated TCNQ molecules or from the dimers themselves however more work is needed to reach a conclusion.

From the μSR experiments we observed a similar behaviour to that within MEM(TCNQ)$_2$ within the KTCNQ-H_4 and the KTCNQ-F_4 [14, 15]. In ZF the muons are sensitive to the dynamics within the system where below T_{SP} the relaxation is electronic in origin and can be modelled by a single exponentia. However, above T_{SP} the relaxation changes to a Gaussian form which is due to depolarising of the muon ensemble by the static nuclear moments within the TCNQ molecule. Within the critical region the relaxation is modelled using a stretched exponential function which accounts for the convolution of the exponential and Gaussian relaxations. We observe a β parameter that goes from just below 1 to 2 as the sample is heated through the transition. At low temperatures, where $T < 300$ K, the relaxation can no longer be modelled using a single exponential and within KTCNQ-H_4 a sum of two exponentials is needed. This may be due to there being more then one muon stopping site within the material. The λ and asymmetry both show a rise starting at 200 K which may be when the excitations along the quasi-1D stacks of TCNQ come into the muon time scale. There is a missing fraction at low temperatures which requires further investigation before its origin is understood.

Within KTCNQ-F_4 the transition is similar to the KTCNQ-H_4 sample however the using μSR we have confirmed that the SP transition has been shifted to approximately 160 K. The relaxation at low temperature is more complicated as there is evidence of an oscillatory component that has been modelled using a sum of two F-μ^+-F states and a exponential relaxation. One F-μ^+-F site shows a temperature dependence and the other is temperature independent where the F-μ^+ distances were calculated in section 6.5.9. Using this analysis it is possible to identify two muon stopping sites within the sample. However, there is a slow relaxing background that accounts for most of the asymmetry which may be coupling of the muon to the

cyano groups on the TCNQ molecule.

Due to time constraints with the experiment it was not possible to get a complete set of LF data for this sample and so this poses a problem as we could not detect the decoupling of this F-μ^+-F state and, hence study whether there is another contribution to the muon relaxation. Such an investigation is paramount and will be attempted in the future.

From the work described within this chapter it is clear that simply by changing the substituents on the TCNQ ring this has dramatic effects on the magnetism and coupling of the TCNQ dimers within the SP state. More work is needed to reinforce these preliminary studies but current results suggest that these TCNQ based magnetic systems may show complex behaviour and simple altering of the TCNQ moiety can lead to an effective way to tune the magnetic properties of the desired materials.

There is a large amount of future work that needs to be undertaken to fully understand the magnetism within these materials. The simplest and one of the most necessary are experiments on the structure of both KTCNQ-F_x and KTCNQ-Br_2 to see whether there are dramatic steric changes caused by the addition of the large bromine atoms to the ring that results in no SP transition being observed. More magnetic measurements are needed so one can calculate exchange energies involved in the dimerisation of the TCNQ spins and begin to quantify the effect of substitution of the protons on the TCNQ ring for other elements. Muon data from $Ni(TCNQ\text{-}D_4)_2$ under an applied pressure suggest that there is evidence that the system falls into a paramagnetic state with pressure which may be due to dimerisation of the TCNQ units i.e. they lock out and the remaining magnetism is from the paramagnetic isolated Ni ions. To understand whether this mechanism is true and if a Peierls transition occurs under applied pressure, a pressure study of KTCNQ may be necessary.

Bibliography

[1] J. C. Bonner and M. E. Fisher. *Phys. Rev.* **135** (1964) A640

[2] W. E. Estes, D. P. Gavel, W. E. Hatfield, D. J. Hodgson. *Inorg. Chem.* **17** (1978) 1415

[3] O. Kahn. Molecular Magnetism. VCH Publishers, New York. (1993) 251

[4] L. N. Bulaeskii. *Soviet Physics - Solid State* **11** (1969) 921

[5] J. W. Bray, H. R. Hart Jr., L. V. Interrante, I. S. Jacobs, J. S. Kasper, G. D. Watkins, S. H. Wee and J. C. Bonner. *Phys. Rev. Letts* **35** (1975) 744

[6] E. Pytte. *Phys. Rev. B.* **10** (1974) 4637

[7] S. D. Obertelli, R. H. Friend, D. R. Talham, M. Kurmoo and P. Day. *J. Phys.: Condens. Matter.* **1** (1989) 5671

[8] J. G. Vegter, T. Hibma and J. Kommandeur. *Chem. Phys. Lett.* **3** (1969) 427

[9] Y. Takaoka and K. Motizuki. *J. Phys. Soc. Jpn.* **47** (1979) 1752

[10] M. Konno, T. Ishii and Y. Saito. *Acta Cryst.* **B33** (1977) 763

[11] Y. Lépine, A. Caillé and V. Larocholle. *Phys. Rev. B.* **18** (1978) 3585

[12] A. Bosch and B. Van Bodegom. *Acta Cryst.* **B33** (1977) 3013

[13] S. Huizinga, J. Kommandeur, G. A. Sawatzky, B. T. Thole, K. Kopinga, W. J. M. de Jonge and J. Roos. *Phys. Rev. B.* **19** (1979) 4723

[14] S. J. Blundell, F. L. Pratt, P. A. Pattenden, M. Kurmoo, K. H. Chow, S. Takagi, Th. Jestädt and W. Hayes. *J. Phys.: Condens. Matter* **9** (1997) L119

[15] B. W. Lovett, S. J. Blundell, F. L. Pratt, Th. Jestädt, W. Hayes, S. Tagaki and M. Kurmoo. *Phys. Rev. B.* **61** (2000) 12241

[16] M. R. Crook and R. Cywinkski. *J. Phys.: Condens. Matter* **9** (1997) 1149

[17] K. Nishiyama, Y. Morozumi, T. Suzuki and K. Nagamine. *Phys. Letts.* **111** (1985) 369

[18] Hp. Baumeler, R. F. Kiefl, H. Keller, W. K undig, W. Odermatt, B. D. Patterson, J. W. Schneider, T. L. Estle, S. P. Rudaz, D. P. Spencer, K. W. Blazy and I. M. Savic. *Hyperfine Interact.* **32** (1986) 659

[19] R. Kadono, A. Matsushita, K. Nishiyama, K. Nagamine. *Hyperfine Interact.* **87** (1994) 979

[20] L. R. Melby, R. J. Harder, W. R. Hertler, W. Mahler, R. E. Benson and W. Mochel. *J. Am. Chem. Soc.* **84** (1962) 3374

[21] D. Dolphin, W. Pegg and P. Wirz. *Can. J. Chem.* **52** (1974) 4078

[22] http://www.sigmaaldrich.com/united-kingdom.html (July 2012)

[23] http://www.tcichemicals.com/en/gb/ (July 2012)

[24] F.L. Pratt. *Physica B.* **710** (2000) 289

[25] G. A. Bain and J. F. Berry. *J. Chem. Educ.* **85** (2008) 532

[26] J. G. Lussier, S. M. Coad, D. F. McMorrow and D. McK. Paul. *J. Phys.: Condens. Matter.* **7** (1995) L325

[27] A. I. Smirnov, V. N. Glazkov and S. S. Sosin. *J. Exp. Theor. Phys. Letts.* **77** (2003) 442

[28] A. I. Smirnov, V. N. Glazkov, L. I. Leonyuk, A. G. Vetkin and R. M. Eremina. *J. Exp. Theor. Phys.* **87** (1998) 1019

[29] R. C. Wheland and J. L. Gillson. *J. Am. Chem. Soc.* **98** (1976) 3916

[30] M. D. Harvey and T. D. Crawford and G. T. Yee. *Inorg. Chem.* **47** (2008) 5649

[31] M. R. Bryce, A. M. Grainger, M. Hasan, G. J. Ashwell, P. A. Bates and M. B. Hursthouse. *J. Chem. Soc. Perkin Trans.* **1** (1992) 611

[32] J. H. Brewer, S. R. Kreitzman, D. R. Noakes, E. J. Ansaldo, D. R. Harshman and R. Keitel. *Phys. Rev. B.* **33p** (1986) 7813

[33] T. Lancaster, F. L. Pratt, S. J. Blundell, I. McKenzie and H. E. Assender. *J. Phys.: Condens. Mater.* **21** (2009) 346004

[34] T. Lancaster, S. J. Blundell, P. J. Baker, M. L. Brooks, W. Hayes, F. L. Pratt, J. L. Manson, M. M. Conner and J. A. Schlueter. *Phys. Rev. Lett.* **99** (2007) 267601

[35] T. Lancaster, S. J. Blundell, P. J. Baker, W. Hayes, S. R. Giblin, S. E. McLain, F. L. Pratt, Z. Salman, E. A. Jacobs, J. F. C. Turner and T. Barnes. *Phys. Rev. B.* **75** (2007) 220408(R)

[36] R. E. Long, R. A. Sparks and K. N. Trueblood. *Acta. Cryst.* **18** (1965) 932

[37] A. J. Steele, T. Lancaster, S. J. Blundell, P. J. Baker, F. L. Pratt, C. Baines, M. M. Conner, H. I. Southerland, J. L. Manson and J. A. Schueter. *Phys. Rev. B.* **84** (2011) 064412

[38] R. Kadono, A.Matsushita, K. Nishiyama and K. Nagamine. *Hyperfine Interactions* **87** (1994) 979

Chapter 7

Controlling Nickel Nanoparticle Size in a Metal/Metal-Organic Matrix Through the Use of Different Solvents

7.1 Introduction

In a recent publication, it was reported that a novel high-temperature metal-organic magnet (T_C >∼400 K) could be synthesized by reacting bis-(1,5-cyclooctdiene) nickel ($Ni(COD)_2$) with the organic acceptors (A);
2,3-dichloro-5,6-dicyano-1,4-benzoquinone (DDQ), tetracyanoethylene (TCNE) and 7,7,8,8-tetracyanoquinodimethane (TCNQ) to produce charge transfer salts Ni_2A, via a redox reaction, using dichloromethane (DCM) as the solvent [1]. The Ni_2A systems were reported to be amorphous yet still show bulk ferromagnetic behaviour at room temperature (see figure 7.1) similar to $V(TCNE)_x{\cdot}y(DCM)$, where $x = 2$ and $y = 0.5$ approximately [2]. It was suggested that in this charge transfer compound there was antiferromagnetic exchange between the donor and acceptor spins that resulted in a ferrimagnetic system [2]. Miller *et al.* further investigated the

Ni_2A system by reacting $Ni(COD)_2$ with tetracyanoethylene (TCNE) in tetrahydrofuran (THF) which resulted in a mixed product material where it was suggested that one component consisted of Ni nanoparticles formed from the decomposition of $Ni(COD)_2$ and accounted for the remanent magnetisation at room temperature. Another component that was thought to be present was $Ni(TCNE)_2 \cdot THF$ which is a paramagnetic compound that displays magnetic ordering at low temperatures. Reacting the $Ni(COD)_2$ and TCNE in a 1:2 ratio resulted in a paramagnetic $Ni(TCNE)_2$ compound with a temperature independent magnetic component below 200 K [20]. There have also been other cyano-based metal-organic room temperature ferromagnets reported such as Prussian Blue analogues [4–6]. These compounds have the chemical formula $A_k[B(CN)_6]_l \cdot nH_2O$ where Prussian Blue itself has a T_C = 5.5 K (with formula $Fe_4^{III}[Fe^{II}(CN)_6]_3 \cdot 15\ H_2O$) where the low transition temperature is due to the weak interactions between the low spin Fe^{II} (S = 0) and the high spin Fe^{III} (S = 5/2) ions with the distance between them being ∼10 Å. The properties of these magnets can be tuned by using different transition metals and oxidation states in the A and B sites. Mallah *et al.* used chromium (III) in the B sites as the electrons are within the t_{2g} orbitals and are delocalised over the cyanide ligands which provides an exchange route in three spacial directions [5]. The study of Prussian Blue analogues have been extended to include various transition metals and mixed valency states where room-temperature ferromagnetism is observed [7].

Varying the solvents within metal-organic reactions can lead to dramatic effects. Miller and Epstein who reproduced the $V(TCNE)_x \cdot y(DCM)$ using different solvents: Tetrahydrofuran (C_4H_8O) and acetonitrile (CH_3CN). It was shown that simply by varying the solvent the T_C was changed with the most polar solvent resulting in the lowest transition temperature[1]. $V(TCNE)_x \cdot y(THF)$ shows a T_C = 210 K and $V(TCNE)_x \cdot y(CH_3CN)$ has a T_C = 140 K [8–10]. The reduction in transition temperature was attributed to the increased disorder induced by the more polar solvent. From x-ray diffraction studies the structural short range order is greater

[1]The polarities of the solvents used by Miller and Epstein in decreasing order: Acetonitrile, THF and DCM

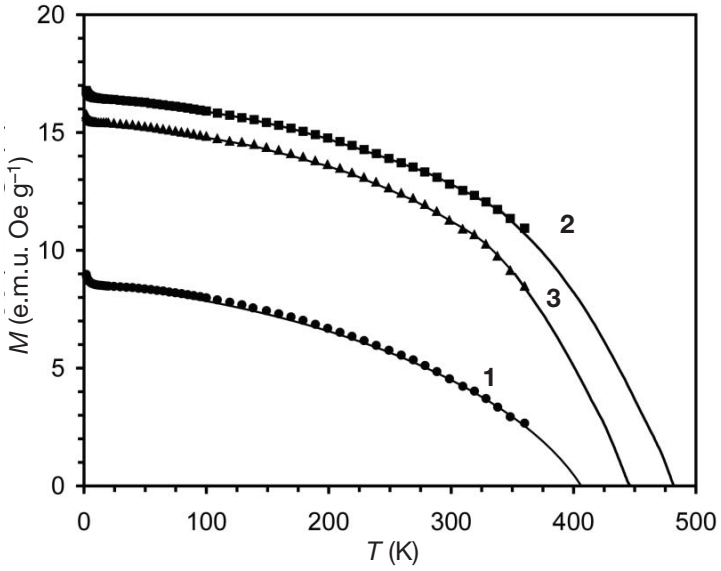

Figure 7.1: Temperature dependence of the field cooled magnetisation (B = 25 G) of the three samples synthesised by Jain *et al.* where 1. DDQ, 2. TCNQ and 3. TCNE [1].

in the less polar solvent: DCM (25 Å), THF (15 Å) and CH_3CN (10 Å) [8, 9]. The increased randomness is due to the affinity of the solvent for the V(II) ion; THF and acetonitrile can bond with the magnetic ion via the oxygen and nitrile group respectively. If a solvent group is directly bonded to the vanadium then this will create a spinless spacer between the ions within the structure and interrupt the magnetic exchange. Since the isonitrile group is most effective at bonding to the vanadium it is no surprise that this shows the lowest T_C [10]. Miller and Epstein used the Random Magnetic Anisotropy (RMA) theory developed by Chudnovsky *et al.* [11, 12] to show that this was a 3-dimensional system with some random anisotropy and disorder. $V(TCNE)_x \cdot y(CH_3CN)$ showed a remarkable difference to the other two materials where a spin glass phase was present at low temperatures ($T_f \sim 10$ K) indicating the possible of the existence of magnetic frustration [9]. Using a Chemical Vapour Deposition (CVD) method with reactants $V(CO)_6$ and TCNE resulted in a non-stochiometric sample ($V[TCNE]_x$) that shows more structural order then when a wet chemical route is used [13]. Although thermal analysis confirmed there was trapped CO within the compound, this accounted for less than 1% and so there was

a dramatic change in magnetic properties, especially for M(H), when using the CVD preparation route. The saturation magnetisation of the bulk solvated sample reached ~85% of the value calculated for a $V(TCNE)_2 \cdot 0.34(CH_2Cl_2)$ system (16.6 emu Oe g^{-1}) where as the film reached 98% of the expected saturation magnetisation value for the stoichiometric $V(TCNE)_2$ sample (18.18 em Oe g^{-1}) illustrating the remarkable difference. At low temperatures within all the solvent systems considered there is a glassy component and although within $V(TCNE)_x \cdot y(DCM)$ the solvent does not influence the T_C the disorder created does increase the effect of the spin glass phase. The CVD method results in a material that lacks the structural defects which leads to a different response shown by the $M(H)$ curves and enhanced chemical and magnetic stability [13].

In this work we are focusing on TCNQ analogues in a similar fashion to Jain *et al.* [1]. TCNQ was first discovered by Acker and Hertler and it was noted to be a very effective at stabilising an anion radical [14]. $Ni(TCNQ)_2 \cdot 3H_2O$ was one of the many compounds that were synthesised where the Ni and TCNQ were in their stochiometric ratio with water present as a stabilising ligand [15]. Clérac *et al.* synthesized an unsolvated form of $Ni(TCNQ)_2$ that was reported to show a magnetically glassy behaviour and a freezing temperature of 20.8 K. Their work suggested two spin centres within the material and the possibility of antiferromagnetic interactions between different spins. Although powder x-ray diffraction data were obtained, the crystal structure could not be determined and it was proposed that $Ni(TCNQ)_2$ has a tetragonal structure where a =16.90 Å and c = 8.78 Å [16] (also see Chapters 4 & 5).

$TCNQF_4$ is another derivative of TCNQ that behaves in a similar fashion and is also effective at stabilising an anion radical. TCNQ and $TCNQF_4$ salts can have different crystal structures, which is due to the different electronic and spatial extent of the two organic acceptors, and both salts show interesting magnetic properties [17]. $AgTCNQF_4$ has been synthesised and has been shown to form a monoclinic structure where the $TCNQF_4$ units are stacked parallel along the b-axis with the Ag atom in a tetrahedral environment [17].

The precursor used by Jain *et al.* in their metal-organic redox reactions was $Ni(COD)_2$, which is a widely used material with many applications [18] such as in the creation of Ni nanoparticles. Such a process is effective due to the material's labile nature and its autocatalytic decomposition from Ni(0) to bulk Ni. There are many synthetic routes to control the decomposition, one of the simplest is applying energy to the system using sonication [19] which has been used to produce Ni particles encapsulated in carbon that behave superparamagnetically [23, 24]. Nanoparticles that are dispersed within a matrix can show some very interesting magnetic properties that are related to interactions between the moments on each particle. Competing interactions and changes in particle size can cause a system to show superparamagnetic, super spin glass or super ferromagnetic properties [22–24].

Here we report on the synthesis and magnetic characterisation of Ni nanoparticles dispersed within a metal-organic matrix. The Ni nanoparticle size can be controlled using different solvents and it is a room temperature syntheic process. The samples synthesized can be separated into two general categories; one showing larger Ni particles of approximately 10 nm and the other with particle sizes of 1-2 nm. In addition, both types particle are embedded within a paramagnetic metal-organic matrix, probably consisting of radical-anion form of $TCNQF_4$ and Ni ions, and we provide evidence that this matrix may be important in mediating magnetic interactions between the Ni nanoparticles.

7.2 Experimental

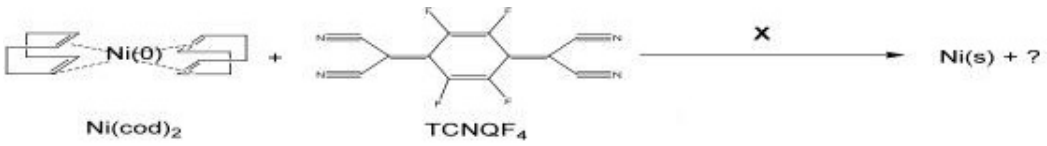

Figure 7.2: Reaction scheme where **X** = DCM, THF/DCM, THF/MeCN, THF/DCB or THF/PhCN.

$Ni(COD)_2$ (98+%) was purchased from Strem Chemicals UK and the $TCNQF_4$

(99.99%)was purchased from Durham Research and Synthesis. The solvents were dried, degassed and stored under an inert atmosphere. The $TCNQF_4$ was dissolved in a solvent and and added to the $Ni(COD)_2$ in a 1:2 ratio which produced a dark brown/black precipitate almost immediately except when using nitrile based solvents where a green intermediate was bypassed. All reactions were conducted under argon using a Schlenk line where the ratios of solvents used are shown in Table 1. Note that THF was used to stabilise the $Ni(COD)_2$ so that decomposition did not occur so rapidly, preventing bulk nickel formation and enhancing the chance of $Ni(COD)_2$ reacting with the $TCNQF_4$ to form a charge transfer system as TCNQ derivatives are very effective at stabilising radical anions.

Sample	$Ni(COD)_2$ Solvent	$TCNQF_4$ Solvent	Ratio
1	-	DCM	-
2	THF	DCM	1:4
3	THF	MeCN	1:4
4	THF	DCB	1:4
5	THF	PhCN	1:4

Table 7.1: Solvents used in the reaction of $Ni(COD)_2$ and TCNQ. DCM = dichloromethane, THF = tetrahydrofuran, MeCN = acetonitrile, DCB = dichlorobenzene and PhCN = benzonitrile.

Elemental analysis[2] was performed on a Dionex DX120 as well as ICPMS (Inductively Coupled Plasma Mass Spectroscopy)[3] was performed using a Perkin Elmer-Sciex Elan 6000; the results were used to obtain information on the compositions of each sample. An important parameter is the N:Ni ratio which gives the stoichiometry of the system and, assuming an ideal system of $Ni_2(TCNQF_4)$, one would expect N:Ni = 2:1. The compositional data of the five materials synthesized are shown in Table 2. Using these data we calculate the following N:Ni ratios; Sample 1: 1.22:1; Sample 2: 3.48:1; Sample 3: 2.98:1; Sample 4: 1.07:1; Sample 5; 1.51:1. Clearly,

[2]Used to determine the carbon, nitrogen and hydrogen content

[3]Used to determine the nickel content

all five samples do not agree with the $Ni_2(TCNQF_4)$ formula unit. In fact the following stoichiometries are suggested from these results: Sample 1: $Ni_{3.3}(TCNQF_4)$; Sample 2: $Ni_{1.2}(TCNQF_4)$; Sample 3: $Ni_{1.3}(TCNQF_4)$; Sample 4: $Ni_{3.7}(TCNQF_4)$; Sample 5: $Ni_{2.7}(TCNQF_4)$.

Sample	1	2	3	4	5
Ni (%)	27.30	12.70	13.80	32.70	26.30
C (%)	25.05	35.94	39.04	24.91	31.32
H (%)	1.13	1.88	2.83	2.10	2.55
N (%)	7.97	10.54	9.82	8.32	9.48
Total (%)	61.45	61.06	65.49	68.03	69.65

Table 7.2: Table showing the elemental analysis of the samples. Ni content was determined using inductively coupled plasma mass spectroscopy (ICPMS).

Different experiments were undertaken to study both the structure and magnetic properties of the materials. A JEOL 2100F FEG Transmission Electron Microscope (TEM) was used to obtain TEM and Electron Energy Loss Spectroscopy (EELS) images of the samples for morphological and compositional studies. A Siemans D5000 with a Cu source was used record Powder X-Ray Diffraction (PXRD) patterns from each sample to gain further insight into the composition and crystallinity of the materials. Magnetic characterisation was carried out using a Quantum Design Magnetic Properties Measurement System (MPMS) at magnetic fields of up to 5 T and in a temperature range of 2 K to 300 K.

7.3 Results and Discussion

7.3.1 Physical Characterisation

TEM and EELS compositional images for sample 1 are shown in Fig. 7.3. Particles are clearly visible and, at 70-80 nm, are relatively large; EELS revealed that these areas are very Ni rich. The EELS N map (Fig. 7.3.4) suggests that the majority of nitrogen (and hence organic material) in the sample resides between the particles (i.e. in the matrix). A similar conclusion is suggested when considering the EELS F map. However, there is evidence for nickel within the matrix suggesting that it is a metal-organic compound albeit rich in organic material. The diffuseness of the particles in the TEM images for samples 1, 2 and 4 suggest that they are actually composed of an agglomerate of smaller particles.

The TEM and EELS images for sample 2 (Fig. 7.4) are similar to those of Fig.7.3 except the particle sizes are almost half the size of the particles in sample 1. From the EELS images it is clear that these small particles are Ni rich and are probably Ni nanoparticles in an organic/metal-organic matrix. The images of both samples 1 and 2 suggest that the particles are clustering though this is less pronounced in sample 2. Clustering in magnetic nanoparticulate systems is not uncommon and in many cases it is possible to see chaining of the particles or formations of rings so that there is flux closure [25, 26].

Sample 3 displays a radical difference to the previous two samples (Fig. 7.5). The particles are very small ($\sim$2-8 nm) and appear to be very well dispersed within the matrix. Due to the small size of the particles it was not possible to perform EELS over a large area and we were confined to using only a 'spot' analysis. From the EELS spot analysis (Fig. 7.5.2) we found that there was a peak at 855 eV which corresponds to Ni suggesting that although these particles are small they are also Ni rich and most likely Ni nanoparticles. The Bright Field (BF) and High Angle Annular Dark Field (HAADF) images show the extent of this dispersion of the particles within the matrix.

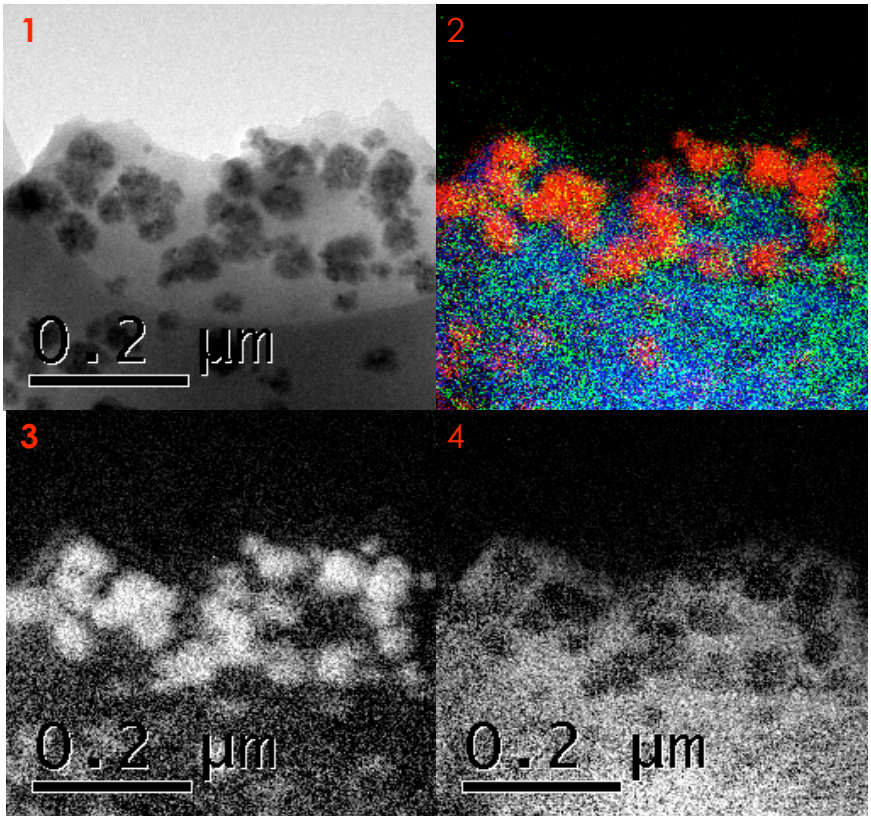

Figure 7.3: Sample 1 (solvent DCM) shows Ni rich areas within a crystalline matrix. 1) Elastic image; 2) overlay of EELS maps Red=Ni, Green=N and Blue=F ; 3) Ni map using EELS; 4) N map using EELS.

Fig. 7.6 shows a generic picture indicative of Sample 4. Using DCB instead of DCM has produced a similar result to Sample 1 though the particle sizes are much smaller and, from the EELS images, it is clear that the particles are very Ni rich; clearly we are observing the same type of material with Ni nanoparticles in an organic/metal organic matrix. Note that the N map (Fig. 7.6 .4) suggests a nitrogen content that is more homogeneous than seen for samples 1 and 2 but this may be due to the imaged sample being quite thin with organic matrix above and below the nanoparticle regions.

Sample 5 (Fig. 7.7) is similar to Sample 3 but it is only from the HAADF image that one can detect evidence for the existence of nanoparticles. The nanoparticles appear very well dispersed and the presence of a matrix is still detectable. Note

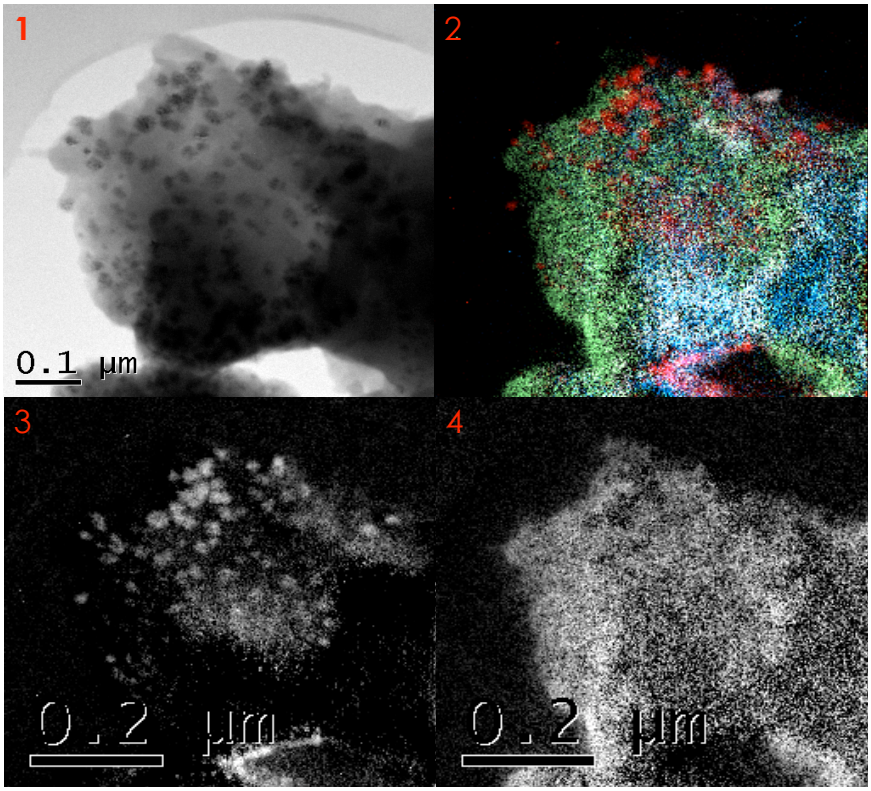

Figure 7.4: Sample 2 (solvent THF/DCM) also shows Ni rich areas. 1) Elastic Image; 2) overlay of EELS maps Red=Ni, Green=N, Blue=F and White=O; 3)Ni maps using EELS; 4) N map using EELS.

that the nanoparticles are so small that it was not possible to perform any type of EELS to determine their composition, however, given the similarity to sample 3, it may be reasonable to assume that these particles are also Ni rich.

Powder Diffraction experiments were performed on the different samples. Samples 1,2 and 4 all have characteristic face centred cubic (FCC) Ni peaks within the x-ray diffraction patterns. The peaks are very broad due to the small nature of the Ni nanoparticles. This supports the conclusion from the TEM images that within these three samples the main component is Ni nanoparticles however at low angles there does appear to be structure that could be attributed to the metal-organic matrix. This is most prominent in Sample 2 (solvent THF/DCM) where there are visible peaks that do not match any phase of bulk Ni and, given the small values of 2θ, they may be associated with a structure that has large cell parameters e.g. a

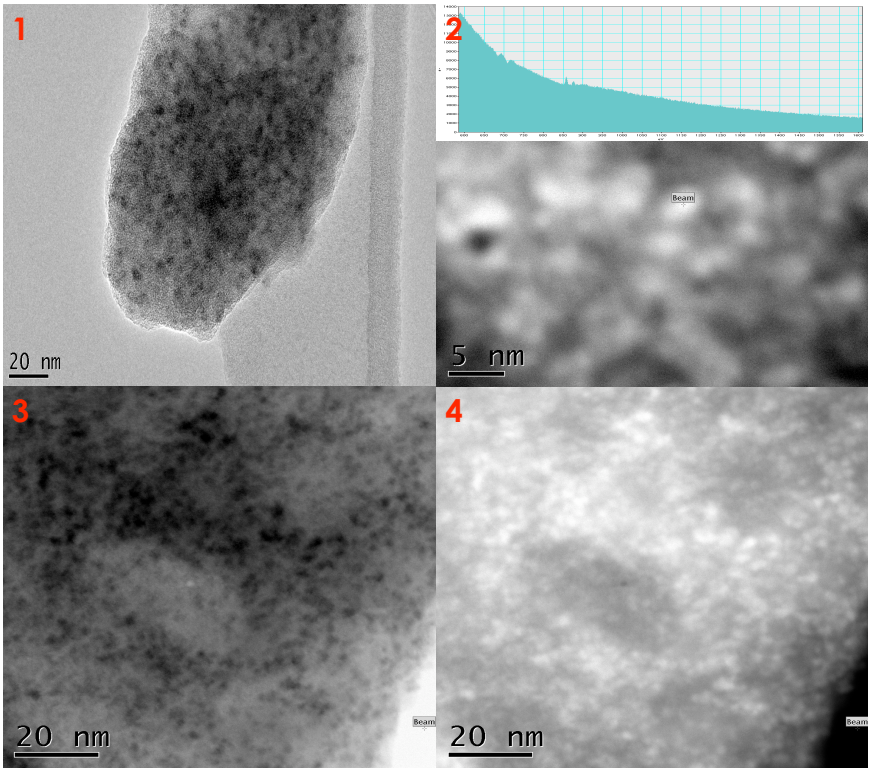

Figure 7.5: Sample 3 (solvent THF/MeCN). 1) Image of area showing small particles 5 nm; 2) spot analysis using EELS of a particle in TEM image, graph shows peak at 855 eV which corresponds to Ni; 3) BF Image showing small particles; 4) HAADF image, the brighter areas have a higher Z number.

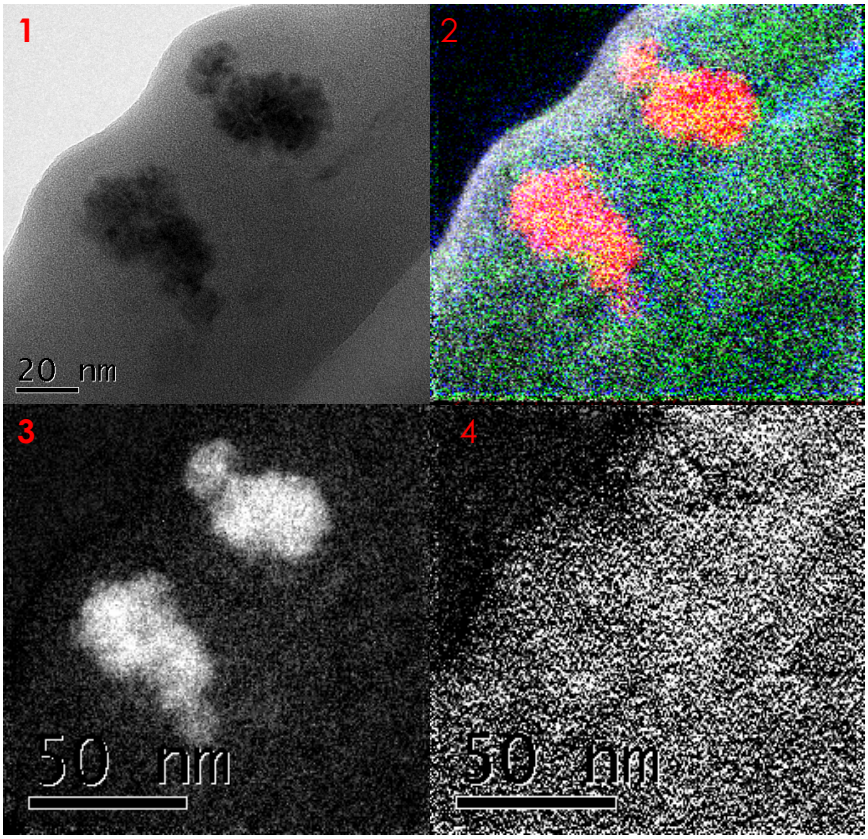

Figure 7.6: Sample 4 (solvent THF/DCB) shows the Ni rich areas within a matrix. Picture 1) elastic image 2) overlay of EELS Maps Red=Ni, Green=N, Blue=F and White = O 3) Ni Map using EELS 4) N Map using EELS.

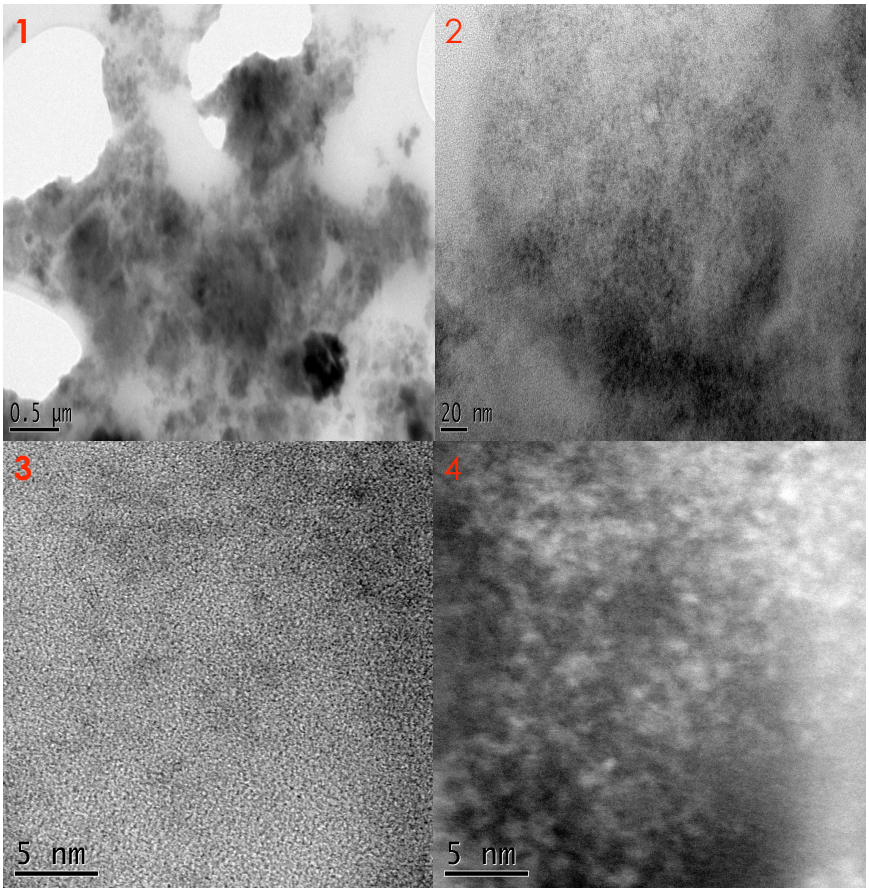

Figure 7.7: Sample 5 (solvent THF/PhCN) 1) Image of area where there is no strong evidence for particles 2) A close up image of the material where the darker areas may be Ni rich. 3) BF Image showing small particles 4) HAADF image.

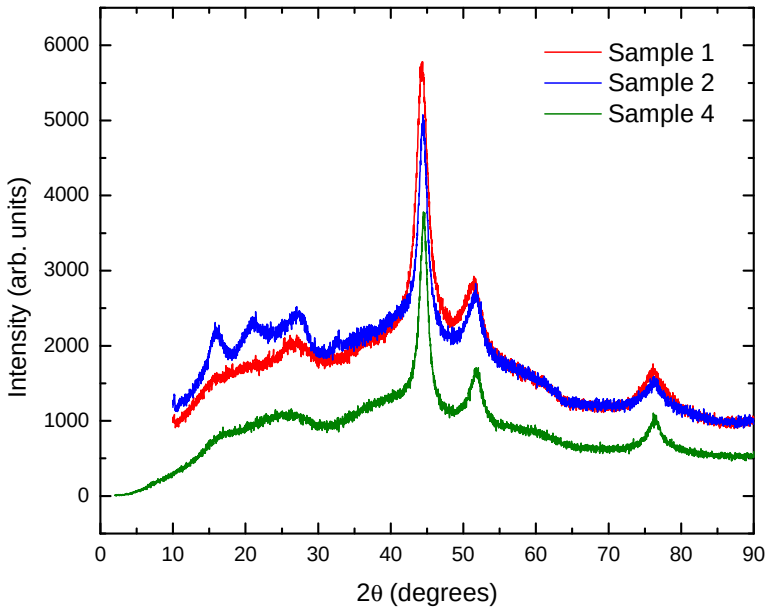

Figure 7.8: X-ray diffraction patterns for Samples 1 (blue), 2 (red) and 4 (green). Sample 2 show more structure at low angles then Samples 1 and 4 indicating a more crystalline matrix or extra phase.

$TCNQF_4$ based material. Using the Scherrer equation one can calculate the average particle size using the full width half-maximum of the peaks [27]. From our data we calculated the particle sizes from the (111) peak at approximately 2θ =44.3° as 4.94 nm, 6.77 nm and 7.24 nm for Samples 1,2 and 4 respectively.

Samples 3 and 5 have no peaks that are directly associated with fcc N and, recalling the TEM images, this is consistent with very small particles (∼1nm) that are dispersed throughout an organic matrix that is predominately a derivative of $TCNQF_4$. In fact the XRD patterns are completely different at small angles compared to Samples 1, 2 and 4 and there is structure at larger d-values suggesting a much bigger unit cell, again that is possibly a $TCNQF_4$ derivative. Moreover, there is no substantial evidence when comparing the calculated diffraction pattern of bulk $TCNQF_4$ to our data confirm this as many of the peaks do not overlap the $TCNQF_4$ data [28]. However, the structure at low angles (2θ) the specific material is hard to

identify but it may have formed the stoichiometric product of $Ni(TCNQF_4)_2$ which could be what makes up a large amount of the matrix and is also paramagnetic similar to $Ni(TCNQ)_2$ [16]. However from our work there is no obvious similarity between these low angle peaks and that of $Ni(TCNQ)_2$ except that the peaks with a d-spacing from 3-6 Å are in a similar range to that observed for $Ni(TCNQ)_2$. Note that the low angle peaks common to both sample 2 and sample 3 suggest that the matrix is identical in these systems; we note that these samples exhibit the lowest nickel concentrations of all five samples (see table 2). The XRD pattern associated with sample 5 suggests that it is amorphous but, from the TEM images (Fig. 7.7), there is evidence that there are very small particles that are most probably nickel however these particles may be too small ($\geqslant 1\ nm$) to scatter the X-rays coherently.

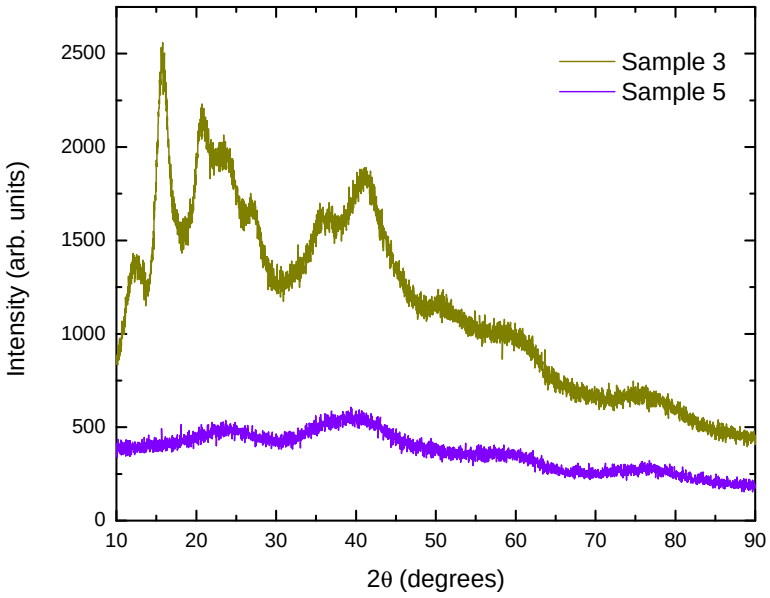

Figure 7.9: X-ray diffraction patterns for Samples 3 (blue) and 5 (red).

The TEM, EELS and XRD data demonstrate that varying the solvent has a significant impact upon the creation of nickel nanoparticles through the decomposition of $Ni(COD)_2$. The general similarity of samples 1, 2 and 4 suggests that neither DCM nor THF with DCM or DCB are unable to prevent the decomposition process. The resulting materials are inhomogeneous with nickel nanoparticles embedded in

a metal-organic matrix and the compositions deduced from elemental analysis and ICPMS clearly do not represent the true nature of the samples. In fact the EELS maps of samples 1 and 2 indicate that the nickel content within the matrix is also very inhomogeneous implying a range of metal-organic compositions exist; the corresponding EELS map for sample 4 suggests that matrix in this material has a very low nickel content even though the results of table 2 suggest that it is the most nickel-rich sample with respect to the nitrogen concentration. On the other hand the TEM and XRD data suggest that using the solvents THF and either acetonitrile or benzonitrile stabilises $Ni(COD)_2$ and, instead of following the decomposition path to form large nanoparticles of bulk nickel plus a metal-organic matrix, a more homogeneous material is synthesized, possibly a nickel salt with $TCNQF_4$ is formed via a charge transfer reaction. The different polarities of solvents and their effect on the crystallinity is discussed later.

7.3.2 Magnetic Characterisation

The magnetic properties of the five samples differ from each other though samples 1, 2 and 4 are similar and are different to samples 3 and 5. Therefore we deal with these two groups of samples separately.

Samples 1, 2 & 4

The magnetisation vs. temperature data (Fig. 7.10) for the three samples, measured in an applied field of 2.5 mT show a similar response to that expected for a superparamagnetic nanoparticulate system, with the FC data appearing to saturate as the temperature is lowered. The individual blocking temperatures vary between samples, as indicated in Table 3 which might be expected for nickel nanoparticles with differing sizes as $T_B \propto V$ where V is the volume of the superparamagentic particle [29]. However, PXRD data suggest that sample 1 has the smallest particle size, with sample 2 the next largest and sample 4 the largest; the blocking temperatures do not follow this trend. Also, the value for the FC magnetisation at the lowest tem-

peratures is similar for samples 1 ($M(4\text{K}) = 1.40$ $\text{Am}^2\text{kg}^{-1}$) and 4 ($M(4\text{K}) = 1.39$ $\text{Am}^{-2}\text{kg}^{-1}$), while that of sample 2 ($M(4\text{K}) = 0.88$ $\text{Am}^2\text{kg}^{-1}$) is radically different. Note the calculation of the magnetisation was simply done by dividing the measured magnetic moment by the mass of the sample, and the TEM/EELS data demonstrated that the samples are inhomogeneous. Therefore the magnetic fraction of the samples responsible for the data of (Fig. 7.10) is not necessarily correctly represented by the bare masses of the samples used in the magnetic measurement, which we will refer to as the mass fraction. In fact, assuming all the nickel detected in the ICPMS measurement is responsible for the magnetic signal, and correcting the magnetisation for this mass fraction, we obtain the following magnetisations at 4 K: sample 1, $M = 5.13$ $\text{Am}^2\text{kg}^{-1}$; sample 4, $M = 4.25$ $\text{Am}^{-2}\text{kg}^{-1}$; sample 2, $M = 6.93$ $\text{Am}^2\text{kg}^{-1}$.

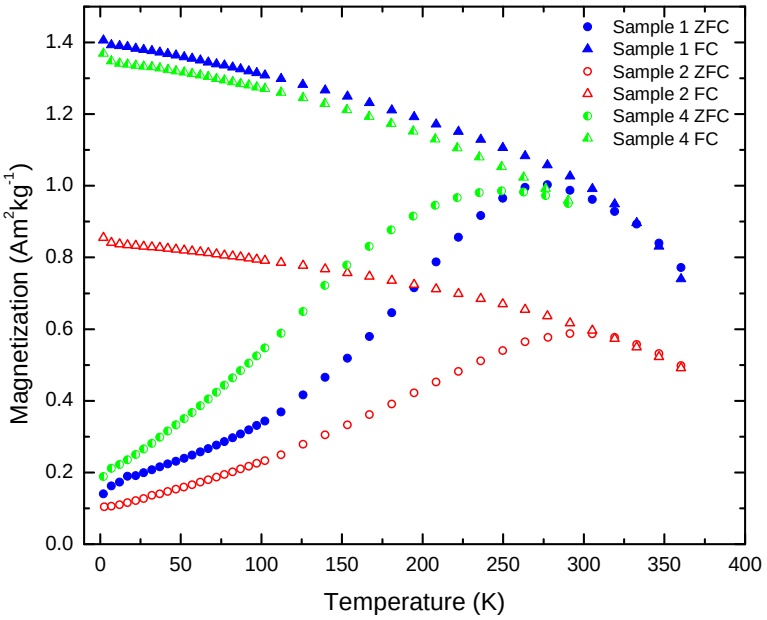

Figure 7.10: Magnetisation vs. temperature for Samples 1, 2 & 4 at 2.5 mT. All samples have a similar behaviour and show a blocking temperature, however it varies slightly between samples.

Within Table 3 We have used particle sizes calculated from a Langevin function fit for M vs. H data at 290 K, which will be explained later, as well as from the

PXRD data and calculated the blocking temperature (T_B) where we used a value of K_1 = -4.5 x 10^3 Jm^3 [30] and the formula $T_B = KV/k_B ln(\alpha t/\tau_0)$ where α = 100 and $\tau_0 = 10^{-9}$ s [29]. As can be seen the calculated T_B values for particles of the order of 7-10 nm is much lower then what we are observing and from the blocking temperatures seen in Fig. 7.10 we calculated that the particle size should be an order of magnitude larger then what we have seen from the magnetic data and PXRD (Scherrer equation) data. If the particles seen in the TEM data are correct then these also do not correspond to the calculated values of T_B and it is more likely that what were are seeing are aggregates of much smaller particles. The typical particle sizes calculated using T_B and those determined from M vs. H or PXRD data suggest that the matrix may be causing there to be a favourable anisotropic magnetisation on the surface of the particles that require a much higher temperature in order for the direction of their magnetisation to be altered. The M vs. T data were recorded in an applied field of 2.5 mT and at this field value one would expect to probe only the particles and not the paramagnetic matrix that may exist. It has been previously observed that the blocking temperature in films of Ni nanoparticles within a matrix can be tuned depending on the material of the matrix and increased above what is expected [31, 32]. Using a CeO_2 matrix Abiade *et al.* were able to show that small nanoparticles (8 nm) could be tuned to have a T_B higher then room temperature and that this was related to the interparticle spacing. It is also worth noting that T_B was observed to increase as the degree of crystallinity of the matrix increases [32]. This supports the observation that sample 2 has the highest T_B and suggests that sample 4 has the lowest degree of crystallinity of the matrix.

Sample	Particle Size	Number Density	Moment $\langle \mu_i \rangle$	T_B	Calculated T_B	Calculated Particle Size	Calculated T_B
					From Langevin Function	from observed T_B	From PXRD Data
	(nm)	(kg^{-1})	(μ_B)	(K)	(K)	(nm)	(K)
1	7.49	1.37 x 10^{19}	22315.7	281.8	3.12	27.85	1.57
2	7.75	1.65 x 10^{19}	24648.5	295.6	3.63	28.30	4.05
4	8.47	1.77 x 10^{19}	32191.0	250.7	4.55	26.79	4.95

Table 7.3: Particle sizes and Number Densities from the Langevin function fit at 290 K with T_B taken from Figure 7.10. T_B and particle sizes were calculated from the particle sizes from the Langevin function fit as well as the PXRD data for comparison.

The magnetisation vs. applied field data for sample 1 are shown in Fig 7.11. At 290 K there is a ferromagnetic component that appears to approach a saturation value of approximately 3 Am^2kg^{-1} above about 1 T however one must consider at this temperature that the only component is the ferromagnetic particles which may not make up the total nickel mass fraction. At lower temperatures, a second component appears, the magnitude of which increases with decreasing T and it cannot be saturated at 5 T, the highest field achievable in the experiment.

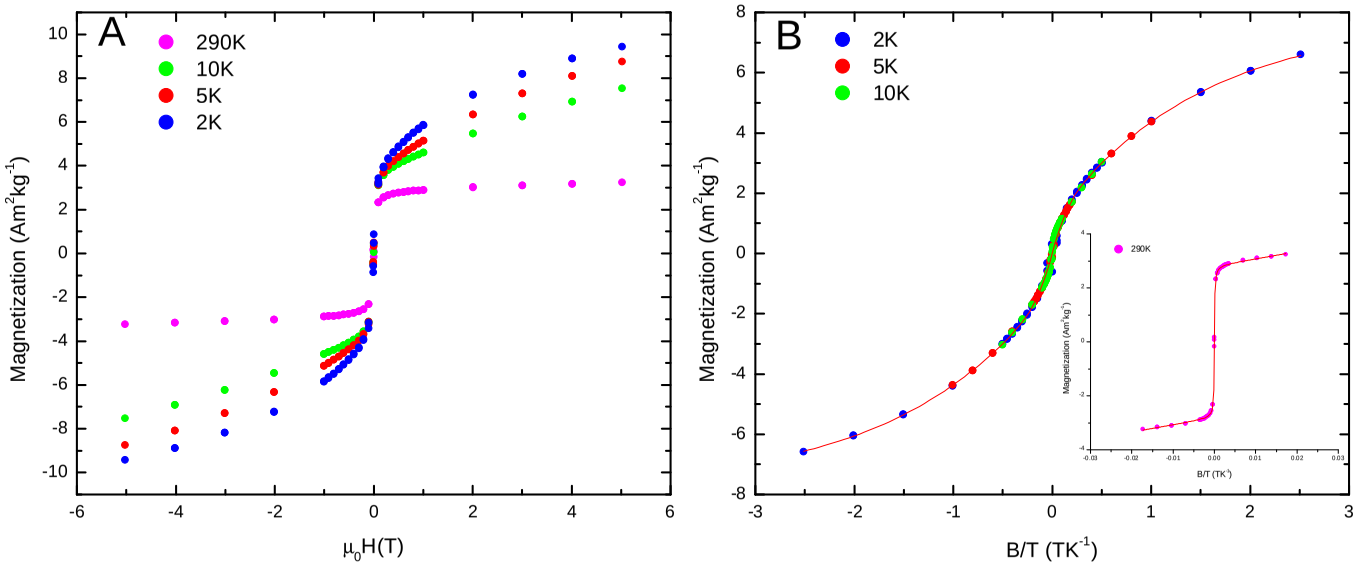

Figure 7.11: **A:**Magnetisation vs. applied field for sample 1 (solvent: DCM). **B:** M vs. B/T where once the magnetisation from the Langevin component has been subtracted the low temperature data can be scaled onto the 2 K curve. *inset:* Langevin function and a linear component fit to the 290 K data when plotted as M vs. B/T.

The data recorded at 290 K can be fitted with a combination of a Langevin function and a linear component (see equation Equation 7.1). From this linear component we were able to determine the susceptibility of the secondary phase at 290 K to be $1.109\times10^{-7}\mathrm{m^3kg^{-1}}$.

$$M = (N\langle\mu\rangle\mu_B) \times \left\{ \coth \frac{\langle\mu\rangle\mu_B B}{k_B T} - \frac{k_B T}{\langle\mu\rangle\mu_B B} \right\} + \chi(T)\mu_0 H, \tag{7.1}$$

where χ is the mass susceptibility in units of $\mathrm{m^3kg^{-1}}$.

Parameters obtained from the Langevin Function fits to the data are shown in Table 3, and the particle sizes were calculated from the value of the average magnetic moment along with the bulk value of the magnetisation of nickel (55.2 $\mathrm{JT^{-1}\ kg^{-1}}$). For the case of sample 1, the particle size of 7.49 nm supports the PXRD result of 4.94 nm (as they are similar orders of magnitude) and suggests that the TEM image shown in Fig. 7.3 are likely to be showing clusters of nickel particles rather than individual nanoparticles. The fitting parameters obtained from the 290 K dataset were used to calculate a Langevin function at lower temperatures. This calculated ferromagnetic component was then subtracted from the magnetisation measured at 10, 5 and 2 K. These data could then be scaled onto the low temperature curve (see Table 4 for scaling factors). The higher temperature datasets were scaled onto the 2 K data, plotted as M vs. B/T, and describes the second component shown in Fig 7.11B. A fit to the data was performed which comprised of a two-term Langevin function shown in equation 7.2,

$$M = (N_1\langle\mu_1\rangle\mu_B) \times \left\{ \coth \frac{\langle\mu_1\rangle\mu_B B}{k_B T} - \frac{k_B T}{\langle\mu_1\rangle\mu_B B} \right\} + (N_2\langle\mu_2\rangle\mu_B) \times \left\{ \coth \frac{\langle\mu_2\rangle\mu_B B}{k_B T} - \frac{k_B T}{\langle\mu_2\rangle\mu_B B} \right\}. \tag{7.2}$$

The parameters that were obtained for the fit to Fig. 7.11B are shown in Table 4. Since the data have to be scaled onto the 2 K curve by multiplying by a factor (Sc) affecting only the magnitude of the magnetisation it implies that, as the temperature is decreasing, the number of magnetic moments responding to the magnetic field is

also decreasing. This may be expected if the system has a ground state where the value of the magnetic moment is zero. Note that although we have used a two-term Langevin function (equation 7.2) to fit to the data, this may only be an empirical fit and not be a true physical representation of the magnetic response of the system. This type of behaviour has been reported previously where a Langevin function with a linear term has been fit to particles dispersed in a diamagnetic matrix where the system should behave superparamagentically and the particle sizes calculated from the magnetic moments of the particles are unrealistic for a Langevin function fit (i.e. sub-nanometer) [23]. Bound magnetic polarons have also been modelled using the Langevin function which also illustrates the application of the Langevin function to low moment clusters [33]. This is also a similar result to our study of producing Ni nanoparticles from the decomposition of $Ni(COD)_2$ by varying the temperature where a two-term Langevin function is fit to the scaled data but produced particle sizes suggesting sub-nanometer clusters had formed which we have shown exist in the reaction precursor pure form in the following chapter 8 [34].

Sample	Moment $\langle\mu_1\rangle$ (μ_B)	Moment $\langle\mu_2\rangle$ (μ_B)	N_1 (kg^{-1})	N_2 (kg^{-1})	Particle Size 1 (nm)	Particle Size 2 (nm)	5 K Sc	10 K Sc
1	1.9	20.2	3.95×10^{23}	9.82×10^{21}	0.33	0.73	1.35	1.55
2	1.8	11.5	9.32×10^{23}	4.34×10^{22}	0.32	0.40	1.25	1.35
3	1.7	13.0	1.29×10^{24}	2.59×10^{22}	0.22	0.63	1.638	1.565
4	1.9	14.8	8.60×10^{23}	3.58×10^{22}	0.33	0.65	1.27	1.50
5	2.1	19.1	7.12×10^{23}	2.41×10^{22}	0.34	0.71	1.410	1.565

Table 7.4: Parameters from the two-term Langevin Function fit to the data for all Samples. In the case of Samples 1, 2 and 4 the results are once the 'ferromagnetic' step modelled by Equation 1 has been subtracted that show the samples particle size calculated from the moment and the number densities (N) for each respective sample/particle size. For Samples 3 and 5 there was no need to subtract any ferromagnetic/superparamagnetic contribution.

Sample 2 (see supplementary data figure D.1 for M vs H data) shows a similar field-dependent magnetisation behaviour at 290 K to sample 1 where the particle sizes calculated from the PXRD and seen from the TEM data show that they are of similar magnitudes. Adopting the analysis used for sample 1, a Langevin function with a linear term can be fitted to the data at 290 K (See Table 3). From the linear term the susceptibility is 1.425×10^{-7} m^3kg^{-1}. The lower temperature data can be treated in a similar fashion to the magnetisation vs. applied field for sample 1, with a ferromagnetic component, calculated using the 290 K fitting parameters, being subtracted from the lower temperature data. The resulting $M(B/T)$ curves are scaled onto the 2 K curve and a two-term Langevin function can be fit to the scaled data; the resulting moments, particle sizes and densities can be calculated and are shown in Table 4. Again we observe a similar situation to sample 1 where, as the temperature decreases, the number of responding particles also appears to decrease.

Sample 4 (see supplementary data figure D.2 for M vs. H data) again shows a similar response and particle sizes of the same order of magnitude to samples 1 and 2. A Langevin function plus a linear term can be fit to the the data at 290 K (see Table 3); the susceptibility is calculated as 2.078×10^{-7} m^3kg^{-1}. Also, a similar analysis of the lower temperature $M(B/T)$ results in the fitting parameters shown in Table 4 and an apparent variation of moment density with temperature.

The $M(B,T)$ data of samples 1, 2 and 4 suggest that initially dissolving the $Ni(COD)_2$ in THF has had an effect on the second magnetic phase of the material. Samples 2 and 4 exhibit a much greater magnetisation at 5 T at low temperatures; at 2 K and 5 T both samples 2 and 4 have a magnetisation of approximately 15 Am^2kg^{-1} where as sample 1 has a magnetisation of approximately 6.5 Am^2kg^{-1}. However the issue of mass fraction may play a substantial role. All three samples show a similar particle size from the Langevin function fit at 290 K and the linear component has a similar susceptibility but it is slightly higher in Sample 4. The second component that behaves differently to the dominant ferromagnetic step in the M vs. B is similar in all three cases where a two term Langevin function can be fit

to the scaled data. The fact that the data scale implies that similar physical origin to the magnetism is applicable to all the samples and there is a possibility that the total number of magnetic moments responding to an applied field is decreasing as a function of temperature in each material.

Samples 3 & 5

The two samples both behave paramagnetically at high temperatures which is shown in Fig. 7.12 however although the solvents used are similar there is a difference in behaviour of the samples at low temperature. Sample 5 shows a transition at $\sim$5 K that may be a blocking temperature associated with the Ni nanoparticles indicated in Fig. 7.7. Since the applied field is very small (2.5 mT) it is of no surprise that we are seeing a coercive field associated with the sample at these very low temperatures. Other than at very low T, there is no difference between the zero field cooled (ZFC) and field cooled (FC) data of sample 5. Sample 3 shows a different response as, although it appears to be a paramagnetic material, the ZFC and FC curves do not lie on top of one an other. This would generally suggest that there may perhaps be a slight amount of coercivity within the system however the FC under-shoots the ZFC which is not accounted for by the error within the measurement. This may be explained by solvent evaporation from the sample itself within the magnetometer as a change in mass would be reflected in different mass magnetisations. The magnetisation of Sample 5 may be slightly lower then that of Sample 3 due to the particle size being slightly larger in the latter material.

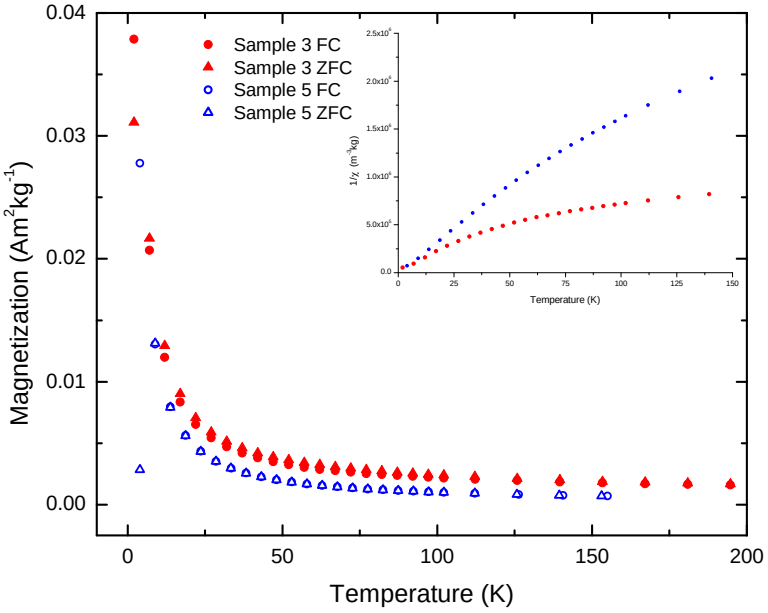

Figure 7.12: Magnetisation vs. temperature for samples 3 & 5 at 2.5 mT. Both samples appear paramagnetic at high temperatures however, sample 5 undergoes a transition on the ZFC curve at very low temperatures. The inset shows a plot of $1/\chi$ vs. T which shows that the samples do not behave strictly like paramagnets at low temperatures where there is evidence of a non-zero intercept on the x-axis.

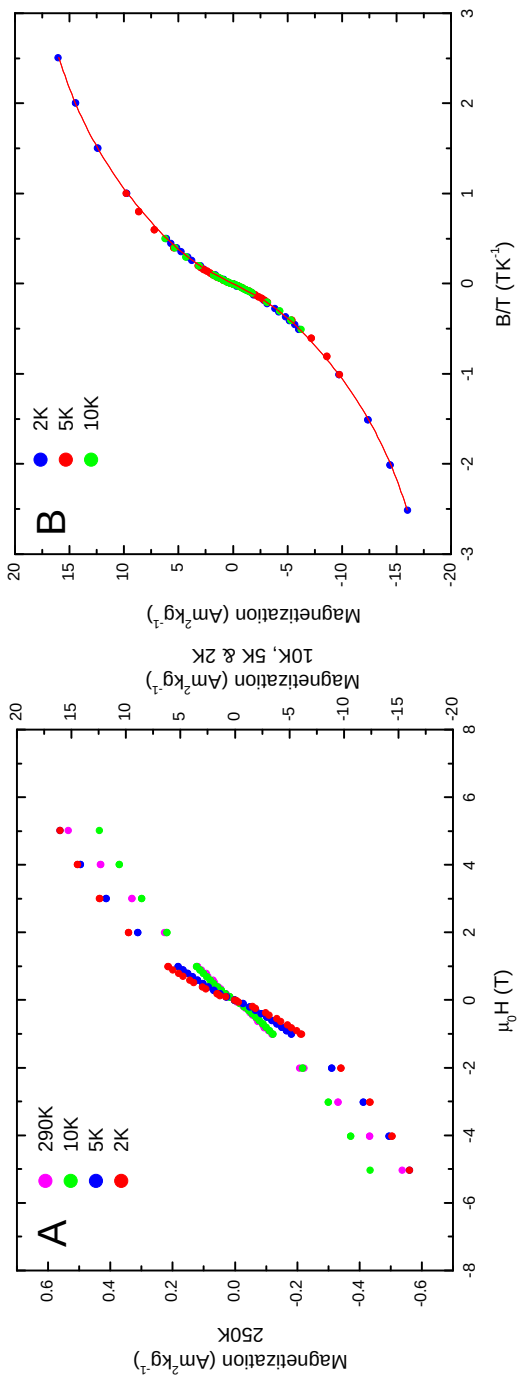

Figure 7.13: **A:** Magnetisation vs. applied field **B:** A scaled M vs. B/T plot for sample 3 (solvent: THF/MeCN). The fit to the data is a two-term Langevin function.

The magnetisation vs. applied field data for sample 3, measured at the 290 K, is linear suggesting a paramagnetic or supeparamagnetic response. At low temperatures, a non-linear response of M with B is observed but this is not a simple paramagnetic behaviour, scaleable by plotting as a function of B/T; the 5 K and 2 K the high field data points lie on top of one an other. However, scaling is possible as long as the 10 and 5 K data are divided by 1.990 and 1.638 respectively in order for the curves to fall onto the 2 K data set. A 2-term Langevin function (see Equation 7.2) can be fitted to the data and the parameters obtained from the fit can be seen in Table 4. This form of scaling is the same as that observed for samples 1,2 and 4 and suggests that the low temperature magnetism of sample 3 has a similar origin to those three samples.

Sample 5 shows a similar behaviour for the hysteresis loops (see figure D.3) as for sample 3 where the data can be scaled onto one an other when plotted as M vs. B/T. The 10 and 5 K curve must be divided by 1.565 and 1.410 respectively to lie upon the 2 K data set. Once again the two-term Langevin function can be fit to this data and give sub-nanometer size particles (see Table 4). Hence, both samples 3 and 5 show a similar low temperature scaling behaviour to sample 1, 2 and 4 (once the ferromagnetic step has been subtracted from the low temperature data in these latter samples). Therefore, it is most likely that, by using a nitrile based compound, the formation of larger nickel nanoparticles is suppressed, but the low temperature paramagnetic phase is common to all samples, regardless of solvent.

7.4 Discussion

The dielectric constants[4] of the solvents used vary greatly; DCM (8.93), THF(7.52), 1,2-DCB (10.12), MeCN (36.64) and PhCN (25.90) [35, 36]. $Ni(COD)_2$ is decomposed catalytically by halocarbons so it is no surprise that, in the presence of DCM or

[4]The dielectric constant is a good indicator of the polarisability and polar nature of the solvent molecule

DCB, the material falls apart and results in the formation of Ni nanoparticles [37,38]. The solvent THF works well in stabilising $Ni(COD)_2$ and creating a stable solution of Ni(0) using THF should allow the $TCNQF_4$ to undergo a redox reaction with the nickel atoms resulting in a metal-organic compound. The results of samples 2 and 4 demonstrate that when using a halocarbon solvent, regardless of the inclusion of THF within the reaction, Ni particles of a substantial size are formed from the decomposition of $Ni(COD)_2$. The inclusion of THF in the reaction mechanism results in similar particle sizes to sample 1 however the additional component for both samples 2 and 4 have a higher susceptibility as shown from the susceptibilities calculated from the 290 K M vs. H data. This indicates that, by simply including the THF, more of the additional magnetic component is produced than in sample 1 and this component may be simply Ni clusters [34]. Alternatively, the enhancement of this additional component may be due to the fact that the THF is stabilising the $Ni(COD)_2$ for long enough to allow the reduction of the $TCNQF_4$ molecule resulting in a Ni(II)-$TCNQF_4$ compound that forms part of the organic matrix. The low angle powder diffraction data (see Fig. 7.8) of sample 2 suggest that a crystalline phase exists with a larger lattice constant than nickel (the lowest angle feature suggests $d = 5.6$ Å) and typical of $TCNQF_4$-based solids. The low angle PXRD data of sample 1 and, to lesser extent, sample 4 also suggest the existence of very broad diffraction peaks. Thus it may be that simply adding THF to DCM has, in sample 2, enhanced the crystallinity over that exhibited by sample 1, perhaps by slowing down the reaction sufficiently to allow small crystallites to form . However, using THF with the increased polarity solvent, DCB, resulted in poorly resolved diffraction peaks at small angles perhaps suggesting a more rapid reaction leading to an amorphous material or very small crystallites.

Using isonitrile solvents (samples 3 & 5) results in systems that show somewhat different magnetic properties compared to samples 1,2 and 4. Isonitrile molecules are extremely good coordinating ligands as they can donate the lone-pair on the nitrogen of the cyano-group and they have an ability to stabilise a negative charge. There are many examples of divalent Ni that form crystals where there are coordinating isocyanide ligands such as acetonitrile [39, 40]. It is also possible to use isocyanide

ligands to stabilise zero-valent Ni atoms where $Ni(COD)_2$ has been used as a starting material and, simply by reacting with the isocyanide molecule in a solvent under an inert atmosphere, one can obtain a stable Ni(0) compound [41]. Molecules similar to benzonitrile have been used in synthetic routes to create stable Ni(0) compounds where $Ni(COD)_2$ is again used as the source of Ni(0); slow addition of the ligand to a $Ni(COD)_2$ solution resulted in an isocyano-Ni(0) stable compound [42, 43].

The remarkable difference between samples 1, 2 & 4 and samples 3 & 5 with varying solvent has a precedent in Miller and Epstein's work on $V(TCNE)_x \cdot y(\text{solvent})$ where they saw a dramatic shift in transition temperature when using more polar solvents [9, 10]. However, in our samples we attribute the dominant magnetic component at low fields to be a result of bulk Ni or Ni nanoparticles/clusters which are most prominent in samples 1, 2 & 4. When looking at the values for the magnetisation at $B_{app} = 5$ T for all the samples, except sample 1, the magnetisation is of the same order of magnitude and similar values, especially once the Langevin-step function has been subtracted suggesting that despite the overall nickel nanoparticles mass being different the matrix is largely very similar with regards to elemental content. This implies that using THF as a precursor results in more of the additional magnetic component component, dominant at lower temperatures, being created. This additional component may be a result of Ni clusters (i.e. subnanometer) or a metal-organic compound similar to the $V(TCNE)_x$ that has a large amount of structural disorder but behaves as a ferromagnetic material at low temperatures [16, 34]. The disorder may be due to co-ordination of the spineless solvent molecules within the structure replacing possible sites for the $TCNQF_4$ molecules and creating a disruption in the exchange pathway.

It may also be possible for the isocyano solvents to stabilise the Ni(0) atoms through bonding of the electron rich cyano-groups to the atom or atomic cluster making it less favourable for the Ni to form larger nanoparticles and creating atomic clusters with a distorted surface that allows for further bonding of isocyano ligands to the surface. On opening the reaction mixture to air, as was done by Jain *et al.* [1] in Ni2TCNQ, may result in the decomposition of these stable Ni(0)-isocyano com-

pounds or atomic clusters. It may be that $TCNQF_4$ may also be reduced by the surface of the Ni atomic clusters rather then individual Ni(0) atoms and the cyano-group on the $TCNQF_4$ may act as an effective stabilising surface ligand. If one uses an isocyanide solvents this may result in the surface of the Ni clusters being stabilised by the spineless solvent rather then the $TCNQ_4$ which would create more disorder and disrupt the magnetic exchange pathways between particles causing the overall blocking temperature to decrease.

The work of Finney and Finke on nanocluster nucleation and growth suggest that a four step double autocatalytic mechanism is present within system, where the zero-valent transition metal self-assembles to give bulk metal particles [44, 45]. They concluded that as well as being four mechanistic steps each with its own rate constant, low concentrations and high temperatures are used to favour the creation of nanoclusters as opposed to larger particles. Finney and Finke also extended their research to look at the kinetics of the autocatalytic decomposition reaction with varying reaction conditions [46]. They reported that the products of the metal reduction reaction can be changed from bulk metal to nanoclusters depending on the choice of solvent. By using a more polar solvent (propylene carbonate vs. acetone) Finney and Finke showed that the auto-catalytic decomposition reaction resulted in smaller nanoclusters rather than the bulk transition metal [46]. They presumed that the more polar solvent is a more effective stabilizer and slows down the rate of agglomeration. This is especially important when the solvent can also be a stabilising ligand and it has been predicted that solvents with higher dielectric constants are more effective as a ligand [47]. One example of a purely solvent stabilised system is work by Reetz and Lohmer where they showed that Pd nanoclusters could be stabilised by the propylene carbonate solvent molecules [48]. However recent work by Finke's research group presented results that did not fit with solvent-only stabilised nanoclusters where anion coordination was also needed to form Ir nanoclusters rather then bulk metal. What was observed was that solvents with a higher dielectric coupled with the existence of an anion, in their case $[BF_4]^-$, lead to dispersed nanoclusters in solution where as using a less polar solvent and counter anion gave bulk metal particles [49]. We believe that, within the $Ni(COD)_2$ and

$TCNQF_4$ reaction, using more polar solvents has created a similar effect to that observed by Finney and Finke, where the high dielectric constant solvents produce nanoclusters; this effect is clearly pronounced in the difference between samples 3 and 5. However it may also be that the $TCNQF_4$ anion is also included in stabilising the nanoclusters similar to Starkey Ott and Finkes recent work. To confirm this more work is needed on the decomposition reaction of $Ni(COD)_2$ in the presence of a strong electron acceptor with different polarity solvents as the reaction medium.

7.5 Conclusion

We have synthesised five samples where the nanoparticle size and distribution can be controlled simply by varying the reaction solvents. Using only DCM as the solvent (Sample 1) similar to Jain et al. [1] creates a material that has two clear magnetic components; one that is superparamagentic Ni nanoparticles and a metal/organic based matrix. By initially dissolving the $Ni(COD)_2$ in THF, this stabilises the zero-valent Ni atoms and using halocarbon solvents (Samples 2 and 4) also produces Ni nanoparticles but the blocking temperature can be controlled by varying the polarity of the solvent as previously discussed. From our TEM and PXRD data it is clear that the particles are Ni rich and agglomerate together where the average particle size is small (<10 nm). The particle size was also confirmed from our room temperature magnetic measurements where our the fit to the data resulted in similar small particles to the PXRD data. Interestingly when the blocking temperature is calculated for these tiny nanoparticles it is much lower than what we observed which draws the conclusion that the matrix must have a significant role in hardening the magnetic response of these nanoparticles. Once the room temperature magnetic component is subtracted from the low temperature M vs. B curves we see the magnetism of the matrix fall into an antiferromagnetic groundstate as $T \rightarrow 0$. This is similar to our results from work on magnetic clusters in $Ni(COD)_2$ [34] which suggests that the matrix may simply be atomic clusters within an organic based matrix where we measured the transitions of Ni clusters to an antiferromagnetic groundstate as $T \rightarrow 0$ and is discussed in more detail in chapter 8. A similar two-term Langevin function could be fit to the data which suggests a there may be a particle size distribution but from the moments calculated it possible to confirm that the response is from low moment clusters. However it may also be that a stoichiometric metal-organic compound has been created which also shows antiferromagnetic properties as T decreases which acts as a medium for magnetic exchange to harden the nanoparticles and increase the blocking temperature.

Using a nitrile based solvent, as well as THF, leads to very small well dispersed particles that behave similarly to paramagnetic systems, but Sample 5 may pass

through a blocking temperature at low temperatures, or indeed exhibit another type of magnetic transition. The particles detected in Samples 3 and 5 do not appear to behave in a superparamagnetic fashion and the data from the M vs. B/T can be scaled onto the 2 K data set and a two term Langevin function can be fitted to the data in an analogous fashion to the second phase of Samples 1, 2 and 4. Essentially we have created a material with a magnetic response that resembles the matrix of Samples 1,2 and 4.

From our work we have been able to control the both the nanoparticle size and the matrix by simple variation of the solvent, when using a nitrile based solvent we are able to create very small well dispersed atomic clusters within an organic based matrix, however when using a halocarbon based solvent it is possible to create Ni nanoparticles within a matrix that exhibits a much higher blocking temperature and thus magnetic anisotropy then what is expected for particle sizes of a similar size.

Bibliography

[1] R. Jain, K. Kabir, J. B. Gilroy, K. A. R. Mitchell, K. Wong and R. G. Hicks. *Nature* **445** (2007) 291-294

[2] J. Manriquez, G. Yee, R. McLean, A. Epstein and J. Miller. *Science* **252** (1991) 1415-1417

[3] J. S. Miller and K. I. Pokhodnya. *J. Mater. Chem.* **17** (2007) 3585-3587

[4] S. Ferlay, T. Mallah, R. Ouahes, P. Veillet and M. Verdaguer. *Nature* **378** (1995) 701-703

[5] T. Mallah, S. Thiebaut, M. Verdaguer and P. Veillet. *Science* **262** (1993) 1554-1557

[6] A. Ito, M. Suenaga and K. Ono. *J. Chem. Phys.* **48** (1968) 8 3597

[7] J. M. Herrera, A. Bachschmidt, F. Villain, A. Bleuzen, V. Marvaud, W. Wernsdorfer and M. Verdaguer. *Phil. Trans.* **366** (2008) 127-138

[8] P. Zhou, S. M. Long, J. S. Miller and A. J. Epstein. *Phys. Letts. A.* **181** (1993) 71-79

[9] P. Zhou, B. G. Morin, J. S. Miller and A. J. Epstein. *Phys. Letts. A.* **181** (1993) 71-79

[10] P. Zhou, B. G. Morin, J. S. Miller and A. J. Epstein. *J. Appl. Phys.* **73** 10 (1993) 5648-5650

[11] E. M. Chudnovsky and R. A Serota. *Phys. Rev. B.* **26** (1982) 2697

[12] E. M. Chudnovsky and R. A Serota. *J. Phys. C.* **16** (1983) 4181

[13] K. I. Pokhodnya, D. Pejakovic, A. J. Epstein and J. S. Miller. *Phys. Rev. B.* **63** (2001) 174408

[14] D. S. Hertler and W. R. Hertler. *J. Am. Chem. Soc.* **84** 17 (1962) 3370-3374

[15] L. R. Melby, W. Mahler, W. E. Mochel, R. J. Harder, W. R. Hertler and R. E. Benson. *J. Am. Chem. Soc.* **84** 17 (1962) 3374-

[16] R. Clerac, S. O'Kane, J. Cowen, X. Ouyang, R. Heintz, H. H. Zhao, M. J. Bazile and K. R. Dunbar. *Chem. Mater.* **15** 9 (2003) 1840-1850

[17] S. A. O'Kane, R. Clerac, H. H. Zhao, O. Y. Xiang, J. R. Galan-Mascaros, R. Heintz and K. Dunbar. *J. Solid State* **152** 1 (2000) 159-173

[18] G. Wilke. *Ange. Chem. Int. Ed. Engl.* **27** 1 (1988) 185-206

[19] K. S. Suslick *Science* **247** 4949 (1990) 1439-1445

[20] Y. Koltypin, A. Fernandez, T. C. Rojas, J. Campora, P. Palma, R. Prozorov and A. Gedanken. *Chem. Mater.* **11** 5 (1999) 1331-1335

[21] P. B. Oliete, T. C. Rojas, A. Fernandez, A. Gedanken, Y. Koltypin and F. Palacio. *Acta. Mater.* **52** 8 (2004) 2165-2171

[22] O. Petracic. *Superlattice Microst.* **47** 5 (2010) 569-578

[23] X. Chen, S. Bedanta, O. Petracic, W. Kleemann, S. Sahoo, S.Cardoso and P. P. Freitas. *Phys. Rev. B.* **72** 21 (2005) 1-5

[24] M. Bandyopadhyay and S. Dattagupta. *Phys. Rev. B.* **74** (2006) 1-5

[25] K. J. Quinn. *Masters Thesis* Durham University (2009)

[26] A. Ceylan, C. C. Baker, S. K. Hasanain and S. I. Shah. *Phs. Rev. B* **72** (2005) 134411

[27] A. L. Patterson. *Phys. Rev* **56** (1939) 978-982

[28] T. J. Emgea, M. Maxfielda, D. O. Cowana and T. J. Kistenmachera. *MCLC* **65** 3 (1981) 161-178

[29] S. Blundell. Magnetism in Condensed Matter Oxford University Press (2001)

[30] J. J. M. Franse. *J. Phys. Colloques* **32** Cl (1971) 186 - 192

[31] J. T Abiade, S. Ho Oh, D. Kumar, M. Varela, S. Pennycock, H. Guo, A. Gupta and J. Sankar. *J. Appl. Phys.* **104** (2008) 073910

[32] D. Kumar, H. Zhou, T. K. Nath, A. V. Kvit and J. Narayan. *Appl. Phys. Lett.* **79** (2001) 17 2817-2819

[33] E. Quinteroa, M. Quinteroa, M. Morocoimaa, G. E. Delgadob, L. Laraa, J. Goméz, and P. Bocarandaa *Rev. Mex. Fís* **S53**(2007) 163

[34] A. Berlie, I. Terry and M. Szablewski. A Magnetic Study of Low Moment Nickel Clusters Formed From The Solid-State Decomposition of Nickel Bis-1,5-cyclooctadiene. *To be published 2012*

[35] J. G. Stark and H. G. Wallace. Chemistry Data Book John Murray; Student international edition edition (1970)

[36] D. R. Lide. CRC Handbook of Chemistry and Physics 87^{th} Edition CRC Press (2006)

[37] R. A. Schunn, S. D. Ittel and M. A. Cushing. *Inorg. Synth.* **28** (1990) 94-98

[38] C. A. Tolman, D. W. Reutter and W. C. Seidel. *J. Organomet. Chem.* **117** (1976) C30

[39] A. Getsis and A Mudring. *Z. Anorg. Allg. Chem.* **634** (2008) 2130-2132

[40] A. Getsis and A Mudring. *Z. Anorg. Allg. Chem.* **634** (2008) 619-621

[41] S. D. Ittel. *Inorg. Synth.* **28** (1990) 99-104

[42] C. L. Perrine, M. Zeller, J. Woolcock, T. M. Styranec and A. D. Hunter. *J. Chem. Crystallogr.* **40** (2010) 289-295

[43] S. Otsuka, T. Yosida and Y. Tatsuno. *J. Am. Chem. Soc.* **93** 24 (1971) 6462-6469

[44] C. Besson, E. F. Finney and R. G. Finke. *Chem. Mater.* **17** (2005) 4925-4938

[45] E. F. Finney and R. G. Finke. *J. Colloid Interface Sci.* **317** (2008) 351-374

[46] E. F. Finney and R. G. Finke. *Chem. Mater.* **20** (2008) 1956-1970

[47] L. Starkey Ott and R. G. Finke. *Coord. Chem. Rev.* **251** (2007) 1075-1100

[48] M. T. Reetz and G. Lohmer. *Chem. Commun.* **16** (1996) 1921-1922

[49] L. Starkey Ott and R. G. Finke. *Inorg. Chem.* **45** (2006) 8382-8393

Chapter 8

A Magnetic Study of Low Moment Nickel Clusters Formed From The Solid-State Decomposition Reaction of $Ni(COD)_2$ (COD = 1,5-cyclooctadiene)

Something smells fishy, could it be the $Ni(COD)_2$?

8.1 Introduction

Nickel Bis-1,5-cyclooctadiene ($Ni(COD)_2$) is a well known source of Ni(0) that has been used and studied for many decades. It was first prepared by Wilke in 1966 and has since found many uses in chemical synthesis due to the ease of oxidation of the nickel [1–3]. The crystal structure was studied and solved by Direks and Dietrich where the nickel was shown to be in a quasi-tetrahedral environment with carbon-carbon double bonds coordinated to the diamagnetic Ni atom [4]. However, poor

orbital overlap results in the COD (1,5-cycloocatdiene) ligands being labile and the structure can fall apart very easily, yielding bulk Ni.

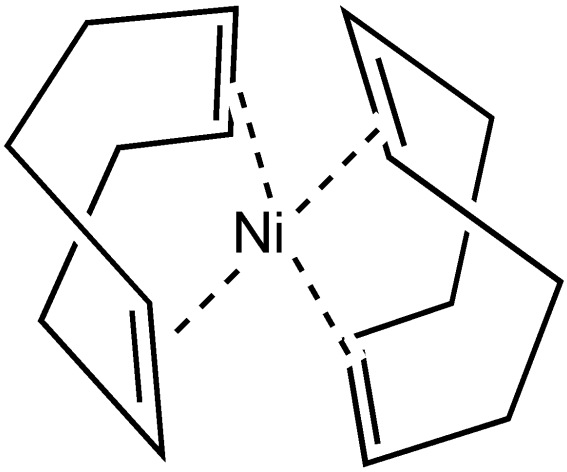

Figure 8.1: A structural diagram of $Ni(COD)_2$. The structure is quasi-tetrahedral in nature and not square planar.

Since $Ni(COD)_2$ decomposes in air, or on exposure to heat ($T_{Dec} \approx 60°C$)[1] [5], to produce bulk Ni readily, it has become a favourable starting material for making Ni nanoparticles, usually by the thermal decomposition of $Ni(COD)_2$ in colloidal systems [6–9]. However, we have discovered that $Ni(COD)_2$ is an incredibly suitable material for the study of magnetic Ni clusters due to the ease that is needed to prompt decomposition. Atomic clusters are an area of research that has received a large amount of interest where the physical properties of the clusters behave differently from the bulk [10]. The properties of such sub-nanometer clusters can depend on the number of atoms within the cluster and the geometry (which can again differ greatly) from the bulk. One example of this is Mn_n clusters where when $n = 3, 4$ the cluster falls into a ferromagnetic groundstate, however when the magnetic geometry is more complex i.e. when $n = 5, 6$ [11]; For $n = 5$ the cluster can either display a collinear or non-collinear arrangement which are both degenerate however for $n = 6$ the atomic arrangement is non-collinear coupled spins [12]. Experimental work has been conducted on Ni clusters where the magnetic moment was measured as a function of cluster size (n number of atoms) [13–15]. It was observed that as the

[1] See supplementary material

cluster size decreased, generally, the magnetic moment increased. Apsel *et al.* used a Stern-Gerlach deflection technique to determine the cluster size and calculate the magnetic moment using a Langvin function as they assumed that the clusters were showing a time averaged magnetic moment. They calculated that for a Ni_5 species the moment was 1.8 μ_B which decreased rapidly towards Ni_{10} and then fluctuated where the bulk value of 0.61 μ_B was reached when $n = 740$ [13]. The magnetic moment was shown to strongly depend on cluster size where a large moment was measured for clusters that have a large surface area and a small moment for clusters that are highly compact. Billas *et al.* have also conducted some impressive experiments on clusters of Ni, Fe and Co to study the magnetic moment as a function of temperature and cluster size. Their results showed that the magnetic moment increased as the cluster size decreased for Fe, Co and Ni. However, the magnetic moment for the larger clusters of Ni ($n = 140 - 560$) showed a trend similar to that predicted by the Heisenberg Model where the moment increased at a decreased finite temperature below room temperature. For smaller clusters ($n = 40 - 50$) the response of the magnetic moment was different where the was some evidence that the moment rose in value and then started to decrease [15].

Theoretical studies have also been carried out on Ni clusters to provide insight into the geometry and moment of individual clusters [16, 17]. Khanna *et al.* modelled the magnetic moment of clusters using a Langevin function where they predicted that the moment rose as $n \rightarrow 2$ however there were variations in the moment due to different geometries causing different surface areas for each value of n. Khanna *et al.* also comment on other predictions of the calculations of magnetic moment by other groups stating that discrepancies may arise if the atomic spacing is considered to be similar to the bulk metal where the cluster's moment will be sensitive to the local geometry and exchange distances. Khanna and Reuse calculated that for Ni_3 the moment will equal 0.67 μ_B and for Ni_5, 1.6 μ_B which is close to an experimental result of 1.8 μ_B obtained by Reddy *et al.* [16] and Resuse and Khanna [18]. Khanna *et al.* have also reported that the electronic structure shows band-like behaviour at $n = 14$ suggesting a similarity to bulk behaviour which is radically different to prior experimental data. Very recently Lu *et al.* have calculated geometries and magnetic

moments of individual Ni clusters ($n = 2 - 21$) [17]. They observed that when the $n = 5 - 10$ stable Ni clusters are formed where the growth is based on a square planar geometry where the groundstate for $n = 2$ is 2 μ_B and as n increases so to does the number of geometries each with their own groundstate magnetic moment. Above $n = 10$ the structure becomes more complex.

Another application of $Ni(COD)_2$ is as a starting material for the production of molecular magnetic materials. Perhaps the most notable such report was by Jain *et al.* [19], where charge transfer compounds, used to oxidise the Ni(0) species, resulted in an amorphous material that showed ferromagnetic behaviour at room temperature. In a similar vein, Miller and Pokhodnya [20] synthesised a Ni charge transfer compound using $Ni(COD)_2$ and TCNE (tetracyanoethyene) in THF (tetrahydrofuran). However, the magnetism within the resulting $Ni(TCNE)_2$·3.45THF compound was attributed to Ni nanoparticles that were formed from the decomposed $Ni(COD)_2$. There has also been a large amount of work on using $Ni(COD)_2$ to create nanoparticulate systems under numerous conditions showing the versatility of the starting reagent [21–24]. Within the previous chapter, the material Ni_2TCNQF_4 was discussed where within certain samples the magnetism was due to clusters of Ni atoms.

Within this chapter is reported a magnetic study of solid $Ni(COD)_2$ stored under specific conditions usually supposed to maintain material stability. It is demonstrated that the compound always thermally decomposes to components containing differing magnetic phases; one phase is diamagnetic and others are paramagnetic and/or superparamagnetic. We identify the superparamagnetic component as being associated with nickel nanoparticles, clusters or defect complexes, the density of which depends upon the storage conditions.

8.2 Materials and Methods

$Ni(COD)_2$ (purity 98+%) of 2 g quantity was purchased from STREM. The sample was stored under an inert atmosphere in a -20°C freezer (as recommended [25] by

the manufacturers) for 2 weeks.

All $Ni(COD)_2$ was handled inside a glovebox under an inert atmosphere (<1 ppm O_2). The material was measured using a specially designed quartz sample holder that could be placed inside a Quantum Design MPMS system [27]. Within the sample holder, the material could be easily and efficiently magnetically characterised while sealed under an inert atmosphere. Field dependent magnetisation measurements were made at temperatures between 2 K and 250 K and at applied magnetic fields of up to 5 T. Transmission electron micrographs and diffraction patterns of $Ni(COD)_2$ were obtained with a JEOL 2100F FEG TEM. Further material for electron microscopy was provided by Sigma Aldrich.

A second batch was also purchased to perform similar experiments where selected results have been included in the manuscript and the data can be seen in the supplementary information within the Appendix (figure E.1). It is worth noting that due to limitations the Batch 2 field dependent data could only be obtained down to 5 K whereas Batch 1 data could be collected at 2 K.

8.2.1 Experimental Methods

When making measurements on such magnetometers it is essential to minimise the magnetic contribution of the sample holder and, to this end, several approaches to the mounting of samples have been suggested [28]. For example, plastic drinking straws are frequently used as sample holders, with gelatin capsules being adopted to contain powders. However, such a method is unsuitable when making measurements at high temperatures or when working with air sensitive materials or liquids. Sample holders for high-temperature measurements have been created; one example rolled the sample in aluminium foil which gave a very low background signal and was easily compatible with the oven addition for the Quantum Design MPMS [29]. Another used a fused quartz tube that connected straight to the metal sample holder rod where the sample sat in a slit that was 104 mm from the top of the tube [30]. Air sensitive or liquid samples are usually contained within EPR (or NMR) tubes

because of such tubes' low magnetic susceptibility [28]. The tubes are typically flame tipped using a manifold to pump down the tube and a gas/oxygen flame to seal it. However if the sample is heat sensitive, such a method cannot be used. Being able to measure air sensitive or liquid samples and not expose them to any external energy, such as heat, is a substantial advantage as there are many materials that decompose to give magnetic contaminants. It was therefore necessary to design a sample holder for the air/heat sensitive $Ni(COD)_2$ samples.

A Quantum Design MPMS XL system, with a DC Transport, was used where -5 T $\leqslant \mu_0 H \leqslant$ 5 T and 1.9 K $\leqslant$ T $\leqslant$ 400 K. The sample was located within the second order gradiometer coils, the central coil being positioned at the centre of the core of the superconducting solenoid. The other two gradiometer coils are positioned 1.5 cm above and below the central coil. The sample was usually manually located at the centre of the gradiometer coils and then the magnetic moment was measured as outlined in the introduction; a sample scan length of 4 cm was adopted for all measurements of magnetic moment as described within chapter 3.

The designed sample holder is shown schematically in Figure 8.2. The high purity quartz tube had a diameter 0.5 cm (source: Heraeus Quartzglas). It was constructed by dividing a 12 cm tube in two, with one of the 6 cm sections having an end heat-sealed using an gas/oxygen flame. The sealed end was joined to the other 6 cm tube section, creating a bulb of quartz (typically 3-4 mm) which would be used to support the sample in the middle of the tube. The sample can then be placed inside the tube within a glovebox an under argon atmosphere and a PTFE cap was placed in the end of the tube. Powdered samples were placed in the tube with a specially made long funnel that reached to the quartz bulb so the sample could be inserted and not leave any powder on the walls of the quartz tube [31]. Once the tube had been capped and removed from the glovebox it was further sealed with a small amount of GE varnish (C5-101, purchased from Oxford Instruments), which has a very low magnetic moment and can survive at low temperatures. The sample remained yellow, with no visible decomposition during the initial handling or after subsequent magnetic measurements (see Figure 8.3 (top)). As shown in Figure 8.2,

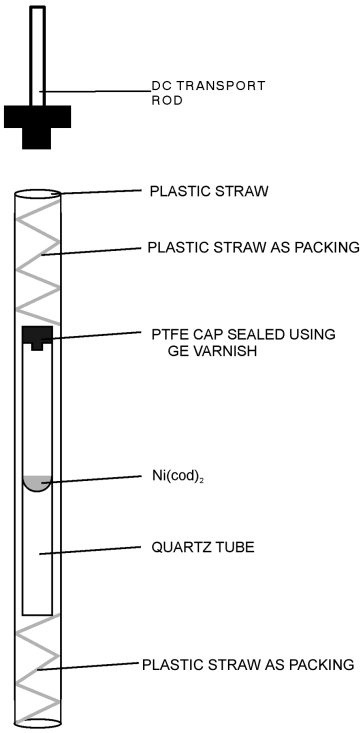

Figure 8.2: Schematic diagram of the sample holder to be attached to an MPMS brass/steel sample rod using the standard straw holder.

the quartz tube was contained within a clear plastic drinking straw with a folded plastic straw [32] used as packing on either end to hold the tube in place. This addition to the quartz tube was to provide a degree of mechanical flexibility to the sample holder while allowing it to be easily attached to an MPMS DC Transport brass/steel sample rod via the standard drinking straw attachment. The tube was inside the MPMS for a long period of time whilst the measurements were being conducted and it was cycled through a wide range of temperatures and applied magnetic fields. The mechanical stability of the tube remained constant during the whole experiment with no degradation of the tube and little, if any, changes of the raw data with time.

As a comparison, a similar sample was also prepared following the conventional method of flame-sealing the quartz tube. A tube of length 20 cm and diameter 0.5 cm was cut into 8 cm and 12 cm sections. The 12 cm section was sealed using a flame at one end to create a quartz bulb for the sample to sit in, the two tubes were

joined with the quartz bulb now in the middle of the tube. An NMR manifold was used so that the sample tube could be pumped down and re-filled with argon inside the glove box and then closed to temporarily seal the tube before it was exposed to an oxygen/propane flame. The quartz tube, measuring 14 cm in length, is shown at the bottom of Figure 8.3. When we prepared the $Ni(cod)_2$ to be measured in a Quantum Design MPMS system the sample was loaded into the quartz tube, which was evacuated and filled with nitrogen. Subsequent flame-sealing of the tube, which took less than 20 seconds, inevitably caused the $Ni(cod)_2$ sample to begin to decompose, despite the sample sitting in the middle of the tube; the yellow crystals transformed into a black solid over a period of 15 minutes. This process could not be stopped even by quickly placing the sample inside the MPMS and cooling the temperature to 250 K. The sample tube was connected to the DC transport rod in a similar fashion to the PTFE-sealed tube. Note that it is recommended to store $Ni(cod)_2$ in a freezer [25] at a temperature of -18 °C, thus magnetic measurements were made below this temperature to prevent decomposition.

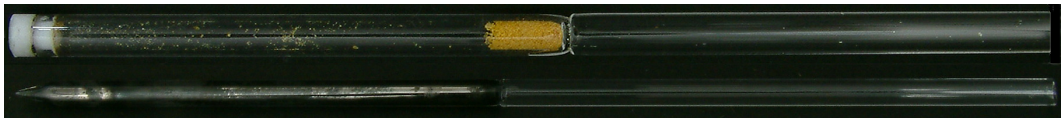

Figure 8.3: Top: Photograph of the specially designed tube taken after sample tube containing the $Ni(cod)_2$ had been left in an ambient atmosphere for 7 days. Bottom: Tube that was flame tipped where the $Ni(cod)_2$ decomposed and formed a Ni film. Pictures are not to scale; the bottom tube is 19.5 cm in length (after flame sealing) and the top is 12 cm in length. Both tubes have an equal diameter of 0.5 cm.

A longitudinal magnetic moment vs. applied field scan was conducted on the empty, PTFE-capped, quartz sample holder to observe the contribution from the background. Initially, the sample holder was centred using a small piece of Ni foil sandwiched between Kapton tape and attached to the outside of the plastic straw so as to avoid contamination of the inside of the quartz tube. The Ni foil could then easily be removed and the background signal measured, the results of which are shown in Figure 8.4. The results from the background scan appear to show a small paramagnetic moment ($\approx 10^{-7}$ Am^2 at 5 T) for both 250 and 10 K. At fields lower

than 3 T the scatter of the data points is larger than the standard error. This is a result of the failure of the MPMS fitting algorithm to fit the raw data successfully, even after detrending (see Figure 8.4B). The complicated data set is a result of the magnetic responses of all the components making up the sample. In fact, even at 4 T, the fitted data are still poor. Nevertheless, the generally small standard errors associated with the data suggest the scans are reproducible and may be subtracted from sample-related data using the background subtraction facility of the MPMS software [26].

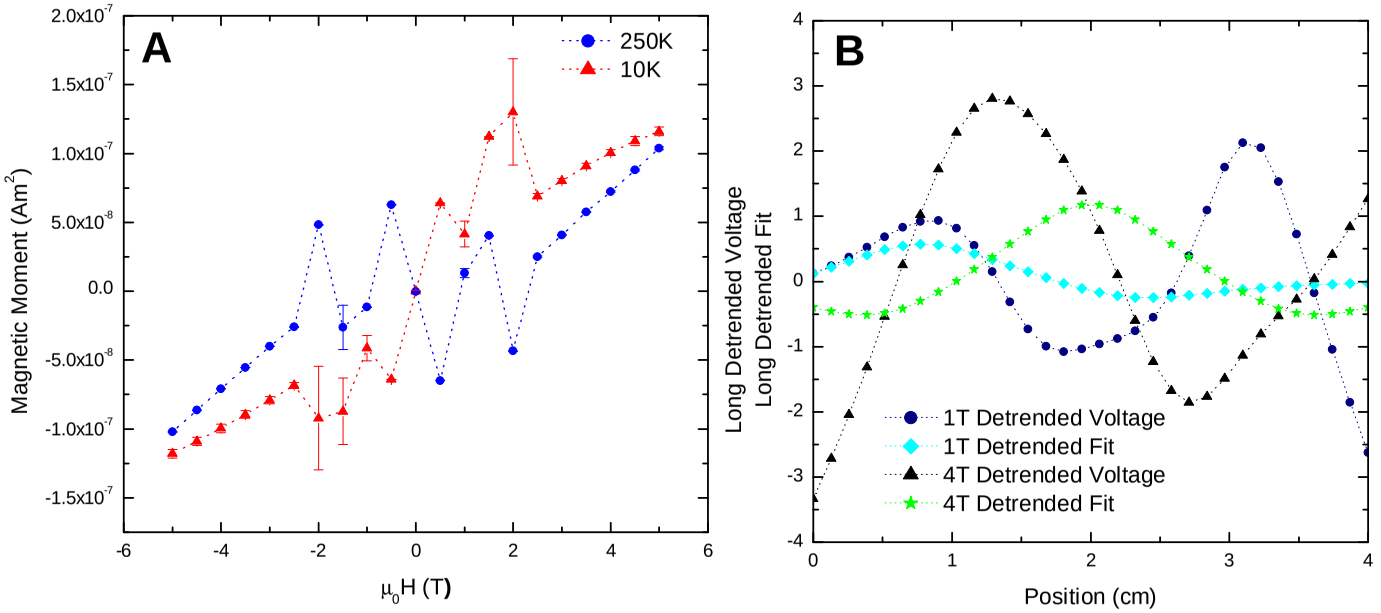

Figure 8.4: **A:** Magnetic moment vs. applied field illustrating the background response of the tube at 250 K (blue circles) and 10 K (red triangles). **B:** Shows the detrended voltage and the detrended fit against position at 250 K. This illustrates that the fit to the raw data at low fields (1 T) and at high fields (4 T) are extremely poor.

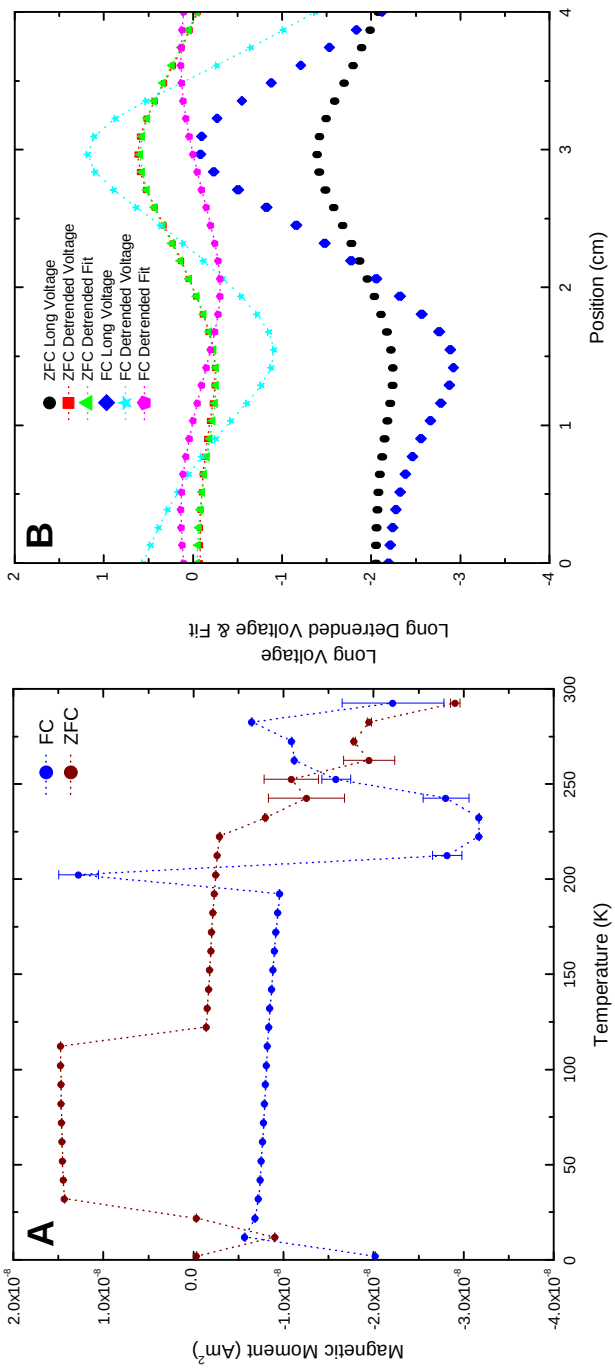

Figure 8.5: **A:** Magnetic Moment vs. temperature showing the Zero Field Cooled (ZFC) and Field Cooled (FC) response where μ_0H = 0.015 T. **B:** Shows the raw data at 50K to illustrate the poor fits to the FC data and that although the response of the ZFC and FC data is similar, the fits to each data set is different.

The temperature dependent data can be seen in Figure 8.5A where the applied field is at 0.015 T. There appears to be no general trend however although the moment is relatively small one encounters the same problem as illustrated for Figure 8.4. The raw data, Figure 8.5B, shows the long voltage for the ZFC and FC measurements at 50 K where the detrended voltage is a combination of three separate scans shown by black circles (ZFC) and blue diamonds (FC). Each individual scan over 4 cm appears to be reproducible with small standard deviation. The detrended voltage and fit for the ZFC data agree however for a similar curve, the detrended voltage and fit for the FC data do not. This illustrates that the moments that the Quantum Design software calculates are not correct and it is the SQUID voltage versus position curves that are needed for background subtraction. From knowing the response of the background one can determine whether the sample that is being measured is what is truly being seen.

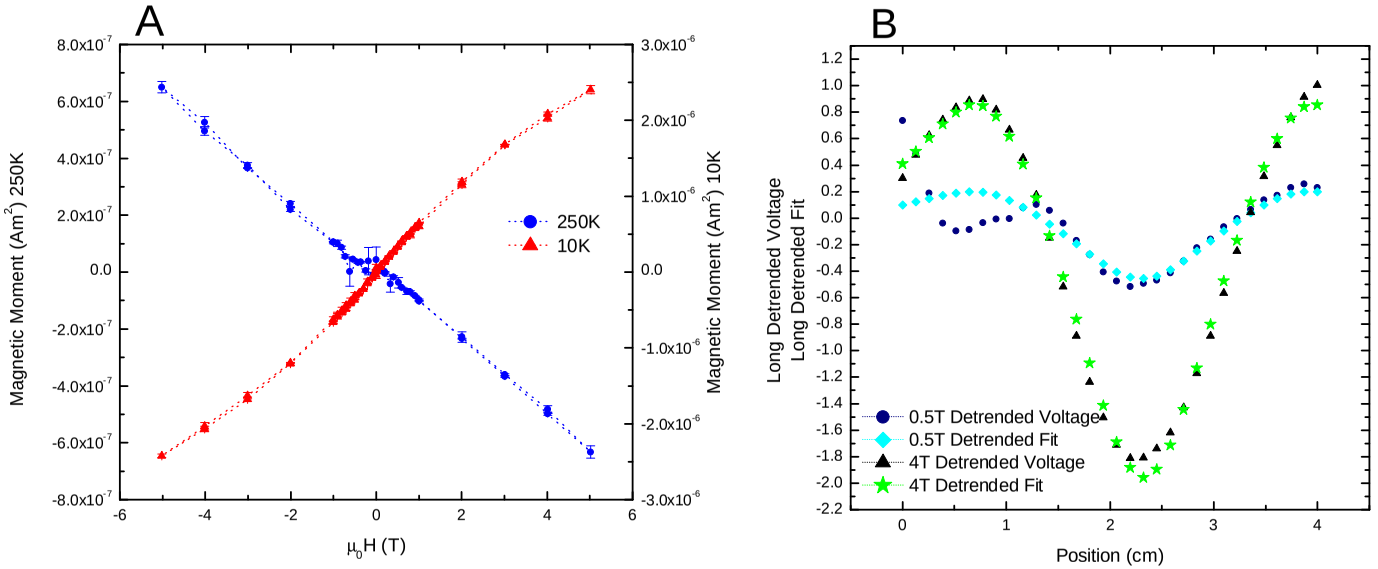

Figure 8.6: **A:**Magnetic moment vs. applied field of the Ni(cod)$_2$ sample at 250 K (blue circles) and 10 K (red triangles)**B:**The raw data at 250 K showing that the fit to the detrended voltage at low fields (0.5 T) is suitable however it improves significantly at high fields (4 T). Long regression fit values for the 250 K data; 1 T: 0.84 and 4 T: 0.90. For the 10 K data: 1 T: 0.88 and 4 T: 0.96.

Figure 8.6A shows the result of hysteresis loops obtained from the $Ni(cod)_2$ sample, which is clearly different from the background shown in Figure 8.4A. The $Ni(cod)_2$ shows a diamagnetic response at 250 K and the moment is larger than that of the sample holder ($\approx 7 \times 10^{-7}$ Am^2 at 5 T for a sample of mass $\approx$ 30.4 mg). The diamagnetic result agrees with Miller and Pokhodnya's work on $Ni(C_4(CN)_8)$ where they see a diamagnetic component for $Ni(cod)_2$ that is attributed to the cyclooctadiene ligands [20]. For fields of less than 1 T the data may suggest a small ferromagnetic component, but the standard errors are relatively large and the influence of the sample holder on the results is significant as indicated in the detrended raw data shown in Figure 8.6B. However, at higher fields the fit to the raw data is good, as demonstrated with the 4 T dataset in Figure 8.6B. At 10 K, there is a strong paramagnetic signal at all fields ($\approx 3 \times 10^{-6}$ Am^2 at 5 T). The transition from a diamagnetic to a paramagnetic signal, with decreasing temperature, suggests the presence of unpaired spins within defects or impurities in the $Ni(cod)_2$; this issue will be discussed in more detail in the next section of this chapter.

The magnetic response of $Ni(cod)_2$, which had decomposed in the flame-sealed sample holder at 250 K saturated at a field of less than 2 T. At 5 T $m = 1 \times 10^{-5}$ Am^2 (for an initial $Ni(cod)_2$ mass of 46 mg) (see Figure 8.7. At 10 K the sample showed a similar response, with $m = 1.4 \times 10^{-5}$ Am^2 at 5 T. Hysteresis loops measured at 250 and 10 K were clearly different those of the $Ni(cod)_2$ measured using the sample holder shown in Figure 1. The presence of spontaneous magnetic moments at both temperatures suggested ferromagnetic ordering within the material that would be expected from the presence of bulk Ni within the sample.

In summary, a quartz sample holder has been prepared to carry out magnetic measurements on air and heat sensitive samples in a Quantum Design MPMS. A PTFE plug seals the sample holder in an inert atmosphere to stop decomposition of the sample, avoiding the use of heat associated with the conventional flame-sealing method. The tube is reusable and works well, especially if the moment of the sample is large ($\gtrsim 10^{-7}$ Am^2). Magnetic measurements can be made over a large temperature range and we have tested the sample holder from 2 K to 290 K. The sample holder

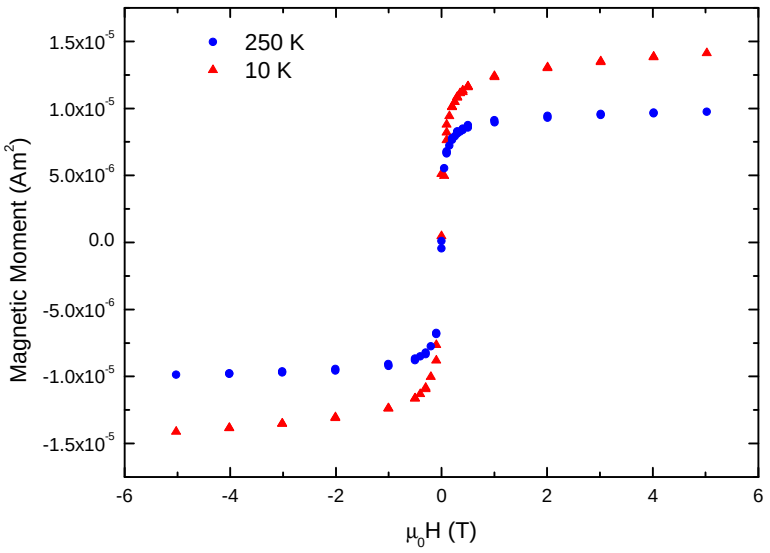

Figure 8.7: Magnetisation vs. applied Field for the flame sealed quartz tube sample of $Ni(cod)_2$.

has been used to investigate $Ni(cod)_2$, which has been shown to be diamagnetic at 250 K, crossing over to a paramagnetic response at 10 K. The data were obtained using the DC transport option on the MPMS but the sample holder could also be used with the Reciprocating Sample Option (RSO) transport as long as the sample is confined with, say, quartz wool, to prevent movement within the tube. It may also be possible, with a slight modification, for the sample tube to also be adapted for a Quantum Design PPMS. The high purity quartz allows the sample tube to be used in an Electron Spin Resonance spectrometer and UV/visible optical absorption experiments may also be made on materials within the sample holder.

8.3 Results and Discussion

Field-dependent magnetisation data can be seen in Fig 1. At 250 K the $Ni(COD)_2$ showed a diamagnetic response that was linear with the applied field, in agreement with previous statements on the magnetic nature of pure $Ni(COD)_2$ [20]. At low fields there is a deviation from the trend line that is due to the competition from

the background of the quartz sample holder and signal from the $Ni(COD)_2$ [27]. By fitting a straight line to the data shown in the inset of figure 8.8 the magnetic susceptibility at 250 K is determined to be χ_D = -4.98(7)$\times 10^{-9}$ m^3kg^{-1}.

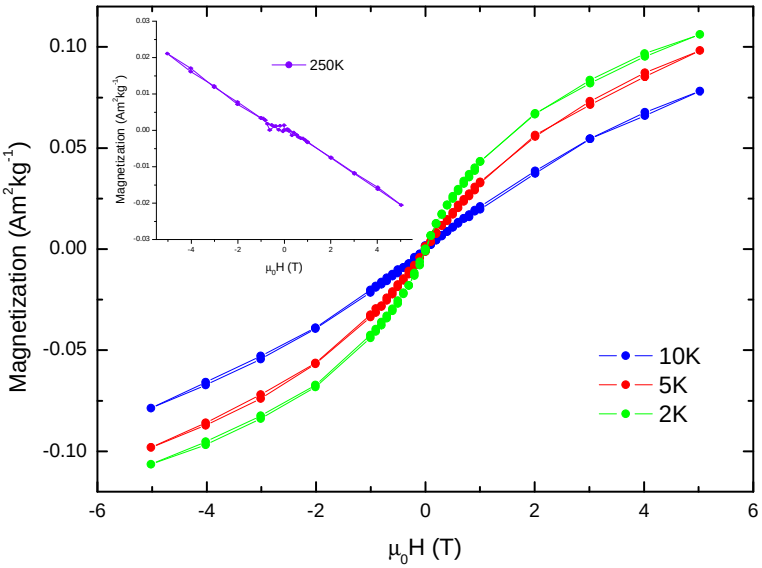

Figure 8.8: Magnetisation vs. applied Field, for the 1st batch of $Ni(COD)_2$, taken at 2 K, 5 K and 10 K. Note that no magnetic hysteresis is observed at any temperature. *Inset:* Magnetisation vs. applied Field at 250 K.

At lower temperatures a large paramagnetic signal dominates the magnetic data. The paramagnetic signal can result from either impurities in the material, defects within the $Ni(COD)_2$ or it may be due to the presence of superparamagnetic nickel nanoparticles or clusters arising from the decomposition of $Ni(COD)_2$. For the case of the 2 K results, the best fit to the data was achieved with a combination of two Langevin functions, which suggests that superparamagnetic nanoparticles are primarily responsible for the paramagnetic response. The fitting function is given in equation 8.1, where N is the number of particles per kilogram, μ is the relative magnetic moment, μ_B is the Bohr magneton and k_B is the Boltzmann constant. Fitting parameters are given in Table 8.1 and, using the bulk saturation magnetisation value of FCC Ni, it is possible to estimate the mean particle sizes to be 0.7 nm and 0.3 nm corresponding to the larger and smaller of the magnetic moments given in

the table. The values are rather small and suggest such a simple interpretation of the origin of the magnetic moments is not completely correct. In fact the more complicated nature of this magnetic phase is also suggested by attempting to scale the data onto one curve, by plotting magnetisation as a function of $\mu_o H/T$, as suggested by equation 8.1. This can only be achieved if the number density is multiplied by an appropriate scaling factor; this is shown in figure 8.9 where all the data have been scaled onto the 2 K data set. An interpretation of this result is that there is a temperature dependence of the number density of nanoparticles. For a simple superparamagnetic system N should be independent of temperature but it appears as if the number of magnetic moments is decreasing as temperature is lowered, while the mean magnetic moment per particle remains constant.

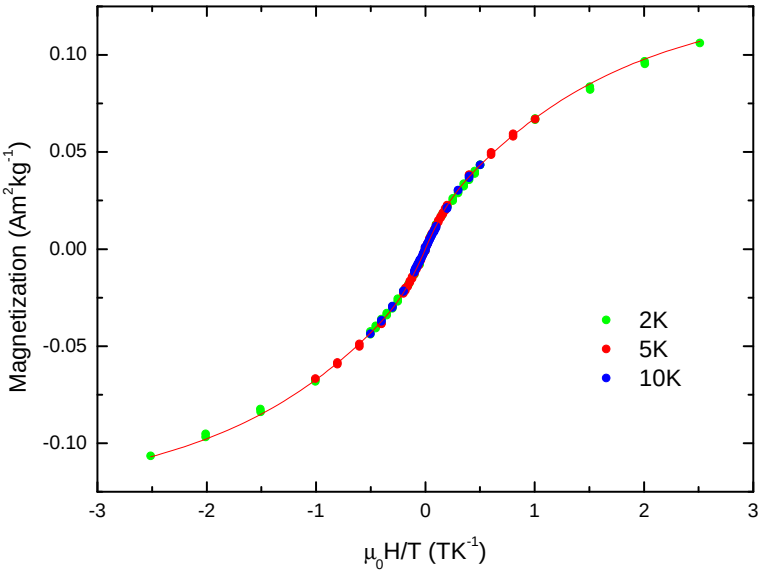

Figure 8.9: Scaled magnetisation vs. $\mu_o H/T$ plots for the 1st Batch of $Ni(COD)_2$ at 10 K, 5 K and 2 K. The 5 K and 10 K data have been scaled by dividing the curves by 1.58 and 2.05 respectively where the red curve is a two-term Langevin Function fit to all the data. Note that 50 K data (not shown in the graph) was also taken and can be scaled onto the $\mu_o H/T$ plot using a scaling factor of 3.3.

$$M = (N_\alpha < \mu_\alpha > \mu_B)\left\{\coth(y_\alpha) - \frac{1}{y_\alpha}\right\} + (N_\beta < \mu_\beta > \mu_B)\left\{\coth(y_\beta) - \frac{1}{y_\beta}\right\} \quad (8.1)$$

Batch Number	**Number of Particles per kg**	**Moment** $\langle \mu_{zj} \rangle$	**Particle Size**
	N_j	(μ_B)	(nm)
1(α) 2K	1.6 x 10^{20}	15.1	0.7
1(β) 2K	7.2 x 10^{21}	1.8	0.3
2(α) 5K	1.8 x 10^{20}	38.7	0.9
2(β) 5K	9.2 x 10^{21}	4.3	0.4

Table 8.1: Parameters from the fit to the data in Figure 8.9 (see Eqn 1) for both Batches 1 and 2 showing the components α and β. [34] *NB:* Batch 2 were scaled onto the 5 K data set, however this will affect values of N and not the particle sizes.

$$y = \frac{< \mu > \mu_B \mu_o H}{k_B T} \tag{8.2}$$

Assuming an FCC Ni structure, with the lattice parameter of $a = 0.352$ nm, the estimated particle sizes listed in Table are approximatly 1 - 2 unit cells. This would suggest that the thermal decomposition of solid $Ni(COD)_2$ has led to the creation of small clusters containing nickel e.g. the the decomposition of two unit cells of $Ni(COD)_2$ would result in a Ni_4 cluster. Such a cluster may be expected to have a maximum magnetic moment of approximately 9 μ_B assuming a spin-only (S=1) moment for each nickel atom. Though a Langevin function is normally used to describe non-interacting superparamagnetic single domain particles, it has been used to describe the low temperature magnetic response of clusters of sub-nanomater scale [13, 16, 36, 37] as well as bound magnetic polarons [38]. However, the fact that two Langevin functions are needed to describe the data of figure 2 may suggest a range of cluster sizes exist within the decomposed $Ni(COD)_2$. The particle sizes will only be a rough estimate as within a cluster one would not expect the interatomic distances to be similar to that of the bulk.

The scaling of the number density is of interest and indicates that the number of clusters contributing to the total magnetic moment of the sample is decreasing with temperature. One interpretation of this result is that individual clusters are unlikely

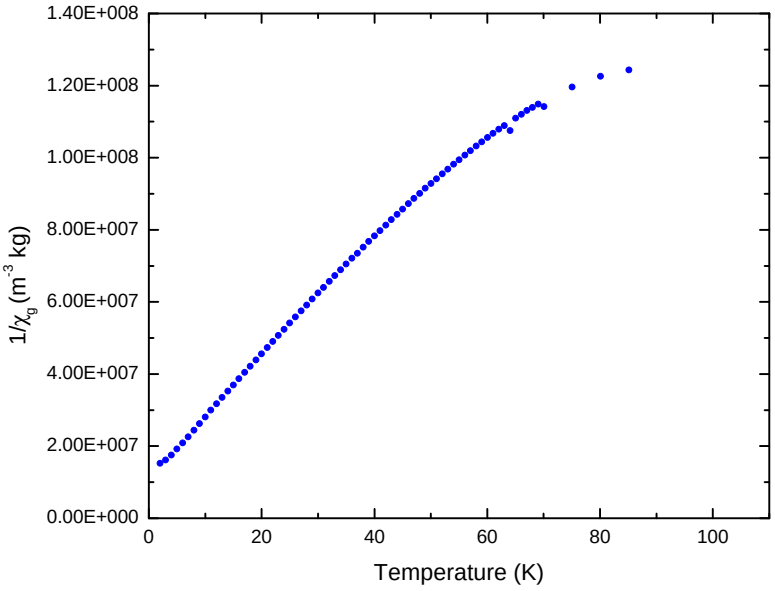

Figure 8.10: Inverse susceptibility vs. temperature of Batch 1. Data were taken with an applied field of 2.5 mT and have been corrected for the diamagnetic susceptibility. Note that the data do not follow a Curie-Weiss law at both high and low temperatures.

to adopt an FCC structure and the temperature dependence of N corresponds to spin state transitions within each cluster [39], with thermal excitation from the ground state to various excited states occurring when the temperature is raised above 2 K.

Figure 8.10 shows that the inverse mass susceptibility is generally a non-linear function of temperature, with the strongest curvature being observed at the highest values of T. However, assuming a Curie-Weiss behaviour at the lowest temperatures the parameters θ = -9 K and $C = 1.2 \times 10^{-6}$ m^3 K kg^{-1} are obtained. Using the total number densities at 2 K (from Table 1), the effective moment is estimated to be 6.4 μ_B, in reasonable agreement with the values presented in Table 8.1. Figure 8.11 shows the sum total of the saturation magnetisation of components α and β from Batch 1 (and Batch 2; see figure E.1) as a function of temperature, deduced from the fits to equation 1. The data show that there is a sharp increase in the saturation magnetisation when increasing temperature above 2 K. The 250 K data

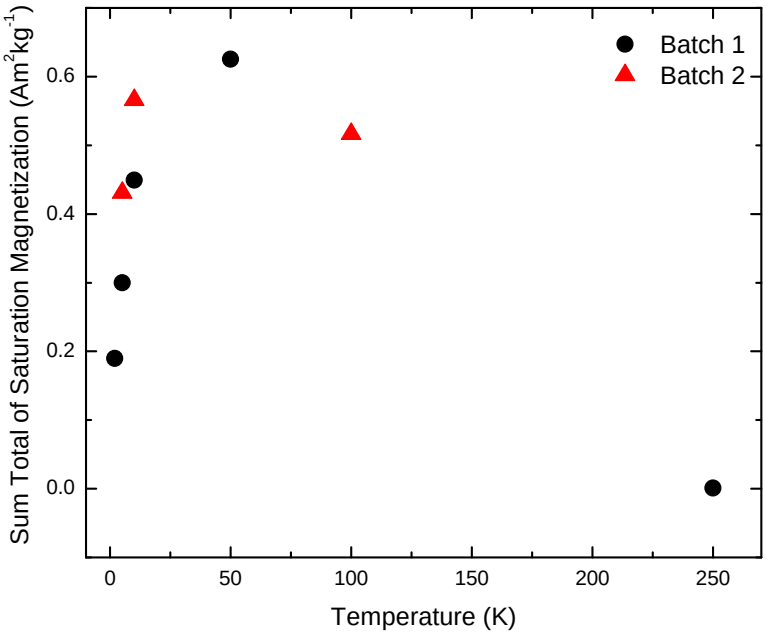

Figure 8.11: Sum total of the saturation magnetisation of components α and β of Batches 1 and 2 as a function of temperature. Note that the data point at 250 K is completely dominated by the diamagnetism of the host material.

point is not included in the analysis as it is completely dominated by diamagnetism at this temperature. One interpretation of this result is that $Ni(COD)_2$ is decomposing at high temperatures to form small clusters that are not HCP or FCC, and are undergoing a spin transition below 50 K. In fact both the curvature of the $1/\chi$ vs. T data and the increase in the saturation magnetisation with increasing temperature are both consistent with the thermal excitation of higher spin states within a magnetic cluster [39].

Indirect evidence for the existence of small clusters was obtained from TEM images of batch 1 $Ni(COD)_2$, shown in figure 8.12. The image does not show any large Ni nanoparticles, but there are some regions that show lattice fringes [40,41] suggesting very small crystalline areas. These are less then 1 nm in length supporting the particle sizes deduced from the two-term Langevin function fits. It is important to note that it was necessary to record the image in a few seconds because further irradiation with the electron beam resulted in the formation of an assembly of nanoparticles.

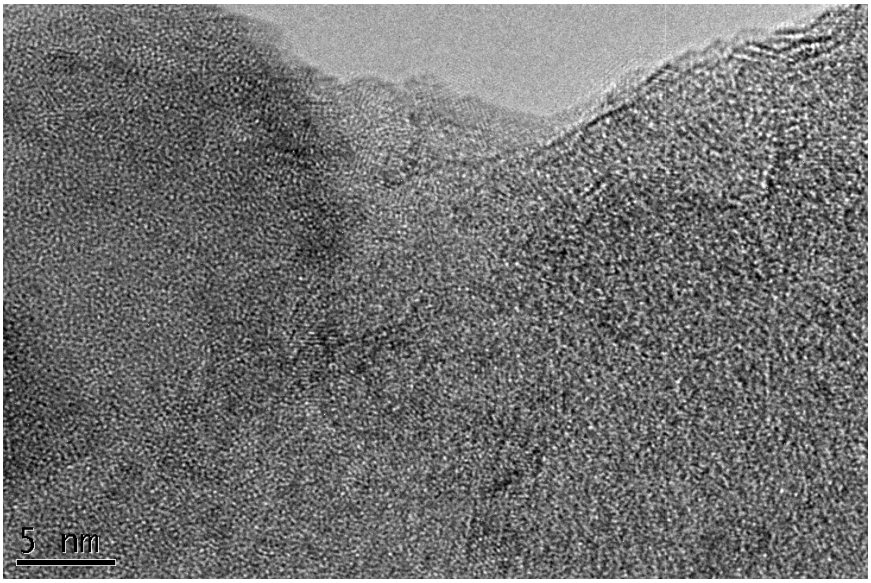

Figure 8.12: High Resolution TEM image of Batch 1. There are no obvious particles that can be seen in the matrix however there may be some crystalline areas approximately 1 nm.

Bright Field and Dark Field TEM images of these particles show that their sizes vary from 2 - 10 nm. The growth may be due to the electron beam providing thermal energy into the matrix allowing the the Ni clusters to combine and form a larger bulk FCC Ni particle [16]. Electron diffraction patterns (see supplementary information, figures E.2 & E.3) taken after exposure to the beam indicate crystalline FCC Ni particles do form [42], where the lattice parameters are slightly larger than bulk values, suggesting that there may be a large amount of surface strain on the Ni nanoparticles. These observations support the conclusions of Rojas *et al.* [43] who reported that electron beam irradiation can promote the growth of FCC nickel particles.

8.4 Conclusion

The magnetic properties of commercially produced and purchased batches of $Ni(COD)_2$ was measured. The samples showed a mixed magnetic phase system, with evidence characteristic of a diamagnetic response of the host material $Ni(COD)_2$ as well as the

presence of nickel clusters which appear to exhibit a temperature induced spin transition at low temperatures. Storing $Ni(COD)_2$ under conditions recommended by the chemical suppliers leads to significant amounts ($\approx$ 2 to 4% of the sample mass) of smaller moment Ni clusters ($\approx$ 2 to 4 μ_B). These particles/clusters (the β phase) are likely to be a consequence of the thermal decomposition of solid $Ni(COD)_2$. The magnetic moment of these samples agree with Apsel *et al.* and Khanna and Reuse for a Ni_5 cluster however the larger moment clusters (α phase) have a magnetic moment that is much higher. The problem with the reported system is that it is hard/impossible to determine the size of the clusters and to work out the moment per atom however from the rough calculations the larger moment particles are still sub-nanometer in size. When comparing to the geometries and total magnetic moment of the clusters calculated by Lu *et al.* the larger clusters fall into values of $n = 15 - 20$ however it would be hard to determine the exact value of n and these occur in a much lower number then the small moment clusters.

On an aside the presence of these low moment clusters does question the use of $Ni(COD)_2$ as a starting material for electronic and magnetic materials such as molecular magnets as there may be elemental Ni as a contaminant. However, we have shown the promise of $Ni(COD)_2$ as a useful material for studying Ni clusters where we present magnetic data taken using a DC transport method which is different to that of previous reports.

Bibliography

[1] G. Wilke. *Angew. Chem. Int. Ed* **72** (1960) 581

[2] B. Bogdanov, M. Kroner and G. Wilke. *Liebigs Ann. Chem.* **Nov** (1966) 699

[3] W. Keim. *Angew. Chem. Int. Ed.* **29** (1990) 235

[4] H. Dierks and H. Dietrich. *Z. Kristallogr.* **122** (1965) 1

[5] R. A. Schunn, S. D. Ittel and M. A. Cushing *Inorganic Syntheses* **28** (1990) 94

[6] D. de Caro and J.S. Bradley. *Langmuir***13** (1997) 3067

[7] J.S. Bradley, B. Tesche, W. Busser, M. Maase, andM.T. Reetz. *J. Am. Chem. Soc.* **122** (2000) 4631

[8] G. Cheng, V.F. Puntes, and T. Guo. *J. Colloid Interface Sci.* **293**(2006) 430

[9] E. Ramirez-Meneses, I. Betancourt, F. Morales, V. Montiel-Palma, C.C. Villanueva-Alvarado, andM.E. Hernandez-Rojas. *J. Nanopart. Res.* **13** (2011) 365

[10] A. W. Castleman, Jr. and S. N. Khanna. *J. Phys. Chem.* **113** (2008) 2664

[11] N. O. Jones, S. N. Khanna, T. Baruah and M. R. Pederson. *Phys. Rev. B.* **70** (2004) 045416

[12] T. Morisato, S. N. Khanna and Y. Kawazoe. *Phys. Rev. B.* **72** (2005) 014435

[13] S. E. Apsel, J. W. Emmert, J. Deng and L. A. Blloomfield. *Phys. Rev. Letts.* **76** (1996) 1441

[14] I. M. L. Billas, A. Châtelain and W. A. de Heer. *J. Magne. Magne. Mater.* **168** (1997) 64

[15] I. M. L. Billas, A. Châtelain and W. A de Heer. *Science* **265** (1994) 1682

[16] B. V. Reddy, S. K. Nayak, S.N. Khanna, B.K. Rao and P. Jena. *J. Phys. Chem. A.* **102** (1998) 1748

[17] Q. L. Lu, Q. Q. Luo, L. L. Chen and J. G. Wan. *Eur. Phys. D.* **61** (2011) 389

[18] F. A. Reuse and S. N. Khanna. *Chem. Phys. Letts.* **234** (1995) 77

[19] R. Jain, K. Kabir, J.B. Gilroy, K.A.R. Mitchell, K.C. Wong and R.G. Hicks. *Nature* **445** (2007) 291

[20] J. S. Miller and K. I. Pokhodnya. *J. Mater. Chem.* **17** (2007) 3585

[21] T. Ould-Ely, C. Amiens and B. Chaudret. *Chem. Mater.* **11** (1999) 526

[22] N. Cordente, C. Amiens, B. Chaudret, M. Respaud, F. Senocq and M. J. Casanove. *J. App. Phys.* **94** (2003) 6358

[23] Y. Koltypin, A. Fernadez, T. Critina Rojas, J. Campora, P. Palmer, R. Prozorov and A. Gedanken. *Chem. Mater.* **11** (1999) 1331

[24] P. B. Oliete, T. Critina Rojas, A. Fernadez, T. Critina Rojas, A. Gedanken, Y. Koltypin and F. Palacio. *Acta Materialia* **11** (2004) 2165

[25] Sigma-Aldrich. *Bis(1,5-cyclooctadiene)Nickel MDMS.* www.sigmaaldrich.com, 25 Jan 2010.

[26] QuantumDesign, www.qdusa.com. *MPMSApplicationNote1014Ð213* (2011)

[27] A. Berlie, I. Terry and M. Szablewski. *Meas. Sci. Technol.* **22** (2011) 017002

[28] Quantum Design, www.qdusa.com. *MPMS Application Note 1014-201.* Jan 2001. (Note that Quantum Design also make a Delrin sample holder that can be used for measuring air sensitive materials)

[29] J. Sese, J. Bartolome and C. Rillo. *Rev. Sci. Instrum.* **78** (2007) 046101

[30] S Bedanta, O Petracic, M Aderholz and W Kleemann. *Rev. Sci. Instrum.* **76** (2005) 083910

[31] We recommend weighing the empty sample tube and again after the sample has been added (whether using the funnel or not) to determine an accurate mass of the sample particularly if the sample is quite adhesive to the funnel wall.

[32] The clear plastic drinking straws are recommended by Quantum Design to be used in magnetic measurements as they have a very low moment and can endure cycling through temperature ranges within the region of 2-300 K.

[33] Quantum Design 2000 MPMS Application Note 1014-203 A (www.qdusa.com)

[34] For the first Batch the average error in the fit is 9% which is substantial however this error is vastly increased when translated to particle size where it becomes 37%. The error in the particle size is not reflective of the fit to the data by Equation 1 as the overall fit has a R^2 value of 0.999 showing a good fit. For Batch 2 the errors in the fit to the data average out at 6% which translates to a 35% error in the particle size where the fit has an R^2 value of 0.999.

[35] The highest spin value of an Ni_4 cluster would be $S = 4$ and so the moment would be $2 \times \sqrt{(4 \times 5)} \approx 9\mu_B$

[36] Xi. Chen, S. Bedanta, O. Petracic, W. Kleemann, S. Sahoo, S. Cardoso and P. P. Freitas. *Phys. Rev. B* **72** (2005) 214436

[37] O. Okada. *J. Phys. Soc. Japan* **48** (1980) 391

[38] E. Quinteroa, M. Quinteroa, M. Morocoimaa, G. E. Delgadob, L. Laraa, J. Goméz, and P. Bocarandaa *Rev. Mex. Fís* **S53**(2007) 163

[39] J. S. Smart. Evaluation of Exchange Interactions from Experimental Data *Magnetism III* ed. GT Rado and J SuhlAcademic Press, New York and London, 1963 63-114.

[40] D. B. Williams and C. Barry Carter. Transmission Electron Microscopy Imaging III 1996 New York: Kluwer Academic/ Plenum Publishers 441-444

[41] P. Fraundorf, W. Qin, P. Moeck and E. Mandell. *J. App. Phys* **98** (2005) 114308

[42] When looking at the ratio of diffraction planes to confirm a FCC cubic phase we should get from the (111):(200) = 1.33 and from (220):(111) = 2 and from (111):(113) = 2.75. We observe 1.38 and 1.93 before imaging and 1.37, 2.02 and 2.97 respectively after imaging.

[43] T. C. Rojas, M. J. Sayagués, A. Caballero, Y. Koltypin, A. Gedanken, L. Ponsonnet, B. Vacher, J. M. Martin and A. Fernández. *J. Chem. Mater.* **10** (2000) 715

Chapter 9

Conclusions and Future Work

Throughout this thesis various topics based on TCNQ based magnetic materials have been covered; within this final chapter the main conclusions and future work will be summarised within different sections.

9.1 Nickel-TCNQ Based Magnetic Material

This protio sample was already synthesised and characterised by Clérac *el al.* [1] in previous work where they concluded the material was a glassy ferromagnet. We have synthesised both the protio and deutero analogues of the $Ni(TCNQ)_2$ magnetic material and although we were not able to reproduce the T_C in the protio sample observed by Clérac *et al.*, exactly it was clear there was a dramatic shift between our protio and deutero samples where the T_C had shifted to a higher temperature on substitution of the H atoms with heavier isotope.

Substitution of the H atoms by deuterons was also shown to have an effect on the sample structure where SEM images of the deuterated sample show larger crystallites are present. There was also observed differences in the kinetics/thermodynamics of the chemical reaction which may suggest that the slower and more difficult precipitation of the deutero product may lead to a more stable material. Although neutron

and x-ray diffraction experiments were attempted, no dramatic conclusions on the structural properties could be drawn except to confirm those previously reported in the literature [1]. However experiments on D1B, a high flux neutron diffractometer, showed very weak magnetic Bragg peaks which may be evidence for a weak short range magnetism.

From the magnetic data the deutero sample is confirmed to be ferromagnetic where the temperature dependence shows hysteresis in an applied field of 25 G. At low temperatures both the magnetization and heat capacity data can be modelled using a 3D spin wave model which again confirms the 3D nature of the ferromagnetism. However the AC susceptibility data show a frequency dependence of the transition in other samples where the dependence is comparable to that observed within the canonical spin glasses. From this perspective the sample has been compared to $La_{1-x}Sr_xCoO_3$ [2] which shows ferromagnetic cluster glass behaviour which may explain the observed behaviour within the Ni(TCNQ-D_4)$_2$ where there are regions of ferromagnetic clusters within a matrix that undergo a percolative ferromagnetic phase transition at T_C and at very low temperatures these clusters interact to form a 3D ferromagnetic system.

This is idea can be further supported by the muon spin relaxation data where in ZF one observes two transitions within the relaxation rate, λ_1. The ZF could only be described by a sum of two exponential relaxations, one which described the dynamics within the system, λ_1 and a slow relaxation component, λ_2, which is likely due to muons experiencing a strong internal field and being dephased outside of the measurement's time window. It was suggested that the muons that are sensitive to the dynamics are located within the wall/edges of these magnetic clusters and the slow relaxing component was due to muons implanting in the centre of these magnetic clusters where the internal field would be strong. Within λ_1 the two transitions were ascribed to be a ferromagnetic transition at $T \sim$20 K and a spin freezing transition at $T \sim$5 K. When a longitudinal field was applied the nuclear component, presumably from the N atoms, could be decoupled with relative ease and at $B_{LF} = 50$ G a heavily damped oscillation was observed within the transition region. This implies

that the muon relaxation is sensitive to the hysteretic nature of the magnetization of the sample. Application of a larger LF could not completely repolarise all the muon ensemble which is suggesting that there are significant dynamics present within the sample associated with the magnetism.

The aged sample showed a similar behaviour to the fresh sample however over time T_C shifted to lower temperatures. This was believed to be due to water absorbance which would lead to a destruction of magnetic exchange pathways. Neutron diffraction data of the aged sample showed similar peaks to that of the hydrated sample which confirms the absorbance of water and a change in structure within areas of the sample. The magnetic susceptibility of the aged sample shows a remarkable decrease in the temperature dependence of the transition and from the AC susceptibility data, the frequency dependence of transition has become weaker than in the fresh sample. Muon spin relaxation data show a similar behaviour to the fresh sample where, under ZF conditions, a reduced T_C was observed though, interestingly, the spin freezing effect at 5 K seemed unaffected.

A brief comparison with the Mn(TCNQ-D_4)$_2$ sample showed that the Mn sample is a more crystalline system where there is more structural information revealed within the diffraction pattern and there are sharper peaks which suggest larger particle size. The remarkable effect of the increased crystallinity is a reduction in the magnetic behaviour observed where there is no clear evidence of the a transition unless the data are plotted at χT vs. T in which case a complex temperature dependence is revealed which is a weak effect. Therefore one could conclude that by increasing the crystallinity of the M(TCNQ)$_2$ may lead to a sample that shows weaker magnetism and that the magnetism is in some way related to a disorder driven process.

Overall the Ni(TCNQ-D_4)$_2$ sample has been confirmed to behave like a 3D ferromagnetic material at low temperatures however the glassiness associated with the transition suggests that the sample is a cluster glass material. The muon data also show a ferromagnetic transition and a spin freezing transition which when combined with the other structural and magnetic data suggest the sample might not be strictly nanoparticulate but made of clusters of Ni(TCNQ-D_4)$_2$ where the magnetism may

be driven by disorder and the percolative nature of the ferromagnetism.

Future work would be to study the magnetism of the sample at sub-2 K temperatures to look at the glassiness of the material using both magnetic susceptibility measurements and muon spin relaxation. This would demonstrate the nature of the ferromagnetism at low temperatures and perhaps reveal a more complex behaviour than suggested by the current results. Another avenue of research is to attempt to create thin films of the sample using evaporation. Miller and Epstein showed that more crystalline $V(TCNE)_x$ could be made using evaporation [3] where by a similar result for $Ni(TCNQ)_2$ would allow for a more detailed understanding of the magnetism within the sample. From the work within this thesis on the $Mn(TCNQ\text{-}D_4)_2$ sample increasing the crystallinity of the sample may lead to dramatic effects associated with the magnetism.

9.2 KTCNQ and Derivatives

Throughout this chapter preliminary work was presented on the ability to tune the spin-Peierls (SP) transition within the samples which ultimately reflects the varying nature of the TCNQ-TCNQ interaction when the substituents are changed on the aromatic ring. Since the moment of the sample is low, or essentially zero below the SP transition, this made the magnetic measurements difficult as the magnetometer was measuring a moment that was very small.

Structural data was only collected on the KTCNQ-D_4 sample which was refined resulting in similar lattice parameters to that previously reported in the literature for the protio form [4]. However to get the best refinement possible a KI phase had to be included in the fit to the data. However, the collected data was not good enough to be able to get a full refinement where the atomic positions could be refined as well as the anisotropic thermal factors. It was not possible to collect magnetic data on this sample which may be due to the large diamagnetic KI impurity which dominated the signal at 1000 G.

KTCNQ-H_4 was measured using both a magnetometer and μSR. The magnetic experiment showed an SP transition between 300 - 400 K which was expected however there was an artefact at $\sim$100 K that could not be explained. It was suggested that this may be due to the magnetic history of a sample where a large applied field may have influenced the freezing of a disordered magnetic state of the dimerised TCNQ anions. However, it could also be related to the defects within the sample (probably TCNQ-related) which may be coupling magnetically and leading to a remanence which is sensitive to the applied field. Nevertheless, more research is needed on this system to probe the exact origin of this anomaly. μSR showed that the technique is sensitive to the SP transition where the relaxation between 300 - 450 K describes the dynamics associated with the dimerisation of the TCNQ anions which was similar to that observed within MEM$(TCNQ)_2$ [5,6]. Below 300 K the relaxation could only be modelled by an exponential relaxation which may mean the muons are sensitive to the electronic fluctuations even at these low temperatures. At low temperatures a missing fraction was observed and on heating the relaxation rate peaks at 250 K. The peak may be due to the fluctuations coming into the time scale of the muon however the change in asymmetry may be due to low frequency excitations.

By substituting protons on the TCNQ ring it was possible to alter the temperature that the system undergoes a spin Peierls transition where addition of F atoms shifts T_{SP} to approximately 150 K. For the brominated compound there was no clear evidence of a SP transition and it appeared that the magnetic ordering was destroyed. To study these materials further structural data is needed, especially to explain the lack of ordering within KTCNQ-Br_2 as it may be that the large bromine atoms distort the structure to such an extent that the TCNQ-Br_2 molecules cannot dimerise. A muon experiment was conducted on the KTCNQ-F_4 where a similar behaviour through the SP transition was observed as for KTCNQ-H_4. At low temperatures it was possible to model the relaxation to using two F-μ^+-F states where the two muon sites associated with this state were predicted to be between the TCNQ-F_4 dimers and between two F atoms on a single TCNQ-F_4 molecule. However there is a slow relaxing background that accounts for most of the asymmetry which may be coupling of the muon to the cyano groups on the TCNQ molecule.

9.3 Nickel Nanoparticles in a Metal/Metal-Organic Matrix

Five samples were synthesised based on the precursors $Ni(COD)_2$ and $TCNQF_4$ where a magnetic material was produced that was shown to be nickel nanoparticles or clusters encapsulated within an organic/metal-organic matrix. It was found that the particle sizes could be tuned through the use of different solvents. When a halocarbon was used this led to larger particle sizes where the resultant magnetism could be separated into two distinct components: superparamagnetic Ni nanoparticles and that of the matrix. At high temperatures, the superparamagnetism dominated the behaviour of the sample however at lower temperatures the magnetism of the matrix was more obvious and if the ferromagnetic component was subtracted the resultant magnetism could be modelled using a scaling relationship and a two-term Langevin function. The scaling behaviour where the M vs. B data could be scaled onto the 2 K data set shows that the magnetism within the matrix falls into an antiferromagnetic groundstate where moments are locking out and the two-term Langevin function models the size distribution of magnetic clusters. An important result is that the particle sizes determined using the PXRD data and TEM images largely agree, yet those calculated from blocking temperatures associated with the nanoparticles are much lower suggesting the matrix plays an important role in hardening the magnetism of the nanoparticles.

When a nitrile based solvent was used within the reaction of $Ni(COD)_2$ and $TCNQF_4$ this led to smaller Ni clusters being produced but still encapsulated within a matrix. The magnetism showed no signatures of superparamagnetic behaviour but, at low temperatures, the data resembled that of the halocarbon samples where a scaling relationship and two-term Langevin function was used to describe the data. This supports the idea that the the matrix in the halocarbon samples may consist of small magnetic Ni clusters that interact at low temperatures and fall into an antiferromagnetic groundstate.

From our work we have been able to control the both the nanoparticle size and

the matrix by simple variation of the solvent; when using a nitrile based solvent we are able to create very small well dispersed atomic clusters within an organic based matrix. However, when using a halocarbon based solvent it is possible to create Ni nanoparticles within a matrix that exhibits a much higher blocking temperature and thus magnetic anisotropy than what is expected for particle sizes of a similar size.

9.4 Low Moment Ni Clusters Formed Within $Ni(COD)_2$

The magnetic properties of commercially produced and purchased batches of $Ni(COD)_2$ was measured. The samples showed a mixed magnetic phase system, with evidence characteristic of a diamagnetic response of the host material $Ni(COD)_2$ as well as the presence of nickel clusters which appear to exhibit a temperature induced spin transition at low temperatures. Storing $Ni(COD)_2$ under conditions recommended by the chemical suppliers leads to significant amounts ($\approx$ 2 to 4% of the sample mass) of smaller moment Ni clusters ($\approx$ 2 to 4 μ_B). These particles/clusters (the β phase) are likely to be a consequence of the thermal decomposition of solid $Ni(COD)_2$. The magnetic moment of these samples agree with Apsel *et al.* [7] and Khanna and Reuse [8] for a Ni_5 cluster, however the larger moment clusters (α phase) have a magnetic moment that is much higher. The problem with the reported system is that it is hard/impossible to determine the size of the clusters and to work out the moment per atom though, from the rough calculations, the larger moment particles are still sub-nanometer in size. When comparing to the geometries and total magnetic moment of the clusters calculated by Lu *et al.* [9] the larger clusters fall into values of $n = 15 - 20$ however it would be hard to determine the exact value of n and these occur in a much lower number than the small moment clusters.

As an aside, the presence of these low moment clusters does question the use of $Ni(COD)_2$ as a starting material for electronic and magnetic materials such as molecular magnets as there may be elemental Ni as a contaminant. However, we have

shown the promise of $Ni(COD)_2$ as an incredibly useful material for studying Ni clusters where we present magnetic data taken using a DC transport method which is different to that of previous reports.

Bibliography

[1] R. Clérac, S. O'Kane, J. Cowen, X. Ouyang, R. Heintz, H. Zhao, M. J. Bazile and K. R. Dunbar. *Chem. Mater.* **15** (2003) 1840

[2] J. Wu and C. Leighton. *Phjys. Rev. B.* **67** (2003) 174408

[3] K. I. Pokhodnya, D. Pejakovic, A. J. Epstein and J. S. Miller. *Phys. Rev. B.* **63** (2001) 174408

[4] M. Konno, T. Ishii and Y. Saito. *Acta Cryst.* **B33** (1977) 763

[5] S. J. Blundell, F. L. Pratt, P. A. Pattenden, M. Kurmoo, K. H. Chow, S. Takagi, Th. Jestädt and W. Hayes. *J. Phys.: Condens. Matter* **9** (1997) L119

[6] B. W. Lovett, S. J. Blundell, F. L. Pratt, Th. Jestädt, W. Hayes, S. Tagaki and M. Kurmoo. *Phys. Rev. B.* **61** (2000) 12241

[7] S. E. Apsel, J. W. Emmert, J. Deng and L. A. Blloomfield. *Phys. Rev. Letts.* **76** (1996) 1441

[8] F. A. Reuse and S. N. Khanna. *Chem. Phys. Letts.* **234** (1995) 77

[9] Q. L. Lu, Q. Q. Luo, L. L. Chen and J. G. Wan. *Eur. Phys. D.* **61** (2011) 389

Appendices

Appendix A

Supplementary Information and Data for Ni(TCNQ-D_4)$_2$

Within the appendix can be found information as well as additional data that is not shown within chapter 4. This includes data related to the structure and also magnetism of the samples.

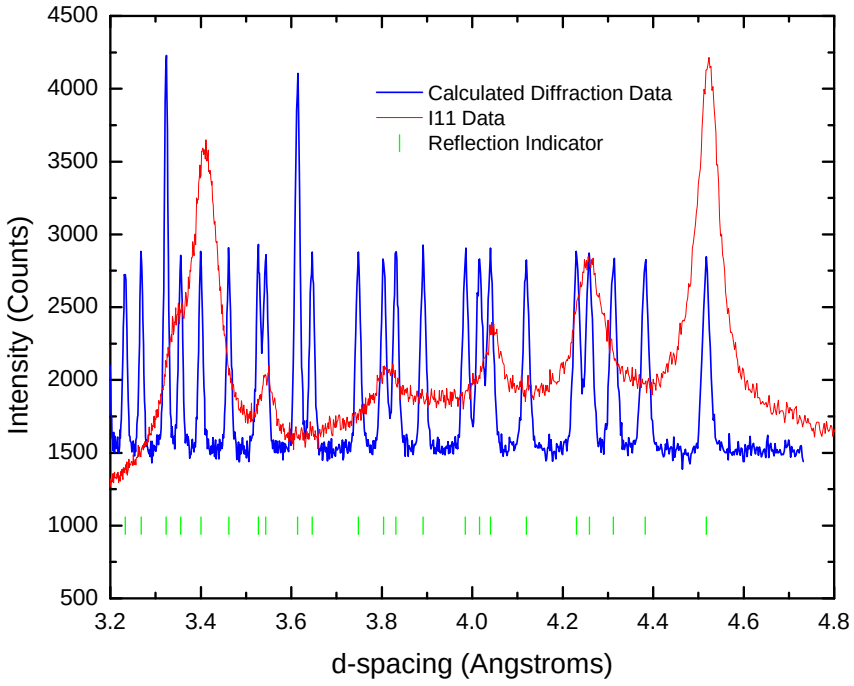

Figure A.1: Diffraction data collected on I11 plotted with the calculated theoretical structure from Treor90 with space group P 4/mmm. The green ticks are where reflections are expected to appear and from the data it is clear that the space group does not match the atomic structure from the diffraction data.

A.1 AC Susceptibility Data

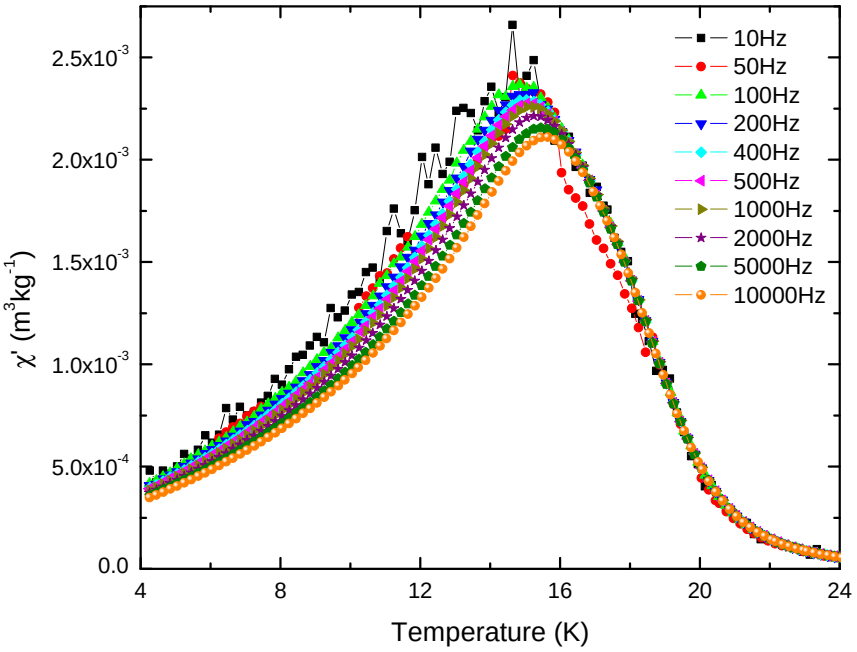

Figure A.2: Real component of a fresh sample of $Ni(TCNQ\text{-}D_4)_2$.

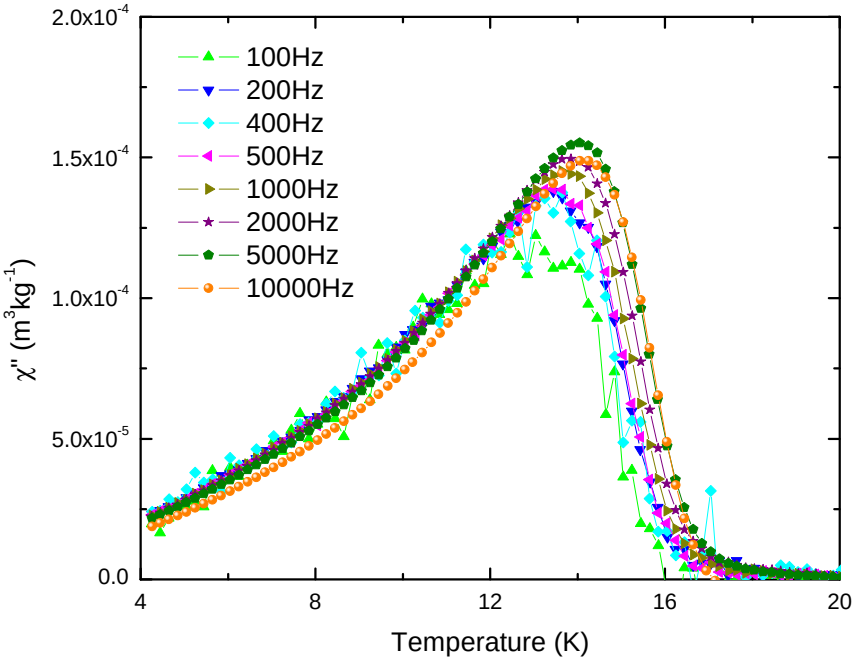

Figure A.3: Imaginary component of a fresh sample of Ni(TCNQ-D_4)$_2$.

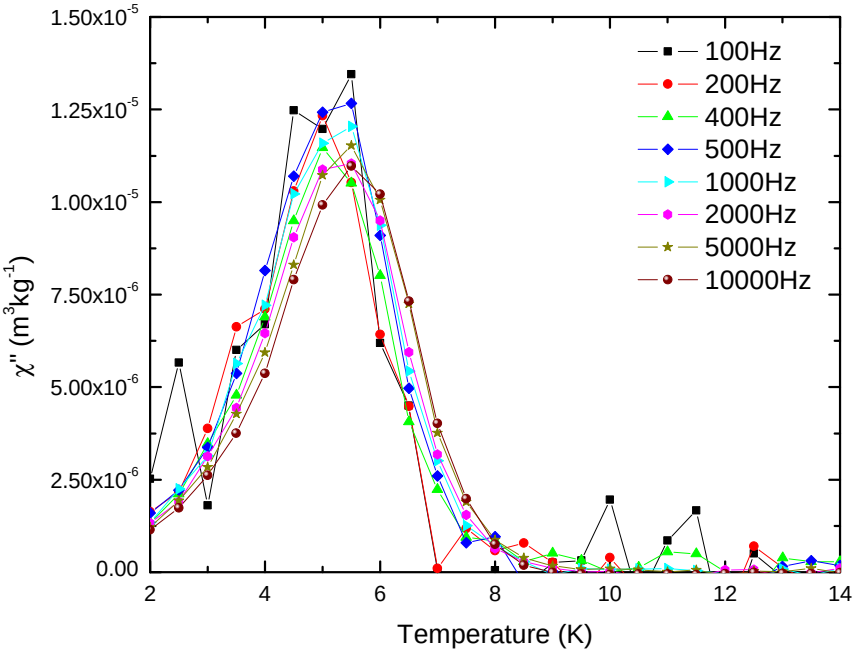

Figure A.4: Imaginary component of the aged sample of Ni(TCNQ-D_4)$_2$.

A.1.1 Analysis of the Imaginary Susceptibility

The imaginary susceptibility of AB4 and AB5 were analysed in a similar manner to the real component of the susceptibility using both an activated behaviour as well as the Vogel Fulcher model. If the data is modelled using a purely activated behaviour the values are unphysical and so this illustrates that the VF law must be a better description for the data and there is some glassy interactions associated with the transition, or lossy component of the susceptibility.

The results for AB4 are within the able below.

Parameter	Value
T_{f0} (K)	9.0(2)
φ	0.059
$E_{\mathrm{a}}/k_{\mathrm{B}}$ (K)	19(2)
f_0 (MHz)	17.6

Table A.1: Parameters from the analysis of the imaginary component of the susceptibility for AB4.

The data in table A.1 shows that the lossy component of the magnetism shows a frequency dependence similar to a spin glass, as the value of φ is low. The VF analysis yields an activation temperature similar to the ferromagnetic transition observed within the DC susceptibility data. The fluctuations are also faster and are higher then that observed for the dynamic component within the muon spectroscopy measurements.

A similar trend is seen in the sample AB5 where the values, shown in table A.2, are similar to AB4, except the value of T_{f0} showing that the in reality there is a difference between the two samples which may simply be stoichiometry.

This analysis was based on using the values from a fit of $T_f = T_0 + log(\omega)(T_0\varphi)$ where the value of the intercept could be fed into the VF analysis and held constant.

Parameter	Value
T_{f0} (K)	11.2(2)
φ	0.051
E_a/k_B (K)	21(2)
f_0 (MHz)	18

Table A.2: Parameters from the analysis of the imaginary component of the susceptibility for AB5.

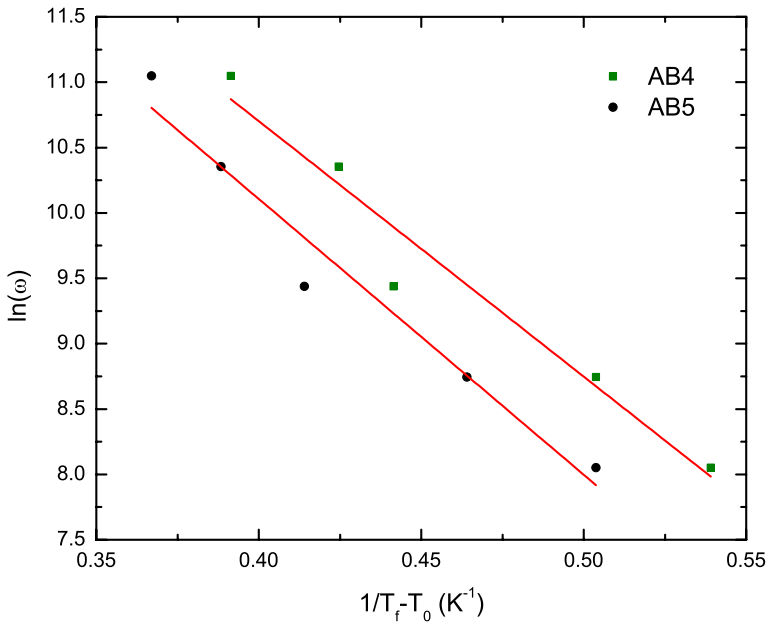

Figure A.5: .

Vogel-Fulcher analysis of the imaginary component of the susceptibility for AB4 and AB5.

Appendix B

Supplementary Information from Muon Experiment on $Ni(TCNQ\text{-}D_4)_2$

This appendix contains supplementary information from the μSR experiments performed on both the fresh and aged samples of $Ni(TCNQ\text{-}D_4)_2$.

B.1 Aged Sample

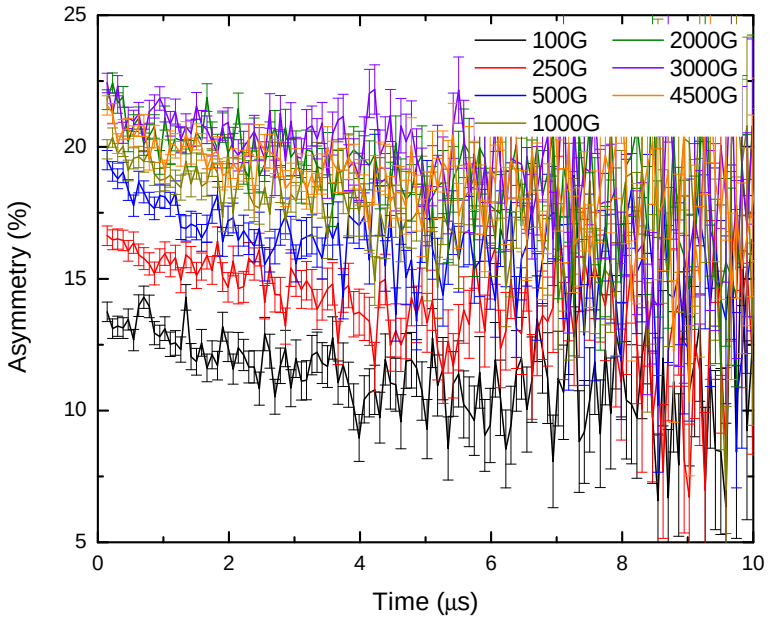

Figure B.1: Asymmetry vs. applied LF at 5 K where the relaxation between all fields is largely similar however the asymmetry changes as the field is increased.

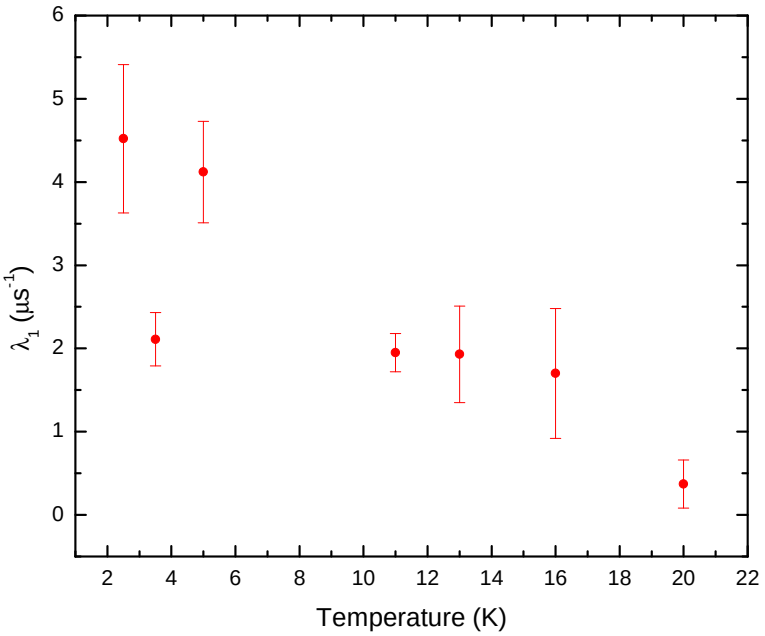

Figure B.2: Relaxing parameter, λ_1, for the aged sample with an applied longitudinal field of 50 G.

B.2 Pressure Dependence

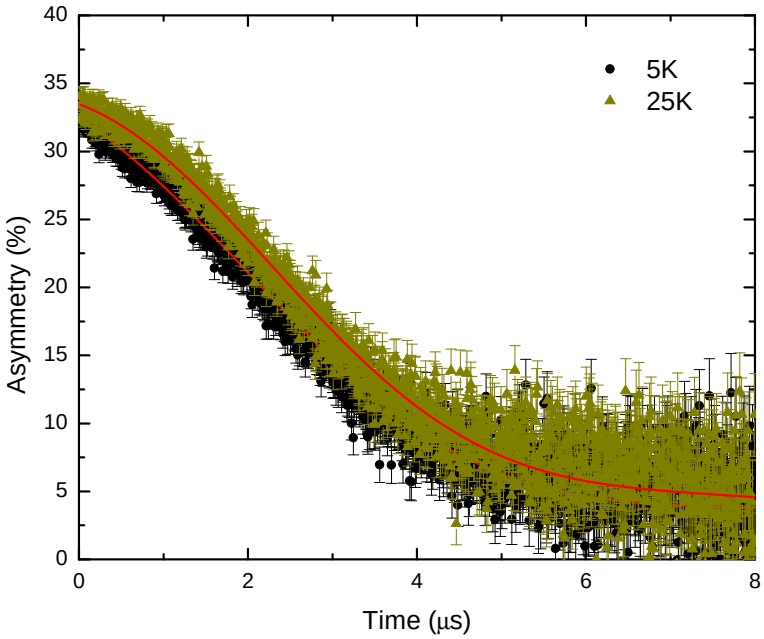

Figure B.3: Raw μSR data in zero field and zero applied pressure.

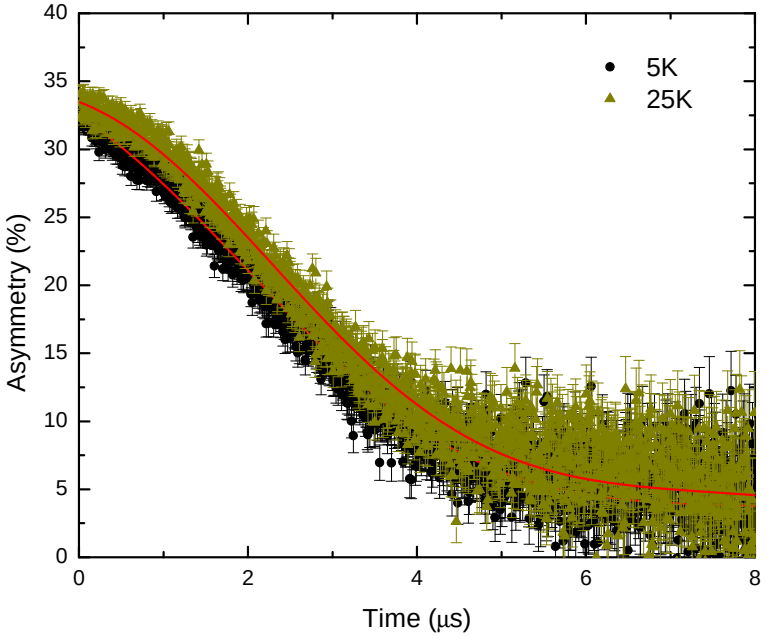

Figure B.4: Raw μSR data in zero field and 15 kbar applied pressure.

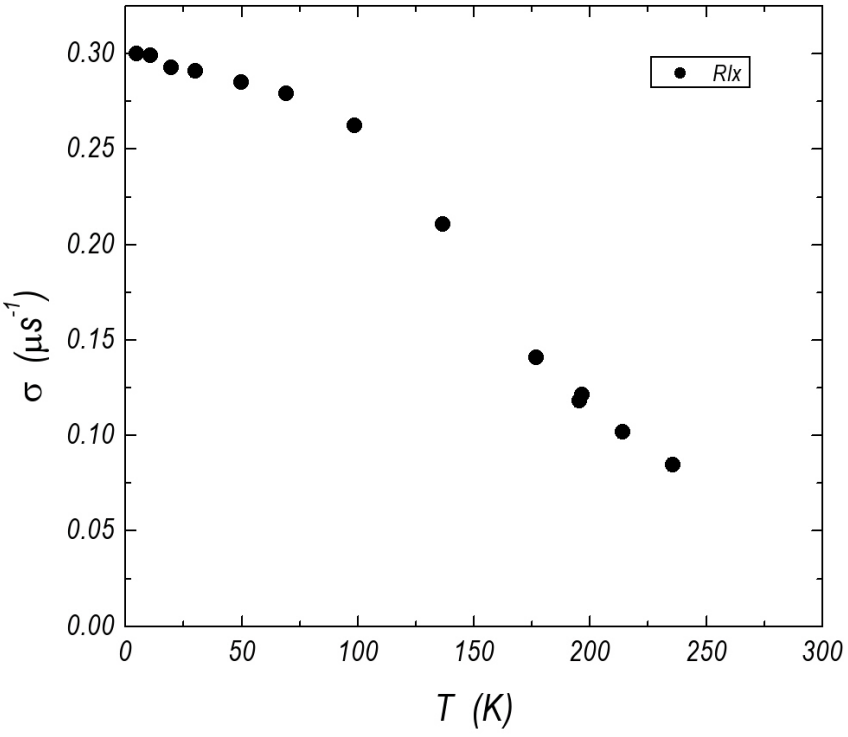

Figure B.5: Relaxation of CuBe pressure cell background on GPD.

Appendix C

Supplementary Information for the Chapter on KTCNQ and Derivatives

C.1 KTCNQ-H_4 μSR Measurements

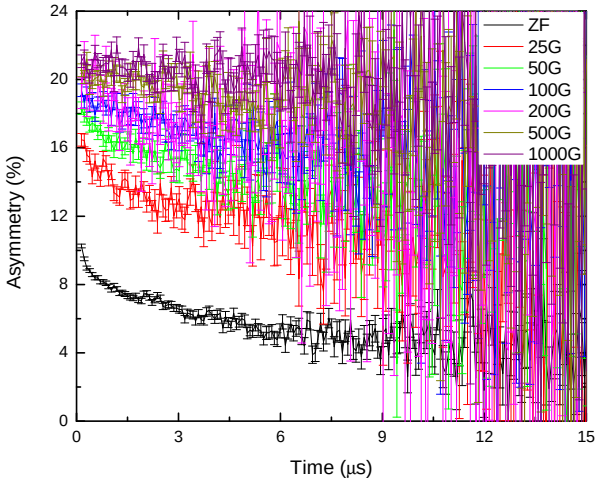

Figure C.1: μSR spectra for KTCNQ-H_4 at 30 K with an applied field.

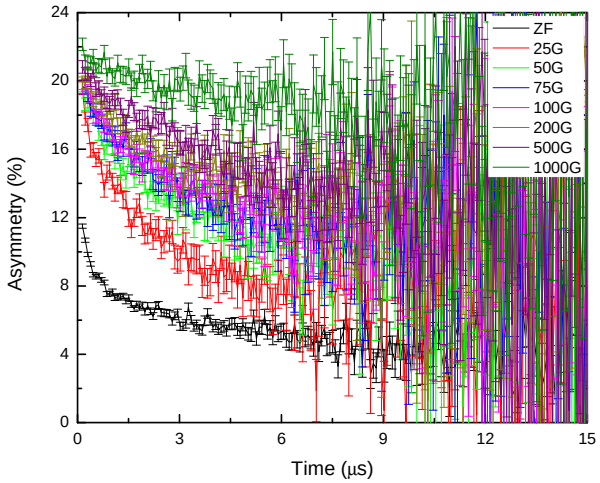

Figure C.2: μSR spectra for KTCNQ-H_4 at 225 K with an applied field.

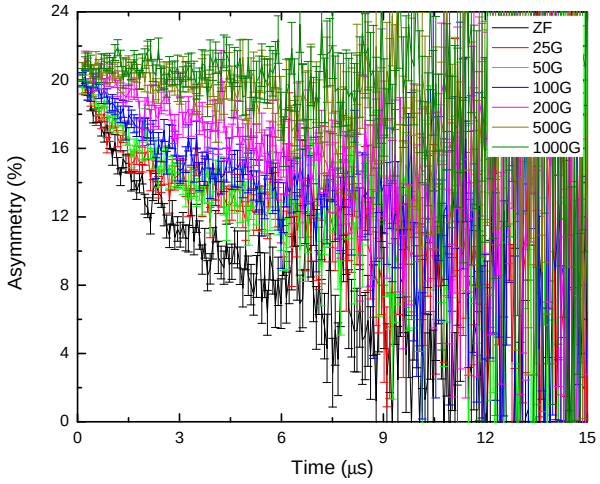

Figure C.3: μSR spectra for KTCNQ-H_4 at 340 K with an applied field.

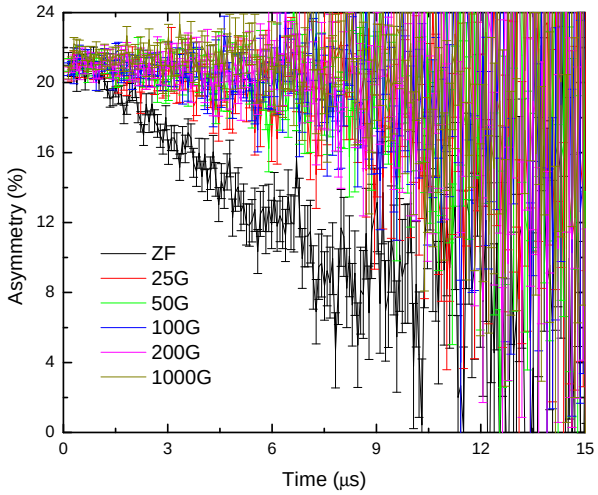

Figure C.4: μSR spectra for KTCNQ-H_4 at 410 K with an applied field.

C.2 KTCNQ-F_4 μSR Measurements

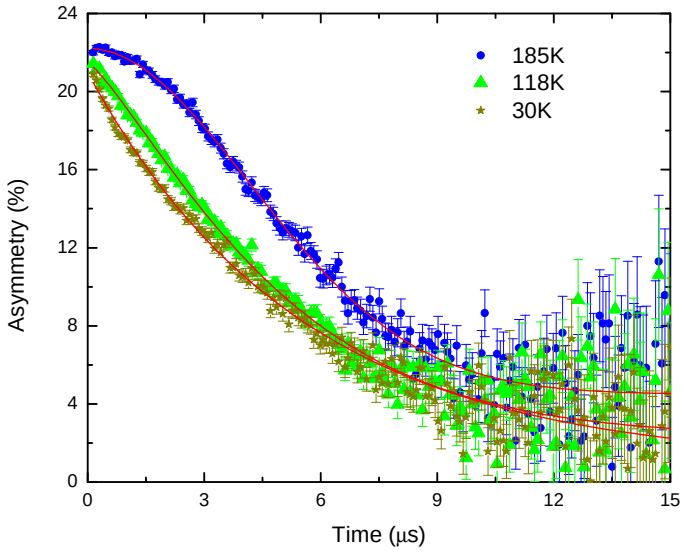

Figure C.5: ZF μSR spectra for KTCNQ-F_4. The solid lines show the fits to the data.

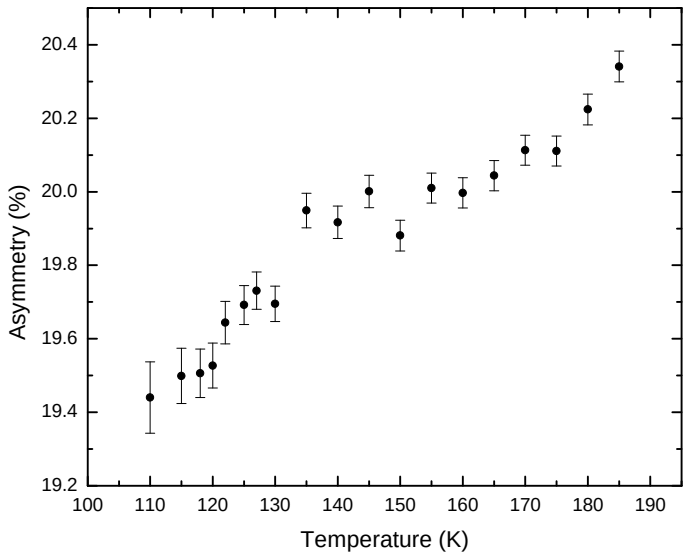

Figure C.6: Asymmetry vs. temperature for the ZF μSR experiment on KTCNQ-F_4.

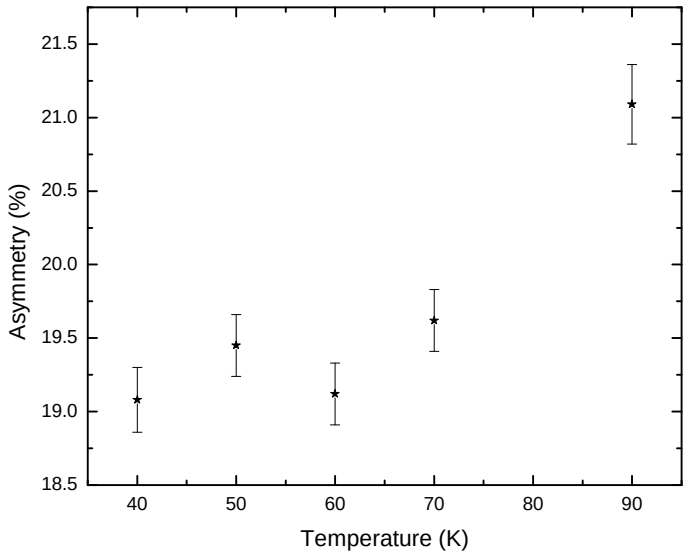

Figure C.7: Asymmetry vs. temperature for the ZF μSR experiment on KTCNQ-F_4 at Low Temperatures.

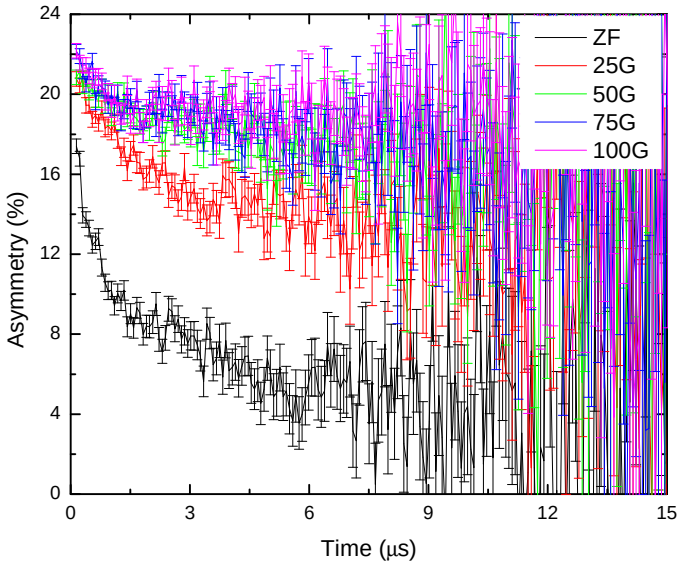

Figure C.8: μSR spectra for KTCNQ-F_4 at 30 K with an applied field.

Appendix D

Data From Magnetic Measurements of the $Ni_x{\cdot}yTCNQF_4$ Magnetic Materials

Within this appendix can be found the measurements on the other samples of the Ni and $TCNQF_4$ based magnetic materials. These are the samples made using the mixture of solvents THF/DCM (sample 2), THF/DCB (sample 3) and THF/PhCN (sample 5). As one can see the data for samples 2 and 3 are very similar to that of sample 1 and sample 5 is similar to sample 3 hence the same behaviour is present for their counterparts presented in the main text of the chapter.

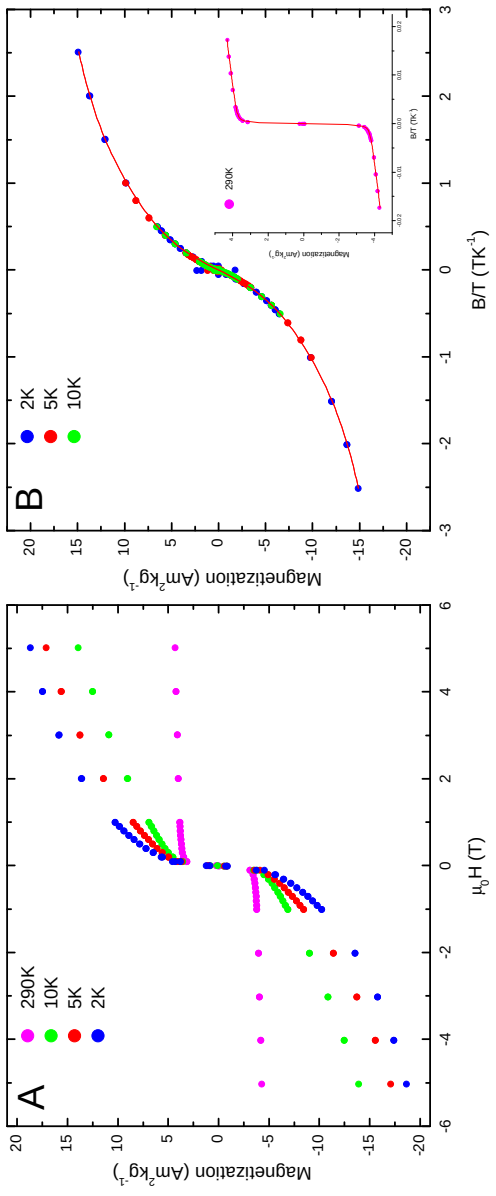

Figure D.1: **A:**Magnetization vs. applied field for sample 2 (solvents: THF/DCM). **B:** M vs. B/T where once the magnetization from the Langevin component has been subtracted the low temperature data can be scaled onto the 2 K curve. *inset:* Langevin function and a linear component fit to the 290 K data when plotted as M vs. B/T.

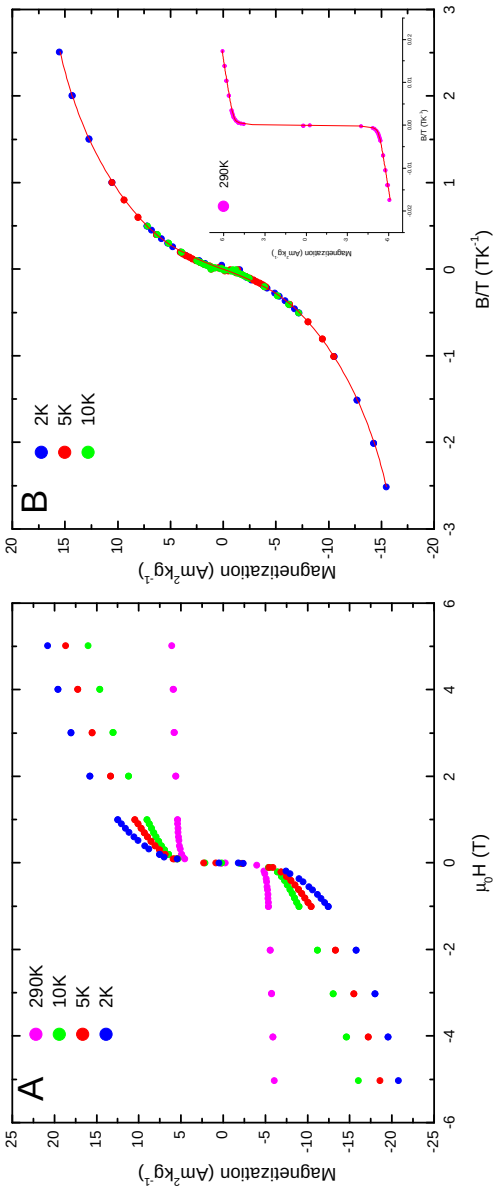

Figure D.2: **A:**Magnetization vs. applied field for sample 4 (solvent: THF/DCB). **B:** M vs. B/T where once the magnetization from the Langevin component has been subtracted the low temperature data can be scaled onto the 2 K curve. *inset:* Langevin function and a linear component fit to the 290 K data when plotted as M vs. B/T.

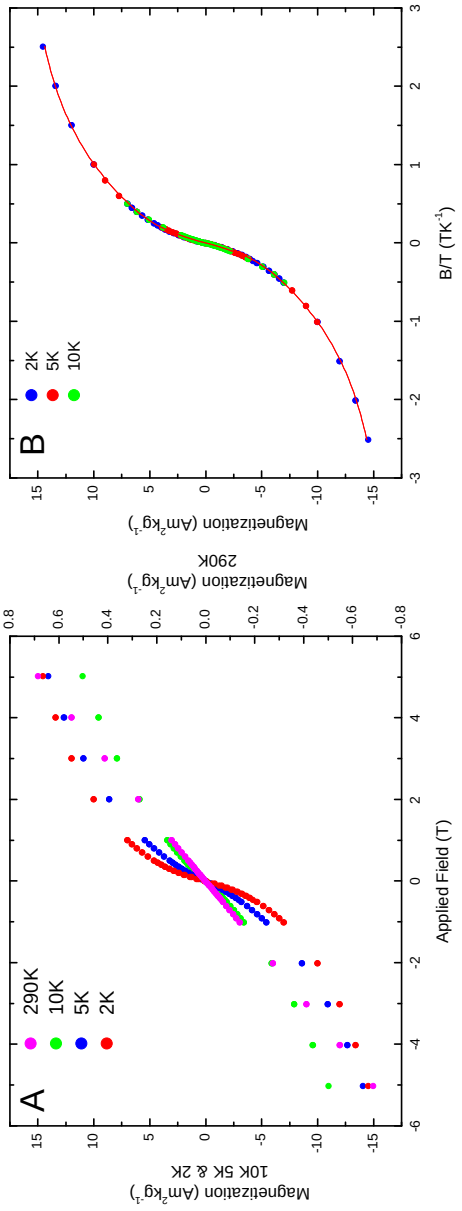

Figure D.3: **A:** Magnetization vs. applied field **B:** A scaled M vs. B/T plot for sample 5 (solvent: THF/PhCN). The fit to the data is a two-term Langevin function.

Appendix E

Supplementary Data for Low Moment Clusters Within $Ni(COD)_2$

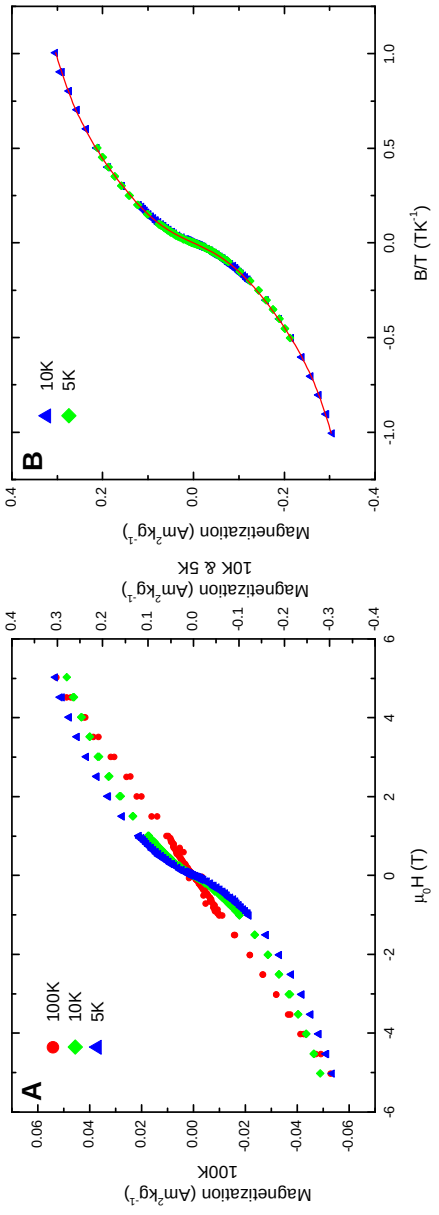

Figure E.1: **A:**Magnetization vs. applied field for Batch 2 **B:** A scaled plot of magnetization vs. B/T.

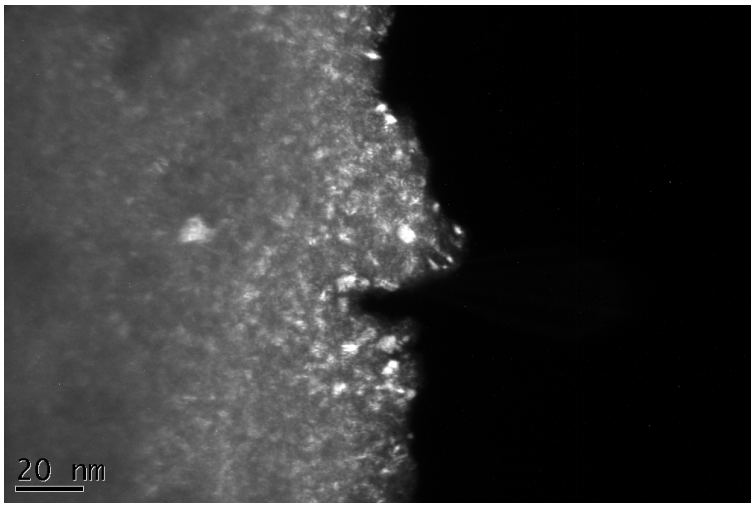

Figure E.2: Dark field image of Ni particles formed from the beam induced decomposition within the TEM

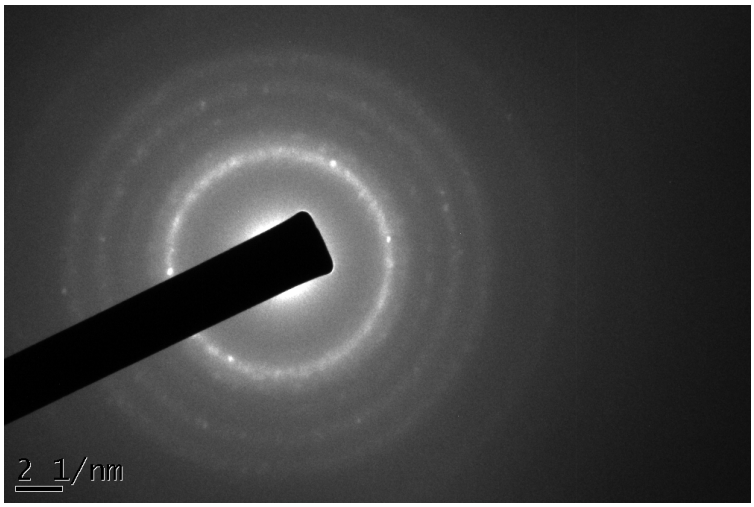

Figure E.3: Electron diffraction pattern of Ni particles formed from the beam induced decomposition within the TEM

Chapter 10

PhD: A History (via Marek Szablewski)

Abraham Duhan

Dr. Med, Professor of Philosophy

Nicaise Le Febvre *FRS*

1610-1669

b. Sedan - France

d. London - England

Apothecary

Christopher Glaser

1615 - 1672(?)

b. Basel - Switzerland

Apothecary - Paris

Nicolas Lemery

1645 - 1715

b. Rouen - France

Dr. Med: - 1683 Caen

J. G. Spitzley

b. Germany

Apothecary - Paris

Guillaume-Francois Rouelle

1703 - 1770

b. Caen - France

Company of Apothicaires - Paris 1750

Jean-Baptiste Michel Bucquet

1746 -1780

b. Paris - France

Dr. Regent Faculty of Nedcine, Paris 1769

"An digestio alimentorum, vera digestio chymica?"

Antoine de Fourcroy

1755 - 1809

b. France

Dr. Med: - 1780 Paris

Nicolas Louis Vauquelin

1763 - 1829

b. St. Andre d'Hebertot - France

Dr. Med: - 1790 Ecole Polytechnique Paris

Fredrich Störmeyer

1776 - 1835

b. Göttingen - Germany

Discovered cadmium 1817

Dr. Med: - 1800 Göttingen

Robert Wilhelm Eberhard Bunsen

1811-1899

b. Göttingen - Germany

Inventor of Spectroscopy

PhD: - 1830 Göttingen

"Enumeratio ac descriptio hygrometrorum"

Richard Anschütz

b. Darmstadt - Germany

Assistant to and successor of Kekulé in Bonn

PhD: - 1874 Heidelberg

Insigni cum laude

Sir Eric Ridal *FRS*

1890 - 1974

b. Sydenham - England

1st PhD student R. E. W. Norrish, Nobel Laureate in chemistry 1967

PhD: - 1912 Bonn

"Das elechtrochemische verhalten des urans und seiner verbindungen"

Daniel Douglas Eley *FRS*

1914 -

b. Wallasey - England

PhD: - 1937 Manchester University

"On some catalytic reactions at gas-solid interfaces"

Martin Willis

1934 -

PhD: - 1959 Nottingham University

"Some properties of organic solids"

Geoffrey Joseph Ashwell

1947 -

b. London - England

PhD: - 1972 - Nottingham University

"Conduction and thermoelectric effects in TCNQ complexes"

Marek Szablewski

1963 -

b. Sheffield - England

PhD: - 1991 Cranfield University

"Multi-functional D-π-A materials for molecular electronics"

Adam Berlie

1985 -

b. London - England

PhD: - 2013 Durham University

"A study of magnetic materials based upon the organic acceptor 7,7,8,8-tetracyanoquinodimethane"